Satellite Galaxies in the Local Group: CDM subhaloes or Tidal Dwarf Galaxies ?

Dissertation

zur

Erlangung des Doktorgrades (Dr. rer. nat.)

der

Mathematisch-Naturwissenschaftlichen Fakultät

der

Rheinischen Friedrich-Wilhelms-Universität Bonn

vorgelegt von

Manuel Metz

aus

Kirchen / Sieg

Bonn, April 2008

Angefertig mit Genehmigung der Mathematisch-Naturwissenschaftlichen Fakultät der Rheinischen Friedrich-Wilhelms-Universität Bonn

1. Gutachter:	Prof. Dr. Pavel Kroupa
2. Gutachter:	Prof. Dr. Klaas S. de Boer
Tag der Promotion:	18.8.2008

Diese Dissertation ist auf dem Hochschulschriftenserver der ULB Bonn unter `http://hss.ulb.uni-bonn.de/diss_online` elektronisch publiziert.

Erscheinungsjahr: 2008

for Ann-Kristin

Contents

Chapter 1

Introduction

1.1 Galaxies: giants and dwarfs in our Universe

Our Universe is populated by an immense number of galaxies of various morphological types and a large range of masses. Based on their appearance, probably the most impressive ones are the large, gas-rich spiral galaxies, which are also the most abundant class of the large galaxies in the Universe. The other major class of galaxies are ellipticals, the most massive ones being typically found in the central regions of galaxy clusters. Much more numerous are, however, the less massive, so called dwarf galaxies. To understand the growth and evolution of the structure in the Universe galaxies are probably the most important probes, as they contain most of the ordinary matter emitting detectable radiation. The analysis of the dynamics of galaxies in clusters, for example, led Zwicky (1933) to conclude that there must be some kind of undetectable matter – nowadays called "dark matter" – that gravitationally holds together the galaxies in a cluster.

Great observational progress in the research of the distribution of visible matter has been made in the recent years due to large galaxy surveys, in particular the Sloan Digital Sky Survey and the 2-degree Field Galaxy Redshift Survey (York et al. 2000; Colless et al. 2001). Together with other measurements, for example of the fluctuations in the cosmic microwave background radiation (Spergel et al. 2007), these observations contributed to the manifestation of a "cosmological standard model" that is believed to be our currently best prescription for the evolution of the Universe. In this theory, the cosmos is *not* dominated by gas, stars, and galaxies, but by the mysterious dark matter and an even more mysterious dark energy (Peebles & Ratra 2003). Since the early 80s it has also become possible to numerically simulate the growth of cosmic structure with continuously increasing resolution (for example Springel et al. 2005), due to the enormous development of computational power and storage capacity. Starting from some reasonable initial conditions, the motion of dark matter particles that interact merely gravitationally is integrated forward in time. This class of simulations was entitled "cold dark matter" simulations, because the particles have small initial velocities, and velocity is associated with temperature akin to thermodynamics.

1.1.1 Galaxies in the context of CDM

According to **cold dark matter** (CDM) simulations of the large-scale pattern in the Universe, the growth of structure proceeds via a hierarchical sequence of condensations and collapses driven by gravity. Instabilities, perturbations, and torques in the accretion process generate filamentary-like networks that agree remarkably well with the observed distribution of galaxies from large-scale redshift surveys, the "cosmic web". Initially small **dark matter haloes**, formed at early epochs, subsequently merge to constitute more massive haloes. An allegory for this process is the "merger tree" as shown in Figure 1.1. In the centres of the massive haloes, luminous galaxies are located, surrounded by **subhaloes** that survived the disruptive effects during the in-fall onto their host halo.

The formation of galaxies has been a key issue in extragalactic and theoretical astronomy for several decades now, and different models for their origin have been proposed, see for example Eggen, Lynden-Bell, & Sandage (1962), Searle (1977), and White & Rees (1978). With the advent of dark matter N-body simulations in an expanding Universe, the origin of galaxies has been related to the structure formation of dark matter. If enough gas is captured in the potential well of the dark matter haloes, star formation sets in to eventually form the galaxies we see today. In modern high resolution CDM simulations, baryonic physics is accounted for by different methods, like semi-analytic galaxy formation models or smooth particle hydrodynamic codes. Such simulations reproduce the large scale structure of the Universe very well, for example, in galaxy clusters. These models phenomenologically describe the dark matter – luminous matter offset, and allow for dissipative gas-dynamical effects, but do by no means have sufficient detail to model individual molecular clouds or star clusters.

On smaller scales there remain, however, some inconsistencies with CDM predictions that are difficult to address today. CDM simulations predict that the dwarf galaxies should be some of the most dark matter dominated objects, and that they should have cuspy density profiles, i.e. steeply rising mass densities in the central regions of dark matter haloes, whereas the profiles inferred of well-observed dwarf spheroidal galaxies and the rotation curves of low surface brightness galaxies show them to have flat inner density profiles (van den Bosch et al. 2000; Palma et al. 2003; Wilkinson et al. 2006). Independent evidence comes from the persistence of globular clusters belonging to the Fornax dwarf galaxy (Goerdt et al. 2006). Recent observational constraints imply that perhaps warm dark matter may need to be considered as a viable alternative to explain these findings (Gilmore et al. 2007). The small number of observed dwarf galaxies is likewise difficult to account for in the CDM picture. There appears to be a lack of dwarf galaxies in the void regions that are enclosed by the high density filamentary network structures (Peebles 1989), and the number of observed satellite galaxies around the Milky Way and Andromeda, about two dozen, and other large galaxies is significantly smaller than the number of dark matter subhaloes expected, about 500, as predicted by models (Klypin et al. 1999; Moore et al. 1999). The latter, so-called "missing satellite problem", is usually addressed by invoking small-scale baryonic processes that suppress star formation in low mass subhaloes (Kazantzidis et al. 2004a, and references therein). In recent years, a lot of effort has been made to push the limits of CDM simulations to make better predictions of luminous CDM sub-structures within Milky Way sized host-haloes (Moore et al. 2006; Mashchenko et al. 2007) and to

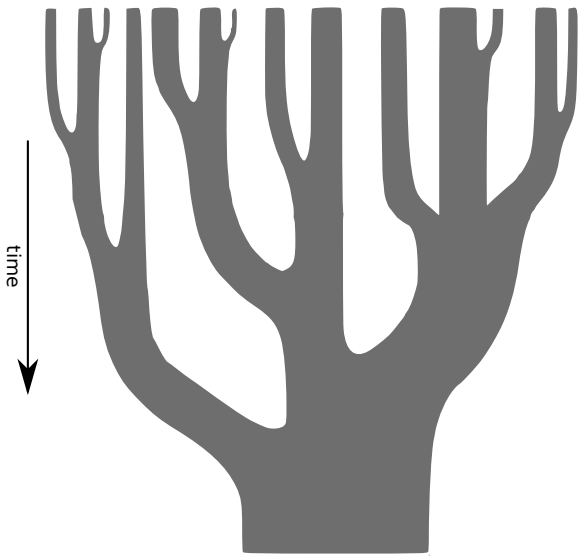

Figure 1.1: Schematic drawing of a cosmological dark matter dominated "merger tree", reproduced after Lacey & Cole (1993). Time increases from top to bottom. As dark matter structures merge they subsequently form more massive haloes – masses are represented by the width of the branches – until they reach the final mass of today, which is at the root of the tree.

address the small scale phenomena, but resolution on galaxy-size scales is still poor. Galaxy formation models must therefore be tuned by hand to match with observations (Springel et al. 2006), since the formation process is way to complex to be understood in its entirety, and to be fully modelled from basic physical assumptions alone.

1.1.2 Dwarf galaxies in the Local Group

The Local Group, first pointed out by Hubble in 1936 as "a typical, small group of nebulæ", is an exceptional place to study the properties of galaxies and their environment in detail (see Mateo 1998; van den Bergh 1999). It is an ordinary, loose collection of two large spiral galaxies, the **Milky Way** and its "sister" the **Andromeda** galaxy, as well as of the smaller spiral Messier 33, and of about 50 **dwarf galaxies** in total. While the Magellanic Clouds are visible by the unaided eye in the southern hemisphere, most of the dwarf galaxies were detected on photographic plates (Shapley 1938; Wilson 1955), since they are typically faint and extended objects. For an example see the Ursa Minor dwarf galaxy in Figure 1.2. The total number of known dwarf galaxies in the Local Group has significantly increased in the last three years: about one dozen very faint, diffuse **dwarf spheroidal galaxies** were discovered with help of the Sloan Digital Sky Survey catalogue data to surround the Milky Way. Similarly a number of dwarf spheroidals were discovered in the vicinity of Andromeda (e.g. Belokurov et al. 2006; Majewski et al. 2007, and references therein).

Local Group dwarf galaxies are unique laboratories to study galaxies in detail, since they are close enough to resolve their stars individually. They are massive enough to have possibly kept back gas in the past for a long time, fuelling star formation processes, and

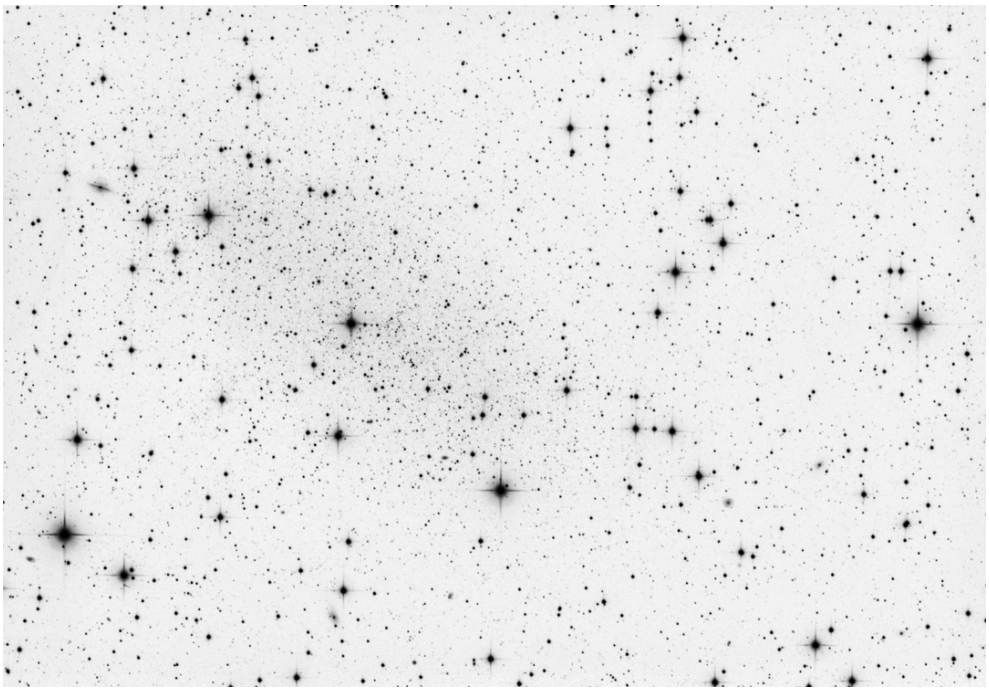

Figure 1.2: A sky image in the direction of the Ursa Minor dwarf galaxy. The galaxy appears as a weak over-density of stars in the left half of the image. Credits: Mischa Schirmer.

they are old enough to learn something about galaxy formation processes in the early Universe and their evolution over a Hubble time[(a)]. Because of the proximity, it is possible to precisely explore their internal properties, like radial density- and velocity profiles, star-formation histories, or the chemical enrichment of stars. In addition one can determine their distribution in space not only in projection, as is the case for distant galaxies (e.g., Holmberg 1969), but good data about their three-dimensional distribution are available. For almost all of the galaxies radial velocities are available, and for some, proper motion measurements have been achieved.

The spatial distribution of those dwarf galaxies that are believed to be gravitationally bound to the Milky Way, the **satellite galaxies** of the Milky Way, has long been known to be anisotropic. Based on spatial alignments it was postulated that some dwarf galaxies, along with several globular clusters, belong to one or two streams of co-moving objects (Kunkel & Demers 1976; Lynden-Bell 1976). Lynden-Bell (1983) first suggested that these co-moving galaxies might be tidally torn off a common progenitor galaxy, an interpretation that was later constrained incorporating radial velocity and proper motion data (Lynden-Bell & Lynden-Bell 1995; Palma et al. 2002). With the advent of large cosmological simulations the idea of Lynden-Bell was, however, often overlooked, since the dwarf galaxies were naturally identified with accreted cosmological sub-structures. Kroupa, Theis, & Boily (2005) highlighted this issue again, pointing out that the spatial alignment of the satellite galaxies can be best represented by a great plane, highly inclined to the Milky Way's stellar

[(a)]The inverse of the Hubble constant H_0 provides an estimate for the age of the Universe; $H_0 = 75\,\mathrm{km\,s^{-1}\,Mpc^{-1}} \Rightarrow t_{H_0} \approx 1.3 \times 10^{10}$ yrs, 13 billion years.

disc. They deemed this to be incompatible with dark matter dominated satellites. This work led to several direct replies attempting to explain the great plane within the picture of the dwarf galaxies being dark matter dominated sub-structures (e.g. Kang et al. 2005; Zentner et al. 2005; Libeskind et al. 2005).

Similarly to the Milky Way satellite galaxy system, the companions of Andromeda appear to be anisotropically distributed as well (Hartwick 2000), and there are indications for a plane-like structure of a subsample of dwarf elliptical and dwarf spheroidal galaxies (Grebel et al. 1999; Koch & Grebel 2006). It has also been shown that the satellite system as a whole is skewed in the direction of the barycentre of the Local Group, a finding for which no plausible solution emerges today. Possible streams of galaxies were identified too, most of them are likely to be unreal but just chance alignments (McConnachie & Irwin 2006b).

1.1.3 Possible origin of dwarf galaxies

There are two fundamentally different origins of dwarf galaxies. As aforementioned, in the context of CDM theory, dwarf galaxies are often thought of to reside in the centres of dark matter haloes formed in the early Universe. As such they would be cosmological building blocks, subhaloes that have not yet merged but survived as leftovers of the early halo formation process until the present. Within this scenario, the anisotropic appearance of the Milky Way satellite galaxies might be directly related to a prolate shape of the Milky Way dark matter halo (Hartwick 2000), but there are also other contradicting findings for the halo shape (e.g. Ibata et al. 2001b; Helmi 2004b; Fellhauer et al. 2006). An anisotropy can also emerge because of preferred mass accretion along filaments. If the orientation of the halo is governed by the direction of preferred mass accretion, this leads to an alignment of the subhalo distribution with the major axis of the parent halo (Knebe et al. 2004), and there might be a correlation to the surrounding larger-scale filamentary matter distribution, the super-galactic plane (de Vaucouleurs et al. 1991).

A very different possible origin for dwarf galaxies arises from fundamental physical principles, conservation of energy and angular momentum. As already pointed out by Zwicky (1956), galaxies can be anti-hierarchically formed: interacting gas-rich galaxies throw out long, thin tidal arms of gaseous and stellar material which fragments, collapses, and forms new bound stellar systems, so-called **tidal dwarf galaxies** (TDG, Mirabel et al. 1992), as is for example shown in Figure 1.3. This process is observed to occur in the local and in the distant Universe (Hunsberger et al. 1996; Duc & Mirabel 1998; Weilbacher et al. 2000; Straughn et al. 2006), whereby the efficiency of the production of TDGs is expected to be higher in the early Universe due to a larger gas content. High resolution images show young tidal dwarf galaxy candidates to consist of star-cluster complexes, a star formation mode typical for intense starbursts (Whitmore et al. 2005; Jarrett et al. 2006). Such star-cluster complexes generally survive the first few hundred Myr, and can evolve into dwarf spheroidal like galaxies (Kroupa 1997, 1998; Fellhauer & Kroupa 2002b, 2005). TDGs may significantly contribute to dwarf galaxy populations in different environments: it has been suggested that half, or even all of the dwarf galaxies could be of tidal origin under standard cosmological structure formation conditions (Hunsberger et al. 1996; Okazaki & Taniguchi 2000). Notably, because the tidal tail is located within the orbital plane of the interaction event, tidal dwarf galaxies born in one single event are expected to be anisotrop-

Figure 1.3: The Tadpole galaxy (UGC 10214). Tidal arms are drawn out of the galaxy due to an interaction process. The two panels on the right side show enlargments of star forming regions in the tidal arms. Credit: NASA, H. Ford (JHU), G. Illingworth (UCSC/LO), M.Clampin (STScI), G. Hartig (STScI), the ACS Science Team, and ESA.

ically distributed in space. An anisotropy might persist for a long time if the orbits do not substantially precess, or are significantly perturbed by external interactions.

The formation of tidal dwarf galaxies is evident in simulations of gas-rich galaxy encounters as well (Barnes & Hernquist 1992; Bournaud & Duc 2006; Wetzstein et al. 2007). In these computer models it is found that tidal dwarf galaxies have a large fraction of gas, leading to a prolonged star-formation, but they are basically devoid of dark matter. Even so tidal dwarf galaxies do not reside in the deep potential well of a dark matter halo, the gas is not inevitably removed immediately with the onset of feedback processes from massive stars and supernovae (Recchi et al. 2007). Unfortunately, very little is de facto known about the longterm evolution and fate of tidal dwarf galaxies. Computations have demonstrated the possible existence of long-lived TDGs on orbits about the main, merged galaxy (Bournaud & Duc 2006). These particular simulations did, however, not have good enough resolution to examine properties of lower mass objects or objects that dropped below a mass limit, 10^8 $M_{\odot}$, which is in comparison with the Local Group of the order of $\sim$ 100 times more massive than a typical dwarf spheroidal galaxy. Thus, the longterm evolution currently needs to be studied separately. In this way it has been found that in the vicinity of a massive galaxy, after several orbits, dark matter free dwarf galaxies may be found to be out of dynamical equilibrium, and being significantly perturbed instead (Kroupa 1997; Fleck & Kuhn 2003).

1.2 Motivation and aim of this work

These studies presented here were motivated by the idea to use the Local Group satellite galaxies as probes of dwarf galaxy formation processes within the framework of the hierarchical structure formation theory. As the Local Group dwarf galaxies are not unambiguously verified to be dark matter dominated, their three-dimensional and global kinematic properties are a part of the evidence to discriminate the two building mechanisms of dwarf galaxies described above: cosmological building blocks or tidal dwarf galaxies? The work presented here aims at performing a thorough study of observed spatial, kinematic, and dynamic properties of the Milky Way and Andromeda satellite galaxies in comparison to theoretical models.

The spatial distribution of the satellite galaxies is studied in Chapter 2. A statistical method is presented that allows to test the hypothesis of the three-dimensional distribution of the satellite galaxies being drawn randomly from a given parent distribution. The method is applied to the Milky Way and Andromeda satellite galaxy system. Until now, the Milky Way and Andromeda have been studied separately only. This is the first consistent analysis of both systems using the same statistical methods.

Given that the satellite galaxies are not isotropically distributed, we address in Chapter 3 the question whether this anisotropy is a signature of a correlated motion of the satellites. For eight Milky Way satellite galaxies proper motion measurements are available that allow us to study their orbital properties. Such an analysis is not possible for the Andromeda system, but its different observing geometry allows us to restrict the possible orbits of its satellite galaxies, which in turn makes it possible to draw conclusions on possible correlations of the orbits.

Both aspects, the spatial distribution and the orbital properties, are tested in Chapter 3 for the outcome of a recent cold dark matter simulation that incorporated a galaxy formation model and was tailored specifically to solve the Milky Way satellite problem. The results are compared to the properties of the Milky Way satellite galaxy system.

Finally we address the question whether observed quantities, internal dynamical and structural properties, of the satellite galaxies can be explained by dark matter free galaxy models in Chapter 4. For this purpose we analyse internal properties of model galaxies, initially set up to resemble tidal dwarf galaxies that orbit in the gravitational potential of a host galaxy.

A new program, SUPERBOX^{++}, was developed as described in Chapter 5. This software can be used to study problems of collisionless galactic dynamics such as the long-term evolution of tidal dwarfs galaxies. An emphasis was made to optimise the code for modern computer architectures, while at the same time keeping it portable for various operating systems.

Chapter 2

Analysis of the spatial distribution of satellite galaxies

The three-dimensional distribution of the Milky Way (MW) satellite galaxies has long been known to show asymmetric patterns (Kunkel & Demers 1976; Lynden-Bell 1976; Majewski 1994; Hartwick 2000; Kroupa, Theis, & Boily 2005). The degree of this anisotropy is esteemed very differently: being an effect of small number statistics, showing signs of the underlying dark matter distribution, or being incompatible with CDM substructures. Similarly, the satellite galaxies of Andromeda (M31) seem to have an anisotropic distribution as well (Grebel et al. 1999; Hartwick 2000; Koch & Grebel 2006).

In the following the spatial distribution of both major Local Group galaxies, the Milky Way and Andromeda, is investigated using the same analysis methods, allowing a direct comparison of the properties of their satellite distribution. The mathematical methods used to fit a plane are described (§2.1.1), and we discuss the problematic nature of methods that quantify a plane-fit based on some measure of its "thickness" alone (§2.1.2). A method to analyse the data based on bootstrapping (§2.1.3) is introduced. In order to study the three-dimensional distribution of the M31 satellite galaxies a transformation to an Andromeda-centric coordinate system is given in the most general way (§2.1.4). These methods are finally applied to analyse the data for the Milky Way (§2.2) and Andromeda (§2.3) satellite galaxy systems in a consistent manner, and we derive the statistical significance of disc-like distributions of satellite galaxies (§2.4).

2.1 Methods for the analysis of spatial data

2.1.1 Plane fitting algorithms

One method to fit a plane to spatial data is known as an algebraic least-squares (ALS) estimator method (see, e.g. Chojnacki et al. 2000), and is similar to the algorithm used by other authors (e.g. Dubinski & Carlberg 1991; Hartwick 2000; Libeskind et al. 2005). The ALS fitting method is an unweighted fitting algorithm. First the centroid of the data points, $\boldsymbol{m}_0$, with components (x_0, y_0, z_0), is calculated. Next an eigenvalue analysis of the matrix T_0

defined as

$$\mathsf{T}_0 = \mathsf{M}_0{}^{\mathsf{T}}\mathsf{M}_0 \quad , \tag{2.1}$$

with

$$\mathsf{M}_0 = \begin{pmatrix} x_1 - x_0 & y_1 - y_0 & z_1 - z_0 \\ x_2 - x_0 & y_2 - y_0 & z_2 - z_0 \\ \vdots & \vdots & \vdots \\ x_\mathrm{N} - x_0 & y_\mathrm{N} - y_0 & z_\mathrm{N} - z_0 \end{pmatrix} \tag{2.2}$$

is performed. Here $(x_\mathrm{i}, y_\mathrm{i}, z_\mathrm{i})$ are the components of a vector pointing from the host galaxy centre to the ith satellite, N is the number of satellites. T_0 is sometimes called the moment of inertia tensor. The eigenvector corresponding to the smallest eigenvalue of T_0 is the normal of the plane and the plane contains the centroid $\boldsymbol{m}_0$. Incorporating the centroid of the data ensures that we really find the plane that has the minimum orthogonal distance to the satellites. Not considering the centroid results in forcing the plane to pass through the coordinate origin instead, i.e. a great plane or great circle fit is performed. The latter is done by most authors when calculating the moment of inertia tensor.

Since the ALS method is an unweighted fitting routine, distance uncertainties are accounted for by a Monte-Carlo method, which we refer to as the applied error (AE) method in the following: all satellites are individually randomly shifted along their line-of-sight with a normal distribution function as the probability function of the magnitude of the shift. The variance of the normal distribution used for the shifting is derived from the distance uncertainty of the measurements. The random shifting is repeated a large number (10^4) of times. For the analysis of the distribution of derived normals of the fitted planes, the same analysis techniques as described below (§2.1.3) for the bootstrap re-sampling method are employed. We note that there are schemes to introduce a weighting in ALS (e.g., Hartwick 2000; Zentner et al. 2005), but as a drawback this also influences the direct interpretation of the derived axis-ratios (see below).

As our second method to fit planes we have implemented a weighted fitting routine based on the orthogonal distance regression (ODR) package provided by Netlib (`http://www.netlib.org/odrpack`). An unweighted fit with the ODR method (i.e. setting all uncertainties equals zero) provides the same result as the (much faster) ALS method. The weights are distance uncertainties in our application. This algorithm is a little bit subtle since it also tries to estimate the errors of the fitted parameters. Even though the fitting parameters converge, the error estimate may not, which can be understood as having weak constraints on the fitting parameters. This only happened in special cases and never when applied to the satellites of the Milky Way or Andromeda directly. Further, the solution provided by ODR is strongly dependent on the weights used. The Cartesian variances σ_x^2, σ_y^2, and σ_z^2 derived from the distance uncertainty σ_r are not independent. Using the variances only leads to a different fit than using the full covariance matrix. Thus, we always use the full covariance matrix, accounting for correlations of the components.

As an example we give the covariance matrix C as derived for Sagittarius and the re-

sulting weight matrices $\mathsf{W} = \mathsf{C}^{-1}$, (a) with and (b) without covariances:

$$\text{(a)} \qquad \mathsf{C} = \begin{pmatrix} 3.73 & 0 & 0 \\ 0 & 0.04 & 0 \\ 0 & 0 & 0.24 \end{pmatrix} \quad \rightarrow \quad \mathsf{W} = \begin{pmatrix} 0.27 & 0 & 0 \\ 0 & 27.9 & 0 \\ 0 & 0 & 4.21 \end{pmatrix}$$

$$\text{(b)} \qquad \mathsf{C} = \begin{pmatrix} 3.73 & -0.12 & 0.31 \\ -0.12 & 0.04 & 0.03 \\ 0.31 & 0.03 & 0.24 \end{pmatrix} \quad \rightarrow \quad \mathsf{W} = \begin{pmatrix} 0.40 & 2.05 & -0.79 \\ 2.05 & 41.9 & -8.13 \\ -0.79 & -8.13 & 6.32 \end{pmatrix} \quad .$$

To demonstrate the influence of the covariances, plane-fits using the ODR method were performed for M31, with and without considering the covariances for various subsets of satellite galaxies. This led to differences in the directions of the normals of the fitted planes typically of the order of 3° to 5°, but up to 17°.

These two fitting algorithms, ALS and ODR, are used because the method described in Kroupa et al. (2005) based on a least-squares linear regression is suboptimal in finding the plane with minimal *orthogonal* root-mean-square height of the satellites, which does, however, not affect the basic argumentation by Kroupa et al. (see also Feigelson & Babu 1992, who discuss the possibly very different results for various linear regression fitting methods).

Koch & Grebel (2006) also used an algorithm based on the ODR method, performing a great-circle fit rather than a plane fitting, i.e. forcing the fitted plane to pass through the centre of the host galaxy as can also be done for the ALS method. They stated that they found a scatter of 5° – 10° between the directions of the normals when rotating their data-set about pairs of random angles compared to the input angles. This is incomprehensible since a plane-fitting algorithm should not be dependent on the spatial orientation of the data points; the fits should be invariant under rotation. We can only conjecture about possible reasons for their finding.

2.1.2 Flatness parameter

One measure of the planarity of the distribution of satellite galaxies is the flattening-parameter $\Delta/r_{\rm cut}$ as given in Kroupa et al. (2005). Δ is the root-mean-square (rms) height of the disc and $r_{\rm cut}$ is the furthest distance to the Galactic Centre in the satellite sample. The alternative flattening-parameter $\Delta/r_{\rm med}$ as suggested by Zentner et al. (2005) is also a measure of the planarity, where $r_{\rm med}$ is the median distance to the Galactic Centre of a sample. Kang et al. (2005) gave a formula to calculate the flattening-parameter $\Delta/r_{\rm cut}$ for an analytic r^{-q}, $q \in \mathbb{R}$, distribution (their equation 1): $\Delta/r_{\rm cut} = (3-q)/(3(5-q))$. This formula is correct under two conditions only: first the analytic formula describes a spherical spatial density distribution (see below) and second the power-law index q is < 3. Here, we derive a more general formula for the rms-height.

The radial distance distribution of the Milky Way satellite galaxies is found to follow a *linear* power-law density distribution, $\rho(r)\,dV \propto r^{-p}$, $dV = dx\,dy\,dz$, with an index $p \approx 2$ (Kroupa et al. 2005), where r is the distance from the Galactic Centre. This definition can lead to confusion, since most people describe radial satellite distributions as *spatial* density distributions in spherical coordinates $\rho_{\rm sph}(r)\,dV$, $dV = r^2 \sin\theta\,d\phi\,d\theta\,dr$, as Kang et al. 2005

did. Therefore we need to perform a coordinate transformation:

$$\rho_{\rm sph}(r) = \rho(r) r^{-2} \propto r^{-(p+2)} \quad . \tag{2.3}$$

For clarity the spherical spatial density function is labelled by the subscript 'sph'. Equation (2.3) is the usual coordinate transformation from Cartesian to spherical coordinates $dV = dx\,dy\,dz = r^2 \sin\theta\, d\phi\, d\theta\, dr$. In general, the root-mean-square of a distribution $f(x)$ of a continuous variant x is given by

$$R(x) = \sqrt{\frac{\int f(x) x^2 dx}{\int f(x) dx}} \quad . \tag{2.4}$$

Plugging $\rho_{\rm sph}$ (Eqn. 2.3) in and substituting $q = p + 2$ we find for the rms in the z-direction

$$\Delta = \sqrt{\frac{\int_0^{2\pi}\int_0^{\pi}\int_{r_0}^{r_{\rm cut}} \rho_{\rm sph}(r) r^{-q} z^2 r^2 \sin\vartheta\, dr d\vartheta d\phi}{\int_0^{2\pi}\int_0^{\pi}\int_{r_0}^{r_{\rm cut}} \rho_{\rm sph}(r) r^{-q} r^2 \sin\vartheta\, dr d\vartheta d\phi}} \quad , \tag{2.5}$$

where we can substitute $z^2 = r^2 \cos^2\vartheta$. Solving the integrals we find:

$$\Delta = \begin{cases} \sqrt{\frac{3-q}{3(5-q)} \frac{r_{\rm cut}^{5-q} - r_0^{5-q}}{r_{\rm cut}^{3-q} - r_0^{3-q}}} & : \quad q \neq 3,5 \\ \sqrt{\frac{1}{3(5-q)} \frac{r_{\rm cut}^{5-q} - r_0^{5-q}}{\ln|r_{\rm cut}| - \ln|r_0|}} & : \quad q = 3 \\ \sqrt{\frac{3-q}{3} \frac{\ln|r_{\rm cut}| - \ln|r_0|}{r_{\rm cut}^{3-q} - r_0^{3-q}}} & : \quad q = 5 \end{cases} \tag{2.6}$$

For $\lim_{r_0 \to 0}$ this converges to 0 for $q \geq 3$:

$$\begin{aligned} \lim_{r_0\to 0} \Delta &= \lim_{r_0\to 0} \sqrt{\frac{3-q}{3(5-q)} \frac{r_{\rm cut}^{5-q} - r_0^{5-q}}{r_{\rm cut}^{3-q} - r_0^{3-q}}} \\ &= \lim_{r_0\to 0} \sqrt{\frac{3-q}{3(5-q)}} \sqrt{\frac{\text{const} - r_0^{5-q}}{\text{const} - r_0^{3-q}}} \overset{q>3}{=} 0 \end{aligned}$$

For $q < 3$ we can set $r_0 = 0$ and find the formula as given by Kang et al. (2005).

Kroupa et al. (2005) derived a *linear* probability distribution $\rho(r) \propto r^{-p}$, $1.8 \leq p \leq 2.6$ for the Milky Way (see also Koch & Grebel 2006 for Andromeda, $1.6 \leq p \leq 2.3$), such that the spherical *volume* density is $\rho_{\rm sph}(r) \propto r^{-q}$, $3.8 \leq q \leq 4.6$. Kang et al. (2005) argued that the formally measured flattening $\Delta / r_{\rm cut}$ of a plane with infinite number of particles following a power-law distribution decreases with power-law index q and converges to zero for $q \to 3$. Indeed Δ *always* converges to zero for $r_0 \to 0$, $q \geq 3$. Δ decreases with power-law index q, but more importantly, Δ is strongly dependent on the minimum radius r_0. This will also influence *any test* that is based on the measured height alone. Nevertheless, the argument by Kang et al. (2005) that a disc-like distribution may be mimicked if the satellite distribution is centrally concentrated with one or two outliers is valid (see also Zentner et al. 2005), requiring more robust statistical methods to be launched, this being one important aim of our study.

For the ALS plane fitting method one can derive the axis-ratios c/a and b/a of the square-roots of the eigenvalues ($\tau_1 \leq \tau_2 \leq \tau_3$) of the moment of inertia tensor: $c = \sqrt{\tau_1}$, $b = \sqrt{\tau_2}$, $a = \sqrt{\tau_3}$. The values (a, b, c) are proportional to the root-mean-square deviation relative to the eigenvectors of T_0. Specifically, $c \propto \Delta$, where Δ is given as above. In addition we use the ratio c/b which indicates whether the triaxial distribution is more oblate ($c/b < b/a$) or more prolate ($c/b > b/a$). Note that this definition of "triaxial, more oblate" and "triaxial, more prolate" is different to the definition based on the triaxiality parameter as given, for example, by Franx et al. (1991). The ratio c/a is a better measurement than $\Delta/r_{\rm cut}$ and $\Delta/r_{\rm med}$ in terms of providing the ratio of the rms height in the direction of the smallest and largest extent, but can only be calculated for the ALS method. However, for a small sample, such as in the dwarf satellite application, quantities like Δ or the ratio c/a may not be a robust measure at all because of small number statistics.

2.1.3 The distribution of normal vectors of bootstrapped samples

In previous works (Hartwick 2000; Kroupa et al. 2005; Kang et al. 2005; Libeskind et al. 2005; Zentner et al. 2005; Koch & Grebel 2006) the planarity of the satellite distribution was quantified based on the 'thickness' of the distribution in relation to some measure of the total spatial extent: $\Delta/r_{\rm cut}$, $\Delta/r_{\rm med}$, or c/a. This is of course a basic requirement to call a distribution "disc-like". However, if we think of a centrally concentrated distribution, any small number of outliers will determine the orientation of the plane and we will always end up with an apparently "thin" disc as discussed in Sect. 2.1.2 (see also Kang et al. 2005; Zentner et al. 2005). Consequently additional information about the robustness of a disc-like distribution is needed to draw some statistically significant conclusions. This can be achieved using a re-sampling technique.

There are two (re-)sampling methods widely used: jackknife and bootstrap. A jackknife sample is created by leaving out one observation at a time. This is not the best method for our analysis because other outliers would still define the disc. And, because of the small number of satellites, we would have a weak statistics. Hence we use the bootstrap re-sampling method. A bootstrap sample is created by drawing *with* replacement n observations from the original sample of size n. This means that a particular bootstrap sample of $n = 15$ may, e.g., consist of five different satellites plus ten times the same satellite. This gives a large number of possible different bootstrap samples for $n \gg 1$,

$$N_{\rm tot} = \binom{2n-1}{n} \quad ,$$

e.g. $N_{\rm tot} = 77\,558\,760$ for $n = 15$.

To perform a plane fitting we need at least three different objects in a sample, which results in a smaller but still very large number of possible bootstrap samples. To correctly calculate the total number of possible distinct bootstrap samples for our application, we generally formulate this as the following question:

What is the number of ways of picking k unordered outcomes with replacement from n possibilities under the condition that at least l are different?

Without the additional condition that at least l are different, the total number is given by

$$N_{\rm tot} = \binom{n+k-1}{k} \quad . \tag{2.7}$$

We start by calculating the number of ways of picking exactly $m = l$ different outcomes. This is given by the number of ways of picking m unordered outcomes *without* replacement from n possibilities times the number of ways of picking $k - m$ unordered outcomes with replacement from m possibilities,

$$N_{m=l} = \binom{n}{m}\binom{m+(k-m)-1}{k-m} = \binom{n}{m}\binom{k-1}{k-m} \quad . \tag{2.8}$$

This can be understood as follows:

$$\overbrace{\underbrace{z_{j_1}, z_{j_2}, \ldots, z_{j_m}}_{m}, \underbrace{z_{i_1}, z_{i_2}, \ldots, z_{i_{k-m}}}_{k-m}}^{k} \quad , \quad i_l \in \{j_1, j_2, \ldots, j_m\}.$$

We first choose exactly m different outcomes from all n possibilities $z_1, z_2, \ldots, z_n$ without replacement (we want all m to be different). The number of possible outcomes is $\binom{n}{m}$. Since we wanted exactly m different outcomes we now can only choose from those m outcomes that have been chosen in the first step (so now the number of possibilities is m). The number of outcomes is iteratively calculated using Eqn. (2.8) for $m = l+1$, $m = l+2$, ..., $m = n$ and summed up:

$${}^{l}N_{\rm tot} = \sum_{m=l}^{k} \binom{n}{m}\binom{k-1}{k-m} \quad . \tag{2.9}$$

With $k = n$, and $l = 3$ in our application, we get ${}^{3}N_{\rm tot} = \sum_{m=3}^{n} \binom{n}{m}\binom{n-1}{n-m} = 77\,557\,275 < N_{\rm tot}$ for $n = 15$. Since the total number of possible distinct outcomes is typically way to large to be fully sampled, a sufficiently large sample is drawn as is the standard approach in bootstrapping.

Note that bootstrapping is different to the sampling method Koch & Grebel (2006) employed, while misleadingly referring to it as bootstrap. These authors fitted a plane through every possible combination of $3, 4, \ldots, n$ objects, an approach that is related to the jackknife method. The different sampling method may have biased their results.

The bootstrapping method allows an estimate of the robustness of a disc-like distribution. The fitting to the re-sampled data is done using the unweighted ALS method. If the satellites are not distributed in a well-defined planar-like sheet, the normals of the fitted planes should show a large scatter. *The amount of scatter of the directions of fitted normals to the bootstrapped samples is the quantity we use to determine the statistical significance of a plane-like distribution*. To test the robustness of a best fitting plane to a set of data-points we quantify the spread of distributions of normals obtained from the large number, e.g. 10 000, bootstrapping samples. A well-defined plane or disc of data points (satellites) will lead to a tight clustering of normals on the Galactic sky, while a weak disc will yield normals scattered over a large fraction of the sky.

For detailed analysis of the bootstrapped data we follow methods described in Fisher, Lewis, & Embleton (1987), see also Mardia & Jupp (2000). The methods described below are only valid for a sample of unit vectors representing axial data, i.e. undirected data. For the present purpose the orientation of the normal of a plane is arbitrary that is, the normal vector $\boldsymbol{n}$ represents the direction of an axis. A matrix U is defined as

$$\mathsf{U} = \begin{pmatrix} \hat{x}_1 & \hat{y}_1 & \hat{z}_1 \\ \hat{x}_2 & \hat{y}_2 & \hat{z}_2 \\ \vdots & \vdots & \vdots \\ \hat{x}_\mathrm{m} & \hat{y}_\mathrm{m} & \hat{z}_\mathrm{m} \end{pmatrix} \quad , \tag{2.10}$$

where $(\hat{x}_i, \hat{y}_i, \hat{z}_i)$ are the cartesian components of unit vectors $\hat{\boldsymbol{n}}_i$, m is the number of unit vectors. An eigenvalue analysis of the matrix

$$\mathsf{V} = \mathsf{U}^\mathrm{T}\mathsf{U} \tag{2.11}$$

is performed. The eigenvector corresponding to the largest eigenvalue ν_3 of V ($\nu_1 \leq \nu_2 \leq \nu_3$) is the (estimated) *principal axis* $\boldsymbol{a}_0$ of the input unit vectors, the normal vectors $\hat{\boldsymbol{n}}_i$, and the principal axis corresponds approximately to the mean direction of the normal vectors. In our application, $\boldsymbol{a}_0$ is the principal axis of the distribution of normals of fitted planes to the bootstrapped sample and we derive its direction on the Galactic sky. The *shape* parameter γ is defined as

$$\gamma = \frac{\ln(\nu_3/\nu_2)}{\ln(\nu_2/\nu_1)} \quad , \tag{2.12}$$

and the *strength* parameter ζ is defined as

$$\zeta = \ln(\nu_3/\nu_1) \tag{2.13}$$

(Fisher et al. 1987; Mardia & Jupp 2000). These two quantities can be used to characterise a distribution of axial data on a sphere. γ describes the 'clusteriness' of the distribution. $\gamma = 1$ indicates the transition between clustered ($\gamma > 1$) and girdled ($\gamma < 1$) distributions. ζ is a continuous parameter indicating the strength of concentration: the larger ζ the more concentrated a distribution is (being clustered or girdled), a uniform spherical distribution has $\zeta = 0$.

In addition the spherical standard distance,

$$\Delta_\mathrm{sph} = \sqrt{\frac{\sum_m \left[\arccos\left(|\boldsymbol{a}_0 \cdot \hat{\boldsymbol{n}}_i|\right)\right]^2}{m}} \quad , \tag{2.14}$$

is calculated where '$\cdot$' denotes the scalar product of vectors. This is the analogue to the linear root-mean-square distance on the sphere. Since we deal with axial data we have to take the absolute value of the scalar product in Equation (2.14). The spherical standard distance implies rotational symmetry but can be considered as an estimate of the upper limit of the opening angle of a sample of normal vectors for non rotational-symmetric distributions.

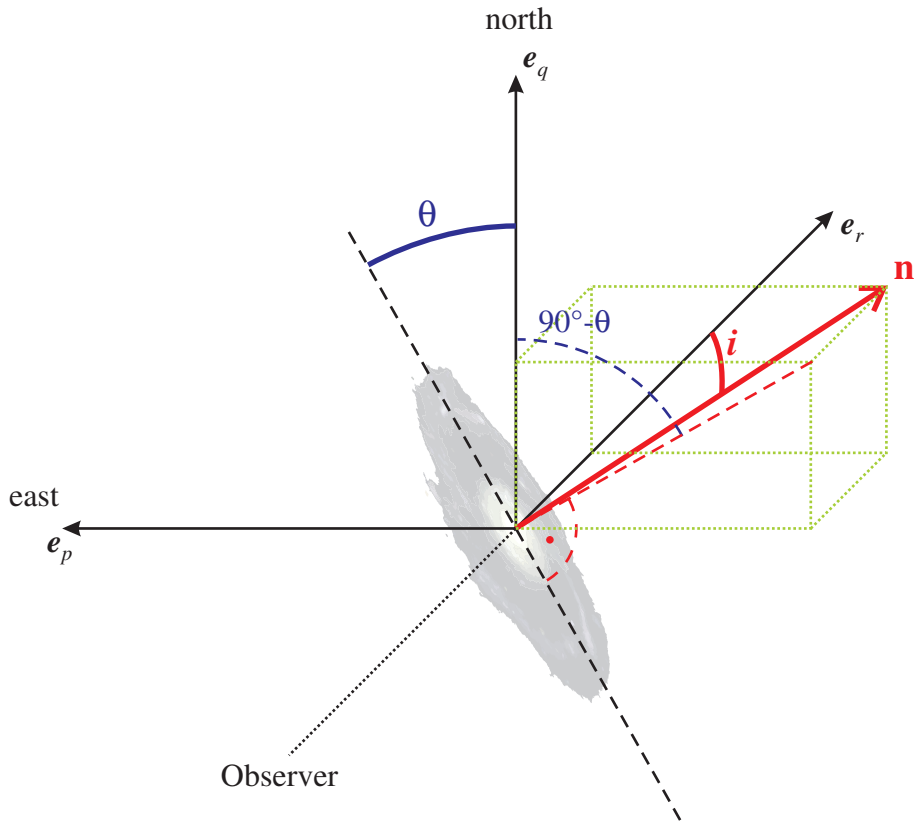

Figure 2.1: An artist's view showing the orientation of the normal vector $\boldsymbol{n}$ to the equatorial plane of a distant galaxy, for example Andromeda, which is used to calculate positions in the extrasolar coordinate system. $\boldsymbol{e}_r$ is the direction from the Sun to the centre of the galaxy, $\boldsymbol{e}_p$ is parallel to the celestial equator, pointing towards east, and $\boldsymbol{e}_q$ is pointing towards the North Celestial Pole. The inclination i is the angle between the normal of the equatorial plane of the galaxy and the line-of-sight, given by $\boldsymbol{e}_r$. The position angle θ is the angle between the projected major axis of the stellar disc of the galaxy and the direction to the North Celestial Pole, conveniently measured from north through east.

2.1.4 Extrasolar celestial coordinate systems

In order to study the three-dimensional distribution and kinematics of satellite galaxies or any other object in a distant galaxy, for example Andromeda or the LMC, it is most convenient to transform their position and velocity vectors relative to the observer into a coordinate system centred on this distant galaxy. The transformation is described in the most general way, using vector and matrix operations, to allow for an as wide as possible range of applications. A mathematically equivalent, but to us less intuitive approach, is to perform all transformations using spherical geometry (see, for example, van der Marel & Cioni 2001; McConnachie & Irwin 2006b).

The basis for the transformation may be any celestial coordinate system. The origin and orientation of the target coordinate system must be given as, or transformed to (i) positional coordinates, (ii) inclination of the target system with respect to the line-of-sight, and (iii) position angle measured from north through east. The basic geometry is illustrated in

Figure 2.1. The transformation is exemplified by transforming into an Andromeda-centric coordinate system, but the algorithm is applicable to any other target system, for example an extrasolar planetary system or any other distant galaxy.

An Andromeda-centric coordinate system

Let $\left(\boldsymbol{e}_x^{\mathrm{M31}}, \boldsymbol{e}_y^{\mathrm{M31}}, \boldsymbol{e}_z^{\mathrm{M31}}\right)$ be the basis of a Cartesian coordinate system centred on Andromeda similar to the galactocentric coordinate system with basis vectors $\left(\boldsymbol{e}_x^{\mathrm{MW}}, \boldsymbol{e}_y^{\mathrm{MW}}, \boldsymbol{e}_z^{\mathrm{MW}}\right)$. We define the coordinate system such that $\boldsymbol{e}_x^{\mathrm{M31}}$ is the direction of the normal to the stellar disc of Andromeda, $\boldsymbol{e}_z^{\mathrm{M31}}$ is the projected direction from the Galactic Centre to the centre of M31 onto the disc of Andromeda (this implies that the M31 longitudinal coordinate of the Galactic Centre is $l_{\mathrm{M31}} = 180^\circ$), and $\boldsymbol{e}_y^{\mathrm{M31}} = \boldsymbol{e}_z^{\mathrm{M31}} \times \boldsymbol{e}_x^{\mathrm{M31}}$.

Equatorial coordinates can be calculated as

$$l = \arctan\left(\frac{y}{x}\right) \quad , \tag{2.15}$$

$$b = \arcsin\left(\frac{z}{x}\right) \quad , \tag{2.16}$$

$$r = \sqrt{x^2 + y^2 + z^2} \quad , \tag{2.17}$$

where x, y, z are the Cartesian components of a vector given in the galactocentric or the Andromeda-centric coordinate system. It is important to note that if we give galactocentric coordinates $(l_{\mathrm{MW}}, b_{\mathrm{MW}})$, the centre of the coordinate system is the Galactic Centre whereas the centre of the standard Galactic coordinate system (l, b) is the Sun.

The reverse transformation from equatorial to Cartesian coordinates is given by

$$x = r\,\cos b\,\cos l \quad , \tag{2.18}$$

$$y = r\,\cos b\,\sin l \quad , \tag{2.19}$$

$$z = r\,\sin b \quad . \tag{2.20}$$

To calculate the Cartesian components of a vector in the Andromeda-centric coordinate system, the heliocentric position vector $\boldsymbol{x}$ is shifted to the centre of M31 and rotated to the Andromeda-centric coordinate system,

$$\boldsymbol{r}_{\mathrm{M31}} = \mathsf{R}_{\mathrm{M31}}\left(\boldsymbol{r} - \boldsymbol{r}(\mathrm{M31})\right) \quad . \tag{2.21}$$

$\boldsymbol{r}(\mathrm{M31})$ is the heliocentric position vector of Andromeda and $\mathsf{R}_{\mathrm{M31}}$ is the appropriate rotationmatrix which is derived next.

The first step is to calculate the rotationmatrix that rotates the 'normal trial' (Murray 1983) parallel to the axes of the Cartesian coordinate system. This is given by the matrix R_{rpq}, where the columns are the triad of unit-vectors $\boldsymbol{e}_r$, $\boldsymbol{e}_p$, and $\boldsymbol{e}_q$:

$$\begin{aligned} \mathsf{R}_{rpq}(\alpha, \delta) &= \begin{pmatrix} \boldsymbol{e}_r & \boldsymbol{e}_p & \boldsymbol{e}_q \end{pmatrix} \\ &= \begin{pmatrix} \cos\delta\cos\alpha & -\sin\alpha & -\sin\delta\cos\alpha \\ \cos\delta\sin\alpha & \cos\alpha & -\sin\delta\sin\alpha \\ \sin\delta & 0 & \cos\delta \end{pmatrix} \quad . \end{aligned} \tag{2.22}$$

$\boldsymbol{e}_r$ is pointing in the direction with equatorial coordinates (α, δ), $\boldsymbol{e}_p$ is parallel to the celestial equator, positive towards the east, and $\boldsymbol{e}_q$ is pointing to the North Celestial Pole (NCP), see for example Murray (1983). Here $\left(\boldsymbol{e}_r\ \boldsymbol{e}_p\ \boldsymbol{e}_q\right)$ is the normal triad of the coordinates of M31 $(\alpha_{\rm M31},\, \delta_{\rm M31})$.

We can now construct a preliminary rotation matrix

$$\mathsf{R}'_{\rm M31} = \mathsf{R}_y(90^\circ - i)\mathsf{R}_x(90^\circ - \theta)\mathsf{R}_{rpq}(\alpha_{\rm M31},\, \delta_{\rm M31}) \quad , \tag{2.23}$$

where $\mathsf{R}_{x/y/z}(\gamma)$ are the matrices which perform a counter-clockwise rotation about the Cartesian coordinate axes by an angle γ:

$$\begin{aligned}
\mathsf{R}_x(\gamma) &= \begin{pmatrix} 1 & 0 & 0 \\ 0 & \cos\gamma & \sin\gamma \\ 0 & -\sin\gamma & \cos\gamma \end{pmatrix} \quad , \\
\mathsf{R}_y(\gamma) &= \begin{pmatrix} \cos\gamma & 0 & -\sin\gamma \\ 0 & 1 & 0 \\ \sin\gamma & 0 & \cos\gamma \end{pmatrix} \quad , \\
\mathsf{R}_z(\gamma) &= \begin{pmatrix} \cos\gamma & \sin\gamma & 0 \\ -\sin\gamma & \cos\gamma & 0 \\ 0 & 0 & 1 \end{pmatrix} \quad .
\end{aligned}$$

$\mathsf{R}_x(90^\circ - \theta)$ corrects for the position angle (see Figure 2.1). After applying this rotation the vector pointing towards the north, $\boldsymbol{e}_q$ is aligned with the projection of the normal vector onto the $(\boldsymbol{e}_p, \boldsymbol{e}_q)$ plane, which is the local approximation of the surface of the celestial sphere at the position (α, δ). $\mathsf{R}_y(90^\circ - i)$ corrects for the inclination of Andromeda. The rotation given in Equation (2.23) is preliminary because it performs a transformation such that *the Sun* is located at $l'_{\rm M31} = 180^\circ$, but we defined the Galactic Centre to be located at $l_{\rm M31} = 180^\circ$. Therefore an additional rotation has to be performed, which is of the order $\arctan\left(8.5\ \mathrm{kpc}/785\ \mathrm{kpc}\right) = 0.6^\circ$.

The procedure to calculate this angle is as follows: (i) transform the vector pointing from Andromeda to the Galactic Centre to the preliminary system

$$\boldsymbol{r}'(\mathrm{GC}) = \mathsf{R}'_{\rm M31}\left(\boldsymbol{r}(\mathrm{M31}) - \boldsymbol{r}(\mathrm{GC})\right) \quad , \tag{2.24}$$

(ii) project this vector onto the plane of Andromeda,

$$\boldsymbol{r}'_{xy}(\mathrm{GC}) = \boldsymbol{e}_x^{\rm M31}(\boldsymbol{e}_x^{\rm M31} \cdot \boldsymbol{r}'(\mathrm{GC})) + \boldsymbol{e}_y^{\rm M31}(\boldsymbol{e}_y^{\rm M31} \cdot \boldsymbol{r}'(\mathrm{GC})) \quad , \tag{2.25}$$

and (iii) calculate the angle β between this vector and the preliminary $\boldsymbol{e}_x^{\rm M31}$-axis

$$\beta = \arccos\left(\frac{\boldsymbol{r}'_{xy}(\mathrm{GC}) \cdot \boldsymbol{e}_x^{\rm M31}}{\left|\boldsymbol{r}'_{xy}(\mathrm{GC})\right|}\right) \quad . \tag{2.26}$$

The direction of the necessary rotation about the $\boldsymbol{e}_z^{\rm M31}$-axis can be calculated by projecting on the $\boldsymbol{e}_y^{\rm M31}$-axis:

$$s_z = \frac{\boldsymbol{r}'_{xy}(\mathrm{GC}) \cdot \boldsymbol{e}_y^{\rm M31}}{\left|\boldsymbol{r}'_{xy}(\mathrm{GC}) \cdot \boldsymbol{e}_y^{\rm M31}\right|} = \pm 1 \quad . \tag{2.27}$$

Now we can calculate the full transformation matrix:

$$\mathsf{R}_{\mathrm{M31}} = \mathsf{R}_z^{\mathrm{S}_z}(\beta)\mathsf{R}_y(90^\circ - i)\mathsf{R}_x(90^\circ - \theta)\mathsf{R}_{\boldsymbol{rpq}}(\alpha_{\mathrm{M31}}, \delta_{\mathrm{M31}}) \tag{2.28}$$

$$= \begin{pmatrix} +0.7703 & +0.3244 & +0.5490 \\ -0.6321 & +0.5017 & +0.5905 \\ -0.0839 & -0.8019 & +0.5915 \end{pmatrix} \quad . \tag{2.29}$$

Note that $\mathsf{R}_z^{-1}(\beta) = \mathsf{R}_z(-\beta)$. We use an inclination $i = 77.5^\circ$ and a position angle $\theta = 37.7^\circ$ (de Vaucouleurs 1958). To calculate the angle β and the matrix $\mathsf{R}_{rpq}(\alpha_{\mathrm{M31}}, \delta_{\mathrm{M31}})$ in Eqn. (2.29) we use a distance of 785 kpc and coordinates $\alpha_{\mathrm{M31}} = 00^{\mathrm{h}}42^{\mathrm{m}}44.3$, $\delta_{\mathrm{M31}} = +41^\circ 16' 09.4''$ for M31, and we employ a distance 8.5 kpc of the Sun from the Galactic Centre.

We need to define a "north" direction for the Andromeda-centric coordinate system. In analogy to the definition of the Galactic North Pole, which is the direction of the normal to the Galactic disc lying in the northern celestial hemisphere, we also define the north direction of Andromeda to be the direction of the normal of its stellar disc that lies in the northern celestial hemisphere[(a)]. Furthermore it is essential to know the actual direction of the inclination for the transformation (whereas this might not be important for other applications): Is the normal vector of the disc pointing towards or away from us? For Andromeda, in Figure 2.2 it can clearly be seen that the bulge of Andromeda is obscured in the northern-west region of the disc, so this part must be in front of the bulge and the normal vector is pointing away from us, as also schematically indicated in Figure 2.1.

The coordinate transformation as given in Koch & Grebel (2006) must be incorrect as the orientation of the triad at the position of Andromeda was ignored, just shifting to the centre of M31. The offset of the directions of the NCP and the NGP was also not correctly calculated. This offset is by chance very small at the position of Andromeda on the celestial sky (compare to McConnachie & Irwin 2006b). According to their transformation, Andromeda would have an inclination of $i = 66^\circ$ and a position angle of $\theta = -16^\circ$. However, since they performed only orthogonal transformations, translation and rotation, the relative orientations of the satellites are preserved.

General transformation

Equation (2.21) is the transformation equation performing the necessary linear operations, translation and rotation, respectively. Generally this becomes

$$\boldsymbol{r}_{\mathcal{T}} = \mathsf{R}_{\mathcal{B}\to\mathcal{T}}\left(\boldsymbol{r}_{\mathcal{B}} - \boldsymbol{r}_{\mathcal{B}}(\mathrm{O}_{\mathcal{T}})\right) \quad , \tag{2.30}$$

where $\boldsymbol{r}_B$ is the Cartesian vector of any object picked to be transformed to the target system $\mathcal{T}$, $\boldsymbol{r}_{\mathcal{B}}(\mathrm{O}_{\mathcal{T}})$ is the vector of the origin of the target system $\mathcal{T}$, both vectors given in the basis coordinate system $\mathcal{B}$. The appropriate rotation matrix $\mathsf{R}_{\mathcal{B}\to\mathcal{T}}$ can be calculated as given in Eqn. (2.23) or (2.28). Equation (2.23) gives the rotation matrix for which the Sun is located at longitude 180°. Equations (2.24) – (2.28) show how to derive the rotation matrix such that the Galactic Centre is at longitude 180°. $\boldsymbol{r}_{\mathcal{T}}$ is the Cartesian vector of the object given in the target coordinate system. Equatorial coordinates follow from Eqs. (2.15) – (2.17).

[(a)] Note that the angular momentum vector of the Milky Way is the Galactic South Pole, and with our definition the same is true for Andromeda.

Example Transformation

We give here an example of how to transform the coordinates of a companion galaxy into the Andromeda-centric coordinate system. We apply the transformation to M33 with coordinates $\alpha = 01^{\mathrm{h}}33^{\mathrm{m}}51$, $\delta = 30^{\circ}39'36''$, and a distance $D = 809$ kpc from the Sun, for Andromeda, $\alpha = 00^{\mathrm{h}}42^{\mathrm{m}}44.3$, $\delta = +41^{\circ}16'09.4''$, with a distance $D = 785$ kpc. First we need to calculate the Cartesian coordinates of M31 and M33 in the heliocentric coordinate system (Murray 1983):

$$\begin{aligned} \boldsymbol{r}(\mathrm{M31}) &= \begin{pmatrix} 579.791 \\ 109.391 \\ 517.785 \end{pmatrix} \text{ kpc}, \\ \boldsymbol{r}(\mathrm{M33}) &= \begin{pmatrix} 638.372 \\ 277.075 \\ 412.543 \end{pmatrix} \text{ kpc}. \end{aligned}$$

Next we apply Eqn. (2.21) using the matrix $\mathsf{R}_{\mathrm{M31}}$ as given in Eqn. (2.29):

$$\begin{aligned} \boldsymbol{r}_{\mathrm{M31}} &= \mathsf{R}_{\mathrm{M31}}(\boldsymbol{r}(\mathrm{M33}) - \boldsymbol{r}(\mathrm{M31})) \quad , \\ &= \begin{pmatrix} 41.737 \\ -15.051 \\ -201.635 \end{pmatrix} \text{ kpc}. \end{aligned}$$

Finally we calculate the Galactic coordinates in the Andromeda-centric coordinate system (Eqs. 2.15 – 2.17):

$$\begin{aligned} l_{\mathrm{M31}} &= 340.2^{\circ} \quad , \\ b_{\mathrm{M31}} &= -77.6^{\circ} \quad , \\ r_{\mathrm{M31}} &= 206.5 \text{ kpc}. \end{aligned}$$

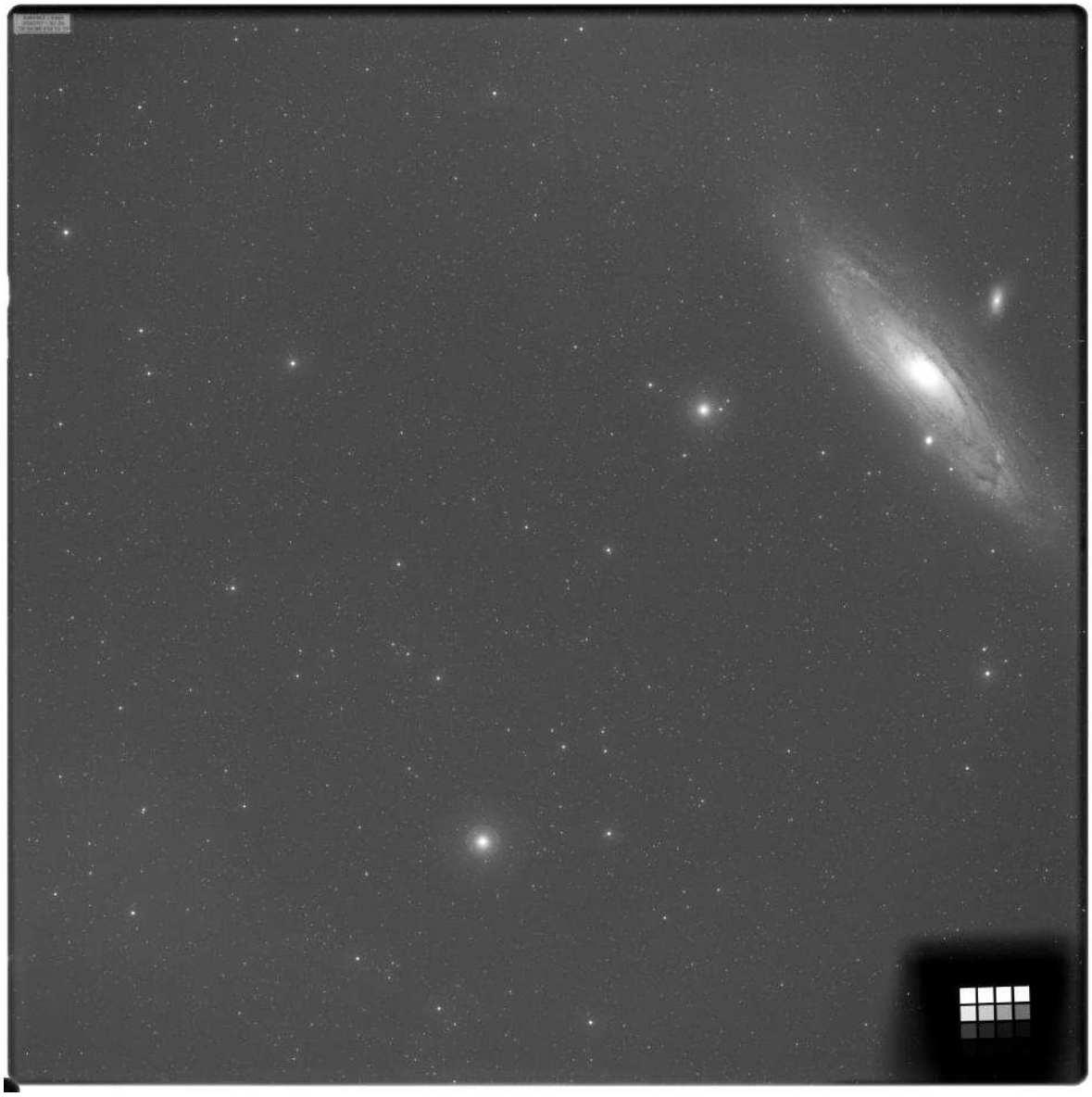

Figure 2.2: An optical image of Andromeda from the second Palomar Sky Survey (POSS II) taken in the J-band. The bulge of Andromeda is obscured by the dust layer of the disc in the northern-west region showing that this side of the disc must be in front of the bulge.

2.2 The Milky Way satellite galaxies

For the Milky Way satellite system we use the data as given in Kroupa et al. (2005, their table 1), supplementing it with the newly discovered companions from the SDSS which subsequently were reported during this research work. A listing with the data for the satellites is given in Table 2.1. Most of the newly discovered dSph satellite galaxies are named after the constellation in which they are found. Only for some of these follow-up observations are available, and most distances and absolute luminosities have to be considered as uncertain, especially for those satellites without deep photometric follow-up observations.

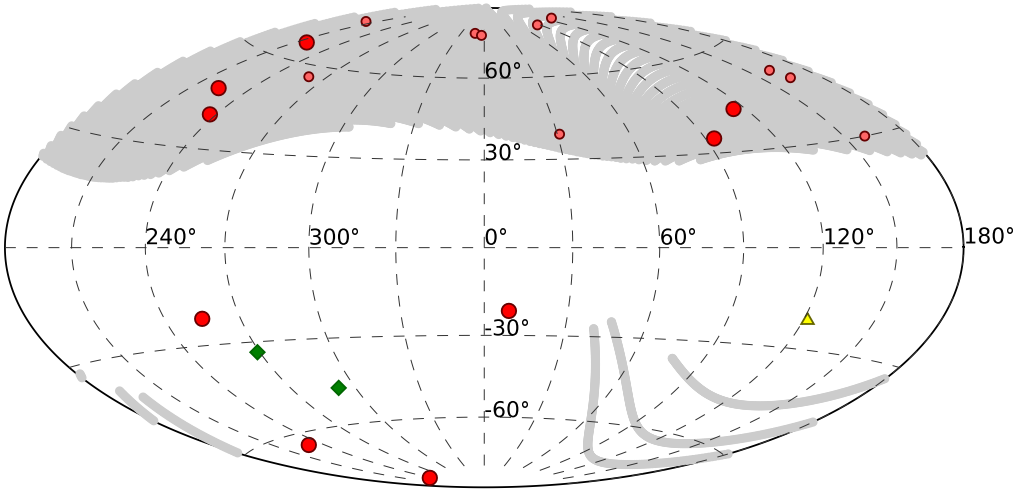

Figure 2.3: An Aitoff projection of the positions for the innermost satellites within 254 kpc of the Milky Way as they would appear from the Galactic Centre (compare to Figs. 2.8 and 2.9 for M31). The Magellanic Clouds are marked by the diamond symbols, the dSph satellites by circles where smaller symbols mark the newly discovered satellites from the SDSS. The position of Andromeda is marked by the triangle. In this projection, the Sun is located at $l_{\rm MW} = 180°$. The grey shaded area is the full sky-coverage region of the SDSS. A projection holds, however, no information about the true spatial distribution of the satellite galaxies, which is shown in Figures 2.4, 2.5, and 2.7.

2.2.1 The classical Milky Way satellite galaxies

First the data of the "classical Milky Way satellite galaxies" is analysed (as also done by Kroupa et al. 2005). These are the most luminous satellites, comprising a complete census of satellites within the virial radius of the Milky Way and brighter than $M_{\rm tot,V} = -8.8$ mag, $L_{\rm V} = 2.6 \times 10^5$ $L_\odot$ (Mateo 1998). We fit a plane for the innermost eleven satellites out to Leo I with a Galacto-centric distance of 254 kpc. For the ALS method, the direction of the normal of the fitted plane is $(l_{\rm MW} = 157.3°, b_{\rm MW} = -12.7°)$ and the distance of the plane from the Galactic Centre is $D_{\rm P} = 8.3$ kpc, which appears to be quite large but is still well within the optical disc of the Milky Way. An edge-on view and a view rotated by 90° about the polar axis of the Galaxy is shown in Figure 2.4, as well as a face-on view onto the fitted disc. The rms-height is $\Delta = 18.5$ kpc, resulting in flattening $\Delta/r_{\rm cut} = 0.07$

and $\Delta/r_{\rm med} = 0.23$. So the distance of the fitted plane from the Galactic Centre is a factor of two smaller than the rms-height of the plane. Note that Kroupa et al. (2005) found $\Delta/r_{\rm cut} = 0.10$, and Zentner et al. (2005) found $\Delta/r_{\rm med} \approx 0.3$ for the same data, both values being larger than those found here. This is an indication that the ALS method provides a better result in the sense that the orthogonal rms is minimized. The derived axis ratios are $c/a = 0.18$ and $b/a = 0.53$, resulting in $c/b = 0.34 < b/a$, a triaxial, oblate distribution of satellites. Libeskind et al. (2005) gave values of $c/a \approx 0.3$, $b/a \approx 0.5$ for the MW in their figure 3, which would mean $c/b = 0.6 > b/a$, i.e. a triaxial, slightly prolate distribution. They based most of their argumentation on these values which we could not reproduce in any case.

Next, the applied error (AE) Monte-Carlo method is applied, randomly shifting the position of all satellites along their line-of-sight vector with a normal distribution function as the probability function of the magnitude of the shift, repeating this 10 000 times. The principal axis of the resulting distribution of the normals is located at ($l_{\rm MW} = 157.4^\circ$, $b_{\rm MW} = -12.6^\circ$) with a spherical standard distance $\Delta_{\rm sph} = 1.2^\circ$. The derived principal axis is in good agreement with the single fit above and the scatter as quantified by $\Delta_{\rm sph}$ is remarkably small about the principal axis.

Using the ODR fitting routine, the pole is located at ($l_{\rm MW} = 158.2^\circ$, $b_{\rm MW} = -29.0^\circ$) with a distance $D_{\rm P} = 3.4$ kpc of the plane from the Galactic Centre. The result is shown in Figure 2.5. The rms-height is $\Delta = 32.6$ kpc, resulting in flattening $\Delta/r_{\rm cut} = 0.13$ and $\Delta/r_{\rm med} = 0.41$. This is an interesting finding that needs to be further explored: The longitude of the derived pole is very similar for the ALS and the ODR method, whereas the latitudes deviate by $\approx 16^\circ$. This can be understood by looking edge-on onto the fitted plane (Figs. 2.4 & 2.5, left panels). Since we are basically sitting in the plane of the satellites, most of the distance uncertainties, which are considered in the ODR method, are along the radius of the plane. As can be seen in Figs. 2.4 and 2.5, for the distant satellites the components of the distance uncertainties along the polar-axis (the ordinate) are the largest. This forces the ODR algorithm to weight positions along the polar-axis down, which results in a different latitude of the pole whereas the longitude of the fitted normal is not affected. *This outcome is an indication that, while the ODR method is robust against single outliers, it can be biased strongly by a systematic alignment of the provided distance uncertainties.* Later we show that this aspect affects the fitting for the Andromeda satellites even more.

To investigate the robustness of the disc-like feature, 10 000 bootstrap re-samplings for the eleven innermost satellites of the Milky Way ($^3N_{\rm tot} = 352\,155$ for $n = 11$, see Eqn. 2.9) are performed with the ALS method. In Fig. 2.6 a smoothed ($l_{\rm MW}$, $b_{\rm MW}$) scatter plot of the locations of the normals of the bootstrap samples is shown in grey-scale, white corresponding to zero density. The smoothing kernel is a Fisher function with smoothing parameter $\kappa = 100$ (Fisher et al. 1987)[(b)]. In addition the contour lines for the density estimate of 0.5, 0.75 and 0.9 are plotted. The plot is centred on the principal axis of the distribution which is located at ($l_{\rm MW} = 158.2^\circ$, $b_{\rm MW} = -11.9^\circ$) and thus is in good agreement with the results of the single fit above. The shape parameter $\gamma = 3.8$ and the strength parameter $\zeta = 4.3$ show that the distribution is strongly clustered around its principal axis,

[(b)]The Fisher function is the equivalent of the Gaussian on a sphere. The larger the smoothing parameter κ is chosen the narrower the smoothing kernel gets.

and well outside the distribution of (γ, ζ) values for an intrinsically isotropic distribution of satellites (Fig. 2.17). The resulting spherical standard distance is $\Delta_{\rm sph} = 13.0^\circ$.

The spherical standard distance $\Delta_{\rm sph}$ found for the AE test is only a tenth of that found with bootstrapping. This shows that the systematic error caused by the distance uncertainties of the Milky Way satellites is significantly smaller than the intrinsic scatter determined with the bootstrapping. So the disc-like feature is not affected much by the distance uncertainties of the Milky Way satellites.

2.2.2 Newly discovered dSphs from the SDSS, and YH globular clusters

We repeat the analysis, now consecutively including the Ursa Major (UMa) and Canes Venatici (CVn) dwarf galaxies, of which the discovery was reported in the course of this research. The results from the single fits, the AE analysis, and the bootstrap analysis are given in Tables 2.2 – 2.4. In the new fits the locations of the poles are only marginally affected by adding the new satellites, since both dSphs are located close to the former fitted disc (see Fig. 2.7). At a distance of $\approx$ 220 kpc CVn is in fact the second furthest satellite galaxy in our sample. For the unweighted ALS method, the orientation of the fitted disc is mostly determined by the outer satellites, nevertheless the orientation is not affected much. Including these two new satellite galaxies, the spherical standard distance $\Delta_{\rm sph}$ found for the AE test remains an order of magnitude smaller than the one for the bootstrapping, showing that the distance uncertainties do not systematically affect our results. Finally we added all those newly discovered dSphs that were reported very recently. These are marked by small circles in the Figures 2.3 and 2.7. The projection was chosen as in Figure 2.4, without adapting the fitting parameters to the new data. Apparently all are close to the DoS, except for one: the Hercules (Her) dwarf, the left-most data-point in the top-left panel of Figure 2.7, is 88 ± 8 kpc off the fitted disc. Without the Hercules dSphs, the fitting results are basically identical to the original fit to the eleven classical satellites: $l_{\rm MW} = 156.2^\circ$, $b_{\rm MW} = -8.0^\circ$, $D_{\rm P} = 6.0$ kpc, and $\Delta = 23.5$ kpc.

With the finding that the dwarf satellite galaxies of the Milky Way are aligned in a plane-like structure, one can ask about the properties of other halo objects, namely the globular clusters. Hartwick (2000) analysed the distribution of a sample of the outermost globular clusters of the Milky Way, and a low-metallicity sample. For both samples a spatial distribution was found different from that for the satellite galaxies. Here we use the latest available data of the Harris (1996) catalogue[(c)], but chose a different selection criterion: globular clusters were selected that are classified as "young halo" (YH) globular clusters according to Mackey & van den Bergh (2005). This selection is different from the low-metallicity cut applied by Hartwick (2000). Young halo clusters are believed to be formed in, or together with satellite galaxies, since their chemical properties are similar to those belonging to the MW dwarf galaxies (Mackey & Gilmore 2004). In total, 30 globular clusters are classified as YH clusters according to Mackey & van den Bergh (2005). Performing the plane fitting routine for this sample, we find the direction of the normal to be ($l_{\rm MW} = 144.1^\circ$, $b_{\rm MW} = -4.3^\circ$), the derived axis-ratios are $c/a = 0.35$ and $b/a = 0.76$, an oblate triaxial distribution. The

[(c)] http://www.physics.mcmaster.ca/resources/globular.html

direction of the normal is only 15.5° off the normal of the plane fitted using the classical eleven Milky Way satellite galaxies. We interpret this as an indication that the oblate, plane-like distribution of the YH globular clusters might be related to the DoS of the Milky Way satellite galaxies.

Table 2.1: The positions of the Milky Way satellite galaxies within the approximate virial radius of 254 kpc. In the first column we give a running number, in the second and third the name and abbreviation, in the forth and fifth longitude and latitude in galactocentric coordinates, and in the sixth the distance with 1σ errors from the Galactic Centre. In the seventh column the absolute luminosity in the V-band of the galaxies is given, taken from the referenced publications. The additional horizontal line marks the row where the list of newly discovered dSph satellites found in the SDSS starts, sorted by their galactocentric distance.

No	Name	Abbrev.	l_{MW} [°]	b_{MW} [°]	r_{MW} [kpc]	L_{V} [10^6 $\mathrm{L}_\odot$]	
1	Sagittarius	Sgr	8.8	−21.5	16.0 ± 2.0	5.1	(i)
2	Large Magellanic Cloud	LMC	269.0	−33.3	50.2 ± 2.2	2090	(ii)
3	Small Magellanic Cloud	SMC	292.2	−47.1	56.9 ± 2.2	575	(ii)
4	Ursa Minor	UMi	114.5	43.1	68.1 ± 3.0	0.29	(iii)
5	Sculptor	Scu	237.5	−82.3	79.2 ± 4.0	2.15	(iii)
6	Draco	Dra	93.6	34.7	82.0 ± 6.0	0.26	(iii)
7	Sextans	Sex	237.1	40.5	89.2 ± 4.0	0.50	(iii)
8	Carina	Car	255.1	−21.8	102.7 ± 5.0	0.43	(iii)
9	Fornax	For	230.5	−63.8	140.1 ± 8.0	15.5	(iii)
10	Leo II	Leo II	216.5	65.5	207.7 ± 12.0	0.58	(iii)
11	Leo I	Leo I	223.9	48.1	254.0 ± 30.0	4.79	(iii)
12	Ursa Major II	Uma II	159.6	30.0	36.5 ± −	0.003	(iv)
13	Willman1	Wil I	164.7	47.7	43.0 ± 6.9	0.001	(v)
14	Coma Berenices	CBe	201.8	75.1	45.2 ± 3.9	0.002	(vi)
15	Boötes II	Boo II	348.1	78.4	47.6 ± −	0.001	(vii)
16	Boötes	Boo	356.6	77.5	57.6 ± 11.9	0.02	(viii)
17	Ursa Major	UMa	162.0	50.8	104.9 ± 20.0	0.04	(ix)
18	Hercules	Her	30.9	38.8	134.2 ± 13.0	0.022	(vi)
19	Canes Venatici II	CVn II	132.7	80.9	150.7 ± 15.0	0.007	(vi)
20	Leo IV	Leo IV	260.0	56.2	160.6 ± 15.0	0.009	(vi)
21	Canes Venatici	CVn	86.9	80.2	219.8 ± 25.0	0.12	(x)

References: (i) Lee & Kim (2000); (ii) van den Bergh (1999); (iii) Mateo (1998); (iv) Zucker et al. (2006a); (v) Willman et al. (2005a); (vi) Belokurov et al. (2007); (vii) Walsh et al. (2007b); (viii) Belokurov et al. (2006); (ix) Willman et al. (2005b); (x) Zucker et al. (2006b)

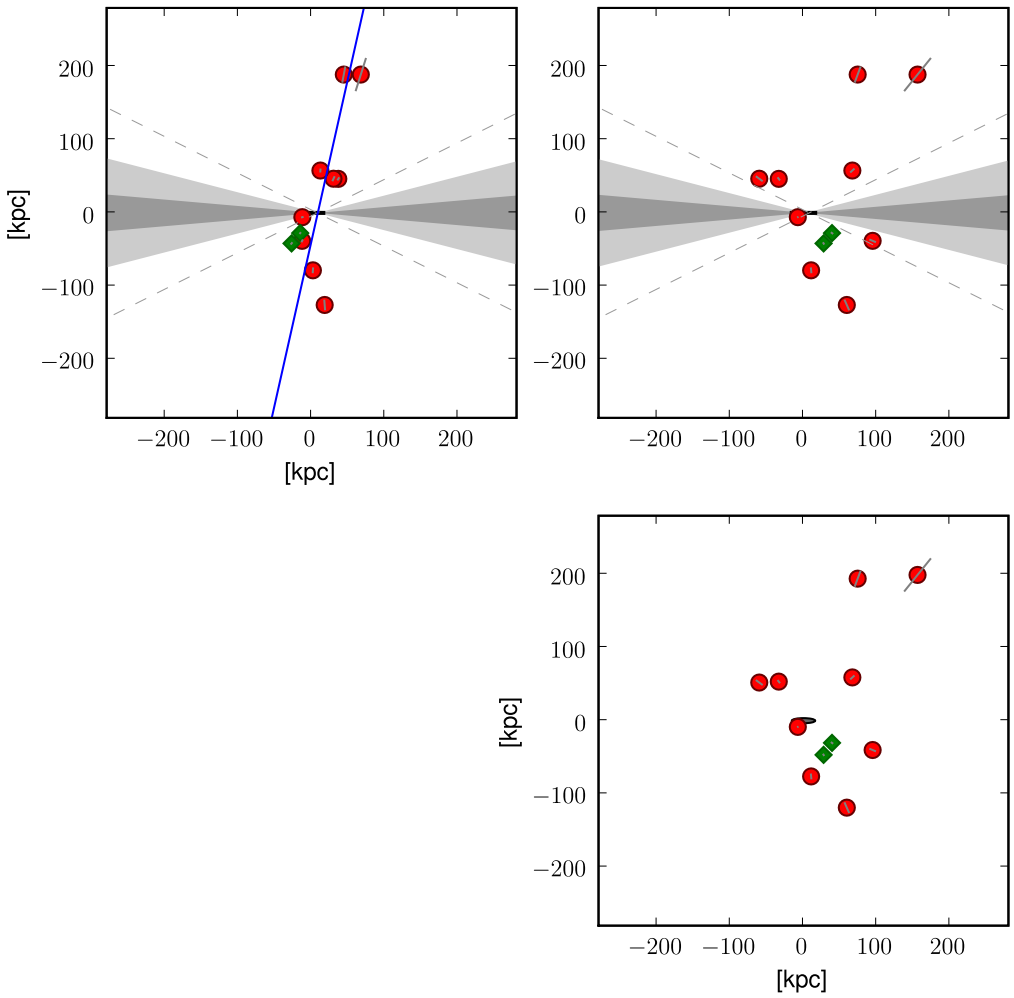

Figure 2.4: Positions of the "classical" Milky Way satellites within the virial radius as seen from infinity. Results of the fitting using the unweighted ALS method are shown. In the top-left panel an edge-on view onto the fitted plane is shown, in the top-right panel a view rotated by 90° about the polar-axis of the Galaxy. The Milky Way is located at the origin and its disc is seen edge-on in these two panels, as is indicated by the thick black line. In the bottom-right panel, a face-on view onto the fitted DoS is shown, the Milky Way's disc is indicated as a black ellipse. The red circles mark the positions of the dSph satellite galaxies, and the green diamonds the two irregular satellites LMC and SMC, respectively. The distance uncertainties along the line-of-sight are indicated by the grey sticks. The grey-shaded area shows the regions of $b = \pm 5°$ and $b = \pm 15°$, which may be affected by obscuration through the Milky Way disc, and the dashed lines indicate the region of $b = \pm 30°$, possibly affected by MW foreground crowding.

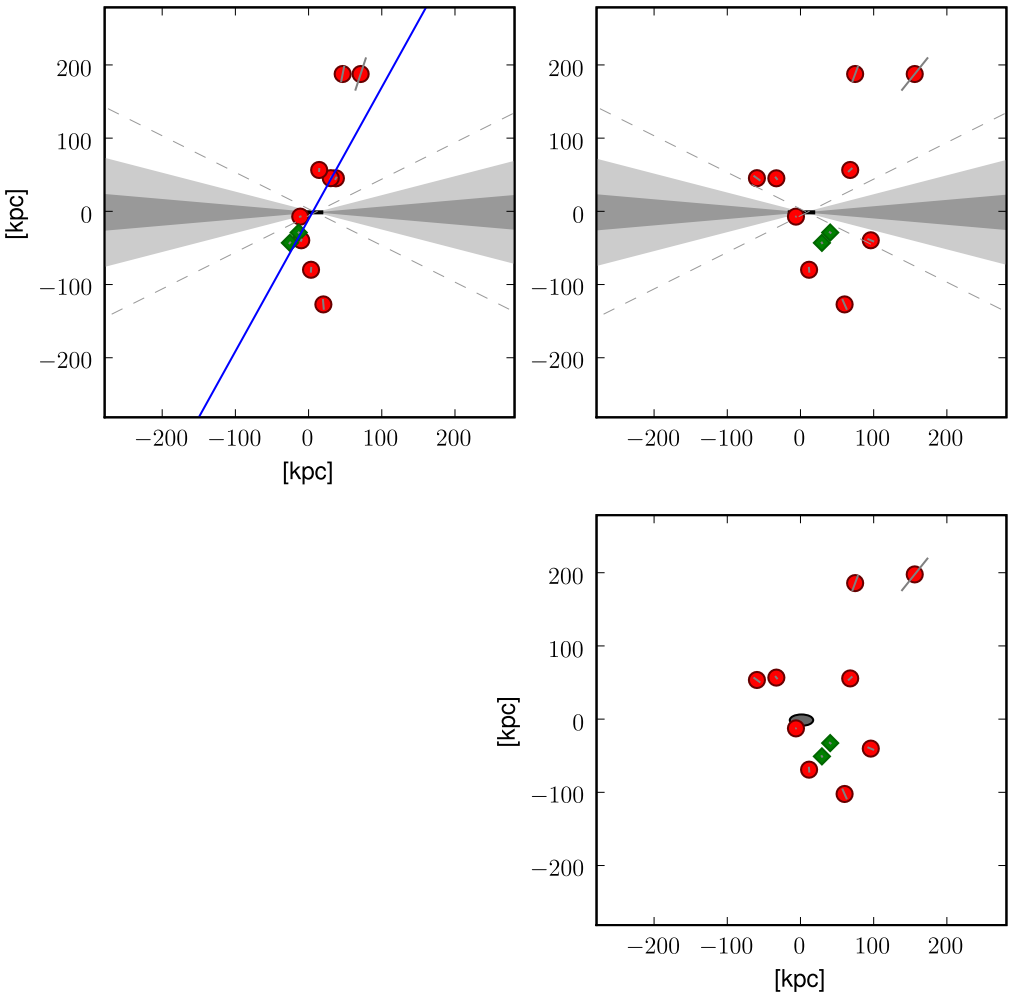

Figure 2.5: As Figure 2.4, now showing the results derived with the ODR fitting method.

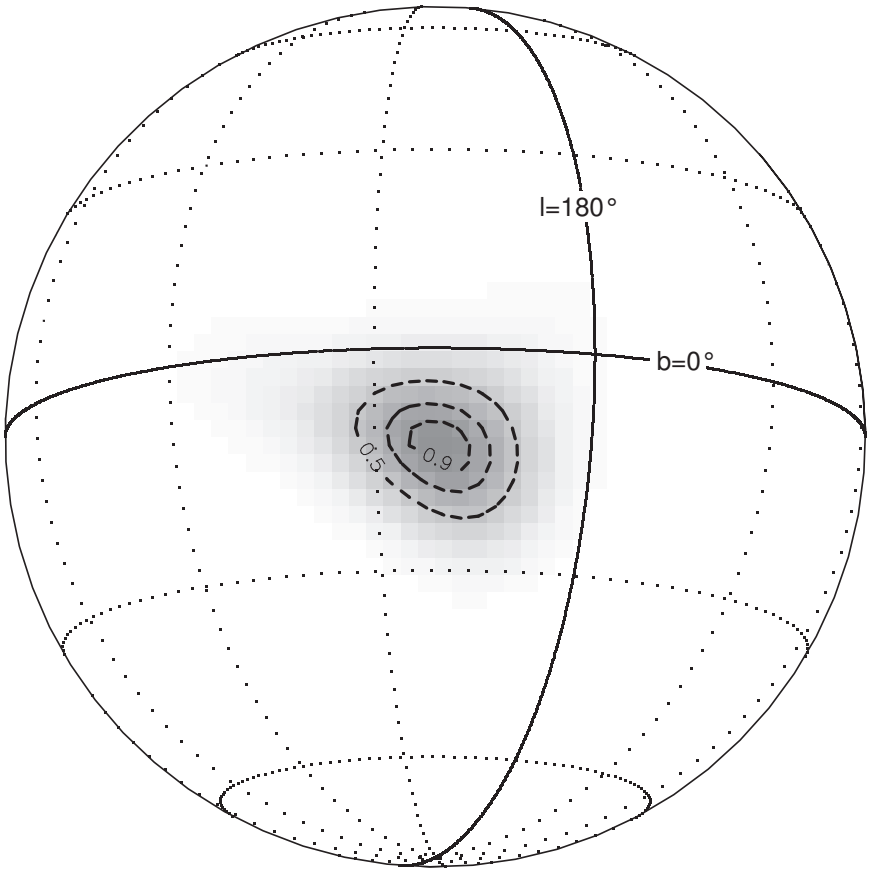

Figure 2.6: A smoothed (l_{MW}, b_{MW}) scatter plot of the distribution of normals of planes fitted to each of 10 000 bootstrap samples for the eleven innermost, "classical" Milky Way satellites. A spherical density estimate is shown using a Fisher density for the kernel function ($\kappa = 100$, Fisher et al. 1987) plotted in grey-scales, white corresponds to 0. In addition the contour lines for the density estimate of 0.5, 0.75 and 0.9 in units of the central density are plotted. The principal axis of the distribution is located at ($l_{\mathrm{MW}} = 158.2°$, $b_{\mathrm{MW}} = -11.9°$).

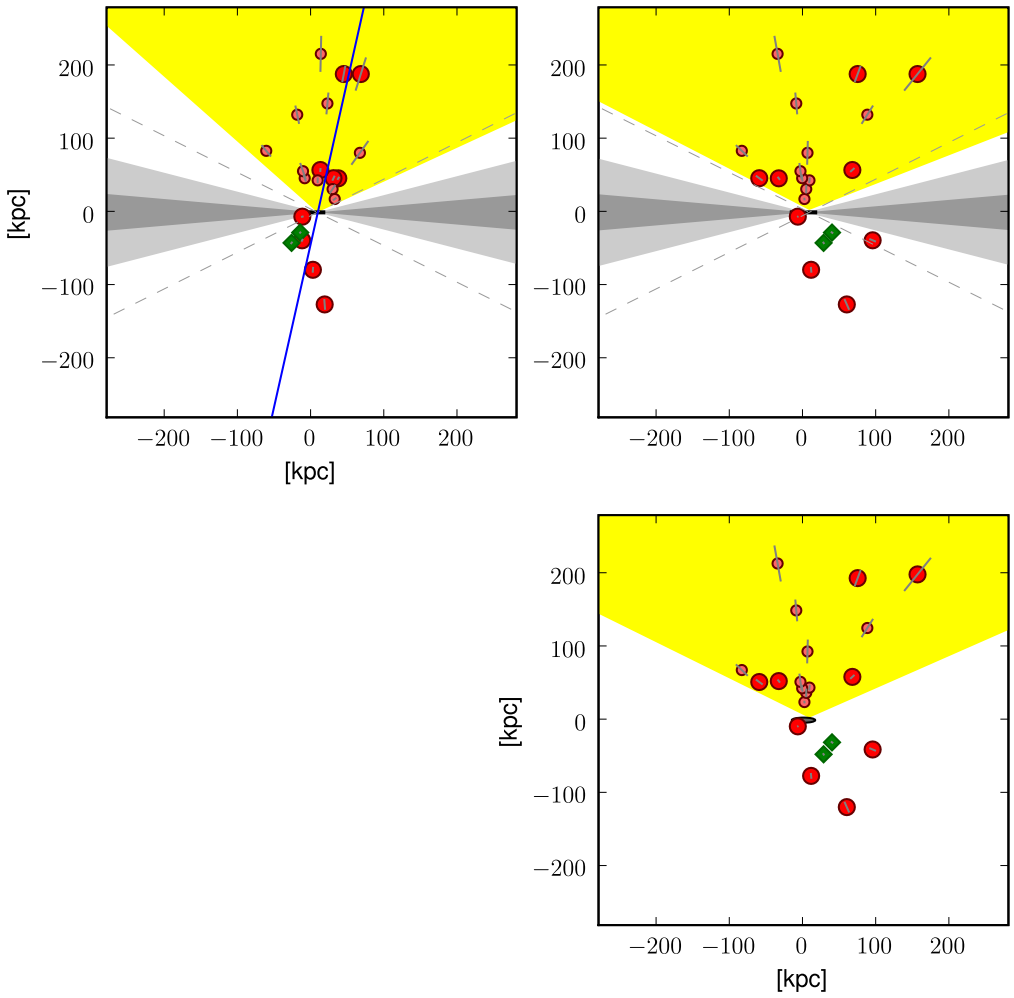

Figure 2.7: As Figure 2.4, now adding the newly discovered dSphs from the SDSS, shown by smaller red symbols.The orientation of the plot was not adapted by a new plane fit, but was kept at the same values as in Figure 2.4. In this plot the projected northern full sky coverage region of the SDSS is indicated by the coloured area. The detection biasing due to the SDSS coverage region towards the Galactic North-pole region is evident.

Table 2.2: Results from the single plane fits for the innermost satellite galaxies of the Milky Way within the approximate virial radius for the two fitting methods: ALS and ODR. Results for the "classical" satellites, and for the data-sets including the UMa and the CVn dwarf galaxies are given. For Andromeda the results for both data-sets, MI and KG (§2.3), as well as for a morphologically (mss8, §2.3.1) and a kinematically motivated (kss8, §2.3.2) subsample of eight satellites, are tabulated. Results are given in galactocentric and Andromeda-centric coordinates, respectively.

method	$l_{\rm MW}$ [°]	$b_{\rm MW}$ [°]	$D_{\rm P}$ [kpc]	Δ [kpc]	$\Delta/r_{\rm cut}$	$\Delta/r_{\rm med}$	c/a	b/a
Milky Way: classical								
ALS	157.3	−12.7	8.3	18.5	0.07	0.23	0.18	0.58
ODR	158.2	−29.0	3.4	32.6	0.13	0.41		
Milky Way: classical + UMa								
ALS	160.5	−14.6	12.5	20.3	0.08	0.25	0.21	0.54
ODR	158.1	−29.1	3.4	31.7	0.12	0.39		
Milky Way: classical + UMa + CVn								
ALS	153.8	−10.2	7.8	22.8	0.09	0.27	0.22	0.55
ODR	157.4	−29.2	2.9	40.9	0.16	0.48		
	$l_{\rm M31}$ [°]	$b_{\rm M31}$ [°]						
Andromeda, MI-data								
ALS	73.4	−31.5	1.0	45.9	0.17	0.42	0.36	0.46
ODR	23.8	−12.5	45.0	54.4	0.20	0.50		
ALS mss8	177.0	−24.1	34.9	29.2	0.11	0.39	0.27	0.67
ODR mss8	177.9	−20.4	37.7	29.5	0.11	0.39		
ALS kss8	69.9	−35.2	1.8	16.5	0.06	0.11	0.12	0.50
ODR kss8	57.9	−28.6	12.8	22.7	0.08	0.16		
Andromeda, KG-data								
ALS	83.5	−31.0	7.5	46.1	0.16	0.46	0.41	0.68
ODR	27.6	−31.1	32.5	68.2	0.24	0.68		
ALS mss8	168.0	−26.7	1.6	9.4	0.04	0.14	0.09	0.68
ODR mss8	168.5	−29.4	1.9	10.2	0.04	0.15		
ALS kss8	73.6	−35.0	3.9	17.9	0.06	0.18	0.15	0.71
ODR kss8	52.9	−35.5	13.7	31.3	0.11	0.31		

Table 2.3: Results from the applied error test for satellite galaxies of the Milky Way and Andromeda. The longitudes and latitudes of the derived principal axis and the spherical standard distance of the distributions for the classical Milky Way satellite galaxies are listed. The recently discovered dSph galaxies in Ursa Major and Canes Venatici are included. The results for the two data-sets used for Andromeda, as well as for two subsamples (§2.3.1 & §2.3.2) of M31 satellites, are given.

Data-set	l_{MW} [°]	b_{MW} [°]	Δ_{sph} [°]
Milky Way classical	157.4	−12.6	1.2
+UMa	160.6	−14.6	1.5
+UMa+CVn	153.9	−10.2	1.5
	l_{M31} [°]	b_{M31} [°]	
Andromeda MI	75.1	−31.7	13.2
mss8	176.6	−24.9	12.5
kss8	70.5	−35.2	2.4
Andromeda KG	82.9	−31.1	8.0
mss8	165.2	−30.9	21.5
kss8	74.2	−35.2	1.6

Table 2.4: Results from the bootstrap re-sampling method for the satellite galaxies of the Milky Way and Andromeda. The same quantities as in Table 2.3 are provided and in addition in columns five and six the shape parameter γ and the strength parameter ζ of the distribution of normals of the fitted planes are tabulated.

Data-set	l_{MW} [°]	b_{MW} [°]	Δ_{sph} [°]	γ	ζ
MW classical	158.2	−11.9	13.0	3.8	4.3
+UMa	161.8	−14.9	12.0	4.0	4.4
+UMa+CVn	156.7	−10.6	12.4	2.8	4.6
	l_{M31} [°]	b_{M31} [°]			
M31 MI	75.5	−31.9	38.6	0.6	3.1
mss8	178.3	−28.5	32.7	1.1	2.7
kss8	69.5	−34.2	9.8	5.9	4.7
M31 KG	83.1	−30.0	27.9	2.9	2.6
mss8	167.1	−29.6	11.8	5.3	1.9
kss8	72.4	−33.8	11.5	14.9	4.2

2.3 The Andromeda satellite galaxies

In order to study the three-dimensional distribution of the satellite system of Andromeda it is most convenient to transform their position vectors relative to the observer into an Andromeda-centric coordinate system (see also McConnachie & Irwin 2006b). A detailed description of the transformation is given in Section 2.1.4 in the most general way. Two different data-sets for the distances of Andromeda and its satellites were incorporated: the first data-set as published by McConnachie & Irwin (2006b, MI data-set, see their table 1) where most of the distances were derived using the tip of the red giant branch method using ground based telescopes (McConnachie et al. 2005). This data-set can be considered as homogeneous data. The other data-set as given by Koch & Grebel (2006, KG data-set, see their table 1): they compiled a list of HST-based distance measurements. The data are given in Table 2.5 for both data-sets converted to Andromeda-centric coordinates.

Figs. 2.8 and 2.9 show an Aitoff projection of the satellite distribution on the Andromeda sky similar to Fig. 2.3 for the Milky Way. The projected error bars due to the combined uncertainties in the distance measurement of the satellites and Andromeda are shown, which are given by

$$\sigma = \sqrt{\sigma_{\mathrm{M31}}^2 + \cos^2(\beta)\,\sigma_{\mathrm{sat}}^2} \quad , \tag{2.31}$$

where σ_{M31}, σ_{sat} are the distance uncertainties of Andromeda and its satellite, respectively, and β is the angle between the lines-of-site to Andromeda and its companion. In each figure, the positions derived from the other data-set are shown with small open symbols for comparison. Note the voids in the regions $l_{\mathrm{M31}} < 180^\circ$, $b_{\mathrm{M31}} < 0^\circ$ and $l_{\mathrm{M31}} > 180^\circ$, $b_{\mathrm{M31}} > 0^\circ$ in both figures. As shown by McConnachie & Irwin (2006b), these regions are only marginally obscured by the Milky Way disc (see their figure 1), the region of maximum obscuration is near IC 10 at ($l_{\mathrm{M31}} = 103^\circ$, $b_{\mathrm{M31}} = 45^\circ$).

Similar to the case of the Milky Way, more faint dwarf galaxies probably remain to be found for Andromeda within the next few years. One of these discoveries was reported by Zucker et al. (2007): the dSph And X is comparable in luminosity to And IX, however the distance determination was difficult. Zucker et al. (2007) gave a distance of 667 ± 30 kpc to 738 ± 35 kpc. Three satellites, And XI – XIII, were reported in another recent paper by Martin et al. (2006). No distances could be determined for the individual galaxies, but combining their colour-magnitude diagrams and assuming all to have the same distance, Martin et al. (2006) derived a combined distance of 740 – 955 kpc. Next, Majewski et al. (2007) reported the discovery of a dSph in the vicinity of Andromeda, named And XIV. They estimated a heliocentric distance of 630 – 850 kpc. Two further dSphs were reported by Ibata et al. (2007), And XV and And XVI, and most recently the discovery of And XVII was reported by Irwin et al. (2008). Given the large distance uncertainties for all these recently discovered dwarf galaxies, we do not include these in our analysis but discuss them later.

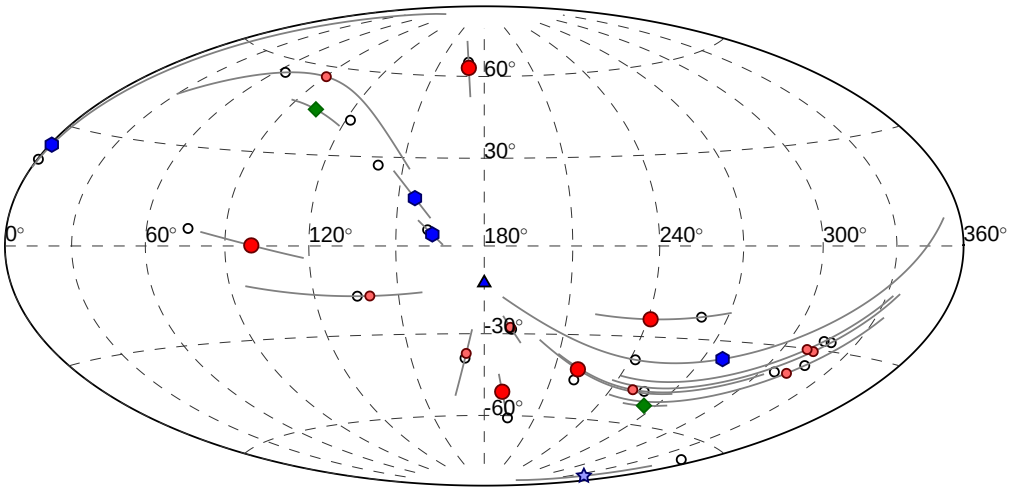

Figure 2.8: The Aitoff projection of the locations of the M31 satellites in the Andromeda-centric coordinate system for the MI data-set. Symbols are chosen as in the previous section: red circles mark dSphs, green diamonds dIrrs. Blue hexagons now mark dE/cE galaxies, and the location of M33 is shown by the blue pentagram. The small open circle mark the corresponding positions for the KG data-set. The projected distance errors due to the combined uncertainties in the distance measurement of the satellites and M31 are shown. The position of the Milky Way is indicated by the triangle.

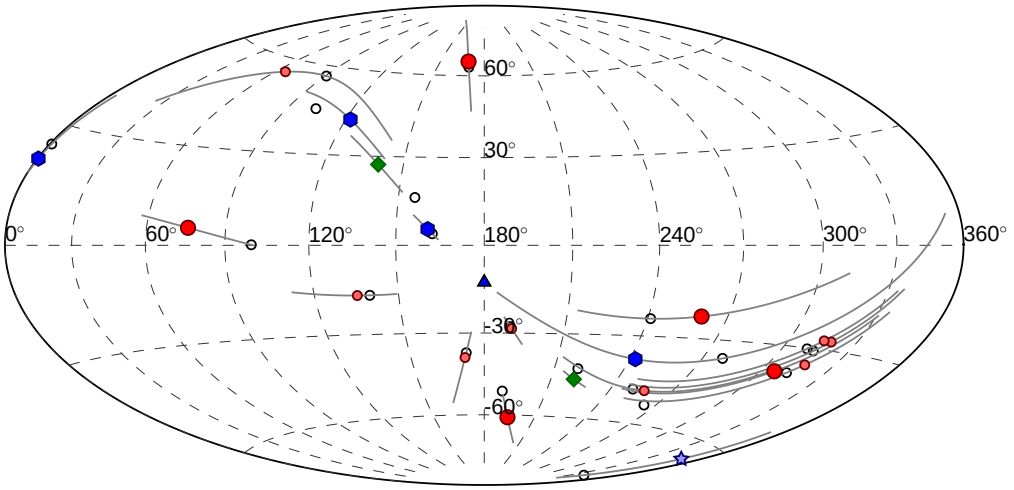

Figure 2.9: As Figure 2.8 for the KG data-set, small open circles now showing the corresponding positions for the MI data.

Table 2.5: Parameters of the Andromeda satellites: the first five columns contain a running number, the name, the morphological type, the sub-sample belonging (morphological or kinematical subsample), and the absolute luminosity in the V-band of the satellite. Columns 6 – 8 list the positions in Andromeda-centric coordinates (§2.1.4) for the first data-set (MI), and the 9th and 10th columns list the radial and perpendicular components of the measured line-of-sight velocity relative to Andromeda (§3.3.1). In the columns 11 – 15, the same data are provided for the second data-set (KG). The asterisks mark satellites for which the possible poles of the angular momentum vector can be restricted (§3.3.1). For the newly discovered satellite galaxies (running numbers larger than 17) distance data was take as reported in the respective discovery paper, citet in the column with the luminosity data.

					MI-data					KG-data				
No	Name	Type		L_V	l_{M31}	b_{M31}	r_{M31}	v_t	v_r	l_{M31}	b_{M31}	r_{M31}	v_t	v_r
				$[10^6\,L_\odot]$	[°]	[°]	[kpc]	$[km\,s^{-1}]$		[°]	[°]	[kpc]	$[km\,s^{-1}]$	
1	M32	cE	m,k	383[i]	278.5	−35.7	6	96.0	−1.8 ★	242.3	−37.9	6	83.2	−47.9
2	NGC 205	dE	k	366[i]	0.9	25.1	40	15.0	55.1	0.5	21.3	58	11.3	55.9
3	And IX	dSph	m	0.17 [iii]	118.3	−11.1	42	68.6	−51.6	65.4	−0.2	40	82.2	24.7
4	And I	dSph	m,k	4.37[ii]	220.1	−42.1	59	71.4	38.9	306.2	−37.8	48	66.9	−46.3
5	And III	dSph	m	0.58[ii]	241.1	−24.1	76	61.0	0.6	260.0	−22.8	68	58.4	−17.6
6	And V	dSph	m	0.58[ii]	99.6	0.2	110	106.2	−38.9 ★	76.0	5.3	117	81.0	−78.9
7	NGC 147	dE	m,k	131[i]	155.8	16.1	145	46.1	−102.5	122.0	42.3	101	100.3	−50.7 ★
8	And II	dSph	k	9.12[ii]	188.7	−50.9	185	47.1	−111.3	193.9	−60.9	160	66.4	−101.0
9	NGC 185	dE	k	125[i]	162.4	3.9	190	17.5	−102.1	160.8	5.5	175	21.5	−101.4
10	And VII	dE	m	27.5[ii]	170.1	63.3	219	14.4	−84.5 ★	169.2	65.6	216	11.0	−85.0
11	IC 10	dIrr	k	160[i]	103.2	45.2	260	26.3	−108.2	140.6	27.2	255	83.3	−73.9
12	LGS 3	dI/dS	k	1.33 [i]	264.0	−53.2	269	8.8	−102.1	220.4	−45.9	284	41.3	−93.8
13	And VI	dSph	m	3.31[ii]	259.8	−3.5	269	53.0	−112.1 ★	260.6	−3.3	266	51.4	−112.8 ★
14	Peg DIG	dI/dS	m	12.0[i]	270.1	−1.0	474	145.5	−93.0	252.9	−4.7	410	110.7	−132.6 ★
15	IC 1613	dIrr	k	63.6[i]	243.1	−46.7	511	39.2	−187.3	244.8	−46.9	505	43.2	−186.4
16	M33	Sc		3020[iv]	340.2	−77.6	207	126.3	−47.6 ★	350.0	−65.2	221	133.7	−18.5
17	And X	dSph		0.15[v]	139.8	−16.7	110	-	-	135.4	−16.7	101	-	-
18	And XI	dSph		0.07[vi]	310.8	−30.8	124	-	-	315.2	−27.5	130	-	-
19	And XII	dSph		0.03[vi]	314.2	−30.6	117	-	-	318.6	−27.5	123	-	-

Continued on the next page.

Table 2.5 – Continued

No	Name	Type	L_V [10^6 $L_\odot$]	l_{M31} [°]	b_{M31} [°]	r_{M31} [kpc]	v_t [km s^{-1}]	v_r	l_{M31} [°]	b_{M31} [°]	r_{M31} [kpc]	v_t [km s^{-1}]	v_r
20	And XIII	dSph	0.05[vi]	312.3	−37.6	136	-	-	315.6	−34.7	141	-	-
21	And XIV	dSph	0.2[vii]	250.6	−48.2	162	-	-	256.6	−48.4	158	-	-
22	And XV	dSph	0.5[ix]	172.8	−36.9	176	-	-	172.1	−38.6	166	-	-
23	And XVI	dSph	0.4[ix]	189.7	−27.8	281	-	-	190.2	−28.4	270	-	-
24	And XVII	dSph	0.2[ix]	90.6	56.5	45	-	-	65.3	55.8	49	-	-

References: [i] Mateo (1998); [ii] McConnachie & Irwin (2006a); [iii] Zucker et al. (2004); [iv] van den Bergh (1999); [v] Zucker et al. (2007); [vi] Martin et al. (2006); [vii] Majewski et al. (2007); [viii] Ibata et al. (2007); [ix] Irwin et al. (2008)

The innermost twelve satellites of Andromeda (without counting M33) lie within $\approx$ 269 kpc, the approximate virial radius of Andromeda, $r_{\rm vir}$, which is approximately of the same order as that of the Milky Way. We assume LGS 3 to be the twelfth satellite, although for the KG data-set And VI is actually closer to the centre. This will be addressed later (this Section and §3.3.2). The results of the fits are given in Table 2.2. For the MI-data the distribution is triaxial and more prolate, while for the KG data-set the distribution is found to be triaxial and more oblate, which is reflected in the further analysis, too. Figs. 2.10 and 2.11 show an edge-on view of the fitted planes and a view rotated by 90° about the polar axis of Andromeda, as well as a face-on view onto the fitted disc for the two data-sets (compare to Fig. 2.4 for the Milky Way). As can be seen the recently discovered dSph And X that was not incorporated in the fitting (marked by a smaller symbol near the centre of the plots), is located close to the fitted plane. If we just recalculate the rms-heights of the fitted disc, now including And X, it increases only slightly to $\Delta = 46.6$ kpc for the MI data-set, $\Delta = 47.2$ kpc for the KG data-set. Interestingly, also the three very recently discovered satellites And XI – And XIII (Martin et al. 2006) all lie very close ($\approx$ 10 kpc for the MI data, $\approx$ 30 kpc for the KG data) to the fitted disc when using a mean combined distance of 847.5 kpc albeit with large uncertainties.

For the applied error method (Table 2.3) the distance of Andromeda is not varied. This would only affect the distance of the plane from the origin. Compared to the spherical standard distance derived for the Milky Way, it is a factor of ten larger for the M31 system, which is not surprising given the much larger uncertainties in the relative distances M31 – satellite. The principal axes come out in good agreement with the poles of the single fits.

However, the ODR method yields poles that are far away from the poles found with the ALS method (Table 2.2). The difference is totally dominated by the large distance uncertainties, which are here not aligned within the fitted plane as in the case of the Milky Way. Instead they are systematically aligned along the line-of-sight from the Milky Way to Andromeda. The components in the direction to the Milky Way are weighted down and the fitted plane appears to be nearly perpendicular to the direction from the MW to M31, a result of the systematic dependencies of the covariances.

McConnachie et al. (2005) showed that the satellite distribution is significantly offset towards the direction of the Milky Way. This offset is also visible in Fig. 2.10, right panels. The offset is reflected by the large distance from the centre of Andromeda along the direction of the normal for the fitted planes when using the ODR method, due to the nearly face-on orientation of the fitted disc. In contrast, the disc-like distribution found with the ALS method is more edge-on, i.e. the systematic offset as identified by McConnachie et al. is within the plane.

As for the Milky Way, 10 000 bootstrap re-samplings for both data-sets of M31 are performed to test the robustness of the plane. The principal axis of the distribution is $(l_{\rm M31} = 75.5°, b_{\rm M31} = -31.9°)$ [$(83.1°, -30.0°)$], being in good agreement with the original fit. We derive a shape parameter $\gamma = 0.6$ [2.9] and a strength parameter $\zeta = 3.1$ [2.6], the spherical standard distance is $\Delta_{\rm sph} = 38.6°$ [27.9°] (numbers for the MI[KG] data-sets). While for the KG data-set the distribution of the directions of fitted normals for the bootstrapped sample is found to be clustered ($\gamma > 1$), for the MI-data it is found to be a girdled distribution ($\gamma < 1$). Fig. 2.12 shows a smoothed ($l_{\rm M31}$, $b_{\rm M31}$) scatter plot of the distribution

of the fitted normals for the MI data-set: there is a distinct peak about the principal axis and a second, weak over-density can be seen nearly 90° off, being the origin of the girdled distribution. The KG data-set does not show a secondary maximum.

And VI has approximately the same distance from Andromeda as LGS 3, both lying close to the approximate virial radius. Including And VI in the fitting routine for the KG-data, where it is actually closer to the centre of M31 than LGS 3, dramatically changes the picture. The pole of the fitted normals is clearly offset from the fits without And VI, the distance of the fitted plane is significantly offset from the centre of Andromeda, and the axis ratios do change significantly: $b/a = 0.63$ and $c/a = 0.57$. More importantly the clustering found for the bootstrapping without And VI for the KG-data disappears completely. If the satellite was within a planar-like distribution, the bootstrapped distribution should become similarly or even more tightly concentrated, as it did when including the UMa dwarf galaxy for the Milky Way. Instead, it gets very weak: $\gamma = 0.3$ and $\zeta = 1.7$. Therefore we treat And VI as an outlier.

In contrast to the Milky Way satellite system, for Andromeda the spherical standard distance derived with the applied error method is of the same order as for the bootstrap method which is a result of the large distance uncertainties for M31 and its satellites. So the results may well be affected by the still too large distance uncertainties for both, Andromeda and its satellite galaxies.

2.3.1 Morphological motivated subsample of Andromeda satellites

Koch & Grebel (2006) found a very pronounced polar disc-like feature for a morphologically motivated subsample of early-type dwarf galaxies. Their procedure was as follows: they first fitted a plane to all seven dSph galaxies in their data-set and then excluded And II (at a distance of $r_{\rm M31} = 160$ kpc $< r_{\rm vir}$) as an outlier because of its large distance to the fitted plane. This disc-like feature of six dSphs was found to be statistically highly significant, albeit we argue that their derived statistical significance is not unbiased (Sects. 2.1.2, 2.1.3, & 2.4.3). Next they included all other morphologically similar galaxies, three dEs and one cE (M32), again finding a disc-like feature with high statistical significance. In a last step they excluded two of the three dEs, but included one transitional type object, the dIrr/dSph Peg DIG at a distance of 410 kpc $> r_{\rm vir}$, because of its close proximity to the disc-like feature found before[(d)]. They also found that smaller spiral galaxy M33 is comprised by the plane of their sub-subsample, though not included in the fitting.

Indeed we confirm an amazingly thin configuration in the KG data when using this sub-subsample consisting of M32, And I, And III, NGC 147, And V, And VII, And VI, And IX, and Peg DIG. In Tables 2.2 – 2.4 we refer to the sub-subsample without Peg DIG as mss8 (morphological subsample of eight satellites). We exclude Peg DIG because it is well outside the approximate virial radius of M31. The fitted configuration is shown in Fig. 2.14. As can be seen, M33 is indeed located very closely to the fitted plane. For the KG data-set the pole of the fitted plane is ($l_{\rm M31} = 168.0°$, $b_{\rm M31} = -26.7°$), with a distance from the centre $D_P = 1.6$ kpc, an rms-height $\Delta = 9.4$ kpc, and with axis ratios $c/a = 0.09$ and

[(d)]However, also note the different scaling of the axes in their figure 3 which makes the distributions appear more planar-like than they truly are.

$b/a = 0.68$. For the weighted ODR method the results are very similar (see Table 2.2). M33 is located very closely to this fitted plane. Including Peg DIG for completeness results in ($l_{\rm M31} = 163.0^\circ$, $b_{\rm M31} = -27.3^\circ$), with a distance from the centre $D_P = 1.2$ kpc, an rms-height $\Delta = 13.1$ kpc, and with axis ratios $c/a = 0.09$ and $b/a = 0.45$. But, this distribution ($b_{\rm M31} = -27.3^\circ$) is not as polar aligned as claimed by Koch & Grebel (2006) due to the incorrect transformation to the Andromeda-centric coordinate system used by them (§ 2.1.4). Also note that, from the Milky Way, we are basically looking face-on onto this fitted plane, which is an important clue as we will show later.

Using the MI data-set without Peg DIG (MI mss8) leads to ($l_{\rm M31} = 177.0^\circ$, $b_{\rm M31} = -24.1^\circ$), $D_P = 34.9$ kpc, and $\Delta = 29.2$ kpc (Fig. 2.13); including Peg DIG we find ($l_{\rm M31} = 182.4^\circ$, $b_{\rm M31} = -23.2^\circ$), $D_P = 35.1$ kpc, and $\Delta = 29.1$ kpc. For this data-set the fitted plane is not as thin as for the KG data, and the offset from the centre of M31 is remarkably larger than the rms-height of the fitted plane. As can be seen in Fig. 2.13, there is now another dE (NGC 147, marked by the blue hexagon to the right of the plane) remarkably offset from the fitted plane.

Further insight comes from the AE test (Table 2.3). When applied to the morphological sub-subsample, the derived spherical standard distance is $\Delta_{\rm sph} = 21.5^\circ$. This is a very large uncertainty in the location of the poles of the fitted normals, a factor three larger than for the full set of twelve satellites within the approximate virial radius used before. For the MI data-set, $\Delta_{\rm sph} = 12.5^\circ$ is of the same order as for the full data-set.

In order to test the robustness of the results, a bootstrap analysis for the sub-subsample without Peg DIG is performed, now using 5 000 re-samplings accounting for the smaller number of possible distinct bootstrap samples ($^3N_{\rm tot} = 6\,231$ for $n = 8$). The results are given in Table 2.4. The principal axes are in agreement with the individual fits. The distribution of directions of bootstrapped normals is marginally clustered and concentrated. However the spherical standard distance for the bootstrapped sample is remarkably smaller than for the AE test. *This indicates that the systematic uncertainties of the distances are larger than the intrinsic scatter of the fitted disc for the KG data.* For the MI data-set the bootstrapped distribution is found not to be clustered but of transitional type. The spherical standard distance is significantly larger than for the KG data-set.

The recently discovered dSph And X is also found to be off the disc-like structure of the mss8 subsample for the KG data-set. For a heliocentric distance of 702.5 kpc its distance from the fitted disc is ≈ 87 kpc ($> 9\sigma$; And II, excluded as an outlier by Koch & Grebel, is ≈ 127 kpc away). To be within ± 10 kpc from the disc, And X would have to be at a heliocentric distance of ≈ 786 – 808 kpc. For the MI data-set And X's distance to the fitted disc is ≈ 32.7 kpc. And X is located on the near side of M31 to the Milky Way, thus adding to the systematic offset of the M31 satellite system towards the barycentre of the Local Group (McConnachie & Irwin 2006b).

We thus find that the apparent disc-like configuration of the dSph/dE satellite sub-subsample for Andromeda as proposed by Koch & Grebel (2006) is present for their data-set only and cannot be reproduced using the MI data-set. The nearly face-on alignment relative to the Milky Way results in distance uncertainties basically perpendicular to the fitted plane (Figs. 2.13 & 2.14). The thin configuration disappears when shifting the satellites

along their line-of-sight in accord with the distance uncertainties as done in the AE test. Comparing the results for the AE test and the bootstrapping suggests that the systematic uncertainties caused by the distance-measurement errors are larger than the intrinsic scatter of the distribution. Thus the thin disc-like configuration found may be just a chance alignment for the KG data-set, but its existence is not completely ruled out.

2.3.2 Kinematical motivated subsample of Andromeda satellites

In Section 3.3.2 we identify a subsample of Andromeda satellite galaxies that might have a common stream motion based on the intersection of their orbital poles (cf. also Lynden-Bell & Lynden-Bell 1995, Palma et al. 2002, and McConnachie & Irwin 2006b). Applying ALS to fit a plane for this kinematically motivated subsample of nine satellites (M32, NGC 205, And I, NGC 147, And II, NGC 185, IC 10, LGS 3, and IC 1613), but for the time being excluding IC 1613, the pole comes out to be located at $(l_{\rm M31} = 69.9^\circ, b_{\rm M31} = -35.2^\circ)$ $[(l_{\rm M31} = 73.6^\circ, b_{\rm M31} = -35.0^\circ)]$ (MI[KG]-data-set), with axis ratios $c/a = 0.12$ and $b/a = 0.50$ $[c/a = 0.15$ and $b/a = 0.71]$, i.e., a highly oblate (disc-like) configuration in both data-sets (Table 2.2). The pole is very close to the pole found for the full sample of twelve satellites within the approximate virial radius. In Figs. 2.15 and 2.16 it is clearly visible that also some satellites are excluded here, shown by open symbols, which lie spatially close to the initially fitted plane. Including the very distant (and possibly bound) satellite IC 1613 outside the approximate virial radius of Andromeda, we find the pole of the fitted normal to be located at $(l_{\rm M31} = 74.4^\circ, b_{\rm M31} = -40.5^\circ)$ $[(l_{\rm M31} = 74.7^\circ, b_{\rm M31} = -40.6^\circ)]$, with axis ratios $c/a = 0.10$ and $b/a = 0.35$ $[c/a = 0.11$ and $b/a = 0.43]$. The latter axis ratio, leading to a more prolate configuration, is totally dominated by this one very distant satellite (IC 1613). We concentrate our further analysis on the sample of eight satellites without IC 1613, because it is located outside the approximate virial radius of Andromeda. We refer to this subsample in Tables 2.2 – 2.4 as kss8 (kinematic subsample of eight satellites).

Applying the AE test to the kss8 subsample, the direction of the principal axis is $(l_{\rm M31} = 70.5^\circ, b_{\rm M31} = -35.2^\circ)$ $[(l_{\rm M31} = 74.2^\circ, b_{\rm M31} = -35.2^\circ)]$, with a spherical standard distance $\Delta_{\rm sph} = 2.4^\circ$ $[\Delta_{\rm sph} = 1.6^\circ]$ (KG [MI] data). The location of the principal axis is in good agreement with the individual fits above, and $\Delta_{\rm sph}$ is for both data-sets significantly smaller than for the full data-sets, and also an order of magnitude smaller than for the mss8 subsample (§ 2.3.1).

Performing the bootstrap analysis with 5 000 re-samplings for the kinematically motivated subsample yields shape parameter $\gamma = 5.9$ and strength parameter $\zeta = 4.7$ $[\gamma = 14.9$, $\zeta = 4.2]$. For both data-sets the distribution of the directions of the fitted planes of the bootstrapped data are strongly concentrated and clustered. The derived spherical standard distance is $\Delta_{\rm sph} = 9.8$ $[\Delta_{\rm sph} = 11.5]$, indicating that the systematic effects caused by the distance uncertainties are smaller than the internal scatter as derived by the bootstrapping.

Even though the morphologically motivated subsample (§ 2.3.1) has a smaller rms-height Δ than the kinematically motivated subsample for the KG-data, and thus appears as a 'thinner' disc, the bootstrap analysis shows that the latter one has a more pronounced planar-like feature. The strong clustering is found in both data-sets. We have therefore uncovered a sample of eight M31 satellites (nine if IC 1613 was included) which span a very pronounced disc-of-satellites that is probably rotationally supported.

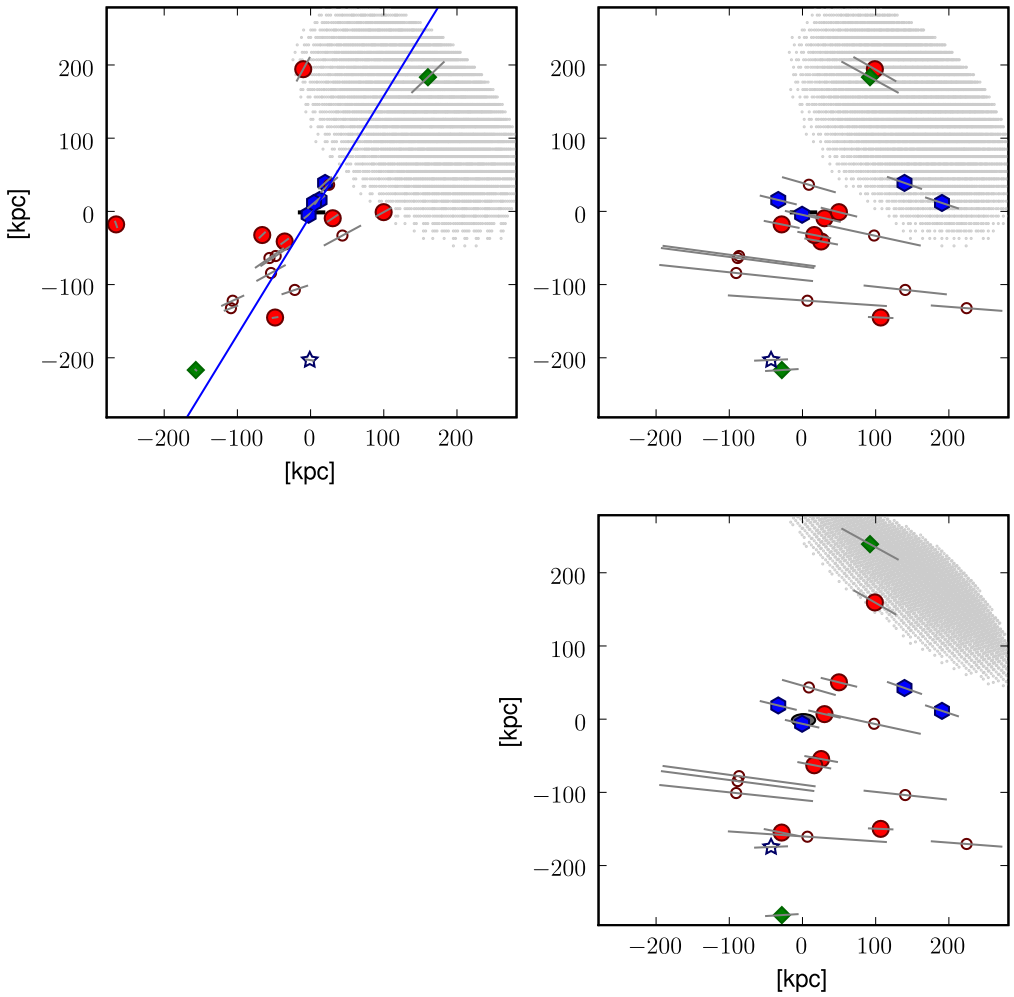

Figure 2.10: The Andromeda satellite system as seen from infinity for the MI data. An edge-on view (top-left panel), and a view rotated by 90° about the polar axis (top-right panel), as well as a face-on view (bottom-right panel) onto the fitted plane, derived using the ALS method, are shown as in Fig. 2.4 for the MW system. The recently discovered dwarf spheroidals And X – And XVII are marked by smaller symbols; these were not incorporated in the fitting. M33, which was also not incorporated in the fitting, is marked by the star. The other symbols are chosen as in Fig. 2.8. The distance uncertainties along the line-of-sight are indicated by the grey sticks. In addition, the grey shaded area indicates the projected region where potentially some satellite galaxy detections may be hindered by foreground MW structures (see also McConnachie & Irwin 2006b, their figure 1).

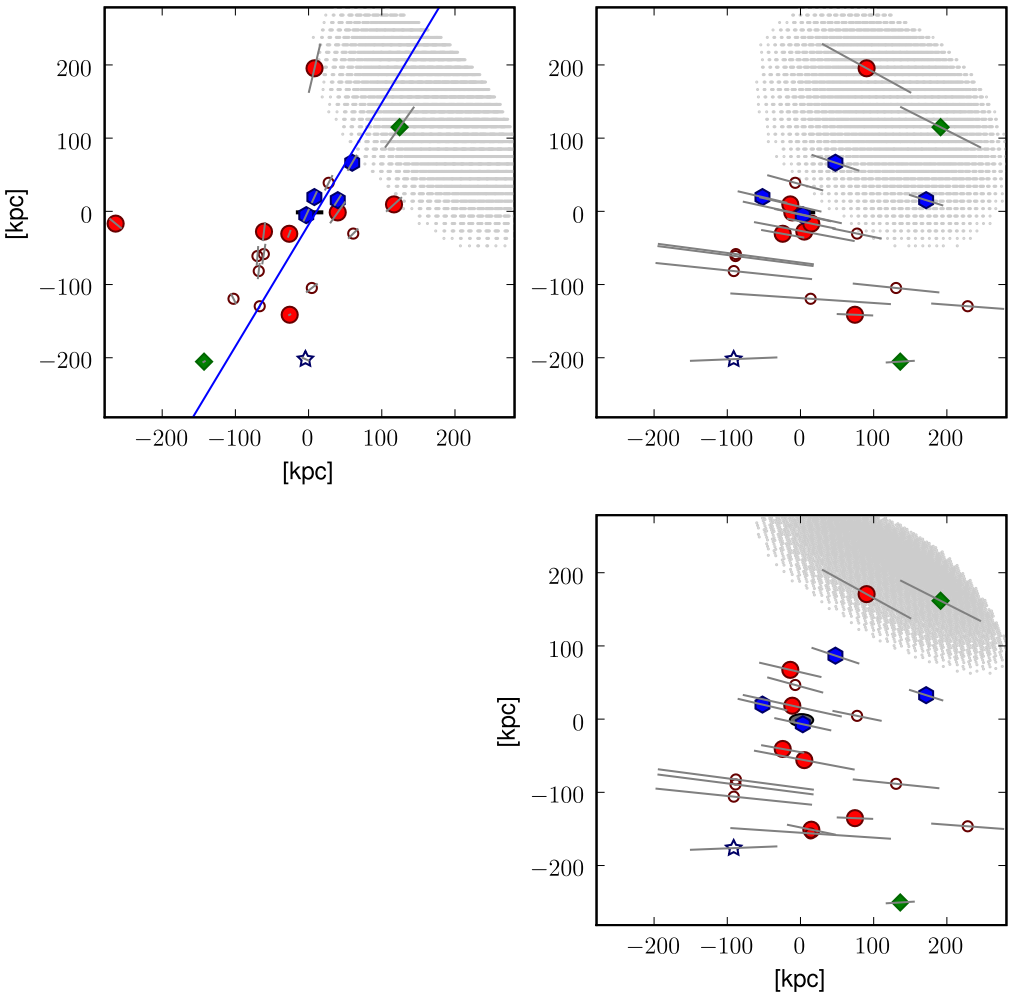

Figure 2.11: As Figure 2.10, plane-fit (ALS) for the KG data.

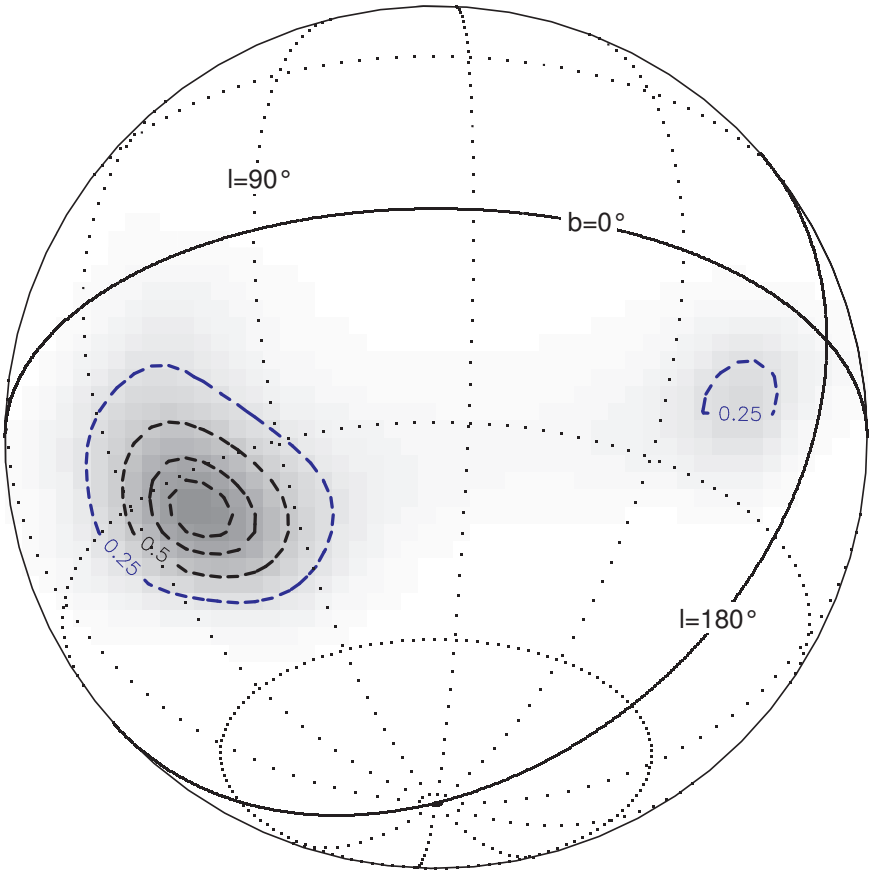

Figure 2.12: A smoothed (l_{M31}, b_{M31}) scatter plot of 10 000 bootstrap samples for the innermost twelve Andromeda satellites for the MI data-set ranging out to LGS 3 as Fig. 2.6. The principal axis of the distribution is located at ($l_{\mathrm{M31}} = 75.5°$, $b_{\mathrm{M31}} = -31.9°$). The plot is shown 30° off-centre from the principal axis. An additional contour line for the density estimate of 0.25 indicates a weak secondary maximum.

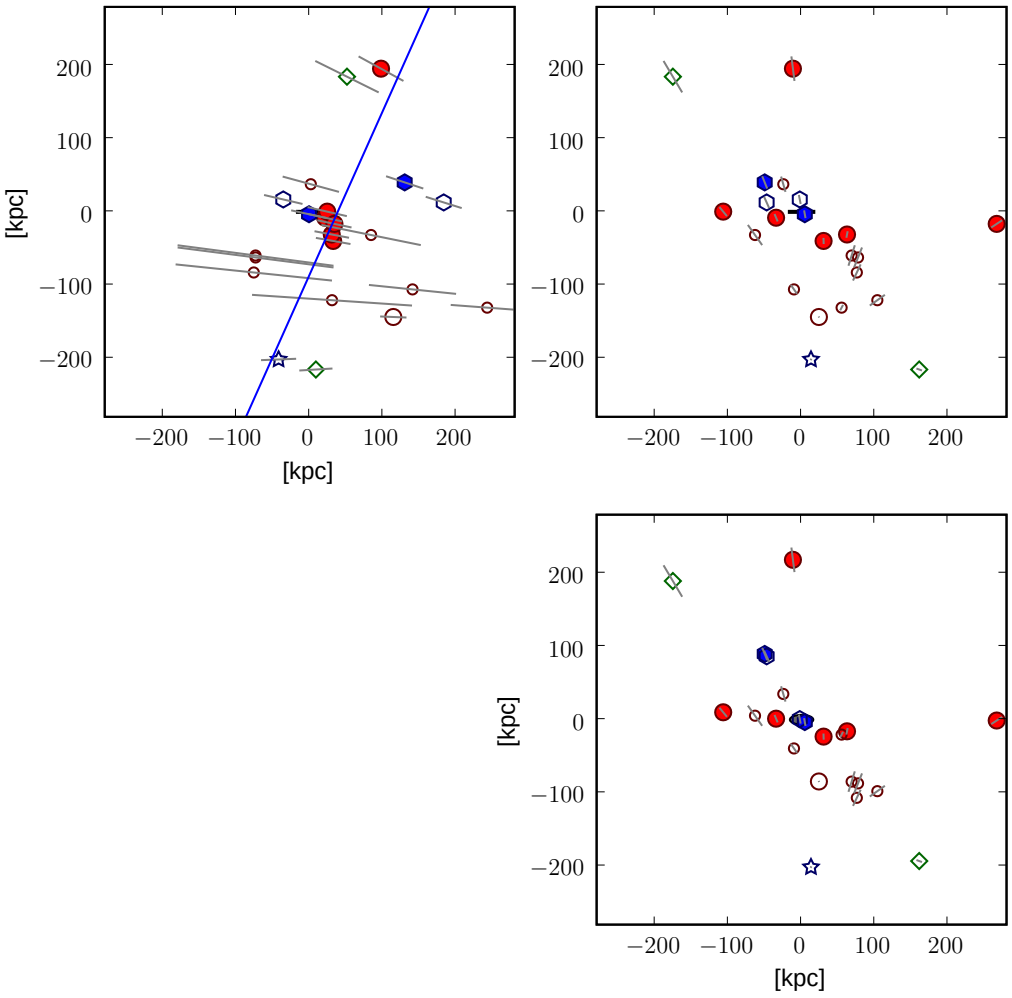

Figure 2.13: Plot as before for the MI data, now showing the results of the fitting for a morphologically motivated sub-subsample (mss8) as proposed by Koch & Grebel. Satellites not incorporated in the fitting are marked with open symbols.

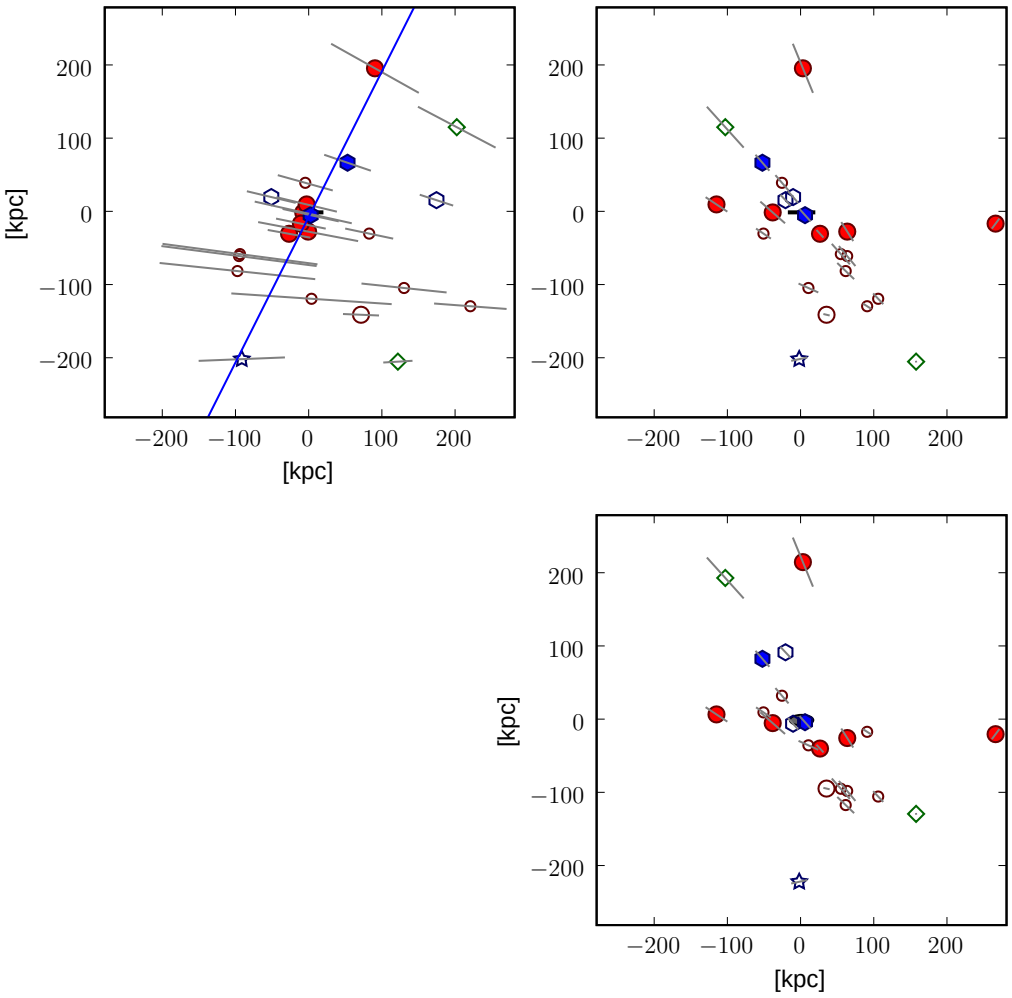

Figure 2.14: As Figure 2.13, plane-fit to the mss8 subsample for the KG data.

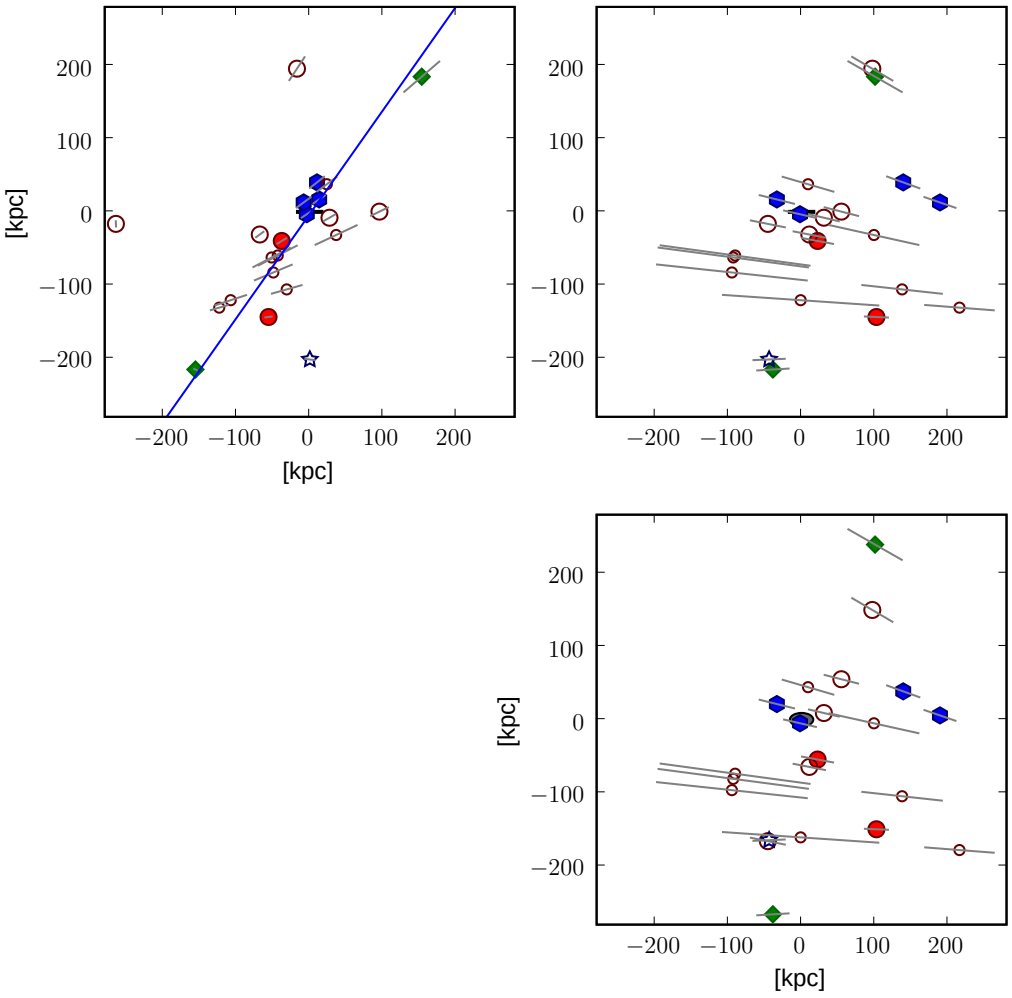

Figure 2.15: Plot as before for the MI data, now showing the results of the fitting for a kinematically motivated sub-subsample kss8. Satellites not incorporated in the fitting are marked with open symbols.

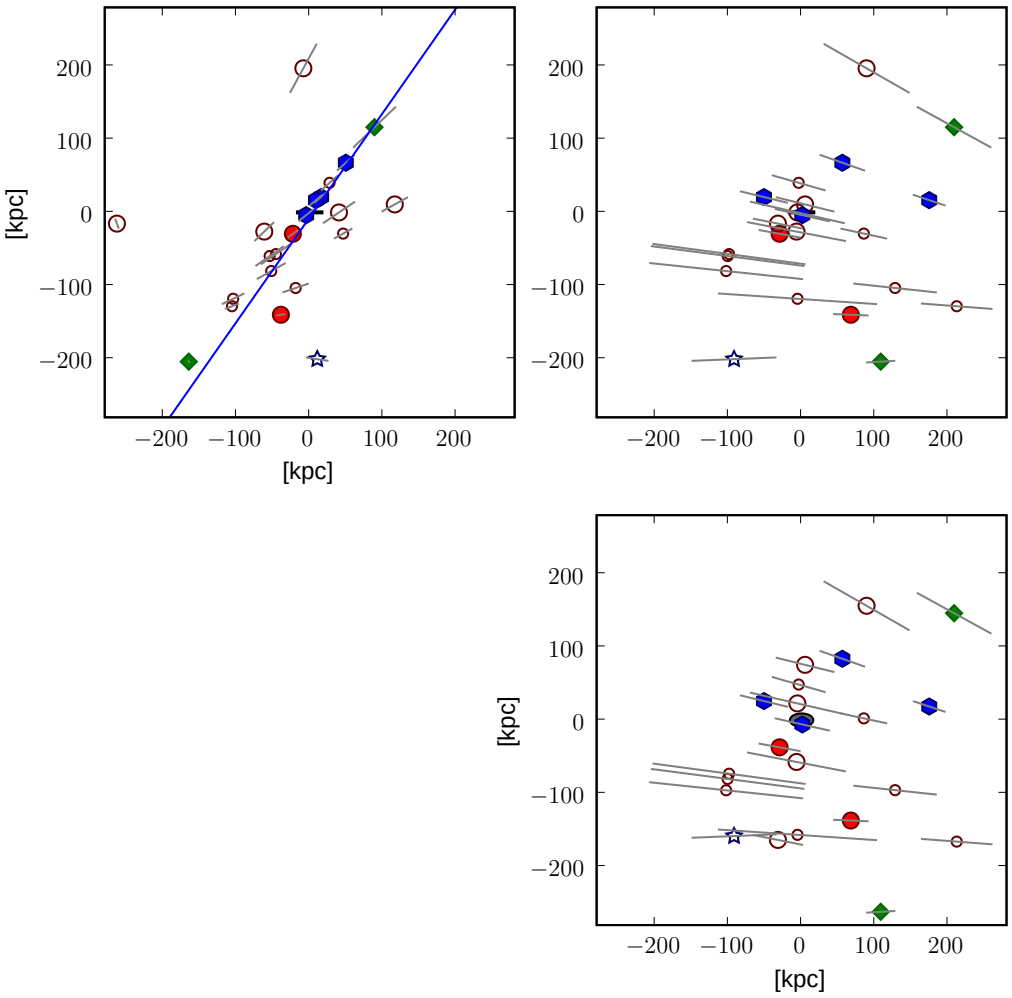

Figure 2.16: As Figure 2.15, plane-fit to the kss8 subsample for the KG data.

2.4 Statistical significance of disc-like distributions

In order to study the possible physical nature of the Milky Way and Andromeda satellite system, the statistical significance of the observed anisotropy, given a parent distribution, needs to be quantified. According to the null-hypothesis, the parent distribution ought to be a dark matter subhalo distribution, which may be spherical, oblate, prolate, or triaxial, and the positions of the satellite galaxies are randomly drawn from this parent distribution. To evaluate the significance of planar distributed satellite systems we compare the bootstrapped samples of the observed distribution with bootstrapped data of random samples from the parent distribution. For this we first create spherically isotropic distributions, where the radial linear probability density is proportional to $\rho(r) \propto r^{-p}$, $p = 2$ ($\Rightarrow \rho_{\rm sph}(r,\vartheta,\phi) \propto r^{-q}$, $q = 4$), consistent with the radial distribution found for the Milky Way (Kroupa et al. 2005) and Andromeda (Koch & Grebel 2006). Random oblate, prolate, or triaxial ellipsoidal distributions with axis ratios c/a and b/a are then constructed by scaling the components of the random spatial position vectors while keeping the volume of the ellipsoid invariant,

$$\begin{pmatrix} x' \\ y' \\ z' \end{pmatrix} = f_V \begin{pmatrix} & x \\ \frac{b}{a} & y \\ \frac{c}{a} & z \end{pmatrix} \quad , \tag{2.32}$$

where the normalisation factor f_V is given by

$$f_V = \sqrt[3]{\frac{a^2}{b\,c}} \quad . \tag{2.33}$$

As shown in Eqn. (2.6), the formally expected relative height of a spherical distribution is dependent on the minimum and maximum radii. Therefore the random samples are set-up with the minimum and maximum radii as found for the Milky Way (see Table 2.1). For ellipsoidally distributed random samples the initial values are scaled such that the final distribution has the expected minimum and maximum radii.

As for the observed data, each random sample is bootstrapped 10 000 times and we calculate the shape parameter γ and the strength parameter ζ of the resulting distribution of fitted normal vectors. Fig. 2.17 (central panel) shows a contour-plot ζ vs. γ derived for 100 000 random samples from an isotropic distribution ($a = b = c$) each consisting of eleven model satellites, bootstrapped 10 000 times. As can be seen from the coloured regions, which show the density distribution, the distribution of normal vectors of bootstrapped random samples is not expected to be randomly distributed in (γ, ζ)-space. They are typically found to be girdled or transitional ($\gamma \lesssim 1$) and marginally concentrated ($\zeta < 3$), while there is also some fraction of clustered ($\gamma > 1$) distributions. For oblate parent configurations (Fig. 2.17, upper panel) much more clustered distributions ($\gamma > 1$) result which are typically also more concentrated ($\zeta \gtrsim 3$). On the other hand, for prolate parent configurations (Fig. 2.17, bottom panel) typically a much higher fraction of girdled distributions ($\gamma < 1$) results, but also with higher concentration parameter ($\zeta \gtrsim 3$). Small concentration parameters are mostly found for an isotropic distribution.

To calculate the significance of an observed distribution, the joint distribution function $D(\gamma,\zeta)$ is computed and the percentile of bootstrapped random samples is derived for

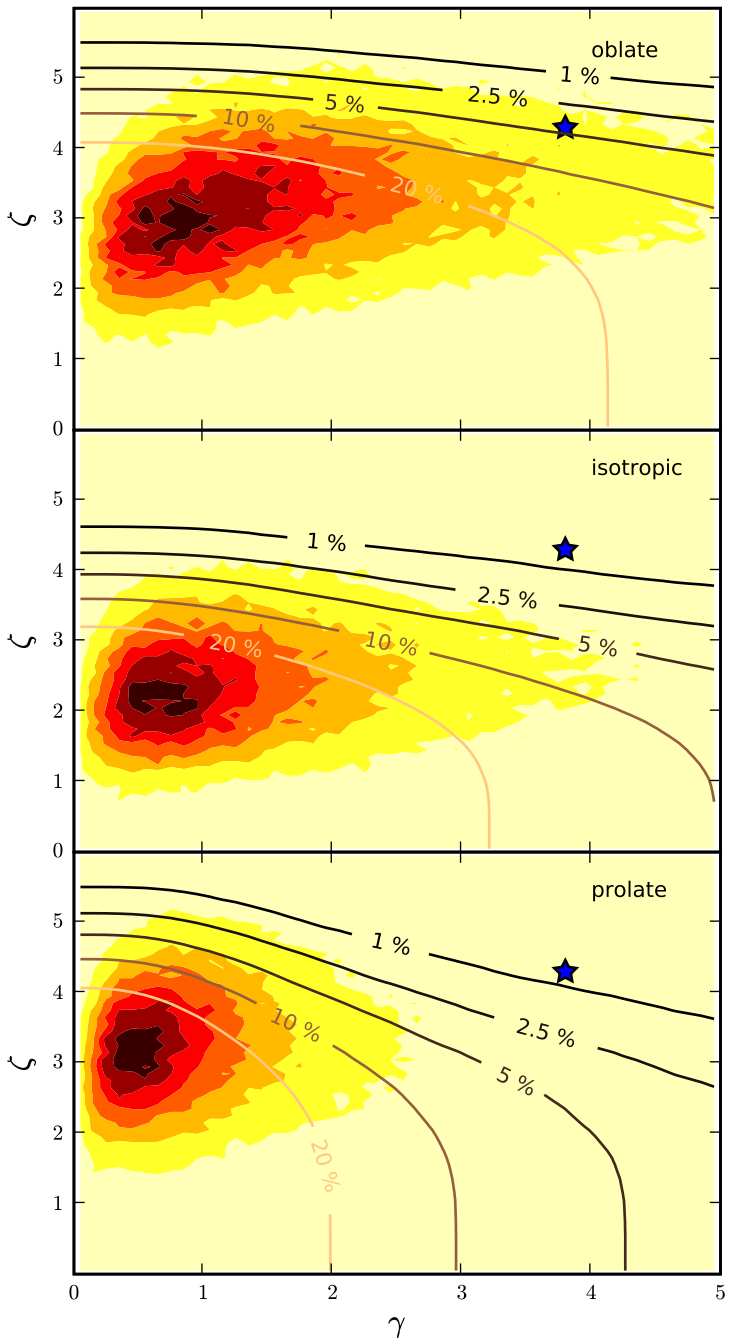

Figure 2.17: A contour-plot of strength parameter ζ versus shape parameter γ for 100 000 random samples, each consisting of eleven model satellites with an isotropic (central panel), oblate ($c/a = 0.5$, $b/a = 1.0$, top panel), and prolate ($c/a = b/a = 0.5$, bottom panel) parent distribution, each individually bootstrapped 10 000 times. The coloured contours show the density distribution of the derived parameters, dark red being high density. The contour lines show the enclosed values with significance levels as labelled. The star marks the parameters derived for the Milky Way.

which both the shape parameter and the strength parameter are larger than found for an observed satellite distribution, e.g. of the Milky Way (Fig. 2.17, solid contour lines). For each parameter pair of initial values c/a and b/a we create 100 000 random satellite samples each consisting of eleven satellites. Each of these samples is individually analysed using the bootstrap method with 10 000 re-samplings. This required a large amount of CPU time and we ran the simulation on the computer system of the Argelander-Institute and the CIP-pool[(e)] of the physics department. The full run took about 7 500 CPU-hours running simultaneously on up to 30 PCs from 500 MHz class to 3 GHz class CPUs using a distributed computing technique.

2.4.1 The Milky Way

The percentile of models found to have bootstrapped distributions more concentrated than for the Milky Way are listed in Table 2.6. Approximate contour lines for a 1, 2, and 5 per cent probability that the Milky Way satellites (the classical data-set) are drawn randomly from a parent distribution with initial axis-ratios c/a and b/a are shown in Fig. 2.18. The values typically obtained for Milky Way sized dark matter haloes (see, e.g., Libeskind et al. 2005) are shown by the grey shaded region.

The same analysis for a sample of twelve satellites is repeated with 20 000 random samples, and the derived shape parameters are compared with those found for the Milky Way satellites including the UMa dwarf galaxy. The resulting fractions are listed in the bottom part of Table 2.6. Including the recently discovered dSph in Canes Venatici, we ran only one test with 13 satellites and 20 000 random samples for a spherical setup. For this run we find 0.3 per cent of the random samples more concentrated than for the Milky Way sample.

The null-hypothesis that the Milky Way satellites are drawn randomly from a spherical or mildly triaxial parent population as it is typically found in cosmological dark matter simulations can be excluded at very high statistical significance, ≥ 99.5 per cent, confirming the results of Kroupa et al. (2005). With increasing triaxiality, the probability increases for more oblate configurations (which are marked with a grey background in Table 2.6). Prolate configurations are basically excluded, except for configurations nearly perfectly triaxial, e.g., for $c/a = 0.5$ and $b/a = 0.7$, where the probability may be of order 1 per cent. Including the UMa dwarf galaxy increases the significance of this result (reduces the propability).

2.4.2 Andromeda

For Andromeda, using an appropriate setup, the percentile values for the case that the satellite distribution within the approximate virial radius is drawn randomly from a spherically isotropic parent distribution is already 12 per cent for the KG-data. This reflects the fact that we find the bootstrapped normals of the M31 satellite system to be much less clustered than for the Milky Way. The distribution of bootstrapped normals for the MI data-set are even less clustered and the percentile value is thus larger. So the hypothesis that the full

[(e)] `http://cip.physik.uni-bonn.de`

Table 2.6: Percentile of bootstrapped random samples for which the shape parameter and the strength parameter indicate a distribution of the normals of bootstrapped satellites more concentrated than found for the Milky Way satellite system. Different setup distributions are used with axis ratios c/a (along rows) and b/a (along columns). The top table gives the percentile for the innermost eleven satellites, the bottom table for the innermost twelve satellites including the UMa dwarf satellite candidate. Parameter combinations for which $c/b < b/a$, i.e., which are triaxial and more oblate, are highlighted by a light grey background colour.

				b/a				
c/a	*0.3*	*0.4*	*0.5*	*0.6*	*0.7*	*0.8*	*0.9*	*1.0*
1.0								0.5
0.9							0.5	0.5
0.8						0.6	0.6	0.6
0.7					0.6	0.7	0.8	1.0
0.6				0.7	0.8	1.1	1.5	2.0
0.5			0.7	0.9	1.5	2.4	3.3	4.1
0.4		0.5	0.9	2.1	4.1	6.3		
0.3	0.2	0.8	2.7	6.9	12.2			
1.0								0.3
0.9							0.3	0.4
0.8						0.4	0.3	0.5
0.7					0.5	0.4	0.6	0.6
0.6				0.5	0.5	0.8	1.1	1.5
0.5			0.4	0.7	1.1	2.0	2.7	3.6
0.4		0.3	0.7	1.6	5.4	3.2		
0.3	0.1	0.6	2.2	6.2	11.6			

M31 satellite system is drawn randomly from a spherically isotropic parent distribution can not be rejected at present, using the available data.

2.4.3 Statistical significance of M31 subsamples

Performing the analysis as described above for the morphologically (§2.3.1) and kinematically (§2.3.2) motivated subsamples would *not* yield the correct significance levels: the null-hypothesis for deriving the statistical significance is that all satellite galaxies within a certain radius trace a parent distribution, i.e., one assumes all satellite galaxies to be of the same origin, namely luminous DM sub-structures. But performing the analysis as above would imply that the eight satellites selected by the morphological or kinematical criterion are luminous dark matter sub-structures, randomly drawn, and the excluded ones are of another origin. Even in the case of the morphologically motivated subsample, where one may argue that all dSphs/dEs have been build due to the same mechanism, some were excluded because of their large distance from the fitted plane. But, they should have been included to derive the significance, because otherwise one implies a different origin of the excluded satellites. Koch & Grebel (2006) did not take this into account.

To derive the significance correctly, the procedure is to set up twelve model satellites

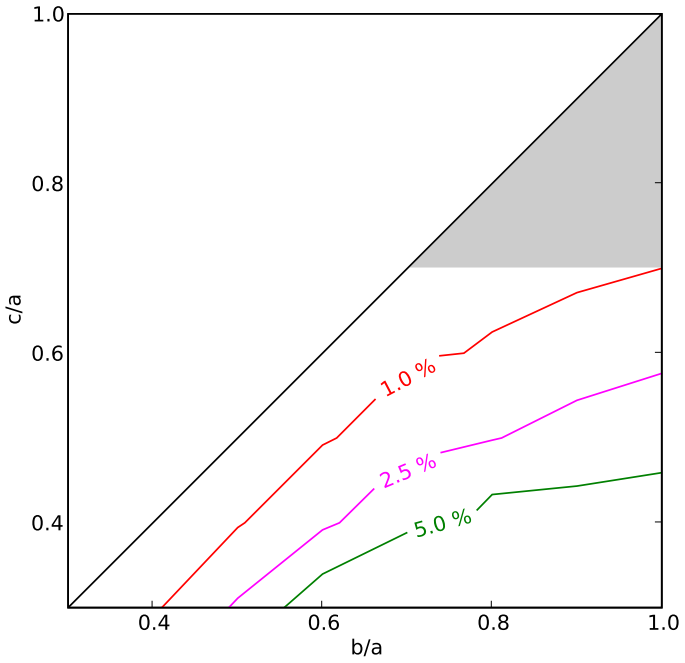

Figure 2.18: Approximate contour lines of the 1, 2.5, and 5 per cent confidence levels for bootstrapped random samples with initial axis-ratios c/a and b/a being representative for the distribution of the eleven innermost MW satellite galaxies. The grey shaded region shows the range of axis ratios typically found for CDM haloes in numerical simulations.

within the appropriate distance range from M31 and then select all combinations of eight model galaxies out of the full sample. For each of these individual subsamples, 495 in total, a full bootstrap analysis has to be performed. Then the fraction of random samples that have subsamples of eight model satellites with a more pronounced disc-like distribution than the observed sample needs to be calculated.

Practically, this analysis can only be performed for a few specific set-ups because the runs take a large amount of CPU time. We performed one run for each of the data-sets, MI and KG, respectively, using an isotropic parent distribution. The differences between both random runs are the minimum and maximum radii, chosen to match the values of the corresponding observed data-sets. We setup 10 000 random samples. The full run took about 20 000 CPU hours, running simultaneously on more than 30 standard PCs.

The percentile value for the case that the *morphologically* motivated subsample is picked from samples that are randomly drawn from an isotropic distribution is 100 per cent for the MI data-set and 95 per cent for the KG data-set. The percentile value for the *kinematically* motivated subsample is 17 per cent for the MI data-set and 10 per cent for the KG data-set. Even though appearing as a 'thin' disc-of-satellites, we conclude that the morphologically motivated subsample is just a chance alignment of galaxies and fully consistent with being randomly drawn from an isotropic distribution. For the kss8 subsample we can also not reject the hypothesis that the satellites are picked from a random sample, but the percentile value is much lower ($< 17\%$) for both data-sets.

2.5 Discussion

The statistical methods to analyse the spatial distribution of the satellite galaxies of the Milky Way and Andromeda is not based on the "thickness" of a planar-like distribution alone, as this is not sufficient to characterise the distribution (Kang et al. 2005; Zentner et al. 2005). The bootstrap method is used to derive the distribution of poles of fitted planes which are analysed using methods based on the statistical analysis of spherical data. These methods quantify the robustness of a planar-like distribution. Thus, a population of satellites that is not planar-like will in our analysis be robustly identified as an unstable distribution of poles.

2.5.1 The Milky Way system

Applying two methods (ALS and ODR) to fit planes, the Milky Way satellite system within 254 kpc is found to be highly anisotropical. All "classical" companion galaxies are aligned in a disc-like structure with an rms-height of only $\Delta = 18.5$ kpc (Table 2.2). This disc-of-satellites is highly inclined with respect to the Milky Way's stellar disc, $|b_{\rm MW}| \approx 12^\circ$, passing the Galactic plane close to the Galactic Centre, $D_{\rm P} \approx 8$ kpc $< \Delta$. The statistical methods, applied to the satellite system of the Milky Way, show that the hypothesis that the Milky Way satellites are drawn randomly from an isotropic distribution can be excluded at a high statistical significance level ($\geq$ 99.5 per cent). It can also be excluded that the distribution is drawn randomly from a triaxial or prolate parent distribution as typically found in cosmological simulations of Milky Way sized haloes (e.g., Jing & Suto 2002; Bullock 2002; Libeskind et al. 2005; Zentner et al. 2005), Diemand et al. (2005a) specifically argued that the distribution of haloes formed early is even more elongated, i.e. more prolate than the smooth host dark matter halo. The null-hypothesis that the satellite system is drawn randomly from a dark matter parent distribution cannot be rejected *only* if the parent distribution is highly triaxial and oblate, i.e. if the parent distribution is already flattened. In this case, and as long as no host-galaxy formation is included in large scale CDM simulations, the disc of the Milky Way has to be *postulated* to be nearly perpendicularly oriented to the oblate host halo, because we find the disc-like structure of satellite galaxies to have a polar alignment. Even so, the required highly triaxial oblate DM-host shape is only marginally consistent with the results of modern CDM structure formation simulations. Furthermore, recent measurements of the shape of the Milky Way potential using the Sagittarius stream indicate it to be almost spherical within about 60 kpc (Fellhauer et al. 2006, see also §6.2).

The discoveries of two additional faint Milky Way companions that were included in the full analysis, increases the confidence in the above statements. Indeed, all the recently detected dSphs lie close to the DoS, except for the Hercules dwarf. It can not be excluded that the Hercules dwarf has been scattered into its current orbit (compare Sales et al. 2007a). However, since the SDSS (York et al. 2000) mostly covers the north pole region of the Galactic sky (Figs. 2.3 and 2.7) the detection is biased towards this region. But there are remarkably large portions of the sky that are way off the DoS – but no satellite galaxies are reported there. To get an answer beyond the possible sky-coverage bias it will be crucial to extend the search for Milky Way companions over a larger area of the sky and particularly at lower Galactic latitudes, as it is planned by the Stromlo Missing Satellite (SMS) survey (Jerjen et

al., in preparation) using the new ANU SkyMapper telescope (Schmidt et al. 2005). We note though that if additional very faint dwarf galaxies are discovered to not lie within the disc-of-satellites as quantified here, as for example the Hercules dwarf appears to be (Table 2.1), we are nevertheless left with the fact that the eleven most luminous Milky Way satellite galaxies are aligned in the disc.

For the Milky Way a significant fraction of dwarf galaxies may be invisible in the optical due to obscuration by the Galactic disc at low Galactic latitudes (e.g., Mateo 1998). Within the virial radius of the Milky Way about half of the total volume has latitude $b \leq 30^\circ$. Andromeda is in that sense a better probe since it's halo is not that much affected by obscuration (McConnachie & Irwin 2006b). A simple estimate for the Milky Way, assuming that all undetected satellites are homogeneously distributed over the whole sky, and further assuming that all satellites with $b \leq 15^\circ$ are undetected, 50 per cent of all satellites with $15^\circ < b \leq 30^\circ$ are undetected, we find that about 35 per cent of all satellites with $b \leq 30^\circ$ may be found more than $1\sigma = \Delta$ off, and about 30 per cent more than 3σ off the fitted disc-of-satellites. This is a very conservative estimate for the Milky Way obscuration. McConnachie & Irwin (2006b) estimated that only regions within $|b| < 15^\circ$ are affected by obscuration, and those with $|b| < 5^\circ$ to be the most strongly affected regions.

2.5.2 The Andromeda system

For the Andromeda satellite system it cannot be excluded that it has been drawn randomly from a spherical isotropic parent distribution. However, we do find the Andromeda satellite system to be anisotropic (left panels in Figures 2.10, 2.11, 2.15 & 2.16), but the details depend on the distance data used. The fitted disc-like structure for all satellites within the approximate virial radius is not as polar-aligned as for the Milky Way ($|b_{\rm M31}| \approx 30^\circ$) and it is approximately twice as 'thick' as found for the Milky Way (Table 2.2).

Two incompatible subsamples of satellite galaxies which have a disc-like distribution can be identified: one morphologically motivated, as proposed by Koch & Grebel (2006), and one kinematically motivated (§2.3.2). Since the disc-like satellite system of the Milky Way is dominated by dSph galaxies, one can speculate about a common building mechanism for all the dSphs in the Local Group that is also the cause for a plane-like alignment of satellite galaxies. If this mechanism was the break-up of a large, gas-rich galaxy or the formation of tidal dwarf galaxies (TDGs) in an early major-merger event, one expects the dSphs to have initially correlated directions of their angular momentum vectors, supporting a disc-like structure. This would favour the morphologically motivated subsample since it is initially composed of dSphs only. However, at least two of the Andromeda dwarf spheroidals within the virial radius do not fit into this picture and were excluded by Koch & Grebel (2006) because of their apparently large distance from the plane. Also only one out of three morphologically similar dEs is found close to the disc. On the other hand we cannot exclude the possibility that some massive TDGs may retain their interstellar medium to appear today as dIrr galaxies (Hunter et al. 2000; Recchi et al. 2007).

The disc-like distribution of the morphologically motivated subsample of dSph/dE galaxies (mss8) around Andromeda is present for the KG data-set only, but cannot be identified for the MI data-set. Comparing the results of the AE and the bootstrap test it follows that even in the KG data-set the systematic errors caused by the distance uncertainties are

larger than the intrinsic scatter as quantified by the bootstrapping. Furthermore, the high significance of the morphologically motivated disc as derived by Koch & Grebel (2006) must be incorrect because of three reasons: firstly they derived their significance based on the thickness of the disc alone, secondly they used the ODR fitting method that is affected by the systematic alignments of the distance uncertainties of the M31 satellites, and thirdly, most importantly, they did not use the correct null-hypothesis to derive the significance. We find the distribution of the morphologically motivated subsample of Andromeda satellite galaxies to be fully consistent with being picked from a random distribution.

The kinematically motivated subsample of eight Andromeda satellites forms a pronounced thin disc with inclination of $\approx 31^\circ$ away from a polar alignment, and that holds true for both data-sets, MI and KG. The kss8 subsample is found to have a much more pronounced disc-like distribution than the morphologically motivated one, although its apparent thickness, as quantified by Δ, is larger. Even though the kinematically motivated subsample has a much higher statistical significance than the morphologically motivated one, we can also not exclude the possibility that this sample is picked from a random distribution.

Interestingly, also all the newly discovered satellite galaxies of Andromeda lie close to its DoS as derived for the whole satellite population and the kinematically motivated subsample (Figs. 2.8, 2.9 and Figs. 2.15, 2.16). This is in particular remarkable given that the Andromeda system is much less affected by obscuration. Majewski et al. (2007) noted that along a radial vector from the centre of M31, connecting NGC 147 and And XIV, in total six satellite galaxies are located in projection, and Irwin et al. (2008) found that And XVII is also on that line. We demonstrated that the new dSphs lie on a straight line not only in projection, but taking their full 3D data into account, we find that they belong to the same disc-of-satellite as previously derived. This holds true despite large distance uncertainties.

2.5.3 The Milky Way versus Andromeda

There is no obvious evidence for a spatial association of the disc-of-satellites of the Milky Way and the Andromeda galaxy or its satellites (but see Sawa & Fujimoto 2005). If Andromeda, located at $l_{\rm MW} = 121.7^\circ$, $b_{\rm MW} = -21.5^\circ$, and its satellites were associated with the disc-of-satellites of the Milky Way, M31 ought to be close to the fitted disc-like structure, and the fitted planes ought to be aligned. Instead, M31 is $\approx 55^\circ$ off the fitted plane of the Milky Way satellites. Similarly, the angle between the normals of the fitted satellite planes of the MW and M31 is $\approx 50^\circ$ – 60°, but would be 0° if they were perfectly aligned.

Fig. 2.19 shows the directions of the spin-poles (SP) of the stellar discs of the Milky Way and Andromeda in supergalactic coordinates (de Vaucouleurs et al. 1991), as well as the spin-poles of the smaller Local Group galaxies LMC and M33 (van der Marel & Cioni 2001; Corbelli & Schneider 1997). Additionally, the directions of the normals of the fitted disc-like structures of the satellite distributions of the MW and M31 are shown. It follows that the spin-axis of the Milky Way lies very close to the supergalactic plane, within about 6°, and the normal of the Milky Way DoS is likewise close to the supergalactic plane, but almost 90° off the spin-axis of the Milky Way. The spin-axis of the stellar disc of Andromeda and the normal of its fitted DoS are both about 30° off the supergalactic pole. If both discs-of-satellites were build up by the individual accretion of galaxies, preferentially from

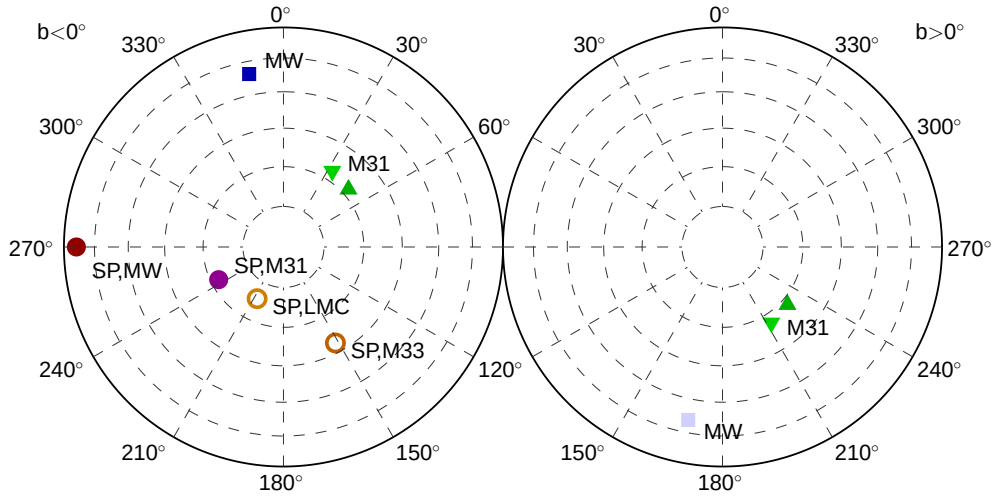

Figure 2.19: A Lambert projection – left for negative and right for positive latitudes – of the directions of the spin poles (SP) of the stellar discs of Milky Way and Andromeda in supergalactic coordinates, marked by filled circles, as well as of the smaller Local Group galaxies LMC and M33, marked by open circles. The directions of the normals of the fitted plane of all satellites of the MW and M31 within their virial radii are marked by squares and triangles, respectively (MI data: triangles pointing downwards, KG data: triangles pointing upwards). The dark square marks the direction of the normal of the Milky Way DoS that is its probable orbital pole as shown later in Section 3.2

the direction of the supergalactic plane, i.e. from the direction of the medium-scale (a few Mpc) matter distribution, then the normals of the discs-of-satellites should be close to the supergalactic pole. The orientation of the Milky Way DoS and the mutual miss-alignment of the discs-of-satellites contradict this notion.

The highly-inclined orientation of the stellar disc of the Milky Way relative to the supergalactic plane can be understood either as being a result of tidal torquing (Navarro et al. 2004) or resulting from the perpendicular collapse of matter onto the supergalactic plane (Doroshkevich 1973; see also Hu et al. 1998). If tidal torquing is responsible for the orientation of the Galactic disc, this begs the question as to why the other discs were not affected, and how tidal torquing affects the discs-of-satellites – one is highly inclined, the other is not. Alternatively, it would appear more natural or intuitive to understand a disc-of-satellites as being the result of stochastically occurring mergers which leave populations of related tidal dwarf galaxies. Such populations would remain visible for highly inclined events relative to the host discs, because populations of TDGs in low-inclination orbits would precess apart and possibly end up merging altogether with their host discs (Peñarrubia et al. 2002) or being more quickly destroyed than on polar orbits.

It appears implausible that for both systems the disc-of-satellites is present due to observational biases only. That would be a very strange coincidence. Rather, these findings strengthen the case that the discs-of-satellites for both, the Milky Way and Andromeda, are signs of a spatial correlation of the satellite galaxies.

Chapter 3

Analysis of orbital properties of satellite galaxies

To constrain the possible origin of the satellite galaxies in the Local Group that were found to be highly flattened for the Milky Way as we showed in the last Chapter, we now study their orbital properties. Based on spatial alignments, Kunkel & Demers (1976), Lynden-Bell (1976), and Lynden-Bell (1982) postulated that some of the dSph galaxies, along with the Magellanic clouds and several globular clusters (GC), belong to one or two streams of co-moving objects. Incorporating radial velocity measurements, Lynden-Bell & Lynden-Bell (1995) further constrained possible streams of satellite galaxies and GCs: they used the great circles of possible locations of angular momenta to identify possible "ghostly streams". Palma et al. (2002) extended the analysis of these so called "polar-paths" by using available proper motion measurements to confine the location of directions of the angular momenta of satellite galaxies to arc-segments of the polar-paths.

Meanwhile further proper motion measurements, especially for more distant Milky Way dSph companions, have become available. In a series of papers Piatek et al. (2003, 2005, 2006, 2007) measured the proper motions of the dwarf spheroidal galaxies Carina, Ursa Minor, Sculptor, and Fornax, respectively, with the Hubble Space Telescope (HST). Here we follow Palma et al.: we incorporate the Piatek et al. measurements to construct new arc-segments of polar-paths for the Milky Way satellite galaxies (§3.2.1). The data is compared to a recent set of CDM simulated luminous subhaloes in MW-like host-haloes that were kindly provided by Noam Libeskind, also analysing their spatial properties (§3.2.2). For both, observations and CDM simulations, we construct a "pole-distance" distribution that is statistically analysed (§3.2.3).

In the second part of this Chapter (§3.3.1), we outline a method how to set restrictions on the possible orbital poles of Andromeda satellites. This information is used to search for possible streams of M31 satellite galaxies and allows us to confine a subsample of them that might share similar orbital properties (§3.3.2, see also §2.3.2).

3.1 Methods for the analysis of orbital properties

3.1.1 Galactocentric velocity vectors and their covariances

In astrometry, velocity measurements are usually expressed as proper motion in right ascension corrected for the declination, $\mu_{\alpha*} = \mu_\alpha \cos\delta$, and proper motion in declination, μ_δ, in units of arcsec yr^{-1} or mas yr^{-1}. Heliocentric radial velocities are usually given in units of $\mathrm{km\,s}^{-1}$. The cartesian space-velocity components (in units of $\mathrm{km\,s}^{-1}$) in Galactic coordinates are given by the equation

$$\boldsymbol{v} = \begin{pmatrix} U \\ V \\ W \end{pmatrix} = \mathsf{B} \begin{pmatrix} v_r \\ (k\,r)\,\mu_{\alpha*} \\ (k\,r)\,\mu_\delta \end{pmatrix} \quad , \tag{3.1}$$

where $k = 4.74057$, the equivalent of one astronomical unit in one siderial year in $\mathrm{km\,s}^{-1}$. Distances are given in units of $1/'' = \mathrm{pc}$, and proper motion in units of $''\,\mathrm{yr}^{-1}$. U is the velocity component in the direction of the Galactic centre, V the component in the direction of Galactic rotation, and W is the velocity towards the Northern Galactic Pole. The rotation matrix B is given by

$$\mathsf{B} = \mathsf{R}_{\mathrm{e}\mapsto\mathrm{g}}\mathsf{R}_{\mathrm{rpq}} \tag{3.2}$$

where $\mathsf{R}_{\mathrm{rpq}}$ is the coordinate triad (Murray 1983) for coordinates (α, δ) as given in Equation (2.22), and $\mathsf{R}_{\mathrm{e}\mapsto\mathrm{g}}$ is the transformation matrix from equatorial to Galactic coordinates

$$\mathsf{R}_{\mathrm{e}\mapsto\mathrm{g}} = \begin{pmatrix} \cos\theta_0 & \sin\theta_0 & 0 \\ \sin\theta_0 & -\cos\theta_0 & 0 \\ 0 & 0 & 1 \end{pmatrix} \begin{pmatrix} -\sin\delta_{\mathrm{N}} & 0 & \cos\delta_{\mathrm{N}} \\ 0 & 1 & 0 \\ \cos\delta_{\mathrm{N}} & 0 & \sin\delta_{\mathrm{N}} \end{pmatrix} \begin{pmatrix} \cos\alpha_{\mathrm{N}} & \sin\alpha_{\mathrm{N}} & 0 \\ \sin\alpha_{\mathrm{N}} & -\cos\alpha_{\mathrm{N}} & 0 \\ 0 & 0 & 1 \end{pmatrix} \tag{3.3}$$

(c.f. Johnson & Soderblom 1987). $\alpha_{\mathrm{N}} = 192.85948^\circ$ and $\delta_{\mathrm{N}} = 27.12825^\circ$ are the equatorial coordinates of the North Galactic Pole, and $\theta_0 = 122.93192^\circ$ is the position angle of the North Celestial Pole relative to the great circle passing through the North Galactic Pole and zero Galactic latitude (ESA 1997, Vol. 1, Sect. 1.5).

The derived velocity components are given in heliocentric coordinates, i.e. in the rest-frame of the Sun, and need to be corrected for the motion of the Sun in the Galaxy to get velocities in the rest-frame of the Galaxy. This is done by correcting for the circular motion of the local standard of rest (LSR) about the Galactic Centre using the IAU recommended value of $V_0 = 220\ \mathrm{km\,s}^{-1}$ circular velocity (Kerr & Lynden-Bell 1986), as well as for the peculiar motion of the Sun with respect to the LSR using the velocity components as given by Dehnen & Binney (1998).

In the simplest case we calculate the uncertainties in the velocity components in Galactic coordinates according to the error propagation theorem, assuming that the measurements of the distance, the radial velocity, and the two proper motion components are independent:

$$\begin{pmatrix} \sigma_U^2 \\ \sigma_V^2 \\ \sigma_W^2 \end{pmatrix} = \mathsf{C} \begin{pmatrix} \sigma_{v_r}^2 \\ k^2\left[(r\sigma_{\mu_{\alpha*}})^2 + (\mu_{\alpha*}\sigma_r)^2\right] \\ k^2\left[(r\sigma_{\mu_\delta})^2 + (\mu_\delta\sigma_r)^2\right] \end{pmatrix} + 2\mu_{\alpha*}\mu_\delta k^2\sigma_r^2 \begin{pmatrix} b_{12}\,b_{13} \\ b_{22}\,b_{23} \\ b_{32}\,b_{33} \end{pmatrix} \quad . \tag{3.4}$$

b_{ij} are the components of the matrix B, and the elements of the matrix C are the squares of the elements of the matrix B, i.e. $c_{ij} = b_{ij}^2$. The cross term arises since the velocity components V and W not only depend on the measured proper motion, but also on the distance r. Equation (3.4) is equivalent to equation (2) as given in Johnson & Soderblom (1987), except that we are using distances in parsec instead of parallaxes used by them.

The variances σ of the component U, V and W are, however, not uncorrelated. We calculate the Jacobi matrix:

$$\begin{aligned} J &= \begin{pmatrix} \frac{\partial U}{\partial v_\mathrm{r}} & \frac{\partial U}{\partial \mu_{\alpha*}} & \frac{\partial U}{\partial \mu_\delta} & \frac{\partial U}{\partial r} \\ \frac{\partial V}{\partial v_\mathrm{r}} & \frac{\partial V}{\partial \mu_{\alpha*}} & \frac{\partial V}{\partial \mu_\delta} & \frac{\partial V}{\partial r} \\ \frac{\partial W}{\partial v_\mathrm{r}} & \frac{\partial W}{\partial \mu_{\alpha*}} & \frac{\partial W}{\partial \mu_\delta} & \frac{\partial W}{\partial r} \end{pmatrix} \\ &= \begin{pmatrix} b_{11} & b_{12}(kr) & b_{13}(kr) & k(b_{12}\mu_{\alpha*} + b_{13}\mu_\delta) \\ b_{21} & b_{22}(kr) & b_{23}(kr) & k(b_{22}\mu_{\alpha*} + b_{23}\mu_\delta) \\ b_{31} & b_{32}(kr) & b_{33}(kr) & k(b_{32}\mu_{\alpha*} + b_{33}\mu_\delta) \end{pmatrix} \end{aligned} \tag{3.5}$$

and find for the correlation matrix C_{UVW}:

$$\mathsf{C}_{UVW} = \mathsf{J}\,\mathsf{C}_{v_\mathrm{r}\mu_\alpha\mu_\delta r}\,\mathsf{J}^\mathrm{T} \quad , \tag{3.6}$$

where the covariance matrix $\mathsf{C}_{v_\mathrm{r}\mu_\alpha\mu_\delta r}$ is given by:

$$\mathsf{C}_{v_\mathrm{r}\mu_\alpha\mu_\delta r} = \begin{pmatrix} \sigma_{v_r}^2 & 0 & 0 & 0 \\ 0 & \sigma_{\mu_{\alpha*}}^2 & 0 & 0 \\ 0 & 0 & \sigma_{\mu_\delta}^2 & 0 \\ 0 & 0 & 0 & \sigma_r^2 \end{pmatrix} \quad . \tag{3.7}$$

With equation (3.6) we find that the diagonal elements of C_{UVW} are the variances as given in Equation (3.4). We give as an example the covariance matrix for the measured proper motion of the Sagittarius dwarf galaxy:

$$\mathsf{C}_{UVW} = \begin{pmatrix} 48.0 & -118.8 & 144.0 \\ -118.8 & 374.3 & -325.2 \\ 144.0 & -325.2 & 444.2 \end{pmatrix} \tag{3.8}$$

The covariance matrix, C_{UVW}, is not affected by the transformation from heliocentric space velocities to galactocentric space velocities as long as the circular velocity of the LSR and the peculiar motion of the Sun with respect to the LSR have no, or negligibly small, uncertainties compared to the uncertainties of the velocity itself.

Having both, the covariance matrices of the galactocentric position vector $\boldsymbol{r}$ (cf. 2.1.1) and the velocity vector $\boldsymbol{v}$, one can in principal calculate the uncertainties of the galactocentric angular momentum vector $\boldsymbol{l} = \boldsymbol{r} \times \boldsymbol{v}$. As we will describe later in Sect. 3.2.1, we were only interested in the uncertainties of the direction of the angular momenta projected onto the Galactic sky. For this we only considered the proper-motion uncertainties (Appendix A) and derived the projected uncertainties geometrically for simplicity. This projection results in arc-segments on the Galactic sky (compare to Palma et al. 2002). If we had also included uncertainties in the positional vectors, the projection would have resulted in a banana-shaped, very narrow region aligned with the arc-segments.

3.2 Orbital properties of the Milky Way satellite galaxies

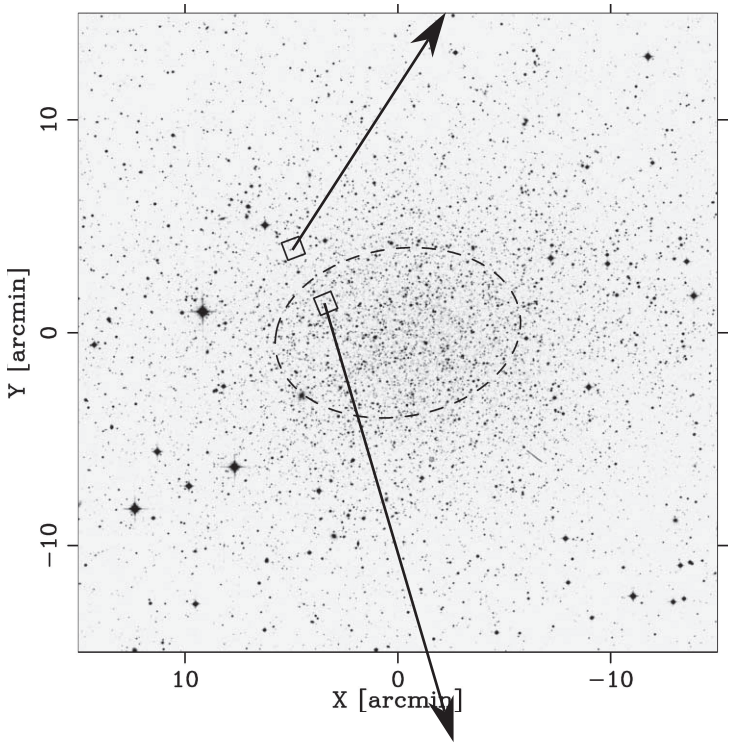

Figure 3.1: An image of the sky in the direction of the Sculptor dSph, taken from Piatek et al. (2006, their figure 1), the horizontal axis showing the direction of right-ascension, the vertical axis the direction of declination. The dashed ellipse indicates the core radius of Sculptor. The two squares mark the fields observed with the Hubble Space Telescope to determine the proper motion of the Sculptor dwarf. We over-plot two arrows, indicating for each field individually the direction and magnitude of the derived proper motion in arbitrary units.

3.2.1 The Milky Way satellite galaxies

A listing of available proper motion measurements for the satellite galaxies of the Milky Way was collected from the literature, and is given in Table 3.1. We do not give a complete list of all available measurements for the LMC and SMC here, but only the most recent ones. The directions of the angular momenta are not significantly affected by this choice. Multiple measurements of the dSph satellite galaxies are presented where available, however each individual measurement is less precise than the most recent LMC/SMC values. We also indicate whether proper motions were determined using ground based techniques (typically based on old photographic plates with long baselines) or using the Hubble Space Telescope (HST). The published proper motion value for Carina (Piatek et al. 2003) was derived without the advanced charge transfer inefficiency (CTI) correction for the STIS camera (Bristow et al. 2005; see also Reif et al. 2004 for an analysis of the time dependentce of the charge transfer efficiency under outer space conditions). Bristow et al. (2005)

Table 3.1: Absolute proper motions of the satellite galaxies of the Milky Way used for the analysis. Positional information of the satellites are provided in Table 2.1. The forth column indicates whether values were measured using ground based telescopes (GND) or the HST. Weighted mean values (MEAN) are indicated as well.

Name	$\mu_\alpha \cos\delta$ (mas yr^{-1})	μ_δ (mas yr^{-1})		Reference
Sgr	-2.65 ± 0.08	-0.88 ± 0.08	GND	Ibata et al. (1997)
	-2.83 ± 0.20	-1.33 ± 0.20	GND	Dinescu et al. (2005)
LMC	$+2.03 \pm 0.08$	$+0.44 \pm 0.05$	HST	Kallivayalil et al. (2006b)
SMC	$+1.16 \pm 0.18$	-1.17 ± 0.18	HST	Kallivayalil et al. (2006a)
UMi	$+0.5 \pm 0.8$	$+1.2 \pm 0.5$	GND	Scholz & Irwin (1994)
	$+0.056 \pm 0.078$	$+0.074 \pm 0.099$	GND	Schweitzer et al. (1997)
	-0.50 ± 0.17	$+0.22 \pm 0.16$	HST	Piatek et al. (2005)
	-0.04 ± 0.07	0.13 ± 0.07	MEAN	
Scu	$+0.72 \pm 0.22$	-0.06 ± 0.25	GND	Schweitzer et al. (1995)
	$+0.09 \pm 0.13$	$+0.02 \pm 0.13$	HST	Piatek et al. (2006)
	$+0.25 \pm 0.11$	0.00 ± 0.12	MEAN	
Dra	$+0.6 \pm 0.4$	$+1.1 \pm 0.5$	GND	Scholz & Irwin (1994)
Car	$(+0.22 \pm 0.09$	$+0.15 \pm 0.09)$	HST	Piatek et al. (2003)[(i)]
	$+0.22 \pm 0.13$	$+0.24 \pm 0.11$	HST	Piatek (2007, priv. comm)
For	$+0.59 \pm 0.16$	-0.15 ± 0.16	GND	Dinescu et al. (2004)
	$+0.476 \pm 0.046$	-0.36 ± 0.041	HST	Piatek et al. (2007)
	$+0.485 \pm 0.044$	-0.354 ± 0.028	MEAN	

[(i)] Proper motion measurement without advanced CTI correction for HST/STIS.

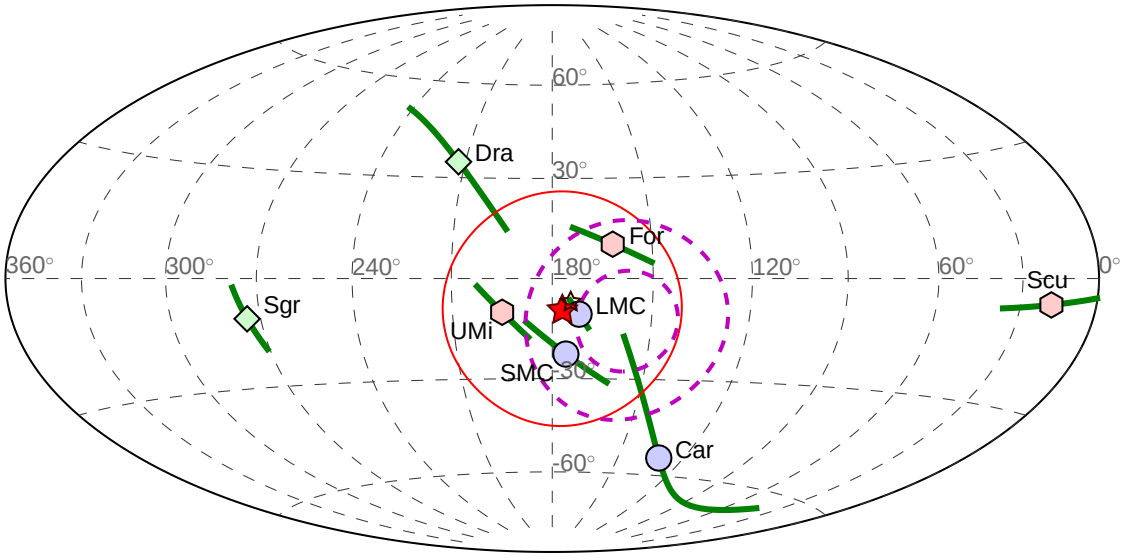

Figure 3.2: Orbital poles of Milky Way satellite galaxies as derived from their measured proper motion and radial velocities. The directions are shown in an Aitoff projection in galactocentric coordinates. The solid lines give the projected arc-segments derived from the uncertainties of the measured proper motions. Different symbols mark data derived by different methods: circles HST, diamonds ground-based measurements, and hexagons the weighted mean values from Table 3.1. The star symbol marks the mean spherical direction $\bar{l}$ of the directions of the angular momenta of the satellites excluding Sagittarius and Sculptor, and the solid loop gives the spherical standard deviation of this sample. The dashed loops show regions with 15° and 30° from the direction of the normal to the plane fitted to the 11 classical Milky Way satellites (the DoS pole). Note the proximity of $\bar{l}$ to the normal of the DoS.

note that their advanced correction is not applicable to the Wide-Field Planetary Camera 2 (WFPC2) aboard the Hubble Space Telescope. Since this instrument is on orbit three years longer than the STIS camera, results derived with WFPC2 might even be more affected by a suboptimal CTI correction. A re-derived proper motion value for Carina is given in the table. For the satellites Ursa Minor, Sculptor, and Fornax a weighted mean proper motion using all available measurements was calculated, taking into account all independent single measurements with HST. These mean proper motion values were used in the following analysis.

In Figure 3.1 an image of the sky in the direction of Sculptor is shown as an illustration for HST-derived proper motions. The two fields used to determine the proper motion with HST are marked by squares (Piatek et al. 2006), and we indicate the directions and magnitudes of the proper motion derived in each of the two fields independently. As can be seen, while the $\mu_{\alpha*}$ components are approximately of the same order for both measurements, the μ_δ components deviate and point to opposite directions on the sky. The fields are also very small compared to the total extent of Sculptor. All this suggests that the systematic errors, which are typically not given, might be of the same order as the formal measurement uncertainties. Nevertheless, this is the best data we have at hand at the current stage until results from the SIM[(a)] of GAIA[(b)] missions become available.

Heliocentric space velocities were calculated (§3.1.1) from the proper motions and radial velocities from the literature, and corrected for the circular motion of the local standard of rest (LSR) about the Galactic Centre using the IAU recommended value of $V_0 = 220\ \mathrm{km\,s^{-1}}$ circular velocity (Kerr & Lynden-Bell 1986), as well as for the peculiar motion of the Sun with respect to the LSR using the velocity components as given by Dehnen & Binney (1998). Positions of the satellite galaxies were transformed to a galactocentric coordinate system (see Table 2.1). Having galactocentric positions and velocities, the directions of the angular momenta or "orbital poles" of the satellite galaxies of the Milky Way were calculated.

The given uncertainties of the proper motion measurements were used to calculate uncertainties of the derived angular momenta (§3.1.1). We did not, however, incorporate uncertainties of any other measured quantity: distance and position of satellite galaxies, their radial velocities, the distance of the Sun from the Galactic centre, the circular velocity of the LSR, and the peculiar motion with respect to the LSR. All these uncertainties are typically negligible since they do not contribute much to the total uncertainty of the directions of the angular momenta (cf. Appendix A). It is though very important to perform a thorough error propagation analysis using the full covariance matrix as done here. Finally, the uncertainties in the direction of the angular momenta were projected onto a unit sphere to derive the arc-segments representing the *projected* 1σ uncertainties of the directions of the angular momenta (see also Palma et al. 2002, and figure 3 therein).

The different proper motion measurements from the literature given in Table 3.1 sometimes differ by more than 1σ. This is an inevitable weakness of currently available data. Most orbital poles are however not overly affected. Sagittarius is on a perpendicular orbit to the DoS for both μ_δ values given in the Table. Likewise, Sculptor is on a counter-rotating orbit for both measurements, ground based and HST, respectively. Only UMi's orbital pole

[(a)] `http://planetquest.jpl.nasa.gov/SIM/`
[(b)] `http://sci.esa.int/gaia/`

changes when incorporating the independent data, albeit then with very large projected uncertainties. If we take the weighted values for the two HST fields only, its pole-distance is $87.3^\circ\ ^{+31.2^\circ}_{-31.0^\circ}$, compared to $37.1^\circ\ ^{+8.7^\circ}_{-7.7^\circ}$ for the mean weighted proper motion of all measurements. Note that the arc-segments are projected uncertainties. While the given proper motion uncertainty for Car is about three times smaller compared to Dra, the projected uncertainty is actually two times larger. Therefore, a large proper motion uncertainty does not necessarily result in a large uncertainty of the location of the orbital pole.

The orbital poles of the Milky Way's satellites and their corresponding arc-segments are shown in Fig. 3.2 by the filled symbols and solid lines, respectively. Different symbols mark data derived from proper motions measured with HST (bluish circles), ground based instruments (greenish diamonds), or mean weighted proper motions from different data (reddish hexagons). The dashed loops show regions with 15° and 30° distance from the direction of the fitted pole of the DoS for the eleven classical Milky Way satellite galaxies ($l_{\rm MW} = 157.3^\circ$, $b_{\rm MW} = -12.7^\circ$; Sect. 2.2). From this figure one can directly identify two satellite galaxies which cannot belong to a possible common stream of satellite galaxies: Sagittarius and Sculptor, both having also been excluded by Palma et al. (2002) as possible stream members. Sagittarius is very close to the Galactic disc and may have precessed sufficiently in the non-spherical potential induced by the Galactic disc, thus being far away from the direction of its initial orbit. Sculptor, however, is more distant and unlikely to be affected much by precession. Compared to the other satellites Sculptor is on a counter-rotating but nearly co-planar orbit about the Milky Way. The star symbol in Fig. 3.2 marks the mean spherical direction $\bar{\boldsymbol{l}}$ of the angular momenta of the other possible stream members: LMC, SMC, UMi, Dra, Car, and For, ($l_{\rm MW} = 177.0^\circ$, $b_{\rm MW} = -9.4^\circ$). The solid loop gives the region with a distance corresponding to the spherical standard distance (Eqn. 2.14), $\Delta_{\rm sph} = 35.4^\circ$, from the mean spherical direction of the sample. The coincidence of $\bar{\boldsymbol{l}}$ and the normal of the DoS provides strong evidence for rotational support.

3.2.2 CDM simulations

In the recent search for an explanation of the DoS in terms of CDM substructures, many teams have proposed solutions with varying degrees of means. One of the most recent works claims to be able to arrive at the DoS for all MW-like host haloes (Libeskind et al. 2005). For comparison to the Milky Way satellites this set of simulated systems of luminous satellite haloes in a MW-type dark matter host halo is analysed. The simulations and galaxy formation models are described in that work and references therein. In short, selected host haloes in a large cosmological dark matter simulation were re-simulated with high-resolution, and galaxy formation was treated by a semi-analytical galaxy formation model (Cole et al. 2000, as extended by Benson et al. 2002). Our data differs slightly from the data used in Libeskind et al. due to an improved semi-analytic galaxy formation model. We analyse a set of eleven dark matter subhaloes containing the most luminous galaxies in each of the six simulated MW-type host haloes. This is a somewhat artificial cut and was chosen by Libeskind et al. (2005) to match the number of the "classical satellite galaxies" of the Milky Way. Only final positions and motions of the subhaloes within their hosts are used for the analysis. It is, however, neither sure that the host galaxy is a disc galaxy, nor

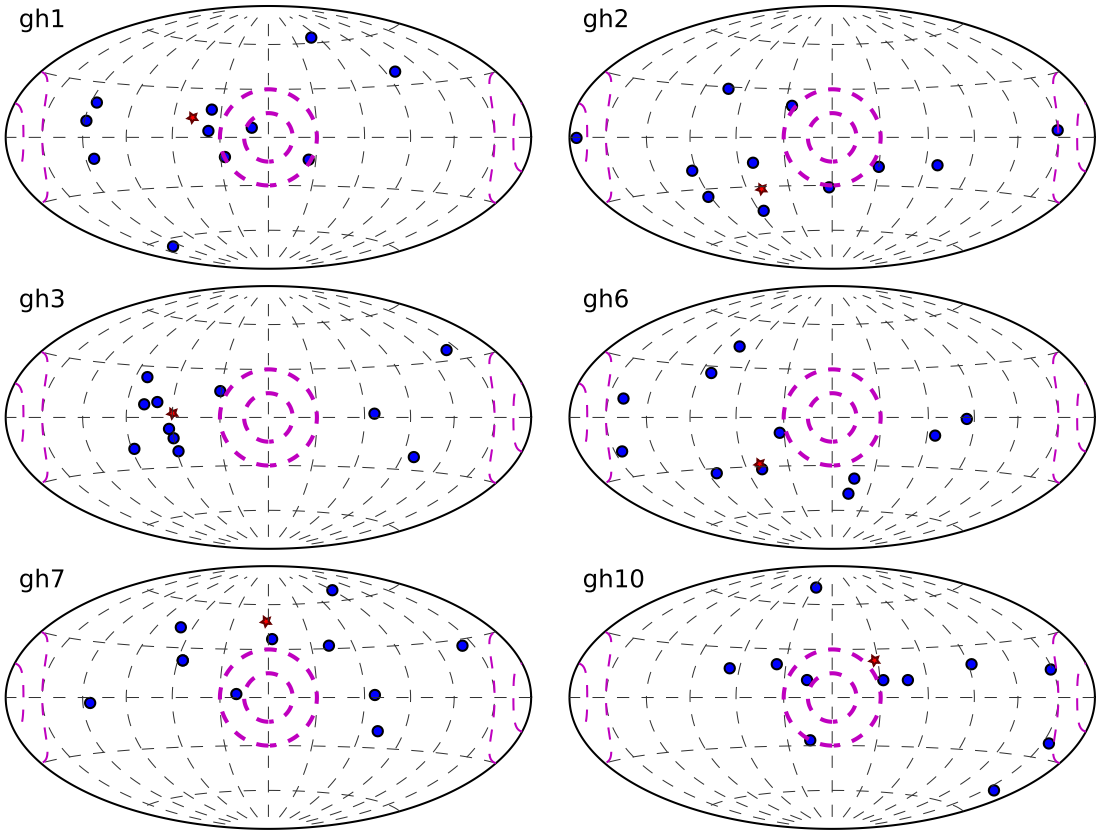

Figure 3.3: An Aitoff projection of the locations of the angular momentum vectors from the six simulations. The projection is centred on the potential rotational axis – the normal of the fitted plane – if the formally fitted discs-of-satellites were rotationally supported for the simulated data (see text for details). The dashed loops give the same regions as in Fig. 3.2, the star symbol indicates the spherical mean direction of the angular momenta. Note that this is in no case closer than $\approx 30^\circ$ to the normal of the fitted planes.

Table 3.2: Shape parameter γ and strength parameter ζ of the distribution of directions of normal vectors, fitted to 10 000 bootstrap samples of the simulated CDM satellite galaxies. The first column gives an identifier of the simulated haloes. For comparison, the values for the Milky Way are given in the last row.

	shape parameter γ	strength parameter ζ
gh1	0.5	3.2
gh2	2.3	4.2
gh3	0.3	3.5
gh6	1.2	3.0
gh7	3.9	2.6
gh10	1.5	2.8
MW	3.85	4.29

how this would be oriented with respect to the host halo. To be a system comparable to the Milky Way (or Andromeda) both attributes have to be postulated to match with those of the Milky Way.

In a first step the bootstrapping analysis as described in Sect. 2.1.3 was applied to the data, to compare the properties of the spatial distributions. The resulting shape- and strength-parameters are listed in Table 3.2. None of the simulated sets has as high values as the Milky Way data ($\gamma = 3.85$, $\zeta = 4.29$): The simulation gh7 has a slightly larger shape parameter than the Milky Way data, but the strength parameter is significantly smaller, which means that the distribution of directions of normals fitted to the bootstrapped data is significantly more widespread than found for the Milky Way. Simulation gh2 has a similar strength parameter but a significantly smaller shape parameter; the bootstrapped normals are less circular or show a multi-modal distribution. The other two data-sets with clustered distributions, gh6 and gh10, are smaller in both parameters, while gh1 and gh3 have significantly smaller shape parameters. The shape- and strength parameter were also compared to the random isotropic sample as described in Section 2.4. At a significance level of $(1 - \alpha) = 99\%$ we can not exclude the hypothesis that the individual samples are drawn from a spherical isotropic parent distribution. Thus none of the simulated Milky Way galaxy haloes appears to reproduce both the shape and strength parameters of the Milky Way's DoS, but are consistent with being randomly drawn instead.

To gain further insights we compare the distributions of the orbital poles of the satellites. Figure 3.3 shows the directions of the angular momenta of all six simulations. In contrast to Fig. 3.2 for the Milky Way data, the coordinate system can be arbitrarily chosen, since no galactic disc is comprised in the simulated data, which would naturally define one axis, the polar axis, of the coordinate system. Therefore a coordinate system has been chosen such that its axes are aligned with the formally fitted spheroid of the spatial distribution of the simulated satellite galaxies. The projection is chosen such that (i) it is centred on the normal, $\boldsymbol{n}$, of the fitted disc - which would be the mean rotational axis *if* the fitted plane was rotationally supported - and (ii) it was chosen such that the plot is centred on the hemisphere that contains the mean spherical direction of the orbital poles $\bar{\boldsymbol{l}}$, which is

marked by a star symbol. So the plots are centred on the direction

$$\boldsymbol{n}_l = \mathrm{sgn}(\boldsymbol{n} \cdot \bar{\boldsymbol{l}})\, \boldsymbol{n} \tag{3.9}$$

where $\mathrm{sgn}(x) = x\,|x|^{-1}$.

The choice of the projection for Fig. 3.3 makes the plots also easily comparable with Fig. 3.2: If the fitted plane is rotationally supported all, or at least most, angular momenta should lie close to the pole of the fitted plane. For comparison the same regions as in Fig. 3.2 are marked by the dashed loops. A strong clustering in or close to this region is not present in the simulations, and the spherical mean direction, even for selected sub-samples, is in no case close to the plane's pole.

For the simulation gh1 there are at least five angular momenta within or very close to the 30° region about the fitted pole. Closer inspection reveals, however, that this sample consists of two spatially distinct sub-groups as is shown in Figure 3.4. Four of the values close to the pole belong to one sub-group of subhaloes at about 200 kpc from the host's centre that have an approximately common stream motion. This motion may be interpreted as an infalling or bypassing group of subhaloes that has not yet disbanded, a mechanism that has been recently addressed by Li & Helmi (2008). The remaining seven subhaloes are all found very close to the centre of the host halo in a more or less spherical distribution, and the directions of their angular momenta are widely spread. Another interesting case is the simulation gh3: while there is no clustering of directions of angular momenta about the normal of the fitted disc, we do find an aggregation of angular momenta about 75° off, almost perfectly lined up like beads on a string of about 60° length. The fact that these angular momenta are not pointing in the same direction as the normal of their fitted disc-of-satellites indicates that their DoS is either transient or it may indicate tumbling. Closer inspection (Fig. 3.4) in fact shows this population to be a relatively thin tube and not a disc, as is also evident from analysis of the shape- and strength-parameters. This system is therefore not a model of the Milky Way satellites. Additionally the observations of the proper motions of the Milky Way's satellites presented in Fig. 3.2 rule out a tumbling DoS. Nevertheless, this system shows that a clustering of the angular momenta of satellite galaxies, while surely not a generic feature of CDM simulations, can appear within the CDM paradigm.

3.2.3 The Pole-distance distribution

For the Milky Way, as well as for the simulated data, a reference direction $\boldsymbol{n}_l$ (Eqn. 3.9) is given. This would be the approximate orbital pole under the hypothesis that the disc-like structure is rotationally supported, a hypothesis borne out for the Milky Way as we have seen. We construct a pole-distance distribution (PDD) by measuring the angular distances of the orbital poles from this reference direction. *If* the disc is rotationally supported, a significant excess of small pole-distances over a random distribution is expected.

In Fig. 3.5 the cumulative pole-distance distribution for the measured angular momenta of the Milky Way is plotted. For the simulations we show the sum of all individual pole-distance distributions. The cumulative pole-distance function expected for a random distribution,

$$D_{\mathrm{PDD}}(\phi) = \frac{1}{2}(1 - \cos\phi)\,, \quad 0 < \phi < \pi \quad , \tag{3.10}$$

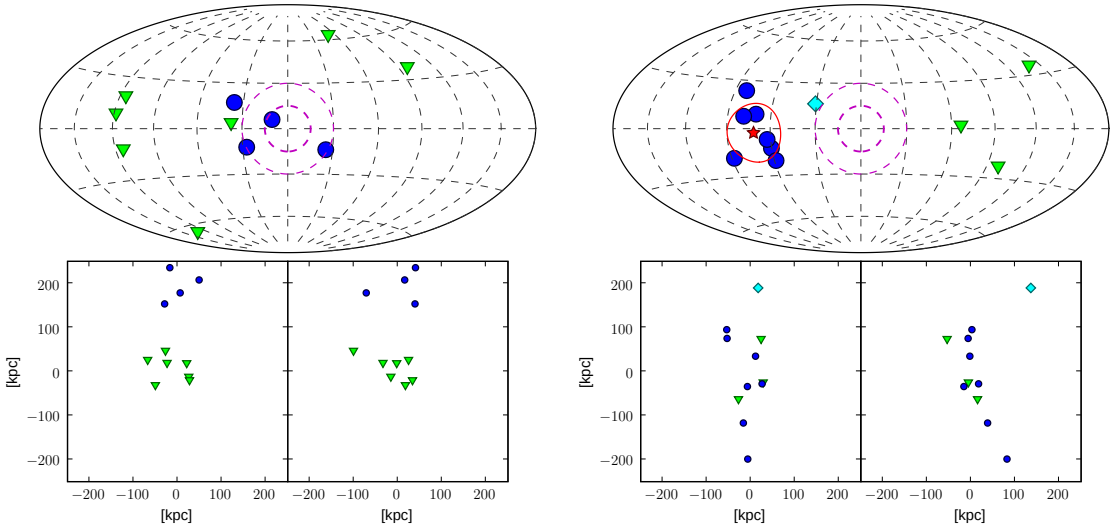

Figure 3.4: Detailed plots of the simulations gh1 (left) and gh3 (right). The top panels show an Aitoff projection of the directions of the angular momentum vectors as in Fig. 3.3. The bottom panels show the three-dimensional distribution of the subhaloes, in the left an edge-on view of the fitted disc, and in the right panel a face-on view, respectively. Different symbols are chosen to identify data in both projections. For the simulation gh1 (left), the group of subhaloes at $\approx$ 200 kpc is clearly distinct from the rest of the subhaloes, and its common group motion is reflected by the clustering of angular momenta in the orbital-pole plot. For the simulation gh3 (right), a star-symbol now shows the mean spherical direction of those angular momenta marked by the dots, and the solid loop indicates the spherical standard distance of this sample. In the lower panels it can be seen that a disc is not present, but rather a tube-like structure that apparently is transient.

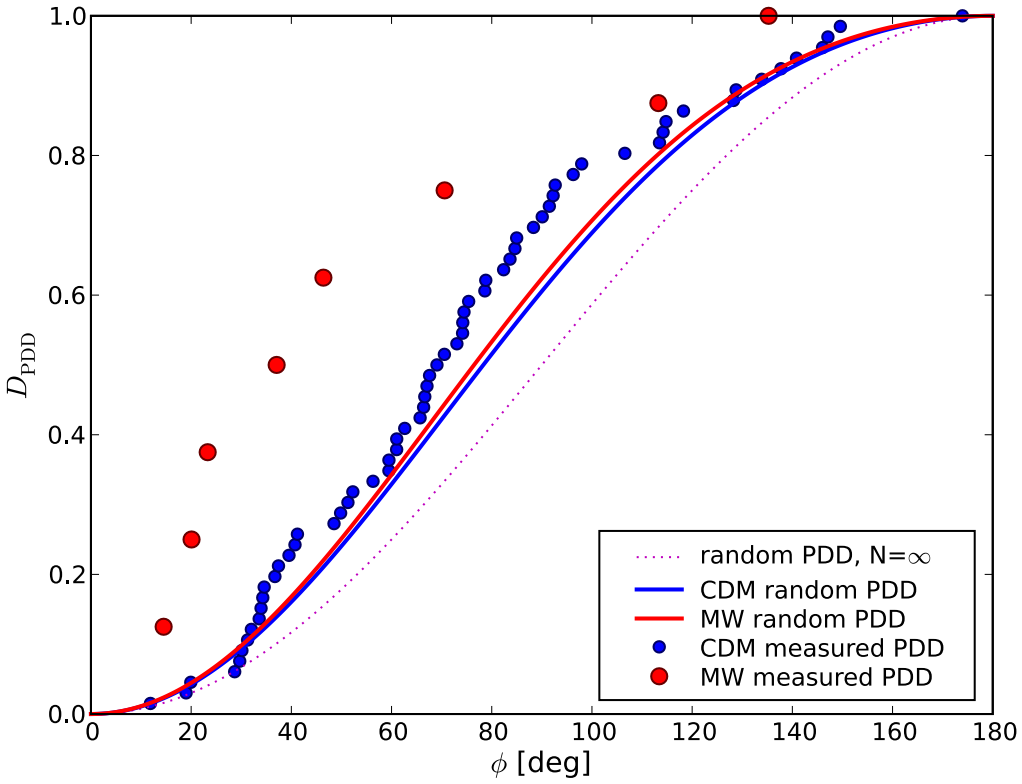

Figure 3.5: Cumulative distribution function of the pole-distance function determined for the Milky Way (red circles) and the CDM simulated (blue circles) satellite galaxies. The continuous curve gives the expected measured PDD for 8 (MW), 11 (CDM), as well as for an infinite number of random directions as given by Equation (3.11).

is shown by the dotted line. Eqn. (3.10) can be derived analytically: given a fixed reference direction on a unit-sphere, the probability to find a random direction within an angular separation $\leq \phi$ from that direction is given by the surface area of a spherical cap with opening angle ϕ divided by the total surface area of the unitsphere: $2\pi(1-\cos\phi)/(4\pi)$.

Equation (3.10) gives, however, not the true parent random distribution for a *measured* PDD, since the measured PDD is biased: we have chosen that direction of the normal of the fitted plane as the reference pole that is the presumable rotation-pole (§3.2.1, §3.2.2). Therefore a biased PDD was constructed by a Monte-Carlo method: N random directions are created and the mean spherical direction $\bar{\boldsymbol{r}}$ of these is determined. As the reference directions the x, y, and z axes are chosen. The pole-distance is measured from $+\boldsymbol{x}$ if the x-component of $\bar{\boldsymbol{r}}$ is positive, from $-\boldsymbol{x}$ otherwise. The same is done for the y and z components. The cumulative biased random pole-distance distribution, created by the Monte-Carlo method, can be fitted[(c)] by

$$D_{\rm PDD}(\phi, N) = \frac{1}{2}\,(1-\cos\phi) + \frac{0.35}{\sqrt{N}}\sin^2\phi \tag{3.11}$$

for $N \geq 5$, $0 < \phi < \pi$ (see Figure 3.6), and the probability function is given by

$$P_{\rm PDD}(\phi, N) = \frac{1}{2}\sin\phi + \frac{0.7}{\sqrt{N}}\sin\phi\,\cos\phi \quad . \tag{3.12}$$

Only in the limiting case, $\lim_{N\to\infty}$, Eqn. (3.11) goes over into $D_{\rm PDD}(\phi) = \frac{1}{2}(1-\cos\phi)$. The cumulative biased random PDD is shown in Fig. 3.5 by solid curves for $N = 11$ (CDM) and $N = 8$ (MW), respectively.

The PDDs were tested against the biased random pole-distance distribution using a Kuiper statistic V and a Watson statistic U^2 (Stephens 1974). Both statistics were originally used for distributions on a circle and are thus useable for the PDD. For both statistics and at a significance level $(1-\alpha) = 99\%$ we cannot exclude that the PDD for each individual CDM simulated subhalo system is drawn from a random biased PDD ($N = 11$), nor can we exclude that the co-added PDD for all simulated systems is drawn from a random biased PDD. The null-hypothesis can also not be excluded for the Milky Way ($N = 8$), but given the very large uncertainties and possible systematics this is not a very strong restriction. Within the uncertainties of the measurements we find the directions of the angular momenta of Dra and Car close to the spherical mean direction ($< \Delta_{\rm sph}$). If we take that case, we can exclude at a very high significance level $(1-\alpha) = 99\%$ that the Milky Way PDD is drawn from a random biased PDD.

The CDM simulated systems show an excess of pole-distances at $\sim 90^\circ$, which implies that the fitted disc-like structure tends to disperse. In contrast, we do find an over-density of small pole-distances for the Milky Way, suggesting that the Milky Way DoS is rotationally supported. Note also that we did not choose a reference direction that minimises the pole-distances for the Milky Way. If we had chosen the spherical mean direction, the over-density of small pole-distances would have been more pronounced.

[(c)]The nice and simple expression found in Eqn. (3.11) suggests that there might also be an analytic way to derive this formula, but we did not find the right approach to solve this yet.

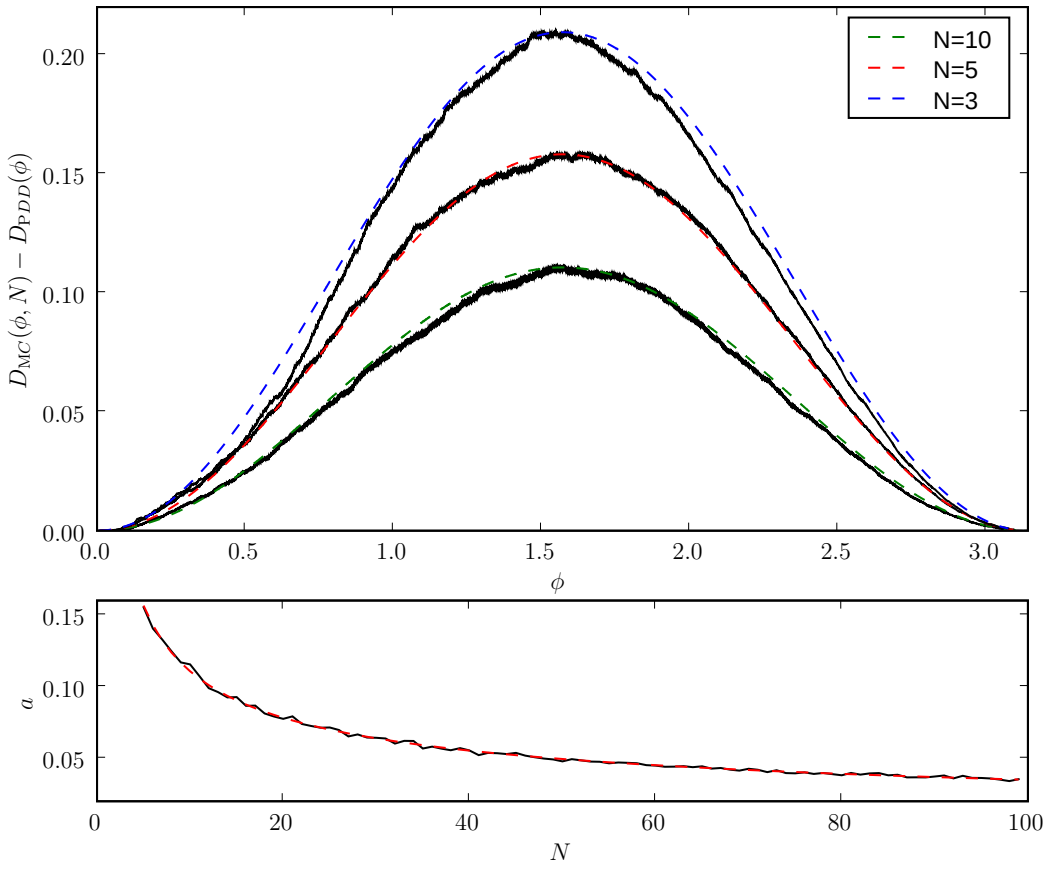

Figure 3.6: In the top panel the differences between a biased PDD constructed with a Monte-Carlo method for 1 000 samplings, $D_{\rm MC}(\phi, N)$, and the unbiased PDD, $D_{\rm PDD}(\phi)$, as given in Eqn. (3.10) for different numbers of random directions (N=3, 5, 10) are shown. The dashed lines show the fitted difference-function of the form $a \cdot \sin^2 \phi$. For $N < 5$ we could, in principle, also derive reasonable fits by simultaneously also fitting the exponent, b, of the term $a \cdot \sin^b \phi$. For $N \geq 5$ the exponent is basically constant $b = 2$. In the bottom panel the $1/\sqrt{N}$ behaviour of the fitting parameter a is shown for a fixed value $b = 2$, $N \geq 5$, in black for the Monte-Carlo simulations and in red for the fitting function.

3.3 Orbital properties of Andromeda satellite galaxies

For the Milky Way, proper motions of some of the satellite galaxies are available – for the Magellanic Clouds and Sagittarius even with a relatively high accuracy – which makes a detailed study of the orbital properties of the satellites possible. When going beyond the Milky Way system to Andromeda, the situation to study orbital properties is much worse. Until now, only for two Andromeda companion galaxies proper motion measurements are available (Brunthaler et al. 2005, 2007). Even having proper motion values at hand, one has to make some assumptions on the relative motion of Andromeda itself with respect to the Milky Way, since this is not known, to get information on the relative motion of a satellite with respect to its host. In the following section we describe, to our knowledge for the first time, a method how to set some constraints on the possible orbits of Andromeda satellite galaxies.

3.3.1 Restricted polar paths

Based on geometrical arguments, Lynden-Bell & Lynden-Bell (1995) constructed a diagram of so-called 'polar paths' for the Milky Way satellite galaxies and globular clusters. The direction of every possible pole of a satellite orbit must be located at a right angle to its direction from the Galactic Centre. Regions in the sky where three or more polar paths (nearly) intersect define the poles of possible streams of satellites. Palma et al. (2002) used proper motion measurements to restrict the possible orbits, which resulted in arc segments of possible poles rather than great circles, as is also done in Sect. 3.2.1. McConnachie & Irwin (2006b) applied the technique of constructing polar paths and used the available three-dimensional spatial data for the Andromeda satellites to construct polar paths for Andromeda. They identified several possible stream candidates of satellite galaxies.

The observer's view of the Andromeda satellite system is very different from that of the Milky Way. While the MW satellites are basically seen from the Galactic Centre, the M31 satellite system is almost seen from infinity. Together with the spatial information relative to Andromeda it is therefore possible to decompose the observed line-of-sight (LOS) velocities into radial and perpendicular components relative to Andromeda. These are, however, only lower limits of their total velocities since only the LOS velocities can be measured.

Fig. 3.7 illustrates how the measured line-of-sight velocity of an Andromeda satellite breaks up into radial and perpendicular components relative to M31. The top panel shows the measured heliocentric velocity vectors v_{LOS} and $v_{\mathrm{LOS}}(\mathrm{M31})$. In the bottom panel the same velocity vectors as in the top panel are shown but now corrected for the LOS velocity of M31, i.e., in the rest-frame of Andromeda, assuming no considerable perpendicular velocity (proper motion) for Andromeda (Kahn & Woltjer 1959; Einasto & Lynden-Bell 1982), although there are arguments which allow for a significant proper motion component of M31 (Loeb et al. 2005; van der Marel & Guhathakurta 2007). The velocity component $v_{\mathrm{T,LOS}}$ perpendicular to the line-of-sight of a satellite galaxy is unknown. Therefore a whole family of velocity vectors is possible for the satellite, illustrated by dotted vectors.

The transformation of velocity vectors into the Andromeda-centric rest-frame is calcu-

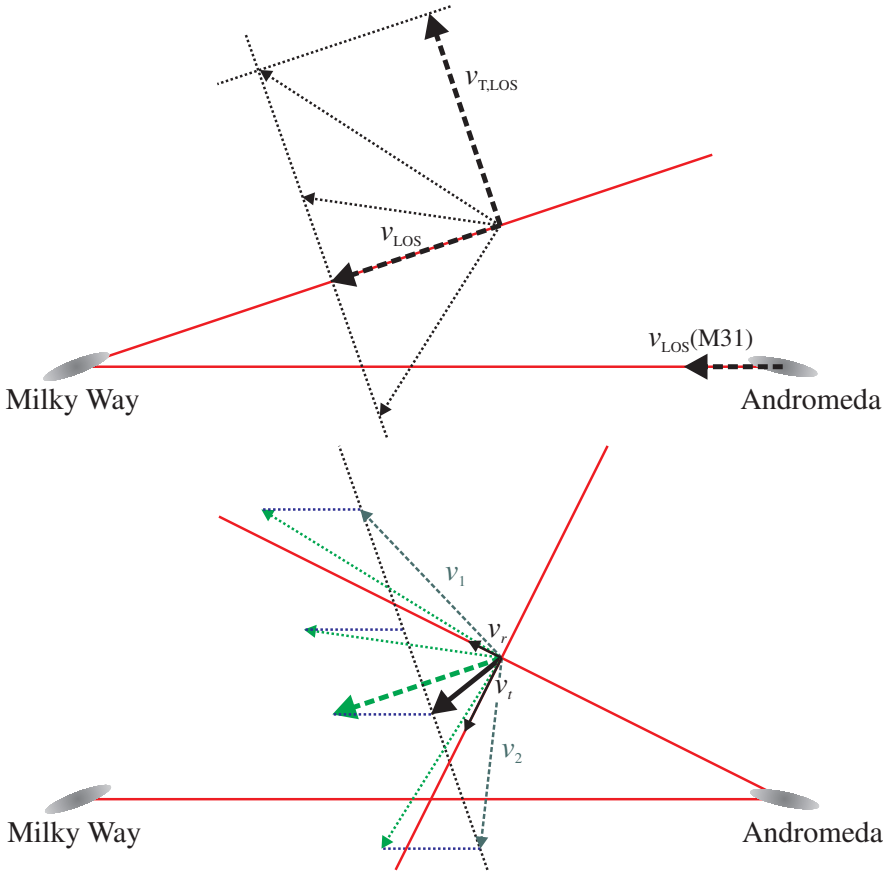

Figure 3.7: Geometrical illustration how to calculate radial and perpendicular velocity components of the measured line-of-sight (LOS) velocity of an Andromeda satellite. In the top panel we show the measured vectors in the rest-frame of the Sun. The velocity perpendicular to the line-of-sight, $v_{T,LOS}$, is unknown, i.e. there is a family of possible total velocity vectors, indicated by dotted arrows. In the bottom panel we show the velocities corrected for the LOS velocity of Andromeda. The corrected LOS velocity of a satellite can be split into a radial component v_r and a perpendicular component v_t relative to M31.

lated by taking the time derivative of Eqn. (2.21):

$$\boldsymbol{v}_{\rm M31} = \mathsf{R}_{\rm M31}\left(\boldsymbol{v} - \boldsymbol{v}({\rm M31})\right) \ . \tag{3.13}$$

Upon setting $\boldsymbol{v}({\rm M31}) \equiv \boldsymbol{v}_{\rm LOS}({\rm M31})$ the line-of-sight velocity vectors of the satellites are calculated in the Andromeda-centric coordinate system. The LOS velocity vector of the satellite can now be split into a radial and a perpendicular component, v_r and v_t, respectively. The values of the radial and perpendicular velocity components relative to Andromeda are given in Table 2.5 (§2.3) for the M31 satellites, negative radial velocity meaning that the component is pointing towards Andromeda, positive that it is pointing away.

This information is used next to set some limits on the possible poles of the orbits of the M31 satellites. In the example shown in Fig. 3.7 without an additional velocity component perpendicular to the line-of-sight, the sense of rotation about M31 would be

counterclockwise (within the MW–M31–satellite plane as shown). Only a large enough velocity component v_1 perpendicular to the LOS and within the MW–M31–satellite plane can reverse the sense of rotation. Any component $v_{\mathrm{T,LOS}}$ perpendicular to the MW–M31–satellite plane cannot reverse the sense of rotation, but can only displace the direction of the angular momentum vector along the polar path by a maximum $\pm 90^\circ$, for $v_{\mathrm{T,LOS}} = \infty$, from the direction derived assuming no perpendicular velocity.

We have to make some additional assumptions about the maximum allowed velocities of the satellites. We assume the satellites are bound to a spherical, isothermal dark matter halo of M31 with circular velocity $v_c \approx 250$ km s^{-1}, truncated at $r_c = 250$ kpc, which corresponds to a total mass of the Andromda halo of $3.68 \cdot 10^{12}$ M$_\odot$. The escape velocity is then given by[(d)]

$$v_e(r) = \begin{cases} \sqrt{2}\, v_c \sqrt{1 + \ln r_c - \ln r} & : \quad r < r_c \\ \sqrt{2}\, v_c \sqrt{r_c / r} & : \quad r \geq r_c \end{cases} \quad . \tag{3.14}$$

A velocity component perpendicular to the LOS in the plane of the MW, M31, and the satellite can either contribute to the perpendicular velocity (giving a total velocity vector $\boldsymbol{v}_2$) or counteract ($\boldsymbol{v}_1$). We calculate the maximum possible velocity vectors $\boldsymbol{v}_{1,\mathrm{max}}$ and $\boldsymbol{v}_{2,\mathrm{max}}$ in the M31 rest-frame with absolute values of the velocities $|\boldsymbol{v}_{1,\mathrm{max}}| = |\boldsymbol{v}_{2,\mathrm{max}}| = v_e(r_\mathrm{s})$ (Eqn. 3.14), where r_s is the distance of a satellite from the centre of M31. The direction of the orbit of a satellite can now be restricted if the perpendicular components of $\boldsymbol{v}_1$ and $\boldsymbol{v}_2$ *both* point in the same direction, i.e. if

$$s_v = \frac{\boldsymbol{v}_{1,\mathrm{max}} \cdot \boldsymbol{v}_t}{|\boldsymbol{v}_{1,\mathrm{max}}||\boldsymbol{v}_t|} \, \frac{\boldsymbol{v}_{2,\mathrm{max}} \cdot \boldsymbol{v}_t}{|\boldsymbol{v}_{2,\mathrm{max}}||\boldsymbol{v}_t|} \equiv +1 \tag{3.15}$$

where '$\cdot$' denotes the scalar product of vectors. This allows us the restriction of the polar paths to at least arcs of 180° which we call "restricted polar paths" (RPPs), i.e. the orientation of the orbit about M31 can be inferred.

3.3.2 Application of restricted polar paths

Restricted polar paths are calculated using heliocentric radial velocities as given in McConnachie & Irwin (2006b, their table 1) for both data-sets. In Table 2.5 we mark the data for those satellites with an asterisk for which we can restrict the poles by the RPP method described above. Only for And VI the poles can be restricted for both data-sets. The polar paths and the resulting RPPs are plotted in Fig. 3.8 for the MI data and in Fig. 3.9 for the KG data (see Sect. 2.3 for details about the two data-sets). Data for the different satellites are plotted in different colours. The polar paths for those satellites which were used for fitting the plane in Sect. 2.3 are plotted with solid lines (satellites 1 – 12 in Table 2.5), for satellites not used in the fitting with dashed lines. The position of the angular momentum vectors of M33 and IC 10 as derived from the measured radial velocities and proper motions (Brunthaler et al. 2005, 2007) are marked by a star, assuming no proper motion for Andromeda. A considerable proper motion component of M31 would shift the direction of the angular momentum vector of M33 and IC 10 along their polar path in Figs. 3.8 and 3.9

[(d)] Note that McConnachie et al. (2005) used $v_e = \sqrt{2} v_c$ in their figure 2 as an approximation for the escape velocity of an isothermal sphere.

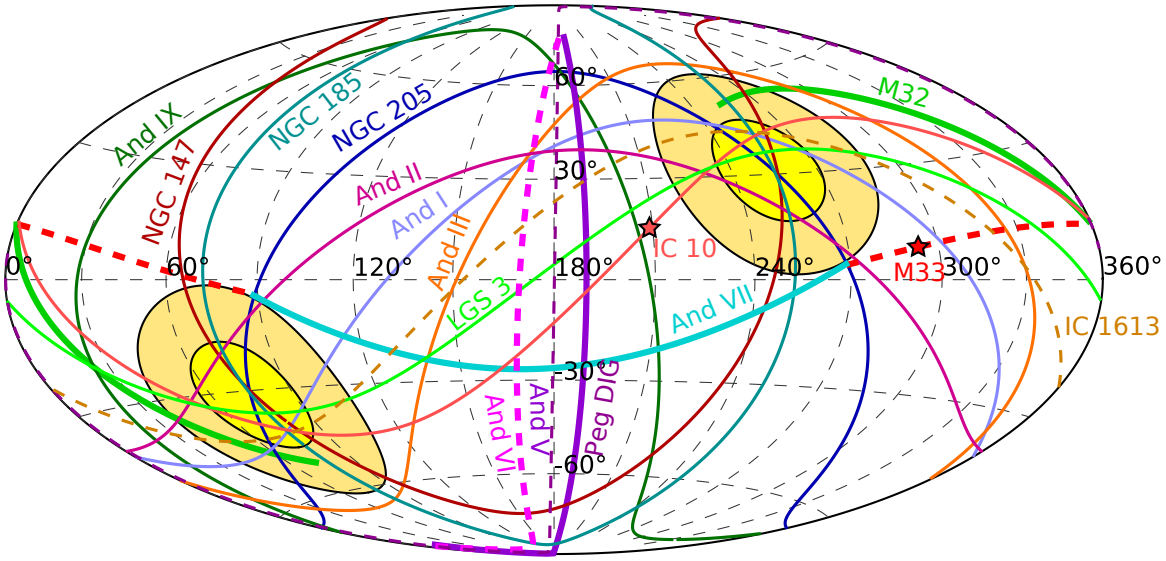

Figure 3.8: Polar paths and restricted polar paths (marked with thicker lines) of the Andromeda satellite galaxies for the MI data-set. An overall view is shown using an Aitoff-projection. Solid paths are for the innermost dozen satellites entering the plane-fitting (§ 2.3) while dashed paths are the polar paths for those satellites not used. The direction of the angular momentum vectors of M33 and IC 10, as derived from measured radial velocities and proper motions, is marked by the star symbols. Regions of 15° and 30° distance from the fitted pole (Table 2.2, entry 'ALS') are indicated by the closed solid loops.

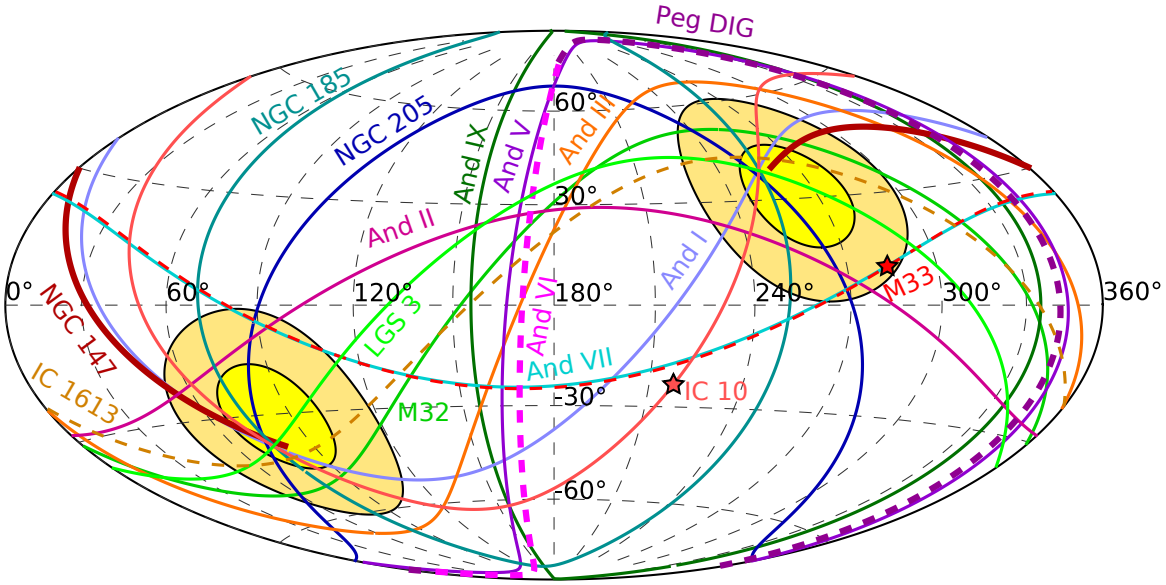

Figure 3.9: As Fig. 3.8, for the KG data-set.

since the measured velocity of M33 is transformed to the rest-frame of M31. In addition we plot loops with distances of 15° and 30° from the pole of the fitted plane using the ALS method for all satellites within the approximate virial radius of M31 (§2.3). Since the direction of the normal is arbitrary for the fitted plane, two regions appear on opposite sides of the sphere.

There is a strong clustering of intersection points of polar paths near the pole of the fitted plane, both in the northern and southern hemisphere. Those satellites whose polar paths intersect there are candidates for kinematic streams. In particular these are: NGC 205, And I, NGC 147, NGC 185, IC 10, LGS 3, and IC 1613 (though the latter was not included in fitting the plane) within 15° from the pole for both data-sets. Within the 30° region, we additionally identify M32 and And II. For the MI data, And II is also found within the 15° region. Both data-sets, MI and KG, thus suggest the same satellites to be members of a possible stream, based on the intersection of their possible kinematical poles coinciding with the direction of the normal to the fitted plane. If this clustering is real, the satellite disc would be rotationally supported. It is this sample of nine galaxies, consisting of M32, NGC 205, And I, And II, NGC 147, NGC 185, IC 10, LGS 3, and IC 1613, that was used in Section 2.3.2 to analyse the spatial properties of the kinematically motivated subsample of Andromeda satellite galaxies. These satellites are exactly those which McConnachie & Irwin (2006b) identified as members of the possible candidate streams, namely iii, iv, and v in their paper. In total they identified five further possible streams. However, the distance uncertainties for Andromeda and its satellite galaxies are so large that an identification of possible streams based on the intersection-points alone may not be sufficient. With the additional argument of a spatially plane-like distributed satellite sample a stronger hint for possible streams emerges.

And VI, which was excluded from the plane fitting as an outlier, is the only satellite for which the polar paths can be restricted in both data-sets. The resulting RPP is nearly perfectly a meridian at $l_{\rm M31} \approx 170°$. Thus, for And VI the pole of the angular momentum vector is far off the pole of the fitted plane, and the orbit of the satellite cannot be located within the plane. For the MI data-set the orbit of And V can also be restricted and the resulting RPP is very close to that of And VI. This may be an indication for a close proximity of the angular momentum vectors of And V and VI.

M33 and IC 10 are the only Andromeda companions for which a measured proper motion is available (Brunthaler et al. 2005, 2007). While M33 is located spatially close to the disc of the morphological subsample (mss8, §2.3.1, Figs. 2.13 and 2.14), as noted by Koch & Grebel (2006), it cannot orbit within this disc: if this disc is rotationally supported, then the common direction of all orbital angular momentum vectors must point either approximately towards $l_{\rm M31} = 177°$, $b_{\rm M31} = -25°$, or $l_{\rm M31} = 357°$, $b_{\rm M31} = +25°$, depending on the sense of rotation. From the RPPs we deduce that the kinematical pole of And VI, which is a member of the mss8 subsample, cannot be close to the latter possible pole. This is evident for both data-sets. For the MI data, the same conclusion can be drawn for And V, also a mss8 subsample member. Thus, the orbital pole of a possible common stream of the mss8 subsample must be located close to $l_{\rm M31} = 177°$, $b_{\rm M31} = -25°$, while the derived orbital pole of M33 is $l_{\rm M31} = 283°$, $b_{\rm M31} = 10°$. These two poles lie $\approx 110°$ apart. From this finding we conclude that M33 and the mss8 subsample cannot have a common orbital plane.

As a caveat we note that the RPP criterion applied above to the polar paths depends on two uncertain matters: the relative distance uncertainties and the true proper motion of Andromeda. Thus we can only treat the restriction criterion as a hint for more plausible regions of polar paths. Also note that a plane fitting algorithm and the appearance of a clustering of intersection points are not independent. The intersection point of the polar paths of two satellites is the direction of the normal of the plane containing these two satellites and the coordinate origin.

3.4 Discussion

3.4.1 The Milky Way system

The derived pole-distance distribution of Milky Way satellite galaxies, which is still affected by large measurement uncertainties, shows an excess of small pole-distances, implying the DoS to be rotationally supported. Within the uncertainties, the two possible stream satellites with the most deviating directions of the angular momenta, Draco and Carina, are consistent with being found close to the suggested orbital pole of the disc-of-satellites ($< \Delta_{\rm sph}$, Fig. 3.2). That case would be highly inconsistent with a random sample ($> 99\%$). In order to be able to draw strong conclusions based on the PDD *alone* we need to await more, and more-accurate proper motion measurements. Measurement campaigns of proper motions with HST are ongoing (for Sextans and Draco, Pryor 2007, priv. comm.; also Wyse 2007, priv. comm.), and forthcoming satellite missions, specifically SIM and Gaia, will certainly achieve a better precision than currently possible. For two satellites, Draco and Carina, currently only one single measurement is available and their projected uncertainties are very large. Even for those satellite galaxies where multiple measurements are available, these often differ, sometimes by more than 1σ, see for example Sculptor (Table 3.1). Until now, only the Magellanic Clouds seem to have reasonably well constrained proper motions that are consistent for multiple independent measurements.

A further argument for a rotationally supported DoS is that the unweighted disc-fitting algorithm (§2.1.1) is most strongly affected by the spatial location of the *outermost* satellite galaxies. We do find, however, a clear alignment of the angular momenta of the *innermost* satellite galaxies with this fitted disc, most strongly for the Large and Small Magellanic Clouds, whose orbital poles are fairly well constrained. The only exception is Sagittarius. But its observed orbit might already significantly deviate from the initial orbit due to precession or scattering processes (Zhao 1998). *It would, however, be rather curious to find a disc-like structure where only the inner satellites orbit within the disc while the outer ones, which mostly define the disc, do not.*

For the CDM simulations, the analysis of the pole-distance distributions shows that none of the theoretical sub-structure systems seems to be a rotationally supported structure as the Milky Way satellite system. The angular momenta of all simulated systems of subhaloes are consistent with being drawn from a random distribution. Instead, the claimed "disc" of simulated subhaloes even tends to disperse rather than being supported by rotation. The CDM subhalo "disc" is therefore a pressure supported flattened tri-axial spheroid rather than a rotation-supported disc. Furthermore, Libeskind et al. (2007) showed that the

mean angular momentum of another simulated satellite system, using a smooth particle hydrodynamic code, is *not* co-aligned with the normal of a fitted plane to these satellites but instead tends to be perpendicular to the long axis of the fitted triaxial ellipsoid. Note however that Libeskind et al. (2007) were only able to resolve galaxies brighter than $M_V \approx -12$ which complicates direct comparisons with the Milky Way satellite populations since, with the exception of the LMC, the SMC, Sgr, and For, the remaining known satellite galaxies are up to four orders of magnitudes fainter than their limit.

3.4.2 The Andromeda system

The observational situation for the Andromeda satellite system is much worse than for the Milky Way. With current technology it is not possible to do anything comparable to the analysis for our own Galaxy. Nevertheless, with some reasonable assumptions about the Andromeda system, we were able to at least restrict possible orbits of some satellite galaxies. Using radial velocity measurements we created restricted polar paths, showing that at least the direction of the angular momentum vector of And VI can be restricted to an arc segment of 180° in both data-sets, i.e. the sense of rotation of the orbit around Andromeda can be determined. For six of the M31 satellites the possible poles can only be restricted for one of the data-sets. Restricted polar paths hint to more plausible regions of the locations of angular momentum vectors on the Andromeda sky.

Combining the polar-paths of the Andromeda satellites with the fitted plane it follows that there may be a kinematic association of some of the M31 satellites: M32, NGC 205, And I, NGC 147, And II, NGC 185, IC 10, LGS 3, and probably, though due to its large distance unlikely being a bound satellite of Andromeda, IC 1613. These satellite galaxies were also identified as possible stream members by McConnachie & Irwin (2006b), while these authors also identified other possible streams which now seem to be less likely. This subsample of eight Andromeda companion galaxies was found to form a very pronounced disc-of-satellites (the kss8 subsample, Section 2.3.2) for the two distance data-sets used.

For the second, morphologically motivated subsample of Andromeda satellite galaxies that was considered in the analysis of the spatial distribution in Section 2.3.1, M33 was found to be encompassed by the fitted plane. We argue that this close proximity of M33 to the disc of the morphologically motivated subsample is a pure chance alignment since the direction of its angular momentum vector, $l_{\rm M31} \approx 283°$, $b_{\rm M31} \approx 10°$, can not be correlated with the possible common orbital direction of the mss8 subsample members, $l_{\rm M31} \approx 177°$, $b_{\rm M31} \approx -25°$. We note, however, that the direction of the orbital pole of M33 is derived under the assumption that Andromeda has a negligible proper motion. A considerable perpendicular motion of M31 would cause the orbital pole of M33 to move along its orbital paths in Figs. 3.8 and 3.9. In contrast, a common orbital pole of satellite galaxies that is defined by the intersection of their polar paths is independent of the motion since it is defined by the relative spatial locations only.

Chapter 4

Internal properties of satellite galaxies

In the last two chapters the spatial distribution of the satellite galaxies in the haloes of the Milky Way and Andromeda, and their orbital properties were examined. The very flat, disc-like configuration of the Milky Way satellites, and the fact that this flattened structure appears to be rotationally supported poses a question on their origin. Since both features appear incompatible with the dSph's being luminous CDM sub-structure, dark matter free tidal dwarfs are a possible alternative. One important question that remains is whether the observed properties of the Local Group dwarf galaxies, such as total luminosities or mass-to-light ratios, are consistent with them being initially dark matter free dwarf galaxies that have orbited the Milky Way several times. This question is addressed in the following section.

4.1 Dark-matter free satellite galaxies

4.1.1 The layout: Satellite galaxy models

We analysed simulations that were carried out in an analog manner as described in Kroupa (1997): satellite galaxies were set-up as Plummer-spheres, having masses of 10^7 $M_\odot$ without dark matter and initial absolute magnitudes $M_V = -11.5$ mag, being represented by 3×10^5 particles. These values correspond to a true mass-to-light ratio $(M/L)_{\rm true} = 3$ for each particle, and the models represent tidal dwarf galaxies that have blown out their gas within the first Gyr after their formation (Recchi et al. 2006). The models were allowed to relax before being injected into the host halo with an isothermal profile of total mass of 2.85×10^{12} $M_\odot$, core-radius 5 kpc, and cutoff radius 250 kpc with circular velocity $v_c = 220$ km s^{-1}. The satellite galaxies started at a distance of 60 kpc and 100 kpc from the centre of the host halo and were given different initial velocities leading to different eccentricities of their orbits (see Table 4.1). The evolution was followed in a live halo. Every satellite evolves by periodically losing matter at its peri-galactic passages (Piatek & Pryor 1995) until a stage is reached when the original satellite is nearly disrupted and has evolved into a quasi-stable remnant. For a detailed description of the initial set-ups of the satellite galaxies and the host halo see Kroupa (1997). The integration was done using the particle-mesh code SUPERBOX (Fellhauer et al. 2000). Properties of the satellite galaxies were compared with a direct N-body code (Klessen & Kroupa 1998; cf. also Fellhauer et al.

2007a), showing that the results agree well. Figure 4.1 shows an all-sky surface brightness plot of a similar, more recent simulation of a dark matter free satellite galaxy (see also § 5.2).

Observational parameters for the modelled satellite galaxies are derived in an automated manner as a virtual observer located in the disc would do: member stars are photometrically selected based on their projected position on the virtual sky. The line-of-sight velocity dispersion is derived within the half-light radius from which an apparent mass-to-light ratio $(M/L)_{\rm obs}$ is calculated under the assumption that the satellite galaxy is in virial equilibrium (Binney & Tremaine 1994). Statistical routines from Beers, Flynn, & Gebhardt (1990) were employed to ensure that velocity outliers are removed from these calculations. The absolute magnitudes $M_{{\rm V},r_{\rm bin}}$ and $M_{{\rm V},r_{1/2}}$ are determined within a fixed projected distance $r_{\rm bin} = 1.5$ kpc and within the projected half-light radius, respectively. For a complete description and a detailed analysis of individual parameters see Kroupa (1997).

4.1.2 Comparison with Local Group satellite galaxies

During their evolution the satellite galaxies change their apparent properties as determined by an observer. In Figure 4.2 the time evolution of the half-light radii and the apparent absolute magnitudes of two simulated satellites, RS1-5 and RS1-113, are shown. In the middle panel we additionally show the galactocentric distance of the satellites. Four snapshots, marked by the star symbols in Figure 4.2 for the two simulations shown there, were taken for each simulation at random time-steps during the last two complete orbits of each simulation for each of the eight simulations. This choice ensures that we are not biased in the selection of the snapshots since the probability to 'observe' a satellite at a particular evolutionary phase (after the disruption) is proportional to the life-time of this phase. As Kroupa (1997) already noted, after the disruption of the satellite galaxies, a significant fraction of stars contributing to $M_{{\rm V},r_{\rm bin}}$ of the quasi-stable remnant are 'extra-tidal' stars. As such $M_{{\rm V},r_{\rm bin}}$ is most likely over-estimated. Therefore we also plot the absolute magnitudes within the half-light radii, $M_{{\rm V},r_{1/2}}$, marked by asterisk symbols in the lower panel of Figure 4.2, which may be considered as the lower limit for the absolute luminosities.

In Figure 4.3 the absolute magnitude versus the half-light radius is shown for observational data: Milky Way (circles) and Andromeda (squares) dSph satellite galaxies. The same data are used as in Belokurov et al. (2007), their figure 8 (Zucker, priv. comm.). For the four snapshots of each simulated satellite we show the two extreme values of the absolute magnitudes, $M_{{\rm V},r_{\rm bin}}$ (dark blue star symbols) and $M_{{\rm V},r_{1/2}}$ (light blue asterisk symbols), respectively. The corresponding values are connected by a thin solid line in the lower panel. For the dSph in Boötes (Boo: Belokurov et al. 2006) two values for the absolute magnitude are given, connected by a thick, dashed line. The second, more luminous value is taken from Muñoz et al. (2006a) which was inferred from a comparison of Boötes' properties with the UMa dSph galaxy. In addition the development tracks of two simulated satellites, RS1-5 and RS1-113, are shown in the lower panel. The tracks start at the upper-left and evolve to the lower-right direction as the satellites become more extended and less luminous. It follows that all models evolve to the parameter region occupied by the observed satellites.

Figure 4.4 shows mass-to-light ratio (in solar units) versus absolute magnitude $M_{\rm V}$ of the observed Local Group dSph satellite galaxies and for the snapshots of the simulated

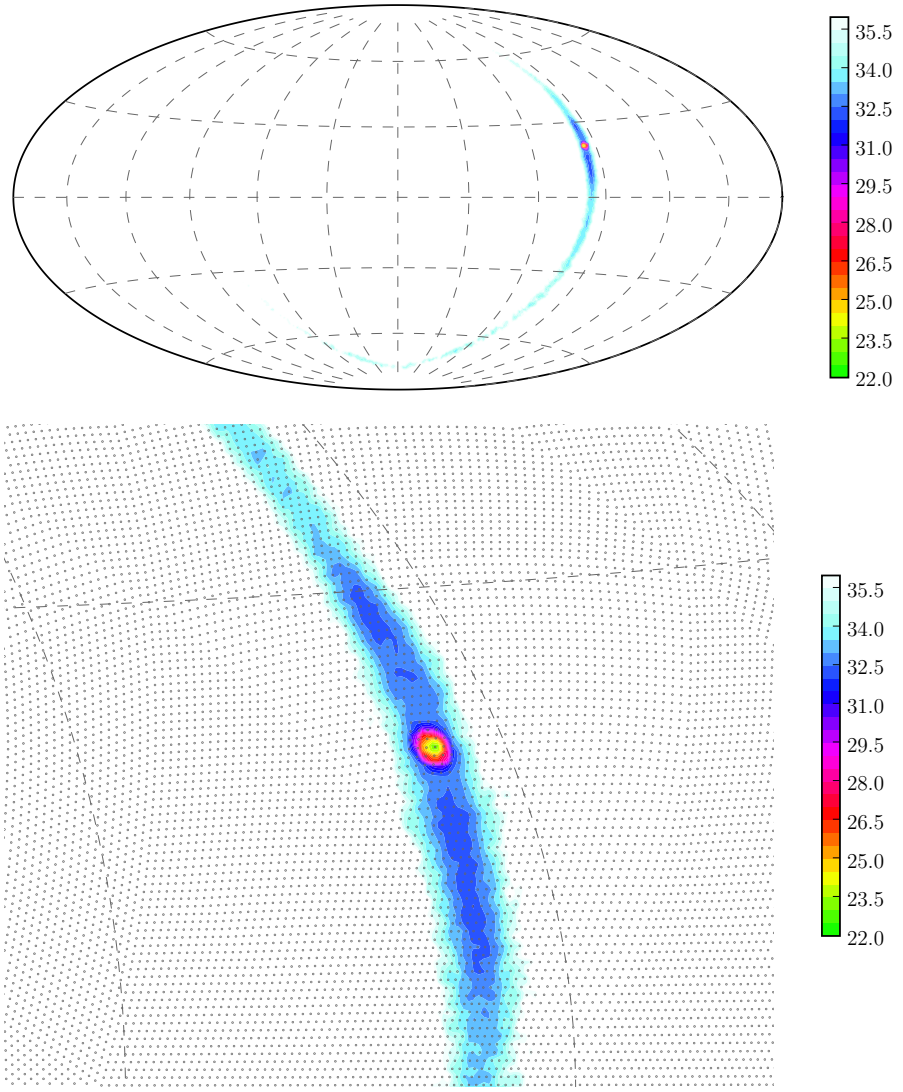

Figure 4.1: In the top panel, an all-sky surface-brightness plot of a simulated dark matter free satellite galaxy, similar to the simulations analysed in this Section, is shown. The contours show the surface brightness in mag/arcsec^2 as indicated by the colourbar. This particular simulation was done with the advanced program Superbox++, described later in Section 5.1. The snapshot shows a satellite galaxy with initial mass 10^7 $M_\odot$, after 3.5 Gyr of evolution and three peri-galactic passages, now close to its apo-centre. In the lower panel a zoom-in of a region around the satellite is pictured, also showing the grid used to generate the surface-brightness plot as grey dots. Note that the tails visible in this plot are likely *not detectable* with the observational facilities of the current all sky mapping programs like the SDSS (see also Muñoz et al. 2007).

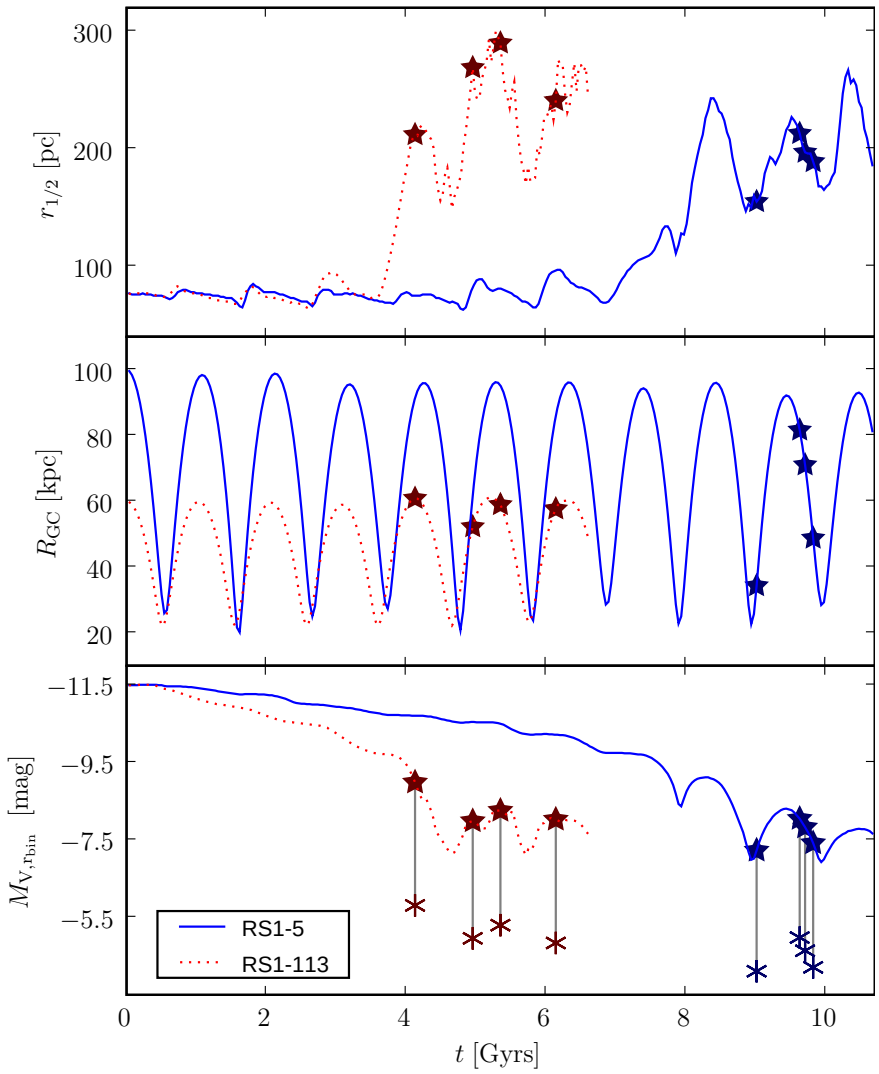

Figure 4.2: The time evolution of half-light radius $r_{1/2}$, galactocentric distance R_{GC}, and absolute magnitude $M_{V,r_{bin}}$ of two simulated satellite galaxies, models RS1-5 (red dotted) and RS1-113 (blue solid). The symbols mark snapshot values derived at random time-steps during the last two completely simulated orbits. For the snapshots of $M_{V,r_{bin}}$, additionally the absolute magnitudes within the half-light radius, $M_{V,r_{1/2}}$, are given, marked by the asterisk symbols. The corresponding values are connected by the thin grey lines for clarity.

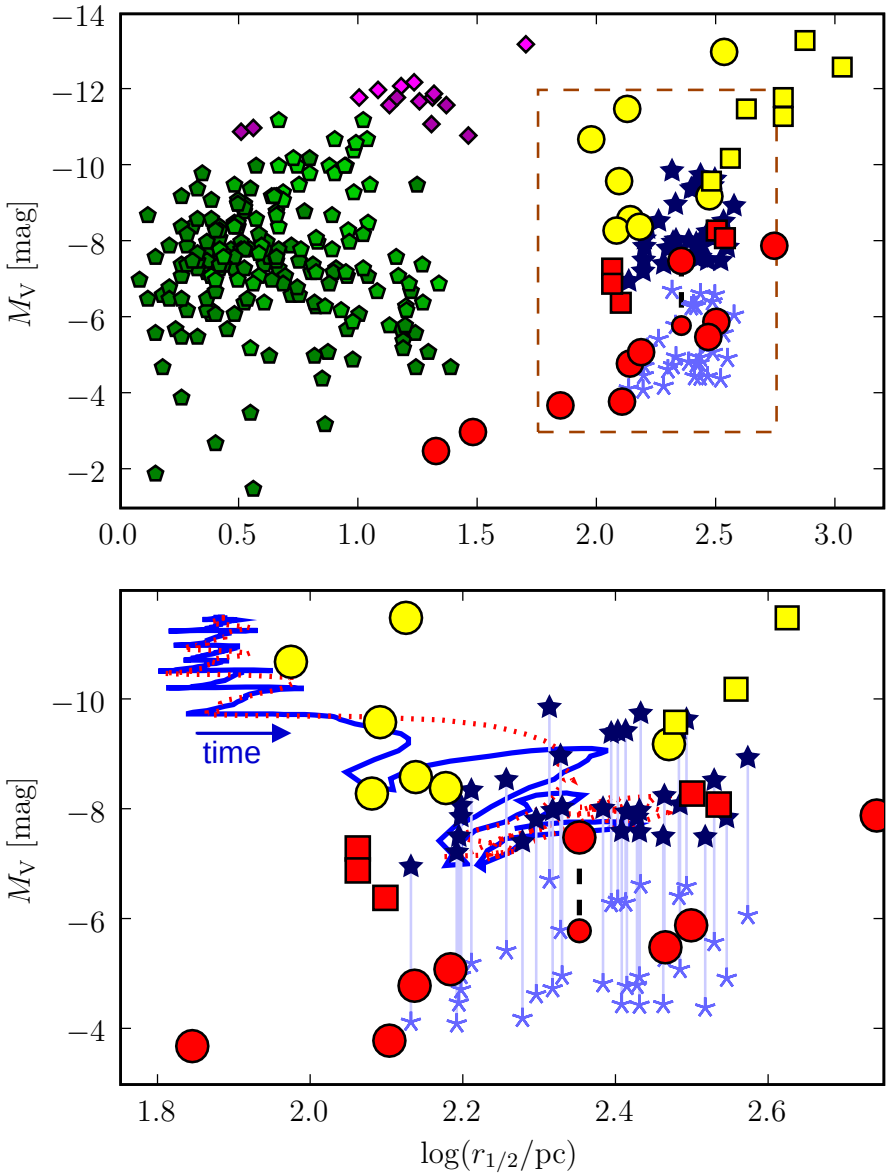

Figure 4.3: Absolute magnitude versus half-light radius for globular clusters (pentagrams), ultra compact dwarf galaxies (diamonds), Milky Way (circles) and Andromeda (squares) dSph satellite galaxies, and simulated satellite galaxies (stars and asterisks). For the observational data of the MW and M31, the red symbols mark the recent additions to the known list of companions from the SDSS, while yellow symbols mark the longer-known dSph's. For the MW dSph galaxy in Boötes two values for the absolute magnitude are given (see text), the values are connected by a thick, dashed line. For the simulated data absolute magnitudes derived within a fixed projected distance r_{bin} (dark stars) and within the variable distance $r_{1/2}$ (light asterisks) are shown. In the lower panel, the region in the top panel marked by the dashed rectangle is enlarged. Corresponding absolute magnitude values for the simulated satellites are connected by light solid lines. The evolutionary tracks of the models RS1-5 (solid curve) and RS1-113 (dotted curve) are shown.

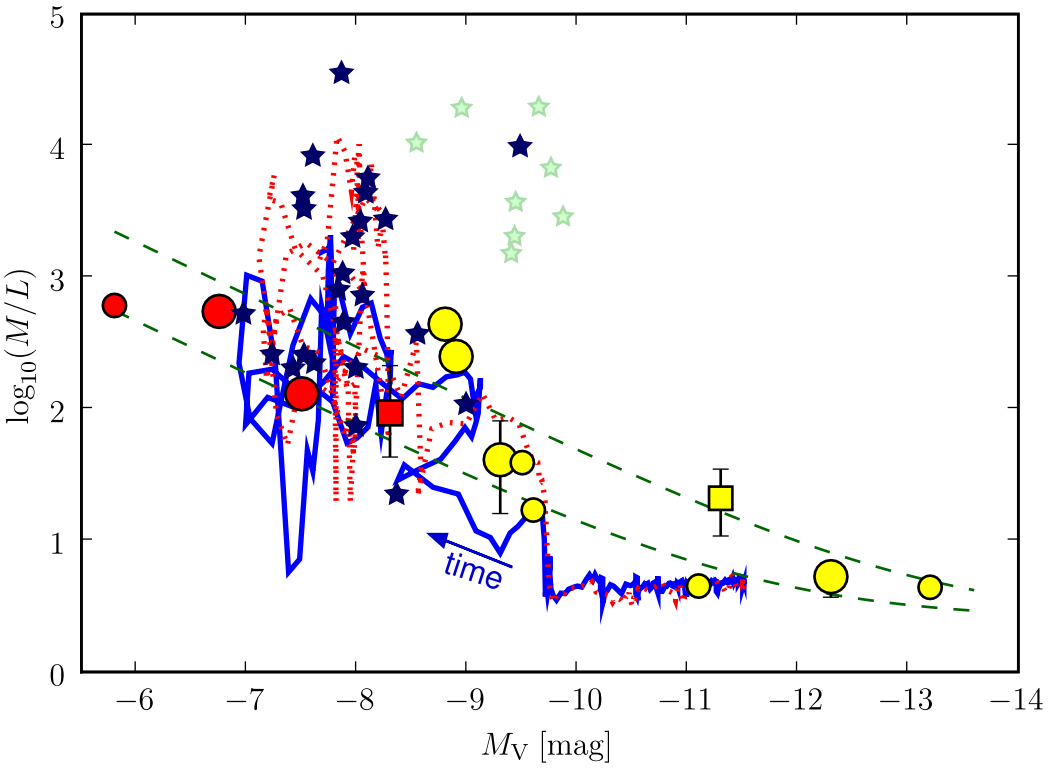

Figure 4.4: Dynamically derived mass-to-light ratio versus absolute magnitude for Milky Way and Andromeda dSph satellite galaxies, for references see Table 4.2; symbols are as in Figure 4.3. For the Milky Way satellites, the data marked with smaller light circles were taken from Mateo (1998), others from more recent studies. The tidal dwarf models are shown as star symbols using the same symbols as in the previous figures. The dashed lines show the expected mass-to-light ratio if stars were in virial equilibrium, embedded in dark matter haloes of masses 1×10^7 $M_\odot$ and 4×10^7 $M_\odot$, respectively. The evolutionary tracks shown here for the simulated satellites start at the lower-right end. In the course of time (as indicated by the arrow) the model satellites get fainter and more disturbed, leading to an increase in the apparent $(M/L)_{\rm obs}$ while the particle value is constant over time, $(M/L)_{\rm true} = 3\ (M/L)_\odot$.

satellites ($M_{V,r_{bin}}$), symbols being as in Figure 4.3. For the Milky Way dSphs smaller symbols mark data taken from Mateo (1998) that were determined from central velocity dispersions. The larger symbols mark more recent values as given in Table 4.2; for Boo symbols are taken as in Figure 4.3. The dashed lines show the expected mass-to-light ratio if stars were embedded in dark matter haloes of masses 1×10^7 $M_\odot$ and 4×10^7 $M_\odot$, respectively (see also Mateo 1998). The evolutionary tracks shown here for the simulated satellites now start at the lower-right end. In the course of time the satellites get fainter and more disturbed, leading to an increase in the apparent $(M/L)_{obs}$ while the particle value is constant over time, $(M/L)_{true} = 3\ (M/L)_\odot$.

4.2 Discussion

In Figures 4.3 & 4.4 it can be seen that dwarf satellite galaxies without dark matter orbiting in massive host haloes span a wide range of observed properties. Energy is pumped into the satellite during peri-galactic passages caused by the interaction with the Galactic tidal field leading to an expansion of the satellite. After the disruption of the initial galaxy, a quasi-stable remnant remains that matches many of the observed properties of today's dSph satellite galaxies of the Milky Way and Andromeda (Kroupa 1997). While initially being identical objects, after several orbits the remnants can appear as objects having very different observed properties, depending on the eccentricities and peri-galactic distances of their orbits. Also during their life-time individual satellites may appear as having different properties during disruptive and subsequent relaxation phases. It is noteworthy that the extreme observable properties are not short-lived states due to projection effects that last for only special states of a satellite's orbits.

Figure 4.3 shows that the simulated satellite galaxies have similar half-light radii and absolute magnitudes $M_{V,r_{bin}}$ as the Local Group dSph satellites, but they are about one or two magnitudes too bright compared to the latest additions from the SDSS. The luminosity within the fixed radius r_{bin} of the simulated satellites is likely to be overestimated compared to the luminosity an observer would deduce, since many extra-tidal stars are included which a real observer would not take into account. The value of the radius r_{bin} is a priori fixed to a specific value, whereas an observer would determine members belonging to the satellite based on the observed surface distribution of stars, and he would therefore determine a somewhat lower absolute luminosity than $M_{V,r_{bin}}$. In addition, of the very faint satellites, only the relatively poorly populated tip of the red-giant branches can be used to estimate their luminosities (see for example figure 2 in Muñoz et al. 2006a). Thus it is not clear whether the observed absolute luminosities of some of the very recently discovered dSph companions of the Milky Way are not underestimated. Muñoz et al. (2006a), for example, compared the colour-magnitude diagrams of Boo and UMa, concluding that Boo must be at least twice as bright as UMa. This clearly shows that there is also a considerable systematic uncertainty in the determination of the absolute magnitudes (and other properties) of the observed very faint companion satellite galaxies.

For the first few orbits, the satellites disperse only slowly, getting fainter, until they approach the state of near disruption. Then the deduced mass-to-light ratio $(M/L)_{obs}$ increases very rapidly since the satellite galaxy is no longer in dynamical equilibrium,

Table 4.1: Properties of simulations: in the first column an identifier is given. The second column lists the total integration time after which simulations were stopped. In the third the initial galactocentric distance is given, and in the forth and fifth columns the mean peri-galactic distance and the mean eccentricity of the orbits are given, respectively.

simulation	t [Gyr]	r_{init} [kpc]	$\overline{r}_{\rm peri}$ [kpc]	$\overline{ecc}$
RS1-4	8.8	100	15.9	0.72
RS1-5	10.7	100	24.6	0.59
RS1-32	5.5	100	3.9	0.92
RS1-64	5.0	100	4.1	0.92
RS1-109	8.8	60	9.1	0.74
RS1-113	6.6	60	22.4	0.46
RS1-24-32	11.0	60	25.6	0.40
RS1-24-64	8.2	60	22.8	0.44

Table 4.2: Observational properties of Local Group dSph galaxies. Where available in the literature we also give error estimates. References for M_V and $(M/L)_\odot$ are given in the last column, if two references are given, the first one is for the absolute magnitude and the second for the mass-to-light ratio (see Figure 4.4).

Name	D [kpc]	M_V [mag]	$(M/L)_\odot$	
UMi	50.2	-8.9	250	[a,g]
Boo	57.6	-7.5	130	
		-5.8	610	[b]
Scl	79.2	-11.1	3	[a]
Dra	82.0	-8.8	440	[a,h]
Sex	89.2	-9.5	39	[a]
Car	102.7	-9.3	41^{+40}_{-25}	[c]
UMa	104.9	-6.75	550	[d]
For	140.1	-13.2	4.4	[a]
Leo II	207.7	-9.6	17	[a]
Leo I	254.0	-12.3	$5.3^{+1.6}_{-1.6}$	[e]
And IX	42	-8.3	93^{+120}_{-50}	[f]
And II	185	-11.3	21^{+14}_{-10}	[g]

References: [a] Mateo (1998); [b] Muñoz et al. (2006a); [c] Muñoz et al. (2006b); [d] Kleyna et al. (2005); [e] Sohn et al. (2007); [f] Chapman et al. (2005); [g] Côté et al. (1999); [h] Evans et al. (2005)

whereas the true mass-to-light ratio $(M/L)_{\rm true}$ is fixed. Interestingly, the models qualitatively reproduce the trend interpreted to be a signature of an universal 10^7 $M_\odot$ dark halo for all dSph satellites, indicated by the dashed lines in Figure 4.4. However, about half of the snapshot values lie significantly above the trend-lines. This can be understood since our automated, virtual observer is kind of naive. A thorough observer will carefully select the stars belonging to a satellite galaxy, which will reduce unrealistic values $(M/L)_{\rm obs}$ to a more realistic regime (see e.g. Muñoz et al. 2006b), but will still end up at too high $(M/L)_{\rm obs}$ ratios compared to the real mass-to-light ratio, $(M/L)_{\rm true}$.

In Figure 4.4 one can also identify a group of snapshot data-points at $M_{{\rm V},r_{\rm bin}} \approx -10$ mag that have much too large $(M/L)_{\rm obs}$ ratios, marked by lighter star symbols. These snapshots belong to the simulations RS1-32 and RS1-64 (while the darker symbols belong to the other six simulations), both having nearly pure radial orbits. This brings the satellites very close to the galactic disc. A disc component is not considered in the simulations presented here, and in particular no gas is included. The additional highly non-spherical potential and effects of disc shocking will considerably affect the properties of the satellites, also depending on the impact angle with the disc. These effects need to be studied in much more detail in the future (see §5.2.2).

The work presented here details the evolution of gas and dark matter free satellite galaxies. But it has to be clarified in more detail how these objects can form and how many of them can condense in tidal arms, which is beyond the scope of this study. Wetzstein et al. (2007) identified at least five very massive objects in their SPH simulation, the largest one, at the tip of the tidal tail, has a mass corresponding to $\approx 3.5 \times 10^8$ $M_\odot$ if the progenitor galaxy is scaled to the size of the Milky Way. Bournaud & Duc (2006) found a mean production rate of somewhat more than six massive substructures ($> 10^8$ $M_\odot$) formed in the tidal tails in their simulations. 20 per cent of these objects survive for more than 2 Gyr. Of the non-surviving ones about two-third fall back onto their host galaxies. The other one-third was considered in their simulation as destroyed because they dropped below a mass threshold of 10^8 $M_\odot$. We argue that these objects should not be considered a priori as being completely destroyed. Instead, we have shown here that satellite galaxies of much lower mass may be identified on the sky and appear similar to today's known dSph galaxies of the Milky Way. This leaves room for a number of tidal dwarf remnants, even for a low number of major interaction events. However, as Bournaud & Duc noted, they did not account for the larger gas fraction of galaxies in the early universe, whereas Wetzstein et al. used a gas fraction of 30 per cent. This is, despite the different treatment of the gas (sticky particles vs. smoothed particle hydrodynamics), a further major difference in the two models. A higher gas fraction may well enhance the efficiency of TDG production. From the current simulations it is also unclear how many lower mass ($< 10^8$ $M_\odot$) TDG candidates form, but observations show that even today's interactions can form of the order of a dozen tidal dwarf galaxies in a single encounter, for example in AM 1353–272, show in Figure 4.5. (Weilbacher et al. 2000)

If some of the dSph galaxies of the Milky Way were of tidal origin, their genesis must have happened at an early time. In all well-studied dwarf spheroidals an old stellar population is present (e.g. Grebel & Gallagher 2004; Tolstoy et al. 2004), they do follow a metallicity-luminosity relation (e.g. Mateo 1998; van den Bergh 1999; Grebel, Gallagher,

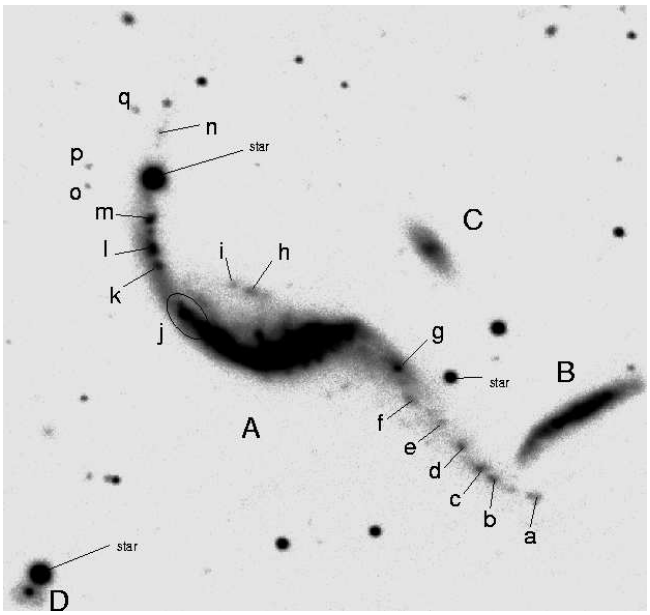

Figure 4.5: An image of an interacting galaxy pair (AM 1353–272, taken from Weilbacher et al. 2000, their figure 21). Within this single interaction-event about one dozen TDG candidates can be identified.

& Harbeck 2003), and they are typically found to have extended star formation histories (e.g. Grebel 2000; Ikuta & Arimoto 2002). The latter two findings require that the galaxies maintained a considerable amount of gas for some time to continue star formation or later turn it on again, and to retain the produced metals. Indeed, Recchi et al. (2007) have shown that dwarf galaxies without a dark matter halo can have star-formation episodes of several hundred Myr without necessarily being quickly destroyed due to stellar winds, radiation pressure, or supernova feedback. Today, the dSphs are almost gas free (Gallagher & Wyse 1994) and do not show ongoing star formation. As such they must have developed from gas-rich galaxies to today's dSph (Mayer et al. 2001; Pasetto et al. 2003, but see also Grebel et al. 2003). For a given metallicity, dSph galaxies have a luminosity 10 to 100 times lower than dIrr galaxies (Grebel et al. 2003), being consistent with initial TDGs that form from pre-enriched material losing over 90 per cent of their mass as a result of tidal forces.

A common ancient stellar population in satellite galaxies of tidal origin can be explained by considering that tidal dwarfs do not solely consist of stars born in star formation events during and after their genesis, but additionally also of old stars from the progenitor galaxy. Elmegreen et al. (1993) argued that a newly born tidal dwarf galaxy consists of about 40 per cent old stars. Similarly, Wetzstein et al. (2007) found that about 30 per cent of the mass of their most massive TDG candidate is in old stars, while being basically void of dark matter. Very recently Helmi et al. (2006) compared the metal-poor tails of the metallicity distribution of the Milky Way's halo and of four of its dSph satellites. While the distributions were compatible among the dSph galaxies, they significantly differ compared to the Milky Way halo. Helmi et al. (2006) conclude that the Milky Way and the dSphs must have had different progenitors, since the dSphs are lacking very metal poor stars. If

dSphs were of tidal origin, their oldest stellar population would consist of stars already pre-enriched in the progenitor galaxy.

It is also remarkable that a number of the dSph galaxies show internal structure or off-centred and twisted isophotes (e.g. Palma et al. 2003; Walcher et al. 2003; Cioni & Habing 2005) which is not expected if they are shielded by a massive dark matter halo. A further challenge of the notion of the suggested universal minimum mass of some 10^7 $M_\odot$ (Mateo 1998; Gilmore et al. 2006) would be the significant mass loss from the dark matter halo due to the Milky Way tides. Given the distorted inner morphology of most of the dSph satellites, why do they still have the same dark matter halo? Tidal mass-loss has been shown to be significant for such satellites (Read et al. 2006a). However, this may not be a robust argument because the minimum halo-mass concerns only the mass within the observed optical light: nothing outside the kinematic data is used; so original total masses might not be that relevant (Gilmore priv. comm., see also Peñarrubia et al. 2008). On the other hand, a TDG population may very naturally show very different evolution histories and internal structures, even if they were born in the same environment (Figures 4.2 – 4.4), as they are not shielded by a massive dark matter halo.

As a final remark, we found an interesting correlation that, to our knowledge, has not been studied yet, in a plot of the half-light radii versus the Galactocentric distance, as shown in Figure 4.6. One group of dSphs seems to have a more or less constant half-light radius, independent of Galactocentric distance, whereas a second group has larger half-light radii that are probably correlated with Galactocentric distance. The peculiar stellar systems Coma Berenices, Boötes II, and Willman 1, all at $R_{\rm GC} \approx 50$ kpc, have remarkably smaller half-light radii. There is an ongoing discussion whether these three have to be classified as dSphs or as globular clusters (Belokurov et al. 2007; Gilmore et al. 2007; Siegel et al. 2008). The correlation is only evident for the Milky Way dSphs. On the other hand, the Andromeda companions, for which data is also plotted in Figure 4.6, appear to have systematically larger radii at a given absolute magnitude M_V (McConnachie & Irwin 2006a, their figure 5) as can be seen in Figure 4.3. McConnachie & Irwin ascribed this to a difference in the mass of the two hosts: Oh, Lin, & Aarseth (1995) found a prescription[(a)] for the tidal radius of a dwarf galaxy orbiting in an isothermal host halo. McConnachie & Irwin noted that there is a degeneracy of parameters, but if the dSphs of the Milky Way and Andromeda are not a priory fundamentally very different, they argued that the host halo mass is the parameter that most likely affects the difference of the tidal radii, and thus also of the more robust half-light radii (see also Peñarrubia et al. 2007). An extraordinary combination of parameters would be needed to explain the more or less constant half-light radius over a wide range of Galactocentric distances as seen in Figure 4.6. On the other hand, it is also not clear how dark matter free tidal dwarfs could account for this finding. And also, why would the Andromeda dSphs be systematically larger? The models analysed in this Chapter do not cover a large enough parameter space to address this question. So it will be important to improve and extend the models.

[(a)] For completeness the relation is: $r_t = a \left[\left(\frac{M}{M_H} \right) (1-e)^2 \right]^{1/3} \left[\left(\frac{(1+e)^2}{2e} \right) \ln \left(\frac{1+e}{1-e} \right) + 1 \right]^{-1/3}$. M is the mass of a dwarf galaxy, M_H is the total mass of the host halo, and e is the eccentricity of the orbit with semimajor axis a.

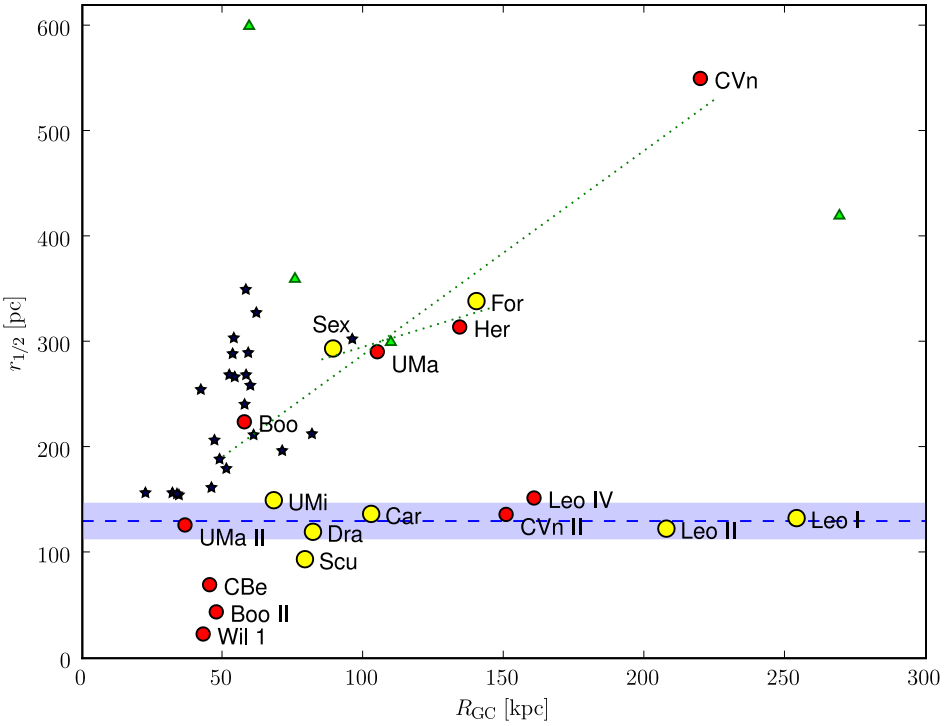

Figure 4.6: Half-light radius, $r_{1/2}$, versus Galactocentric distance, R_{GC}, for the Milky Way dSph satellite galaxies and the snapshot data of the models, the latter marked by the star symbols. For comparison, we also plot the half-light radii for Andromeda satellite galaxies as derived by McConnachie & Irwin (2006a) with triangles. There appears to be a dichotomy of Milky Way satellites: one group of dSphs seems to have very similar half-light radii independent of distance, with mean value $\bar{r}_{1/2} = 130 \pm 17$ pc, shown by the dashed line and the shaded region. The satellites of a second group (Boo, Sex, UMa, Her, For, & CVn) have significantly larger half-light radii, and their half-light radii appear to be larger the more distant a satellite is. The two dotted lines show linear fits for all of these six satellites, and for Sex, UMa, Her, & For only, to indicate the possible relation with Galactocentric distance. The model data cover Galactocentric distances up to 100 kpc only, but appear to better match the properties of the second group rather than being able to reproduce a constant half-light radius. The peculiar stellar systems CBe, Boo II, and Wil1 all have obviously smaller $r_{1/2}$ (their classification is not definite: dSphs or globular clusters; Belokurov et al. 2007; Gilmore et al. 2007).

Chapter 5

A new numerical code to compute the satellite dynamics

The model galaxies analysed in the last section (§4.1) were numerically evolved with the particle-mesh code Superbox (Bien et al. 1991; Fellhauer et al. 2000). Since these simulations were limited in some parameters, for example the number of particles and the number of satellites per simulation, we intended to repeat the same kind of studies with a wider scope of application. To this end we first re-implemented the code as described in the next section.

5.1 Superbox++

5.1.1 The Superbox code

Superbox is a particle-mesh code for collisionless galactic simulations (Sellwood 1987), developed at the Astronomisches Recheninsitut (ARI) in Heidelberg in the late 1980s and early 1990s (Bien et al. 1991). The different ansatz of the Superbox code compared to other particle-mesh codes is to use high resolution sub-grids that are co-moving with places of special interest in an N-body simulation. Such special places are for example satellite galaxies that are evolving in the vicinity of their parent galaxy. The technique used in Superbox differs from adaptive-refinement mesh codes in that the sizes and dimensions of the grids are fixed at the start-time of the program and are not adaptively changing at runtime, but can only be changed manually. This leads to a very rapid computation per time-step. For a detailed description of the principle of Superbox we refer to Fellhauer et al. (2000) and references therein.

Briefly, Poissons's equation, $\nabla^2\phi = 4\pi\rho$, is solved for the mass density, ρ_{ijk}, on a grid (Figure 5.1, left panels). The density is determined by counting the number of particles in each grid-cell. This is a so called "nearest grid point" algorithm. The high-density regions are kept track off by two nested sub-grids for each galaxy individually: one to resolve a galaxy as a whole, the "outer grid", and one to resolve the very dense inner region of a galaxy, the "core grid". The full simulation region, the "system" or "local universe" (LU) grid, is covered by a grid that is common amongst all galaxies in the simulation. The grid based potential, ϕ_{ijk}, (Figure 5.1, right panels) is then arrived at by (i) calculating

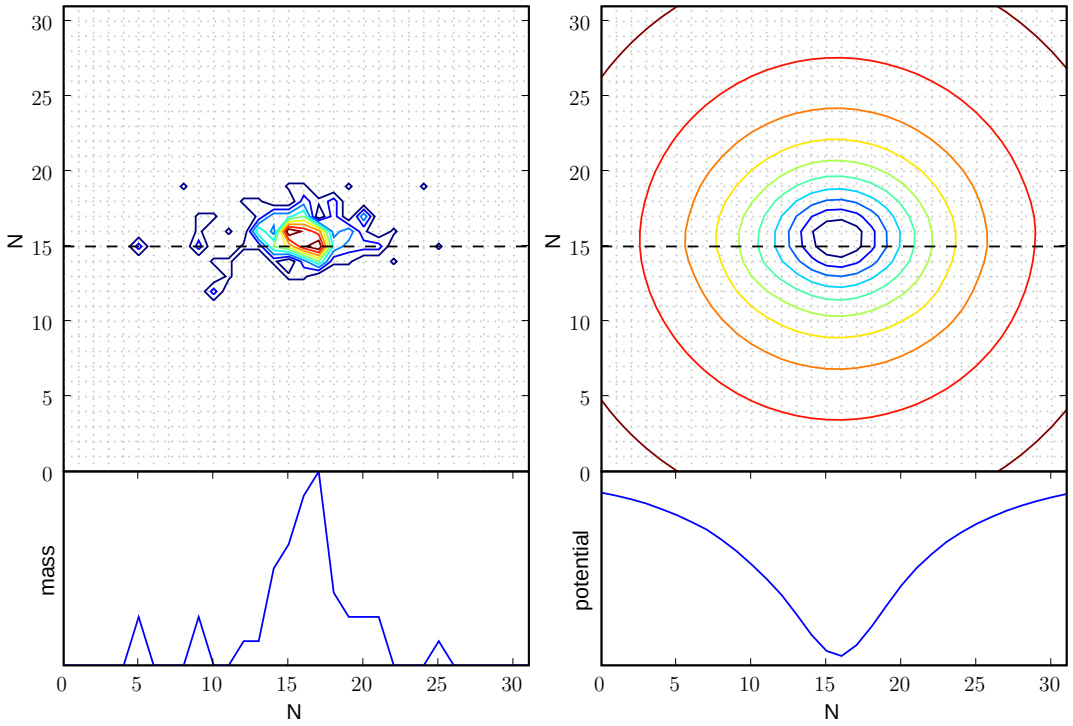

Figure 5.1: On the left, a mass-density distribution is shown in arbitrary units of a randomly set-up model galaxy. In the top-left panel, contour lines of equal mass across a grid boundary are shown. The 32×32 grid is indicated by light dotted lines. In the lower-left panel a cut along the grid boundary, as indicated by the dashed line in the top panel, is shown. On the right, the resulting potential in arbitrary units is shown.

the Fourier transform of the density grid, (ii) multiplying it with the Fourier transformed Greens function cell by cell, and (iii) transforming back to real space by an inverse Fourier transformation. Accelerations for each particle are calculated by numerically differentiating the potential. To be compatible with the existing SUPERBOX program, it is possible to add a static potential to account for the gravitational potential of the Galaxy. Currently, a three-component model is implemented (see Binney & Tremaine 1994): the halo is modelled by a logarithmic potential,

$$\Phi_{\rm halo}(x,y,z) = \frac{1}{2} v_c^2 \ln\left(r^2 + r_{\rm h}^2\right) \quad , \tag{5.1}$$

the disc by a Plummer-Kuzmin model,

$$\Phi_{\rm disc}(x,y,z) = -\frac{G\,m_{\rm d}}{\sqrt{R^2 + \left(a_d + \sqrt{z^2 + b_d^2}\right)}} \quad , \tag{5.2}$$

and the bulge by a Hernquist bulge potential,

$$\Phi_{\rm bulge}(x,y,z) = -\frac{G\,m_{\rm b}}{r + a_b} \quad . \tag{5.3}$$

G is the gravitational constant, $r^2 = x^2 + y^2 + z^2$ and $R^2 = x^2 + y^2$. The parameters v_c, $r_{\rm h}$, $m_{\rm d}$, $a_{\rm d}$, $b_{\rm d}$, $m_{\rm b}$, and $a_{\rm b}$ have to be appropriately chosen, for example as derived from

observations. Other models can be adapted as well. Particles are finally evolved forward in time using a leapfrog scheme.

The original SUPERBOX code is written in the Fortran 77 (F77) programming language. While code written in Fortran is believed to execute generally very fast, this particular code has also some disadvantages. There is no way in Fortran 77 to dynamically allocate memory, which implies that one has to recompile the source code of SUPERBOX every time one wants to simulate a larger number of particles. The same is the case for the number of grid cells. SUPERBOX is limited to grids with fixed dimension $(N \times N \times N)$, $N = 2^M$, M a positive integer, which is equal for all grids and sub-grids, and the side-lengths of the grids are the same in each dimension. However, to accurately simulate a disc-galaxy it might be useful to reduce the side-length in one dimension to get a higher resolution in the polar direction of the disc. Another desirable feature is to use different grid dimensions for different co-moving sub-grids or the grid representing the "local universe".

Nevertheless, SUPERBOX has, beyond any doubt, advantages: the code is highly optimised in the sense that it uses almost as little memory as possible, making it possible to run the code with many particles even on machines with only a small amount of memory. This advantage is nowadays less important since memory gets cheaper and cheaper every month. Even standard desktop PCs have nowadays 1 GB or more of RAM, which makes it possible to simulate some 10 millions of particles. One side effect of the memory optimisation is that SUPERBOX performs most operations with single precision floating point variables, except for some critical sections where single precision variables are casted to double precision and backwards after the critical code section. Single precision operations can, in principal, be executed faster than double precision operations, and modern compilers can even optimise the code such that multiple single precision operations are simultaneously executed in floating-point pipelines (SIMD: "Single Instruction, Multiple Data"), which results in a decreasing runtime.

5.1.2 The Superbox++ code

Reasons to re-implement the SUPERBOX in the C++ programming language code were: to improve the performance by avoiding some bottlenecks, re-write the source to be able to use new features of modern PC architectures, and to have advanced features and the ability to easily extend the feature list, while also keeping memory consumption at a reasonable level. Another core issue was to write the software such that it can easily be integrated in other software projects or, for example, be controlled by an external script. Finally we also wanted to keep the portability of the code, i.e. the code should be usable on different microcode architectures and under different operation systems.

The actual simulation code is designed as a software library called LIBHYPERBOX. This library has some simple interfaces to load and store data, initialise parameters, and start and control the simulation. The program SUPERBOX++ that links LIBHYPERBOX to an executable program, is written in a SUPERBOX compatible manner, i.e. it behaves almost exactly as the original SUPERBOX program. This makes it straightforward to run exactly the same simulation with both programs.

Despite minor performance "tweaks" in the Superbox++ code that enhance the performance of the program compared to Superbox (see Appendix B), there are some conspicuous peculiarities in Superbox which unnecessarily slow down the code, and that can be avoided. We elaborate some of these in the following. To calculate the values of the gravitational potential at each vertex of a grid, for each individual grid one forward and one backward complex 3D-FFT transformation has to be performed. Since the FFT is a very time intensive transformation it is a good ansatz to optimise the FFT code. In Superbox++ we use a portable, yet very fast implementation of the FFT algorithm, provided by the library fftw (Frigo & Johnson 2005, `http://www.fftw.org`). Just using this FFT code already results in a significant performance gain.

Furthermore, multi-threading techniques are used frequently in Superbox++. Multi-threading, or more general "parallel computing", is a way to make usage of multiple CPU cores integrated in modern processor architectures like the AMD Athlon64™ X2 (see Fig. 5.2) or the Intel® Core™ 2 Duo processors. For software that needs lots of computational power it is essential to utilise these multi-core CPUs. The development of CPUs has moved away from faster and faster clocked CPUs (which also waste lots of electric energy) to CPUs which inherit multiple CPU cores that independently can execute program code in parallel[(a)]. This development is independent of processor architecture or manufacturers, like AMD X86_64, Intel IA-64, IBM PowerPC and Cell, or Sun Ultrasparc to name only some. Multi-threading programs utilise multiple CPU cores by separating independent parts of the code and executing them separately in so-called "threads". If two independent threads are initiated at the same time, each single thread can be executed on one of the two (or more) CPU-cores. In an ideal scenario this results in a performance gain of a factor 2. In reality some data has to be synchronised between the threads, which reduces the effective performance benefit. In Superbox++ threads are directly initiated, and also the fftw library uses multiple threads. The MPI library (Message Passing Interface, `http://www.mpi-forum.org`), which is typically used to write parallel code for computer clusters, can also be used on multi-core systems. And some modern compilers (e.g., the GNU compiler since version 4.2) support a kind of automated multi-threading provided by the OpenMP API (Open Multi-Processing, `http://www.openmp.org`). Despite this optimisation for multi-core CPU designs, Superbox++ is portable and not limited to a specific hardware or operating system.

5.1.3 Comparison with Superbox

The differences in the implementation of the algorithm in the codes influence the results derived when performing simulations with Superbox++ compared to the original Superbox. Superbox++ consistently uses double precision floating point operations, while Superbox mostly uses single precision operations, especially for the FFT. Also Superbox++ uses a different FFT implementation, namely the code of the fftw library compared to the Numerical recipes (Press et al. 1992) code in Superbox. At first it might sound a little bit odd that the FFT code can influence the result, since the FFT algorithm is exactly defined. But different

[(a)] "If your program is not fast enough today, it will never be." (Mark Harris, AstroGPU 2007, an allusion to the new demands necessary, to make programs more efficient and ready for future hardware developments.)

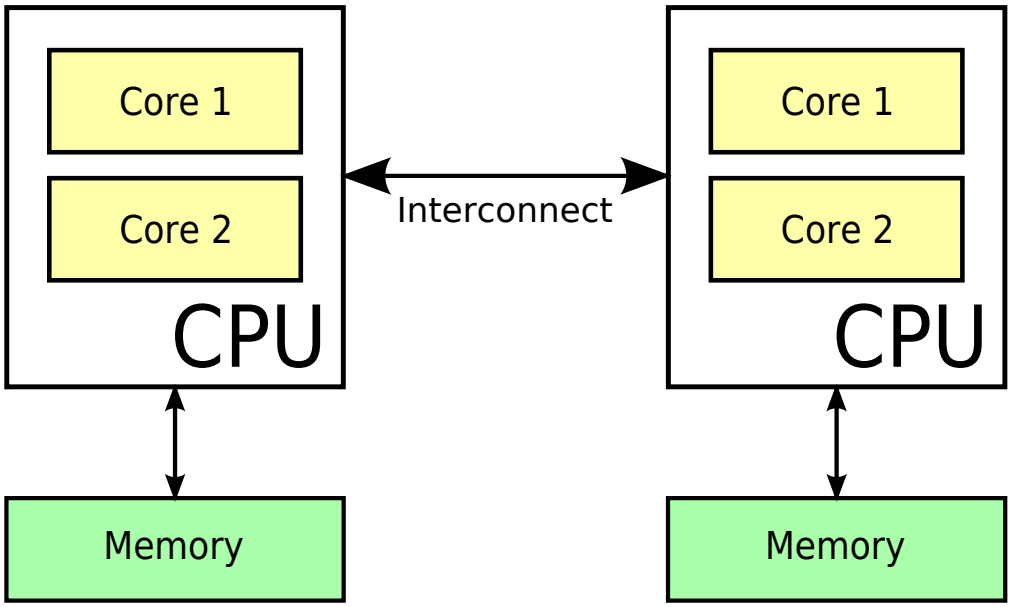

Figure 5.2: Schematic drawing to illustrate the architecture of a modern multi-processor, multi-core workstation as used at the AIfA. Each CPU is equipped with two CPU cores, which can run code in parallel, and a CPU has its own "local" memory. Two (or more) of these CPUs are installed in the same machine, communicating and sharing memory via a fast interconnect.

implementations of the FFT use different concrete ways to implement the algorithm, e.g., using a different order of execution of commands within the code. Such differences can lead to different rounding effects which in the end can influence the result. It is, for example, not guaranteed that executing $(a + b) * c$ gives numerically exactly the same result as $(a * c + b * c)$, while both are mathematically identical[(b)].

So it is important to compare the results derived with Superbox and Superbox++. We consider the results derived with Superbox as reference results for the comparison. In the following, data derived when running a test configuration, `twoiso`, are compared. `twoiso` consists of two identical, unrelaxed isothermal spheres with 100 000 particles each, rotational velocity 150 $\mathrm{km\,s^{-1}}$, and a cut-off radius of 200 kpc. The two galaxies were set to the positions $x = +30, -30$ kpc and each was given a small "kick-off" velocity of $v_y = +10, -10\ \mathrm{km\,s^{-1}}$, respectively. A grid-dimension of 32^3 was chosen with core-, outer-, and system-radii of 16 kpc, 64 kpc, and 348 kpc, respectively. We refer to the latter grid as the "local universe" grid. The time-step was chosen to $\Delta t = 1$ Myr. According to the criterion of Power et al. (2003), results are convergent for radii $\gtrsim 5$ kpc from the centres of the haloes with this choice for a total integration time of $t_0 = 2$ Gyr. In particular the innermost Lagrange radius is larger than this value and thus not expected to be affected by the choice of the finite time-step. The tracking of the co-moving grids was chosen to follow the centre-of-density. This test-setup is in no way a physical meaningful configuration, but it allows us to check several different properties of the code: The grids overlap to a large amount, so the mutual influence of the grids can be tested. The relatively small number of

[(b)] See also `http://www.fftw.org/accuracy/` for comments on that topic.

particles and the small grid dimension amplify possible differences due to particle noise, grid-effects, or undesired effects due to coding differences.

The output of a test-script `testhead.py` is given for the 500th integration step for the first of the two galaxies in the test configuration in Output 1. This script displays the main values derived during the simulations, like positions of the galaxies, energies, and angular momenta. All values are given in physical units: time in Myr, positions in kpc, velocities in $\mathrm{km\,s^{-1}}$, energies in $\mathrm{M_\odot\,km^2\,s^{-2}}$, and angular momenta in $\mathrm{M_\odot\,kpc\ \ km\,s^{-1}}$. All results are in agreement within a few percent.

The evolution of some parameters are studied in detail. In Figure 5.3 the time-evolution of the Lagrange radii is shown for 2 000 integration steps (2 Gyr in total). Values from SUPERBOX are shown as dashed lines and values from SUPERBOX++ as solid lines. As the data are barely distinguishable we additionally plot the relative differences $\Delta r_i = (r_i^{\mathrm{sbpp}} - r_i^{\mathrm{sb}}) / \left(1/2(r_i^{\mathrm{sbpp}} + r_i^{\mathrm{sb}})\right)$ of the Lagrange radii in Fig. 5.4. There is one curve in Fig. 5.4 that shows a significantly larger scatter than the others. This is the line for the 10% Lagrange radius, which is the innermost Lagrange radius. A larger scatter is expected since relative differences are plotted. The Lagrange radii also depend on the location of the tracking-centre which differs for the runs (Fig. 5.5). The relative influence of the tracking-centre on the innermost Lagrange radius is the largest. Nevertheless, all values scatter about the radii determined with SUPERBOX with typically $< 0.5\%$ difference, and even for the innermost radius we typically find differences $\lessapprox 1.5\%$.

In Figure 5.5, left panel, the motion of the centres-of-density (COD) and the centres-of-mass (COM) of both galaxies are shown, as well as the motion of the centre-of-mass in the local universe in Fig. 5.5, right panel, for the test configuration `twoiso`. The motions of the COD and COM agree well for the individual galaxies. However, the motion of the centre-of-mass in the local universe volume, which is the centre-of-mass of all particles, shows a significantly different behaviour on a smaller scale. For SUPERBOX++ the COM in the local universe nearly linearly moves away from the origin, i.e. it constantly drifts in one direction due to not perfectly isotropic setup conditions. This is the expected behaviour if the setup is somewhat anisotropic. For SUPERBOX we see, however that the COM lurches around about the origin similar to a Brownian motion. At some point in time the track even kinks by about 90° which indicates some discontinuities in the SUPERBOX code. These are most likely caused by the single-precision only accuracy of the computations.

We also checked that the derived energies of the system, the kinetic and potential energies, are in good agreement, as are the angular momenta. In general, energies are better conserved in SUPERBOX++ than in SUPERBOX, again, most likely due to the double precision computations.

5.1.4 Future development

The code basis of SUPERBOX++, specifically, the library LIBHYPERBOX, was designed to be as flexible as possible. This allows for easy future implementations of new features. It might, for example, be desirable to include a "sticky particle" scheme to treat for the dissipative effects of gas in galaxies (see, for example, Vollmer et al. 2001; Bournaud & Duc 2006). Another possible extension is to use variable grid dimensions, $(N \times M \times K)$, which

```
                  sb++    Superbox
-----------------------------------------------------------
stepnumber:        500         500
dt         :       1.00        1.00
time       :     500.00      500.00

centre of mass
   x       :   6.873838    6.892486
   y       :   1.547523    1.563747
   z       :   0.003357    0.002694
  vx       : -30.687130  -30.953545
  vy       :  -2.751011   -2.650033
  vz       :   0.133671    0.175620
centre of density
   x       :   1.705151    1.876294
   y       :   0.453548    0.491313
   z       :  -0.274598   -0.278354
  vx       : -22.032600  -22.876480
  vy       :   0.501682    0.229618
  vz       :   0.008505    0.193319
centre of simulation
   x       :   0.007550   -0.002938
   y       :  -0.024086   -0.012662
   z       :  -0.010504   -0.009885
  vx       :   0.054343    0.005372
  vy       :  -0.143957   -0.028488
  vz       :  -0.067604   -0.067051

#stars     :           100000            100000
#bound     :            85739             85894
ekin       :       5.3597e+04        5.3333e+04
epot       :      -4.8647e+04       -4.8488e+04
internal angular momentum
  lx       :       1.0817e+05        1.0767e+05
  ly       :      -1.9337e+05       -1.9281e+05
  lz       :       2.6081e+13        2.6165e+13
total angular momentum
  lx       :       1.9423e+10       -1.4547e+11
  ly       :       2.8078e+14        2.7868e+14
  lz       :       5.4037e+13        5.3964e+13
```

Output 1: Output of the program `testhead.py` for the test configuration `twoiso` at the 500th integration step for the first "galaxy".

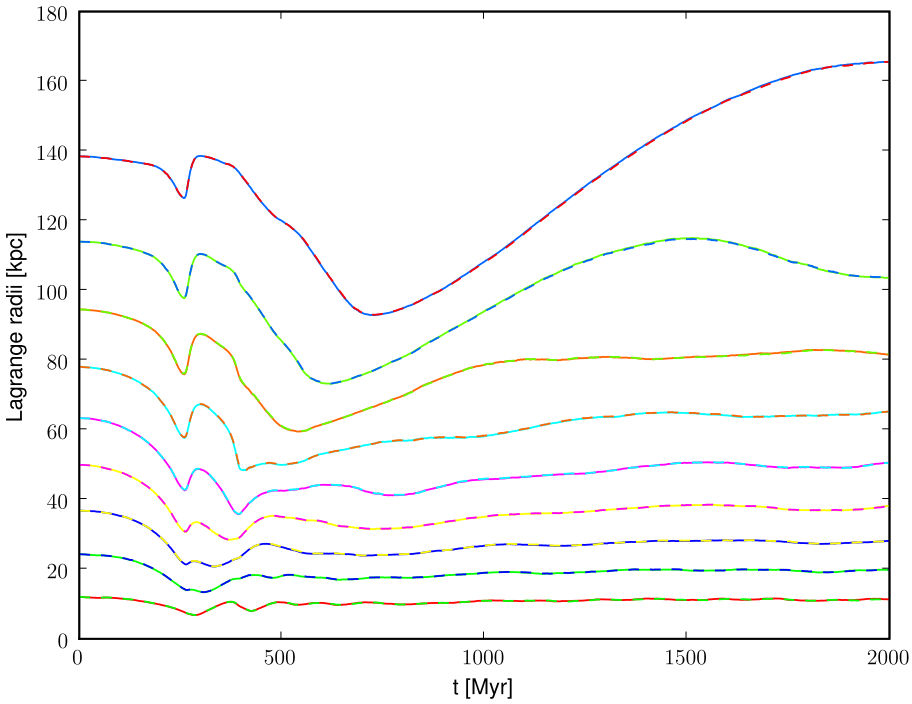

Figure 5.3: Evolution of the 10%, 20%, ... 90% Lagrange radii for the galaxy number 1 in the test configuration `twoiso`. The dashed lines show the radii as derived with Superbox, the solid lines as derived with Superbox++. The "bumps" occur when the two galaxies pass through each other, while the large-scale decrease and later increase of the outer Lagrange radii, for example of the 90% radius, is a signature of the violent relaxation process of the initially unrelaxed isothermal models. For a better discernibility, relative differences for the two codes are shown in Fig. 5.4.

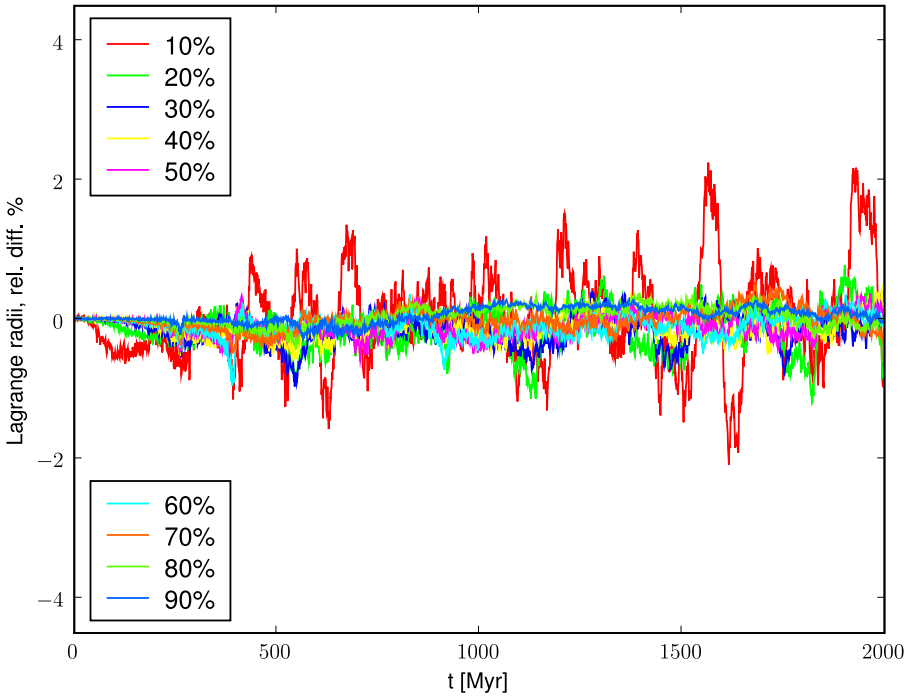

Figure 5.4: Relative difference of the Lagrange radii as shown in Fig. 5.3 from a comparison of results of SUPERBOX with SUPERBOX++. Different radii are shown in different colours. The red coloured curve with the larges amplitude shows the relative difference of the 10% Lagrange radii.

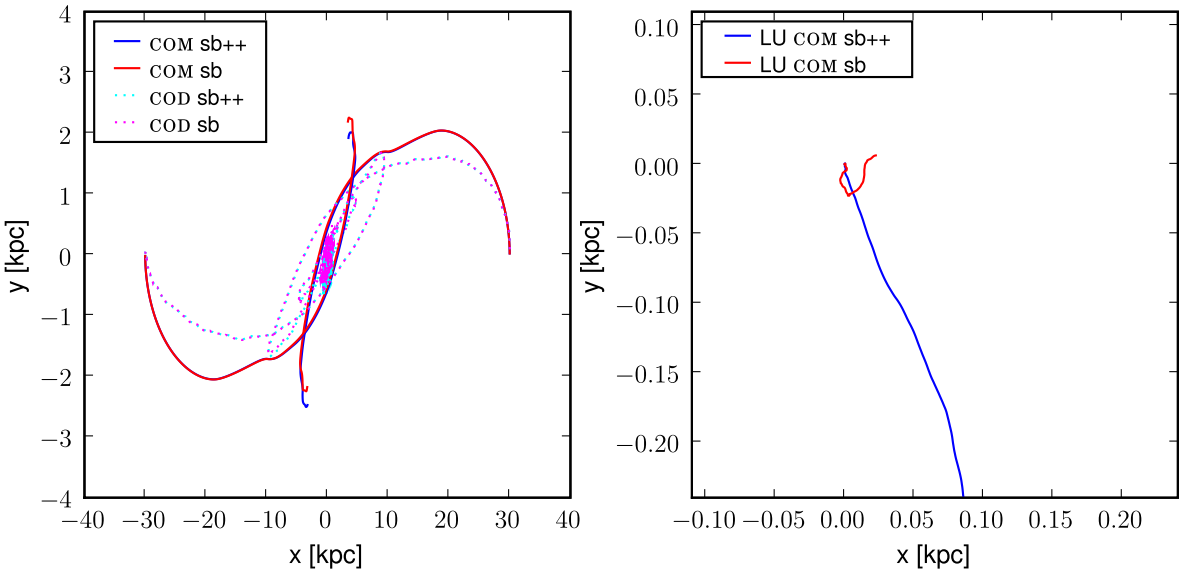

Figure 5.5: In the left panel, the motion of the centres-of-mass (solid lines) and the centres-of-density (dotted lines) for both galaxies of the test configuration `twoiso` in the x-y-plane are shown. The data for SUPERBOX are shown in red and magenta, the data for SUPERBOX^{++} in blue and cyan colours. Note the very different scalings of the x- and y-axis in the left panel, and also the very different scalings of the axes in the left and right panels. In the right panel, the motion of the centre-of-mass in the "local universe"-grid in the x-y-plane is shown. The behaviour of the motion of the centre-of-mass differs significantly: the centre-of-mass basically moves constantly in one direction for the simulation performed with SUPERBOX^{++} – which is the expected behaviour – whereas it lurches around for the run performed with SUPERBOX, a behaviour that is similar to a Brownian motion.

might even have different scaling-lengths, a feature that is already partly implemented. One possible application of this is to use a grid that is squeezed in the z-direction for a spiral galaxy with its galactic plane in the x-y-plane. Another possible future extension of Superbox++ might be to have grids that have different orientations in space. Such a feature is not needed as long as the grids are cubical, i.e., $N \times N \times N$ with identical edge length, but having asymmetric grids at hand it might be a very helpful tool. And, as another very different modification of the code, one can try to adapt the scheme described in Tiret & Combes (2007), to modify the code such that it can solve the Poisson Equation in Modified Newtonian Dynamics (MOND, see §6.5).

Superbox++ is under active development. There are parts of the code that can be optimised further. We expect to be able to enhance the performance of Superbox++ (cf. Appendix B) even more in future versions by optimising the code. We are also elaborating on the possibility to use, for time-critical parts like the FFT, algorithms that can be run on modern graphics processor units (GPU) to speed up calculations significantly. General-purpose computation on GPUs (GPGPU, see `http://www.gpgpu.org`) is a very promising technique to accelerate calculations. While current GPUs are limited to single precision floating-point operations (which can however be extended to double precision algorithmically, see Dekker 1971), future GPUs will support double precision floating-point operations intrinsically and may well outperform other special purpose hardware like GRAPE cards.

5.1.5 A final remark

A lot of time and men power of today's research is invested in the development of algorithms and code implementation in some fields of research. This was also the case in this thesis. The software to analyse the spatial distribution of the satellite galaxies, for example, comprises about 17 500 lines of source code in total, and the full analysis of the statistical significance (§2.4) is based on more than *3 years* of CPU-time. Time for the development of algorithms and their coding in inevitable – it can only be more or less productive, depending on the skills of the application developer. But what is very important is to write efficient software when the task *the computer* has to solve gets complex. Moore's Law[(c)], which is sometimes laxly formulated as "computer performance doubles every two years", is applicable since 40 years now. But today, computer performance does not mean faster clock speed, it means more CPU cores per processor. As explained in this Chapter, there are multiple techniques to use these multi-core CPUs: direct multi-threading programming, the MPI programming interface, or semi-automatic optimisation techniques like OpenMP. All these techniques will become more important in the future and it is essential to use them, along with the possibilities to distribute computational tasks via a network (distributed or grid computing) as done for the bootstrapping analysis.

[(c)] Named after Gordon E. Moore (1965), a co-founder of a famous semiconductor company.

5.2 A first application of Superbox++

5.2.1 Modelling dark matter free dSphs

Having the advanced program SUPERBOX++ at hand, as a first application we performed new modelling of dark matter free dSph galaxies orbiting within the (dark) halo of a Milky Way like galaxy, similar to Kroupa (1997). The halo is represented by an isothermal sphere with total mass of 2.85×10^{12} $M_\odot$, cut-off radius 250 kpc, and an initial circular velocity of $v_c = 220$ km s^{-1}. The halo model was allowed to relax after the initial set-up. Initial models for dark matter free satellite galaxies are set-up as Plummer spheres (Plummer 1911). We generated one very lightweight satellite with initial mass 2.85×10^6 $M_\odot$ with 285 000 particles (S1), one intermediate mass model with 10^7 $M_\odot$ with 10^6 particles (S2), similar to the models analysed in Section 4.1.The latter model represent typical tidal dwarf galaxies after losing its gas, whereas the model S1 might represent one of the least massive TDGs probably being formed. The Plummer-radius for the set-up is $r_p = 300$ pc, and the cut-off radius $r_c = 1.5$ kpc in all cases. The model satellites are placed in the halo at a position $x, y, z = 0, 0, 100$ kpc, and are given an initial velocity of $v_x = 180$ km s^{-1} $< v_c$, resulting in peri-galactic passages at a distances of ≈ 41 kpc.

Figure 5.6 shows an allsky surface-brightness plot of satellite S1 as an observer located in the plane of the Milky Way would deduce if he could identify all stars that originally belonged to the satellite galaxy, see also Figure 4.1 for the model S2. For these plots a mass-to-light ratio of $(M/L)_\odot = 1$ was assumed for the particles in the simulation. The allsky surface-brightness plot was constructed as follows: a uniform grid was generated on the unit-sphere, where all grid-points have the same spherical distance to their direct neighbouring grid-points. This grid is constructed iteratively by starting with the vertices of a regular icosahedron, which are located on the surface of a unit sphere (cf. for example Tegmark 1996). The faces of a regular icosahedron consist of 20 equilateral triangles, and it has 12 vertices. All edges are bisect, the bisected edges of one triangle are connected to form 4 new equilateral triangles, and the new vertices are projected onto the unit sphere. This first iterative step results in a grid with 42 grid-points uniformly distributed on the sphere. Further iterations result in $n_{\rm grid} = 162, 642, \ldots, 10 \cdot 4^d + 2$ grid-points, where d is the number of iteration steps. A luminosity $L_p = f\, L_\odot\, m_p \{(M/L)_\odot\}^{-1}$ is assigned to each particle in the simulation, where $L_\odot$ is the absolute luminosity of the Sun, $(M/L)_\odot$ is the assumed mass-to-light ratio in solar units, m_p is the mass of one particle in solar-masses, and the factor $f = {}^{N_t}/_{N_s}$ is the fraction of the total number of particles, N_t, to the number of particles, N_s, written to the snapshot file that is analysed. The luminosity of each particle is scaled by the distance of a particle to the observer, and then assigned to the closest grid-point on the sky. Finally the cumulative luminosities at the grid-points are divided by the area of the portion of the sky assigned to each grid-point, which is given by $a = (360 * 60 * 60'')^2/\pi/n_{\rm grid}$, where $n_{\rm grid}$ is the number of grid-points as given above. Thus a is the resolution of the projection, for example, $a \approx 4$ deg^2 for a projection grid-size of 10 242. Luminosities are finally converted to magnitudes.

5.2.2 Future advances of the models

There are certain aspects of the dark matter free satellite models that were not addressed in the analysis in Section 4.1, and some are also not or only partly addressed in other published work. One important aspect of the models is to include a realistic model of the stellar disc and the bulge of the Milky Way, which can be done with the code MAGALIE (Boily, Kroupa, & Peñarrubia-Garrido 2001). The presence of a disc component can lead to shocking, and the non-spherical gravitational potential to a precession of the orbits. Furthermore, the decay of satellite orbits might be influenced by the presence of a disc (Peñarrubia et al. 2002), and also their destruction is expected to be influenced.

Another task is to perform a more complete parameter scan for various variants, like: the mass and concentration of the initial models; orbital eccentricity; orbital inclination with respect to the disc. With our advanced program SUPERBOX++ we also seek to study the effects of mutual interactions of the satellite galaxies. How do the orbits of multiple satellite galaxies on co-rotating orbits behave? These kinds of studies require to run a large number of simulations to cover a wide parameter space, and have now become feasible: the SUPERBOX++ code is very efficient, allowing to run one such simulation within about one day with $\sim 10^6$ – 10^7 particles and grids with 128^3 cells.

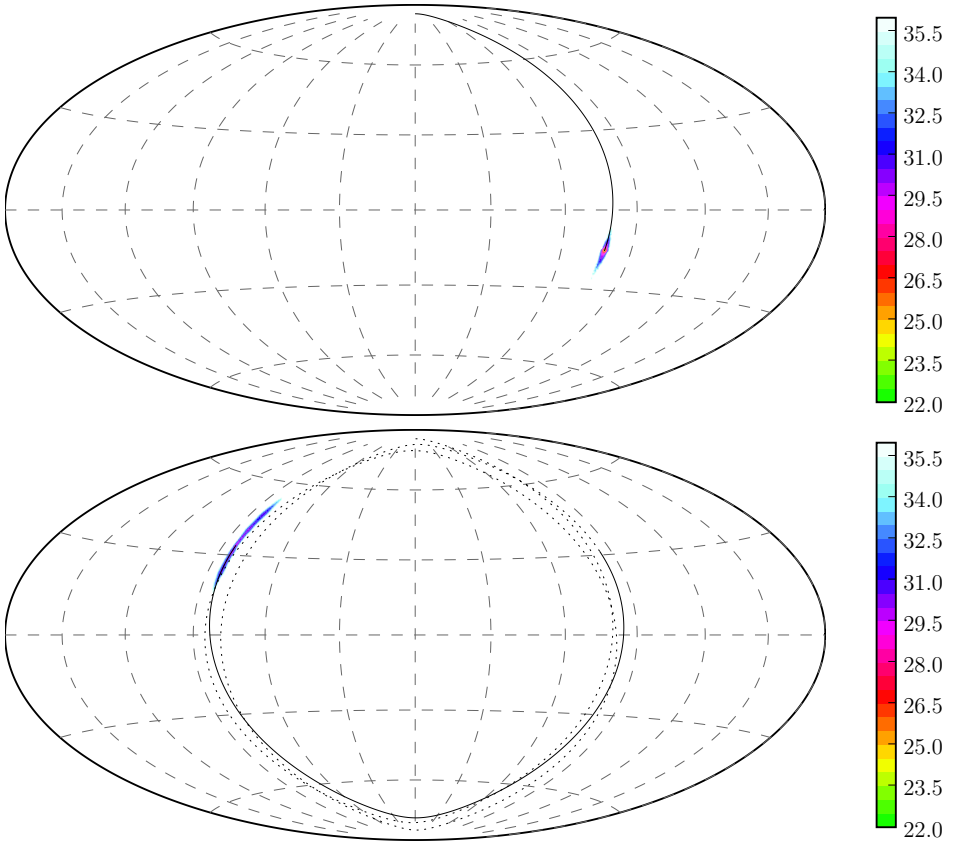

Figure 5.6: Allsky surface-brightness plot of a simulated dark matter free satellite galaxy (S1) with total mass 2.85×10^6 $M_\odot$ and an assumed mass-to-light ratio of 1, being injected into a Milky Way-like host halo. The trace of the projected orbit is plotted as black dotted line and as solid line for the last Gyr. The surface brightness in mag/arcsec^2 is colour-coded as indicated by the colour-bar, the resolution of the projection is 0.25 deg^2. The satellite is shown after 500 Myr of evolution in the top panel. At that point the satellite is at a galactocentric distance of $\approx$ 43 kpc, shortly before its first peri-galactic passage. After 4.4 Gyr of evolution and four peri-galactic passages (lower panel), the satellite is close to its apo-centre at a galacto-centric distance of $\approx$ 99 kpc. The satellite is now strongly distorted and elongated along its orbital path. This initially low-mass satellite galaxy is hardly detectable any more for an observer located on Earth.

Chapter 6

Concluding discussion, remarks & an outlook

"But if history teaches us anything it is that the next important clues will come from a surprising direction. Some observation or calculation will be made that will reorient our inquiries and, if this happens as has happened so often in the past, we will realize that the important evidence has been sitting unnoticed under our noses for decades."

Ostriker & Steinhardt (2003) in a Science review article "New Light on Dark Matter".

6.1 The Local Group satellite galaxies

We have to distinguish two types of satellite galaxies of the Milky Way: first the "classical" ones, the eleven brightest satellite galaxies of the Milky Way within its virial radius of $\sim$ 250 kpc. They can be considered as a complete census of dwarf galaxies brighter than about $L_V = 2.5 \times 10^5$ $L_\odot$ (Mateo 1998, but see below). These galaxies consist of two irregular galaxies, the Magellanic clouds, and nine dwarf spheroidals. Their properties are being studied since the middle of the last century (for example Shapley 1938; Wilson 1955; Baade 1956), and their structural parameters are now fairly well constrained (Irwin & Hatzidimitriou 1995; Mateo 1998; van den Bergh 1999; van der Marel et al. 2002). In recent years, data sets of radial velocities of hundreds of individual stars became available (Koch et al. 2007a,b; Muñoz et al. 2005, 2006b; Sohn et al. 2007; Tolstoy et al. 2004; Walker et al. 2006a,b; Westfall et al. 2006; Wilkinson et al. 2004), that allow to more accurately fit models (King models are commonly used; King 1962; Hodge 1971) to the data and derive, for example, the mass-to-light ratio of the nearby dSph galaxies (see Gilmore et al. 2007, and references therein) under the assumption that they are in virial equilibrium. This model fitting led to the conclusion that the dSphs must be some of the most dark matter dominated objects in the Universe (Figure 6.1). It is this sample of dwarf galaxies (plus the other long known Local Group members; Mateo 1998; van den Bergh 1999) that is mostly used when CDM simulations are compared to observational data (e.g. Benson et al. 2002; Kang et al. 2005; Libeskind et al. 2005, 2007; Read et al. 2006a; Zentner et al. 2005).

The second class are the satellite galaxies that were discovered over the last few years

with help of the SDSS catalogue data. They are very faint and extended, having low surface-brightnesses (Willman et al. 2005b; Sakamoto & Hasegawa 2006; Zucker et al. 2006a,b; Belokurov et al. 2006, 2007; Walsh et al. 2007a)[(a)]. It was only possible to discover these "fluffy" systems by systematically applying data-mining algorithms to the catalogue data, scanning the parameter space for inconspicuous stellar overdensities. Even though discovered in the database, it is hardly possible to determine their properties like absolute luminosity, radius, or distance accurately from the SDSS data alone, but follow-up observations are needed (see for example Zucker et al. 2006a; Walsh et al. 2007b)[(b)]. Even then, the parameters are sometimes only poorly constrained, as the discussion by Muñoz et al. (2006a) about the Boötes dSph indicates. For another companion discovered in the Boötes constellation, Boo II, there is also some debate whether it is a galaxy or rather a globular cluster, probably belonging to the Sagittarius tidal stream (Lee et al. 2007; Walsh et al. 2007b). The latter issue, the question whether a discovered stellar overdensity is to be classified as a globular cluster, possibly in a late disrupting stage, or as a dwarf galaxy is of importance for other objects as well, Willman 1, Seque 1, or Coma Berenices (Willman et al. 2005b; van den Bergh 2006; Belokurov et al. 2007; Gilmore et al. 2007; Siegel et al. 2008), and an active matter of discussion and research.

Regarding the three dimensional space coverage, Andromeda is a better probe since its halo is, compared to the Milky Way, not that much affected by obscuration, either by its own disc or the stellar disc of the Milky Way (McConnachie & Irwin 2006a). As for the Milky Way, new companions of Andromeda were discovered in the past few years (Martin et al. 2006; Zucker et al. 2007; Majewski et al. 2007; Ibata et al. 2007; Irwin et al. 2008). Thus only the faint end of the M31 satellite galaxy luminosity function remains to be explored. One major difficulty is the determination of the three-dimensional location of the satellite galaxies with respect to Andromeda. At a distance of ~ 800 kpc, the distance measurement uncertainties are of the order of 20 – 30 kpc, i.e. the relative differences to Andromeda are determinable with about 30 – 40 kpc accuracy only, one order of magnitude worse than for the Milky Way satellites. Using different distance data-sets can lead to different results, as we have seen in Section 2.3, even though each data-set individually can be considered as being internally consistent. The second difficulty is to determine proper motions of Andromeda and its satellites directly, which was up to now only possible for two galaxies, M33 and IC 10 (Brunthaler et al. 2005, 2007). The transverse velocity of M31 has only been estimated based on very different arguments, like assumptions about the motion of the MW and M31 with respect to the barycentre of the Local Group (Einasto & Lynden-Bell 1982), the survival of the stellar disc of M33 (Loeb et al. 2005), or the statistical average of the motion of Andromeda's satellite galaxies (van der Marel & Guhathakurta 2007). Finally it is more difficult to determine the structural parameters of the Andromeda satellite galaxies.

We point out that the completeness-bias is a two-fold problem: First, there are regions in the sky, those very close to the plane of the Milky Way, $|b| \lesssim 5^\circ$, especially in the direction of the Galactic Centre, where further galaxies might be hidden by the Galactic disc and the

[(a)] The discovery of the CVn II dSph was reported twice, first by Sakamoto & Hasegawa in the issue 653 of ApJ as a letter, and in the subsequent issue of ApJ by Belokurov et al.

[(b)] We knew about the discovery of the Boötes II stellar overdensity before publication, and intended to contribute photometric follow-up observational data derived with the 1m telescope at the Hoher List observatory. Unfortunately, the weather conditions did not allow us to obtain any data.

bulge as we discussed in Section 2.5.1. This does, however, not only affect the Milky Way, but the Local Group as a total. Loeb & Narayan (2007), for example, hypothesised that there might be a galaxy comparable in mass to Andromeda hidden behind the Galactic bulge at a distance of ~ 1 Mpc. This would also mean that almost all its satellites within the virial radius were likely undetectable, since a virial radius of 250 kpc at that distance transforms into an angular radius of 14° on the sky. But it might be possible to more easily detect companions at farther distances. The second bias concerns the sky coverage region of the SDSS that is shown in Figure 2.3. This region was chosen to primarily cover a northern Galactic cap with Galactic latitude $b > 30°$. Consequently, we miss the opportunity to detect galaxies at lower Galactic latitudes – despite possible detection problems due to crowding effects – just due to this sky coverage bias. The Apache Point Observatory, where the SDSS telescopes are located, is on the northern hemisphere of the Earth. A similar search campaign is planed for the southern hemisphere, using the new ANU SkyMapper telescope (Schmidt et al. 2005) located at Siding Spring, Australia: the Stromlo Missing Satellite Survey (Jerjen et al., in preparation). Unlike the SDSS, this survey is planed to cover the whole observable sky, and is expected to obtain about 1 mag deeper photometric data than the SDSS. Most likely, about the same number of dwarf galaxies or more will be discovered by this survey, possibly also at latitudes close to the Galactic equator.

6.2 Dwarf satellites: are they CDM subhaloes?

The "standard" picture

As aforementioned, the dwarf satellite galaxies are mostly believed to be the dark matter dominated building blocks of early structure formation processes in the Universe, that survived until the present as separate entities, not yet merged to form larger galaxies (White & Rees 1978). There are many findings that are interpreted as supporting this notion (see Introduction). The well observed dSph satellite galaxies of the Milky Way seem to be the most dark matter dominated objects we know off in the Universe (Aaronson 1983; Wilkinson et al. 2002; Kleyna et al. 2003; Gilmore et al. 2007). The large velocity dispersion of $\sim 10\ \mathrm{km\,s^{-1}}$ found in all dSph satellites is interpreted as a signature of a large mass-to-light ratio (Figs. 4.4 & 6.1). This result relies on solving the Jeans equation under the *explicit* assumption that the galaxies are in virial equilibrium (but see also Klimentowski et al. 2007; Muñoz et al. 2007). A large M/L ratio implies that most of the mass of the galaxies is in invisible matter, i.e. cold dark matter is the matter of choice. Interestingly, the dSphs are total outliers when one compares their mass-to-light ratios derived from the virial theorem with those of other spheroidal stellar systems like globular clusters, galactic bulges, or elliptical galaxies (Figure 6.1).

The "missing satellite problem", that was pointed out a few years ago (Klypin et al. 1999; Moore et al. 1999), is today usually solved by invoking small scale, subgrid baryonic processes[(c)] (Kazantzidis et al. 2004a, and references therein) that suppress star formation

[(c)] Physical effects, happening on scales much smaller than the resolution of a simulation. They have to be approximated by making assumptions about their average influence over a large volume. One example are semi-analytic galaxy formation models: star formation, gas-heating and -cooling are averaged over a large

in low mass haloes. Within the CDM paradigm, the suppression of star formation is usually empirically explained, either by supernova feedback processes that heat the halo gas (Kauffmann et al. 1993), or the epoch of reionization after the Big Bang, which inhibits the formation of small satellites not already seeded (Benson et al. 2002; Kravtsov et al. 2004; Moore et al. 2006). But the central density profiles of the CDM substructure remain cuspy, despite tidal heating and destruction of the haloes (Kazantzidis et al. 2004b; Diemand et al. 2005b). Even extreme baryon removal cannot evolve a cusp into a core (Gnedin & Zhao 2002). Nevertheless, a lot of effort has recently been made to push the limits of CDM simulations, at least locally, to make predictions of luminous CDM sub-structures within Milky Way sized host haloes (e.g. Libeskind et al. 2005, 2007). Performing hierarchical structure-formation simulations and combining them with algorithms describing dark matter – luminous matter biases, like semi-analytic galaxy formation models (e.g. Kauffmann et al. 1993; Cole et al. 2000), dark matter subhaloes are generated that appear to resemble the dSph satellite galaxies of the Milky Way[(d)]. One common ansatz is to perform a two-stepped simulation: first a low resolution simulation of the growth of large scale structures is performed, and then, in the second step, regions of particular interest are re-simulated with a larger number of particles, i.e. with a higher resolution (Frenk et al. 1996). But even the highest resolution simulations are barely able to account for dwarf galaxies. Libeskind et al. (2007), for example, ran an N-body/SPH simulation with a mass resolution of $\sim 2.6 \times 10^6$ $M_\odot$ and $\sim 1.7 \times 10^7$ $M_\odot$ for gas and dark matter particles, respectively. In a very high resolution simulation, Diemand et al. (2005b) achieved a mass resolution of down to 3×10^5 $M_\odot$ in dark matter, only. So, even in these "high resolution" simulations, one particle is as massive as a typical dSph galaxy. It has also to be kept in mind, that a "particle" in such a simulation is only a proxy – a test particle in phase-space, discrete in mass, space, and in its motion. The high-resolution simulations are still several orders of magnitude away from resolving individual gas- and molecular-clouds, or star clusters.

Another complicating factor is that in the literature different studies use different criteria in the pairing of subhaloes with satellite galaxies, depending on which criteria are chosen to match with. Stoehr et al. (2002) found an "excellent agreement" of the Milky Way satellite galaxies with the most massive subhaloes, whereas Libeskind et al. (2005) argued that the dSph satellites reside in the most massive progenitors of luminous subhaloes, and Strigari et al. (2007) found alternatively also an agreement with the earliest forming haloes. In contrast, Sales et al. (2007b) argued for low mass systems that were accreted very recently, and Li & Helmi (2008) connected the satellite galaxies to haloes that were grouped before accretion (see also Lake & D'Onghia 2008). Not all of these possibilities mutually exclude each other, but it appears to be very controversial within the CDM community which are the main characteristics that make dark matter subhaloes luminous.

The host dark matter halo of the Milky Way as a whole is also not well constrained yet. In recent cosmological simulations, Milky Way sized dark haloes are found to be triaxial, typically more prolate than oblate (e.g. Bullock 2002; Jing & Suto 2002; Diemand et al.

volume and described by analytic functions, whose free parameters are tuned to match with observations. The astrophysical processes generating the feedback are neither well understood nor constrained on these scales.

[(d)] As an aside, we note that in current numerical cosmological simulations the formation of spiral galaxies, the most abundant class of large galaxies, is also an open problem that is not consistently solved (Mayer et al. 2008).

2005a; Libeskind et al. 2005; Zentner et al. 2005). But the findings for the shape of the Milky Way halo differ rather substantially. They span the whole range from halo models that are triaxial (Newberg & Yanny 2004), prolate (Hartwick 2000; Helmi 2004b), spherical (Ibata et al. 2001b; Fellhauer et al. 2006), or oblate (Helmi 2004a; Johnston et al. 2005), all consistent with observed data. As the situation is so ambiguous, it might probably only clear up with forthcoming data from new satellite missions like GAIA or SIM. Such data may also shed light on the question about the lumpiness of the Milky Way dark halo (Johnston et al. 2002; Majewski et al. 2005).

Problems with the "standard" picture

Based on the spatial arrangement of the Milky Way satellite galaxies, we argue that their three-dimensional distribution is incompatible with being drawn randomly from a CDM subhalo population. The 11 classical satellite galaxies are arranged in a very pronounced, thin **disc-of-satellites** (DoS), almost perfectly on a great plane that is highly inclined with respect to the stellar disc of the Milky Way, as we have shown in Section 2.2 (cf. also Kroupa et al. 2005). We have explicitly demonstrated (§2.1.2) that it is *not* a more centrally concentrated distribution of subhaloes compared to the dark matter host halo that explains the "thin" configuration of the disc-of-satellites of the Milky Way, as has been argued by Kang et al. (2005) and Zentner et al. (2005). Libeskind et al. (2005) showed that the overall distribution of dark matter subhaloes is comparable in shape to the dark matter host halo, Diemand et al. (2005a) argued that it is even more elongate, i.e. more prolate. It is this prolate distribution that is the parent distribution of the Milky Way satellite galaxies *if* they were dark matter dominated substructures. As we have shown (§2.4.1), *it can be excluded* at a 99% confidence level, that the satellite galaxies of the Milky Way are drawn randomly from a spherical or prolate parent distribution. Only if the parent distribution were oblate, $c/a \approx 0.5$, it can not be excluded that the satellite distribution is drawn randomly from the parent distribution. But such a realisation is improbable to be found in CDM simulations, and would stand in contrast to the results of Diemand et al. (2005a). In this case the stellar disc would have to be oriented perpendicularly to the host halo of the Milky Way. For most proposed solutions to the Milky Way satellite problem derived from CDM simulations, this has to be postulated as no disc-formation is included (Kang et al. 2005; Zentner et al. 2005; Libeskind et al. 2005; Li & Helmi 2008; Lake & D'Onghia 2008). Applying the bootstrapping analysis (§3.2.2) to a set of satellite galaxies in six CDM simulated Milky Way like haloes that were claimed to reproduce the DoS (Libeskind et al. 2005), *all* were found to be consistent with being randomly drawn from a spherical parent distribution, and to be incompatible with the distribution of the Milky Way satellites. The currently best solution proposed within the CDM substructure concept thus fails to account for the Milky Way dSph satellite galaxies.

Further evidence for an incompatibility of CDM substructures being the observed dSph satellites comes from our finding that indicates that the Milky Way's DoS is a rotationally supported structure (§3.2) rather than a pressure supported, flattened tri-axial spheroid as found in CDM simulations (Libeskind et al. 2007). The orbital poles derived from recent proper motion measurements of Milky Way satellite galaxies indicate a common pole of the orbits of the Large and Small Magellanic Cloud, Ursa Minor, Draco, Carina, and Fornax.

Their mean orbital pole direction is very close to the direction of the normal of the fitted disc to the classical satellites. The Milky Way pole-distance distribution (PDD, §3.2.3), which is still affected by large projected measurement uncertainties, shows an excess of small pole-distances, implying the DoS to be rotationally supported. Within the uncertainties, the two probable DoS satellites with the most deviating pole distances, Draco and Carina, are consistent with being found close to the suggested pole of the disc-of-satellites ($< \Delta_{\rm sph}$, Figure 3.2). In order to draw strong conclusions based on the PDD alone we need to await more and more-accurate proper motion measurements. For the two satellites Draco and Carina, only a single measurement is currently available and their projected uncertainties are very large. For three of the classical dSph satellite galaxies, Sextans, Leo I, and Leo II, no proper motion data are available yet.

Another fact substantiates the claim of a rotationally supported DoS: the unweighted disc-fitting algorithm (§2.1.1 & §2.2.1) is most strongly affected by the spatial location of the *outermost* satellite galaxies. We do find, however, a clear alignment of the angular momenta of the *innermost* satellite galaxies with this fitted disc, most strongly for the Magellanic clouds. The only exception is Sagittarius whose orbit might, however, already significantly deviate from its initial orbit (Zhao 1998). It would be rather curious to find a disc-like structure where only the inner satellites orbit within the disc, whereas the outer ones which mostly define the disc don't. *It is the combination of these findings, together with the results showing that evolved dark matter free galaxies resemble dSphs* (§4.1; Kroupa 1997)*, that strengthen our notion that the dSph satellite galaxies may not have originated from CDM sub-structures.*

In contrast to the Milky Way, the orbital poles of all analysed theoretical sub-structure systems (§3.2.2) indicate that they can not be rotationally supported: they are all consistent with being randomly drawn from an isotropic distribution, and instead rather show evidence of dispersing with time. This would mean that the formally derived normal of the plane is tumbling. This finding is supported by Libeskind et al. (2007), who showed that the mean angular momentum of a different set of simulated satellites, using a smooth particle hydrodynamic code, is *not* co-aligned with the minor-axis of a fitted triaxial ellipsoidal dark matter host halo. Although our sample of theoretical sub-structure systems is limited to six simulated galaxy haloes, we nevertheless have demonstrated an incompatibility between the distribution of the Milky Way satellites and a set of most recent CDM simulations, tailored specifically to solve the Milky Way satellite problem.

For the Andromeda satellite galaxies, the situation is unfortunately uncertain. There is the main difficulty that the distances to Andromeda and its satellite galaxies are only relatively poorly constrained, at least poorly for our application. Therefore we analysed in Sections 2.3 and 3.3 two distinct distance data-sets, one derived with ground based telescopes (McConnachie et al. 2005; McConnachie & Irwin 2006b) and the other a collection of various HST measurements from the literature (Koch & Grebel 2006). For both, the null-hypothesis that the satellite galaxy distribution has been drawn randomly from a spherical parent distribution can not be excluded, although the satellite distribution is highly anisotropic and disc-like (Figs. 2.10 & 2.15). Nor can we exclude the null-hypothesis for the morphological (mss8, as proposed by Koch & Grebel 2006) and the kinematical subsamples (kss8, §2.3.2) of satellite galaxies within the virial radius to be drawn randomly from a spherical parent dis-

tribution. The latter result is important as this conflicts with the high statistical significance claimed by Koch & Grebel (2006) for the morphological subsample. Instead, we find that the mss8 subsample is likely a chance alignment in their data-set, and can not be verified using the second data-set analysed here. The kinematically motivated disc-like subsample, in contrast, is evident in both data-sets, and this disc has virtually the same orientation as the disc derived for the whole M31 satellite sample. It is also excluded that M33 can orbit within the disc of the mss8 subsample, while being located very close to it. This follows from the incompatibility of the RPPs (§3.3.1) of And V and And VI on the one hand, and the measured proper motion of M33 on the other hand. It is noteworthy that all newly reported dSphs are found close to the disc of the kss8 subsample, but mostly far off the disc of the mss8 subsample (see below).

The kinematically motivated subsample of satellite galaxies is substantiated by the "restricted polar path" method introduced in Section 3.3.1. To our knowledge, this is the first direct method to confine the possible orbits of Andromeda satellite galaxies (except from direct measurements, of course) and it arises from simple geometrical considerations. The method is extendable in that a different halo model can be adopted, for example the one derived for Andromeda by Seigar et al. (2006). The halo model assumed in Section 3.3.1, an isothermal halo with a circular velocity of 250 $\mathrm{km\,s^{-1}}$, is a very conservative assumption. The escape velocity at the approximate virial radius of Andromeda is $v_e \approx 350\ \mathrm{km\,s^{-1}}$ for that halo model, whereas the escape velocity derived from the mass model of Seigar et al. (2006) is less than 200 $\mathrm{km\,s^{-1}}$ (see Majewski et al. 2007, their figure 5). As we assumed that a satellite's velocity is at maximum equal to the escape velocity, and confined its orbit if its direction is fixed at that velocity only, a lower escape velocity results in more likely positive restriction criteria (Eqn. 3.15). On the other hand, we assumed a zero transverse velocity for Andromeda (Kahn & Woltjer 1959; Einasto & Lynden-Bell 1982), whereas the results of Loeb et al. (2005) and van der Marel & Guhathakurta (2007) suggest that a non-zero velocity is also possible. This result can also be included in the RPP method. The restricted polar path methods shows that the direction of the orbital pole of And VI can be restricted in both data-sets. For six of the M31 satellite galaxies the possible orbital poles can only be restricted for one of the data-sets. RPPs hint to more likely regions of the locations of angular momentum vectors on the Andromeda sky.

The current CDM simulations of Milky Way like host haloes do not resemble the Milky Way satellite galaxies, their spatial distribution and their orbital properties. It is important to test future revised CDM models and compare them to the Milky Way and Andromeda satellite systems. As this was one important concern of this work, we made the statistical tests available to the community, including our software, available at `http://www.astro.uni-bonn.de/downloads` for further applications, released under an open source licence.

The internal properties of dSph satellites as CDM subhaloes

There are other observational findings that question the approach to interpret the dSphs as ancient, dark matter dominated building blocks. Helmi et al. (2006) found a significant lack of very metal poor stars, $[\mathrm{Fe/H}] \lesssim -3$ dex, in four observed Galactic dSph satellites (Scu, Sex, For, and Car). This indicates that the gas, out of which the stars in these galaxies were

formed, had been homogeneously enriched prior to the formation of the stars. In contrast, stars in the halo of the Milky Way do show a long tail of very metal poor stars (Frebel et al. 2005; Helmi et al. 2006). The stellar population in the halo is believed to be in large parts made up of stars from the dissolved building blocks of the Galaxy. This implies that the progenitors of the Milky Way's dSphs must have been fundamentally different from the cosmological building blocks of the Galaxy. CDM subhaloes that were similar to the present-day dwarf spheroidal satellite galaxies of the Milky Way can therefore not have significantly contributed to the stellar population of the Galactic halo (Unavane et al. 1996; Shetrone et al. 2001; Venn et al. 2004; Helmi et al. 2006).

Gilmore et al. (2007) studied photometric and radial velocity data of a sample of Milky Way satellite galaxies. They interpreted the data as an indication that dark matter does not provide cusped inner mass-density profiles, but cored haloes instead, with a core scale length larger than ~ 100 pc. They suggested this to be due to a possibly different nature of the dark matter particles, such as warm dark matter particles, for example sterile neutrinos (see Biermann & Munyaneza 2007; Biermann et al. 2008), as a viable alternative.

Dwarf spheroidal galaxies – apparently simple stellar systems – seem to be more complicated than was thought. The persistence of sub-structure appears to be a relatively common feature in Milky Way (and Andromeda) dwarf spheroidal galaxies (Cioni & Habing 2005; Coleman et al. 2007; Kleyna et al. 2003; Martínez-Delgado et al. 2001; McConnachie et al. 2007a; Palma et al. 2003; Wilkinson et al. 2004, 2005). If the dark halo of a dSph had a cusped inner profile, any substructure should smear out within a few 100 Myr, whereas it has been found that substructure can persist for up to 12 Gyr in a cored halo potenial (Kleyna et al. 2003; Wilkinson et al. 2005). Recent observations also indicate that the substructure arises not solely from a projected spatial overdensity of stars. Moreover it also has a different kinematic property. Wilkinson et al. (2005) concluded that the presence of kinematical cold substructures in dSphs is consistent with the picture that the dwarf spheroidals buildup via the merging of star clusters (Fellhauer & Kroupa 2002b). Rotation curves of low surface brightness galaxies (van den Bosch et al. 2000; de Blok et al. 2001), and the survival of globular clusters (GC) bound to the Fornax dwarf galaxy (Goerdt et al. 2006; Sánchez-Salcedo et al. 2006) also indicate rather flat inner matter density profiles. The GCs belonging to Fornax, the most luminous dSph satellite of the Milky Way (Table 2.1), would have sunken to its centre and coalesced with the galaxy, if the halo of Fornax had a cusped profile.

An attempt to learn about the internal dynamical properties of the stellar and the dark matter components of dSph satellites in the context of CDM is to model one particular satellite galaxy, or general properties of satellite galaxies, by simulating individual galaxies orbiting the Milky Way (for example Fellhauer et al. 2006, 2007b, 2008; Peñarrubia et al. 2002, 2007, 2008; Read et al. 2006b), similar to the models discussed in this thesis in Sections 4.1 and 5.2. In these kinds of models, either a static or a live dark matter halo is assumed: "static" means that the gravitational potential is described by an analytic formula, that can include not only a description for the MW dark matter halo component, but also one for the baryonic disc and bulge components of the Galaxy (e.g. Johnston et al. 1999). A "live" halo model, in contrast, is build up of dark matter particles that are evolved forward in time as are the dwarf galaxy models (§5.2). The latter halo models thus can react on the motion of the satellite, and a satellite might for example suffer a deceleration

due to dynamical friction (cf. Peñarrubia et al. 2002). Both models have in common that no major mass accretion to the halo is assumed. This is a reasonable assumption for the last ~ 8 Gyr that is consistent with results from large scale simulations, where it is found that the main epoch of accretion is finished by $z = 1$ (Diemand et al. 2007)[(e)]. Furthermore, initial conditions for the satellite galaxy have to be adopted. For their dark matter halos the choice of these are motivated by the more or less scale-free behaviour found in CDM simulations (Moore et al. 1999). The subhaloes, in which the galaxies reside, are modelled like the host halo, but with a lower total mass. The mass of the subhaloes is chosen with some reasonable assumptions, but can in general span a large range of masses, varying from some $\sim 10^6$ $M_\odot$ to $\sim 10^9$ $M_\odot$ (e.g. Read et al. 2006a; Fellhauer et al. 2008; Peñarrubia et al. 2008), typically favouring larger masses to populate the high-mass end of the CDM subhalo mass range. The "tricky part" is the modelling of the stellar component within the subhalo. The main question is whether stars are initially distributed as the dark matter component or not. In recent studies often two component models were used (e.g. Read et al. 2006a; McConnachie et al. 2007b; Peñarrubia et al. 2008), that comprise an extended dark halo and a compact stellar component. These models assume that the dwarf spheroidals are in virial equilibrium, and they are explicitly set up to have a high total mass-to-light ratio. Some data suggest, that even the stellar population itself is not homogeneously distributed, but consists of distinct components with different radial density profiles, which are then also set up as distinct populations in the models (McConnachie et al. 2007a,b).

The various CDM motivated models of dSph galaxies, that depend on two assumed initial properties, the dark matter content and the properties of the stellar component, are interpreted to account for different observed properties. These simulations are used to analyse and explain a wide range of observed features in and around the satellite galaxies of the Milky Way and Andromeda, like their radial density and velocity dispersion profiles (e.g. Read et al. 2006a; McConnachie et al. 2007a; Fellhauer et al. 2008), or properties of stellar streams in the halo possibly being stripped from a satellite galaxy (e.g. Ibata & Lewis 1998; Johnston et al. 1995, 1999; Fellhauer et al. 2006, 2007b). Indirectly, these models can also be used to constrain the dark matter halo of the Milky Way. Fellhauer et al. (2006) for exampled argued, that the observed bifurcation of the Sagittarius stream can only be understood if the host dark halo is close to spherical. Very recently Binney (2008) developed an algorithm that directly allows to fit orbits of stellar streams and to constrain the gravitational potential of the Milky Way directly.

The internal properties of dSphs as dark matter free satellites

The models analysed in this thesis, as described in Section 4.1, differ substantially from those discussed above in that they do not include any dark matter component. This was, at

[(e)]Time before now or lookback time, Δt_e, is in cosmological research often expressed in terms of "redshift" z, since redshift is a direct measurable quantity. Depending on the cosmological model parameters assumed, the lookback time, and thus the time since the Big Bang, can be calculated from the redshift z. For example, for the standard model with $\Omega_m = 0.3$, $\Omega_\Lambda = 0.7$, and $h = 0.7$ we find: $z = 1 \rightarrow \Delta t_e \approx 7.7$ Gyr, $z = 2 \rightarrow \Delta t_e \approx 10.3$ Gyrs, at an age of the Universe of 13.5 Gyrs.

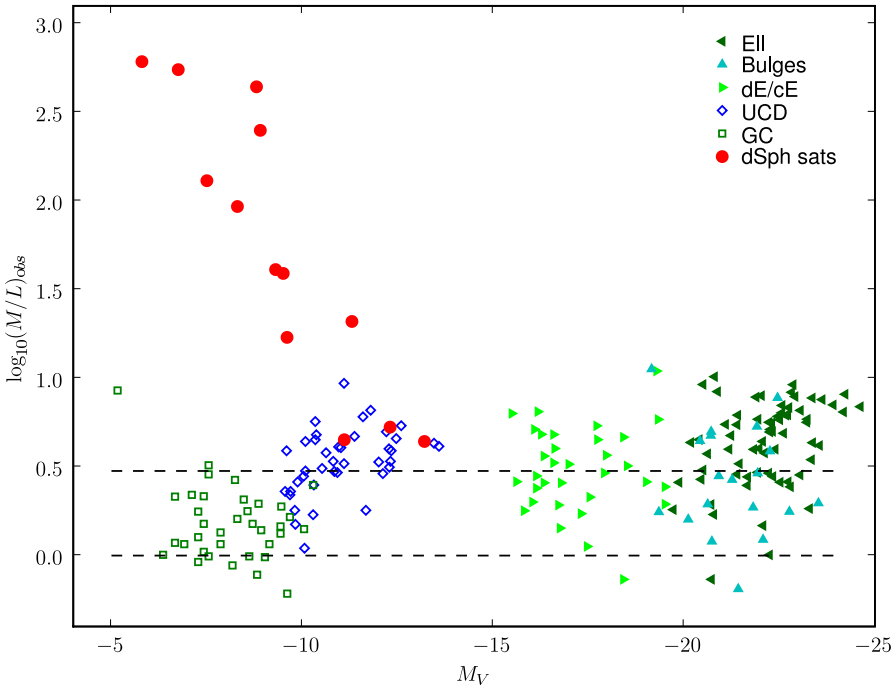

Figure 6.1: Dynamically derived mass-to-light ratio versus absolute magnitude as in Figure 4.4. Additionally to the dSph satellites of the Milky Way and Andromeda, we also plot data for globular clusters, ultra compact dwarf galaxies, dwarf and giant ellipticals, and bulges of spiral galaxies (the additional data were taken from Dabringhausen et al. 2008). The two horizontal lines indicate a constant mass-to-light ratio of 1 and 3 in Solar units, respectively. Compared to the other spheroidal stellar systems, dSph galaxies stand out with extraordinary high dynamical mass-to-light ratios. These are derived from radial velocity dispersion measurements under the assumption that the stellar systems are in virial equilibrium, an assumption that may not be valid at all for the dSph satellite galaxies as we have shown in Section 4.1. Note that *all* spheroidal, i.e. pressure supported, systems have $(M/L)_{\rm obs} \leq 10(M/L)_{\odot}$, apart from the dSph objects.

first, nothing more than an assumption that was made, without any further statement about the origin of those stellar systems (but see below). Indeed, such systems have already been studied by various authors (e.g. Kuhn & Miller 1989; Kuhn 1993; Kroupa 1997; Klessen & Kroupa 1998; Fleck & Kuhn 2003; Read et al. 2006a, whereby Kroupa saw the progenitors of today's dSph satellites as being formed in tidal tails). A key feature of these models is that the stellar systems are not "shielded" from tidal forces by a dark matter halo, such that tides become more important than for dark matter dominated satellite galaxies.

Dark matter free galaxies were placed into a Milky Way like host dark matter halo on orbits with various eccentricities (§4.1). Although their initial properties differ from those of today's dSphs, after a Hubble time they appear very similar to the dSph satellites of the Milky Way for a variety of different initial orbits. During perigalactic[(f)] passages, energy is pumped into the satellites leading to an expansion and loss of outer stars. The remaining quasi-stable remnant matches many of the observed properties, like half-light radii, abso-

[(f)] Perigalacticon: point of closest approach to the Galactic Centre.

lute luminosities, and dynamically determined mass-to-light ratios. The observed properties of individual model satellites can, though, vary substantially, depending on the phase of their orbit. In their evolved states, initially identical objects can have, for example, half-light radii of $r_{1/2} \sim 125 - 400$ pc, a range that matches the values observed for Local Group dSphs, even though their initial half-light radii were smaller than 100 pc. The tidal evolution might also be an explanation why virtually no stellar systems are found in a "gap region" between $r_{1/2} \approx 25$ pc and $r_{1/2} \approx 100$ pc as noted by some authors (Belokurov et al. 2007; Gilmore et al. 2007, see also top panel in Figure 4.3, and Figure 4.6), but this has to be studied in more detail. It is also very interesting that the dark matter free models qualitatively reproduce the trend to have higher dynamical mass-to-light ratios with lower luminosities as plotted in Figure 4.4. This trend is commonly interpreted to be a signature of an approximately universal halo mass of $\sim 10^7$ $M_\odot$ (Mateo 1998). Our models suggest that it might instead be a trend of the increasing impact of tidal heating the lower the stellar mass of a system gets.

Of course, there has been a good motivation to use the dark matter free galaxy models as analysed in Section 4.1 and for the choice of their initial properties: that is the existence of tidal dwarf galaxies. Such objects, observed to form in the local and distant Universe, are discussed in more detail in the next Section.

6.3 Dwarf satellites: are they tidal dwarf galaxies?

A fundamentally different possible origin for low mass galaxies is that they were formed as tidal dwarf galaxies (TDG, Mirabel et al. 1992) in an anti-hierarchical process already pointed out by Zwicky in the middle of the last century (Zwicky 1956, and references therein). The formation of TDGs is observed to occur in the local and very distance Universe (Schweizer 1978; Hunsberger et al. 1996; Duc & Mirabel 1998; Weilbacher et al. 2003; Walter et al. 2006; Straughn et al. 2006). Interacting gas-rich galaxies throw out long, thin tidal arms full of gaseous and stellar material expelled from the discs of the interacting galaxies (Toomre & Toomre 1972). Over-dense regions in the tidal arms fragment, become self-gravitating, and collapse. Star formation sets in in these new born tidal dwarf candidates[g] as is for example observed in the "Antennae" galaxies, NGC 4038/39 (Whitmore et al. 2005), the "Tadpole" galaxy, UGC 10214 (Jarrett et al. 2006), or the "Mice", NGC 4676 (Chien et al. 2007). From observations it is evident that even those interactions taking place in the local Universe, i.e. with a disc gas fraction similar to that of the MW or M31, can form of the order of a dozen TDGs in a single encounter (Elmegreen et al. 1993; Weilbacher et al. 2000, see also Figure 4.5). The production rate is expected to have been higher in the past given the larger gas-fraction in early galaxies (Wetzstein et al. 2007). Monreal-Ibero et al. (2007) found in a classical radius-velocity dispersion plot (Terlevich & Melnick 1981), that observed properties of young TDG candidates fall in a region of the plot that strongly suggests that they are gravitationally bound entities, and they show similarities to other dwarf galaxies. Some tidal dwarfs might become detached from their hosts, appearing as

[g]The term "tidal dwarf candidate" is often used as a precaution, as it is not always evident from single observational data that an over-density in a tidal arm will later form a separate galaxy or whether it becomes unbound and disperses, probably being captured by one of the host galaxies.

ordinary isolated dIrr or dSph galaxies (Elmegreen et al. 1993; Hunter et al. 2000). Tidal dwarf galaxies may significantly contribute to dwarf galaxy populations: Hunsberger et al. (1996) suggested that about half of the current dwarf galaxy population in compact groups could be of tidal origin, and Okazaki & Taniguchi (2000) argued that if only 1 – 2 long-lived TDGs form per wet encounter, the number of dwarf ellipticals can be explained as being tidal dwarfs under standard cosmological structure formation conditions. This number of TDGs per encounter is deduced independently by Delgado-Donate et al. (2003) from direct observations in the local Universe strengthening the case for TDGs being a major contributor to the dwarf galaxy population.

The formation of tidal dwarf galaxies is evident in simulations as well (Barnes & Hernquist 1992; Elmegreen et al. 1993; Duc et al. 2004; Bournaud & Duc 2006; Wetzstein et al. 2007). Recently, Bournaud & Duc (2006) studied the formation and survival of tidal dwarf galaxies produced in encounters of colliding galaxies with gas content typical for galaxies in the local Universe, that is a low disc gas fraction of the order of 10 per cent. In their code the gaseous component was represented by sticky particles, a scheme that is also a possible extension for our SUPERBOX++ code (§5.1.4). They found that about one quarter of their TDGs were "long-lived" objects: they still persisted when the simulations were stopped after 2 Gyr. These "long-lived" tidal dwarfs were predominately formed in the outer regions of the tidal tails (see also Duc et al. 2004), whereas TDGs formed in the inner regions, close to the hosts, fall back and, according to their understanding, merge again with the host galaxies on short time-scales. Wetzstein et al. (2007) used an N-Body/SPH code and showed that tidal dwarfs are dominated by gas; dissipational hydrodynamics is crucial for their formation: about 70 per cent of the mass of a TDG is in gas, whereas they are free of non-baryonic dark matter. More TDGs were formed in models with a larger gas fraction of 30 per cent, indicating that the number of TDGs produced per encounter in the early Universe must have been higher than is observed in the local Universe. To our knowledge, the production of tidal dwarf galaxies has been studied in computer simulations for parabolic orbits only, where the two progenitors merge within a short timescale, but not for hyperbolic orbits which do not lead to a merger. The numbers, masses, kinematics, and other properties of TDGs might differ for hyperbolic interactions, which certainly take place in nature.

The current computer models (Bournaud & Duc 2006; Wetzstein et al. 2007) only cover the upper end of the possible mass range of stellar systems formed in the tails, $\gtrsim 10^8$ $M_\odot$. Many more low-mass objects are expected to be produced, as is evident from observations (Whitmore et al. 2005), that are not resolved in current simulations. It is important to study also their evolution and fate. They may evolve into spheroidal dwarf galaxies via the merging of star-cluster complexes (Kroupa 1998; Fellhauer & Kroupa 2002a), a process that occurs on a relatively short timescale of a few tens to a hundred Myr. Such objects are also known to survive explosive residual-gas removals (Fellhauer & Kroupa 2005).

Notably, an additional anti-hierarchical formation mode for dwarf galaxies has been proposed recently: Kronberger et al. (2008) simulated the effects of the motion of a spiral galaxy through a constant temperature and pressure gas that is similar to the intercluster medium. They found that DM free galaxies can also form from the material stripped off the galaxy due to ram pressure – they termed them "stripped baryonic dwarf" galaxies.

The chemical evolution of young tidal dwarf galaxies has been theoretically studied by Recchi et al. (2007), suggesting that long lasting star-formation episodes, which have been deduced for the Milky Way satellites (Grebel 2001), can be understood in dark matter free galaxies. A small galaxy can be relatively stable against the feedback of ongoing star formation (Hensler et al. 2004), and Recchi et al. (2007) conclude that gas dynamics in the centre of a dwarf galaxy is more strongly influenced by the gas-density and its distribution than by the depth of the potential well. Once gas is removed from the galaxy centre, it can later be re-accreted, replenishing the gas reservoir for further star formation epochs (cf. Recchi & Hensler 2006). Work has been started to study the chemical evolution of young TDGs in more detail (Recchi et al. 2007; Marcolini et al., in preparation). Once TDGs have formed, their chemical evolution is decoupled from each other, which can lead to very different individual chemical evolutions (Calura et al. 2008), also depending on their orbits about the host galaxy.

Tidal dwarfs as progenitors of the Milky Way dSph companions

All simulations of tidal dwarf formation predict a low true mass-to-light ratio[(h)], which is also evident from observations (Walter et al. 2006). But the observational data for Milky Way dSph satellites indicate them to be dark matter dominated objects, having large M/L ratios. The dark matter free models (§4.1), however, clearly show that an apparently high M/L ratio can be caused by tidal physics. In conclusion, this means that, when deriving the dynamical mass-to-light ratio from radial velocity dispersion measurements, *the assumption made that the dwarf spheroidal satellites are in virial equilibrium, is not valid*. Instead, the dSphs may be significantly perturbed. Extratidal features, that are expected to be present if a satellite galaxy is indeed affected by tides, are observed for many satellites, for example also for the remote satellite Leo I at a galactocentric distance of 254 kpc (Sohn et al. 2007), though not for all. While the tidal stream of Sagittarius is very prominent (Ibata et al. 2001a; Majewski et al. 2003), these features are likely overlooked for the distant satellite galaxies, as the stream would contain only very few bright stars that are easily observable (Muñoz et al. 2007), and the surface-brightness of the stream is very low (see also Fig. 4.1 and §5.2).

If an interaction of a gas-rich galaxy with the proto-Milky Way took place in the early Universe, a large number of tidal dwarfs would have likely been produced, being naturally arranged in a disc-like structure: due to the conservation of angular momentum, their orbital poles are determined by the plane of the interaction. Lynden-Bell (1983) already suggested that Milky Way satellite galaxies might be tidally torn-off a common progenitor galaxy. If the orientation of this plane is persistent, which is expected for an almost spherical halo, the satellite galaxies we see today are naturally found in a disc-of-satellites. Only if satellite galaxies are strongly influenced by the non-spherical gravitational potential of the Milky Way's disc, or scatter with another dwarf galaxy, their orbital planes may significantly change (Zhao 1998; Peñarrubia et al. 2002; Sales et al. 2007a). It has, for example, been proposed that Sagittarius was deflected by the Magellanic Clouds (Zhao 1998) into its current orbit which is not within the DoS.

[(h)]The "true mass-to-light ratio" is the ratio that is derived when summing up all the physical masses of the luminous and non-luminous baryonic, and the non-baryonic matter, and setting it in relation to the total luminosity in the visual V-band. This is typically expressed in units of the solar mass-to-light ratio, $(M/L)_{\odot}$.

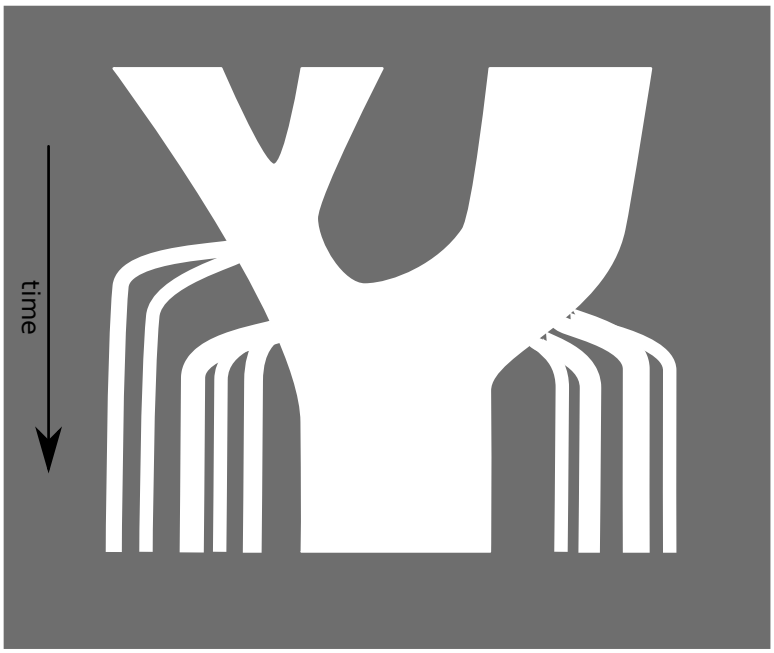

Figure 6.2: The "baryonic mangrove tree". Time increases from top to bottom. As gas-rich structures – the galaxies – merge, they form more massive galaxies, but contemporary with the merging, new sub-structures – tidal dwarf galaxies – are build that survive until the present. Compare this drawing to the merger tree allegory, Figure 1.1, for a dark matter model.

As we have shown, the spatial distribution of the Milky Way satellites is incompatible with being randomly drawn from a spherical or prolate parent distribution (§2.4). Instead, the disc-of-satellites appears to be a rotationally supported structure (§3.2), though the proper motion measurement uncertainties are still large. This is not only consistent with the hypothesis that the dwarf spheroidals were formed as tidal dwarf galaxies, it is a natural outcome. For the Andromeda galaxy, its DoS is not statistically significant, but the satellite galaxies are nevertheless anisotropically distributed (Figs. 2.10 & 2.11). When adding the dSph galaxies discovered during the last three years to surround the MW and M31, we find that they *all* lie close to both discs-of-satellites. This is very remarkable and not expected if they were isotropically distributed. Despite some bias due to the sky coverage region of the SDSS (Figs. 2.3 & 2.7), there are large portions of the sky within the virial radius that are off the DoS, where no satellite galaxies are reported. The same is the case for the Andromeda system, only marginally influenced by obscuration (McConnachie & Irwin 2006b): no satellite galaxies are reported that are far off the DoS. Majewski et al. (2007) noted that along a radial vector from the centre of M31, connecting NGC 147 and And XIV, in total six satellite galaxies are located in projection, and Irwin et al. (2008) found that And XVII is also on that line. We demonstrated that the new dSphs lie on a straight line not only in projection, but taking their full three-dimensional data into account, we find that they belong to the same disc-of-satellite as previously proposed. This holds true despite large distance uncertainties.

If the Milky Way's dwarf spheroidal satellite galaxies are of tidal origin formed in an

interaction in the early Universe, they would share many properties with dark matter dominated cosmological building blocks that need careful inspection to unambiguously distinguish the two scenarios: evolved TDGs would contain old stars (Elmegreen et al. 1993; Wetzstein et al. 2007), may have had long lasting star formation epochs (Hunter et al. 2000; Recchi et al. 2007) probably being replenished by previously expelled gas (Recchi & Hensler 2006), and appear very similar as today's dSph satellite galaxies (Kroupa 1997 and this thesis, Chapter 4). Looking for strong correlations of satellite orbits (Lynden-Bell 1976, 1983; Palma et al. 2002) is an entirely independent line-of-evidence for tidal dwarfs as discussed in Chapters 2 and 3.

One observation that would exclude a satellite galaxy to be of tidal origin would be a direct detection of dark matter in the galaxy. In theoretical particle physics there exists a rich zoo of more or less good candidates for non-baryonic dark matter particles (Bertone et al. 2005), for example neutralinos or WIMPs, and these particles are expected to produce a significant flux in γ-rays due to their decay. While a non-detection is of course no proof for non-existence (it is dependent on the sensitivity of the detectors), until now there is no detection of a high energy γ-ray signal in dwarf galaxies that are thought to be the most dark matter dominated objects, for example in the direction of the Sagittarius dwarf galaxy (Aharonian et al. 2008). So a direct proof for the existence of dark matter particles has to be awaiting.

6.4 A concluding remark

The theory that satellite galaxies are evolved tidal dwarfs is an *alternative* to the hypothesis that they are dark matter dominated dwarf galaxies. Notably, the tidal dwarf theory works *within* the standard cosmological framework.

But – the theory that the satellite galaxies are of tidal origin resulting from an interaction of gas rich galaxies in the early Universe is the *only one* that accounts for the vast majority of satellite galaxy features discussed here self-consistently. The tidal dwarfs would be arranged in the plane of the interaction (§2), and the resulting disc-of-satellites would be a rotationally supported structure (§3). They would contain an ancient stellar population and appear pre-enriched with stellar populations that need not reflect the metallicities of halo population II stars. And they can have long lasting star-formation episodes. The internal dynamics of satellite galaxies are strongly influenced by the tidal interaction with the host galaxy leading to an increased velocity dispersion that can be explained by dark matter free dwarf galaxy models that account for other properties as well, as discussed in Chapter 4.

In accordance with the dark matter merger tree, as shown in the Introduction, if we seek to illustrate the idea that satellite galaxies are born as tidal dwarf galaxies a "baryonic mangrove tree", as shown in Figure 6.2, appears to be a good allegory. Large gas-rich galaxies merge to form more massive ones – and at the same time a number of tidal dwarfs are spawned some of which may remain in the vicinity of their hosts as satellite galaxies.

6.5 Dwarf satellites: how about MOND?

One aspect of the TDG-origin theory for dSph satellites is that while most of their observable features can be accounted for, as shown above, the observed velocity dispersions are remarkably similar, $\sigma_v \sim 10$ km s^{-1}. The dark matter free galaxy models (§4) lead to dSph-like solutions with a larger scatter, $2 \lesssim \sigma_v \lesssim 25$ kms, although this requires further numerical affirmation. This possible discrepancy, which is the only one emerging in the TDG theory, may hint at the possibility that gravitation is non-Newtonian. It is therefore interesting to reconsider the satellite galaxies and the tidal dwarf scenario in the context of Modified Newtonian Gravity (MOND, Milgrom 1983). According to this theory, Newton's law of gravity is only valid in the case of a strong acceleration, as is the case on Earth or in the Solar system, but has to be modified in the case of a weak gravitational field. In MOND this is written as

$$\boldsymbol{g}_{\rm N} = \mu\left(\frac{a}{a_0}\right)\boldsymbol{a} \quad , \tag{6.1}$$

where $\boldsymbol{g}_{\rm N}$ is the Newtonian gravitational acceleration, $\boldsymbol{a}$ is the modified, true acceleration acting on a test particle, and $\mu(x)$ is an interpolation function. $a_0 \sim 1.2 \times 10^{-10}$ km s^{-1} is the critical acceleration of MOND, the value at which the transition from the Newtonian to the MONDian regime of the gravitational law takes place. $\mu(x)$ is a smooth function that has to fulfil the following limiting conditions:

$$\mu(x) \approx \left\{ \begin{array}{lcl} 1 & : & x \gg 1 \\ x & : & x \ll 1 \end{array} \right. \quad , \tag{6.2}$$

but can otherwise be arbitrarily chosen, e.g. one can adopt $\mu(x) = x/\sqrt{1+x^2}$ as proposed by Bekenstein & Milgrom (1984). In recent years, more studies considered MOND as a serious alternative to the dark matter hypothesis, in particular after a relativistic formulation of MOND was introduced (TeVeS, Bekenstein 2004). Only with the relativistic theory it is possible to understand the bending of light as observed by gravitational lensing.

MOND has been originally introduced to fit the rotation curves of spiral galaxies without invoking any kind of non-baryonic dark matter, and has been shown to be applicable from dwarf galaxy to galaxy cluster size scales (Sanders & McGaugh 2002). It has to be mentioned that there are observations that are interpreted to contradict MOND, as they indicate direct evidence for the existence of invisible mass. One of the most famous recent examples of such an observation is the galaxy cluster 1E 0657-56, the "bullet cluster" (Markevitch et al. 2006; Clowe et al. 2006, 2007). This cluster is an interacting system of two galaxy clusters that seem to have passed through each other. X-ray observations of the intracluster gas indicate a very high shock velocity of $\sim 4\,700$ km s^{-1}. The gas is seen as bow-shock fronts, but the bow-shocks lag behind the centres-of-mass as determined by gravitational lensing measurements. The mass distribution is interpreted as the distribution of the dissipationless dark matter haloes, and many groups modelled and interpreted this system in the context of cold dark matter (Clowe et al. 2006; Mastropietro & Burkert 2007; Milosavljević et al. 2007; Springel & Farrar 2007; Nusser 2008). On the other hand, there are claims that this cluster can not be fully understood in CDM, MOND not being ruled out (Zhao 2007; Angus & McGaugh 2008).

Tidal dwarf galaxies have also been recently addressed with the MOND theory. Bournaud et al. (2007) studied rotation curves of three TDGs around NGC 5291, and found that a large amount of unseen material must be present in these galaxies, about a factor of two more massive than the visible matter. They concluded that within the standard CDM theory this undetected mass is most likely cold, molecular gas – baryonic dark matter. Soon after, Milgrom (2007) and Gentile et al. (2007) showed that the observed rotation curves can be naturally explained without any free parameters within the MOND framework. The MOND theory also accounts for the observed velocity dispersion seen among Milky Way dSphs (Łokas 2001), whereby tidal and projection effects would play an important role just as in Newtonian dynamics (§4.1). On the other hand, in MOND the in-spiralling time-scales of globular clusters in dSph galaxies get shorter (Ciotti & Binney 2004; Nipoti et al. 2008), posing a challenge to explain the persistence of GCs in Fornax (Sánchez-Salcedo et al. 2006) but this persistence is also a problem for CDM.

One way to study dynamics of stellar systems in MOND is to perform N-body computations, as done in Newtonian dynamics. The main difficulty is that MOND is a non-linear theory. Poisson's equation in MOND,

$$\nabla \left\{ \mu \left(\frac{|\nabla \phi|}{a_0} \right) \nabla \phi \right\} = 4\pi G \rho \quad , \tag{6.3}$$

has to be numerically solved at each time-step of a simulation. There are currently two software codes developed we know off that solve Equation (6.3) numerically (Nipoti et al. 2007; Tiret & Combes 2007). We are elaborating the possibility to modify the SUPERBOX++ code (§5.1) to also solve Poissons equation in the MOND theory. If this is feasible, it will easily be possible to calculate models of dwarf galaxies as done in Section 5.2 within the MOND framework, and to compare the data with the results derived under the assumption of Newtonian gravity plus dark matter, and with the observations.

It is noteworthy that as long as the *internal* acceleration of a satellite galaxy is in the Newtonian regime, i.e. the internal acceleration is significantly larger than a_0, the results derived for the models analysed in Section 4.1 would not change. Only if the internal acceleration drops below a_0 due to the continuous mass-loss, would the modification of the gravitational law come into play. It is hard to forecast the consequences in detail, but the main effect would be that the galaxies start to appear as if they were dark matter dominated. This is expected to only affect the late stage of the models, when the satellite is almost disrupted and has lost almost all of its mass. The consequence would be that the satellites are more strongly bound during the late stage than the current Newtonian models suggest. This does not necessarily mean that the velocity dispersion drops significantly, but rather that the escape velocity from the galaxy gets larger. Moreover, if MOND is indeed correct *and* no non-baryonic dark matter exists, there would be no difference between a cosmological building block and a tidal dwarf galaxy in terms of non-baryonic dark matter content – there is none. Gravitationally, both types of galaxies would behave in an equal manner. There might be, however, a difference in initial properties like chemical abundance of gaseous material, radial extent, and initial mass density profiles.

6.6 Outlook

The next years will be exciting: new satellite galaxies of the Milky Way and Andromeda are expected to be discovered by upcoming search campaigns. If the new faint satellite galaxies turn out to be isotropically distributed we would be left with the uncomfortable fact that the most luminous satellite galaxies are concentrated towards the disc-of-satellites, whereas the rest would be isotropically distributed. A biasing with luminosity towards the DoS would then have to be explained, as it is not predicted by current standard models. If they turn out to be located within the disc-of-satellites, this would substantiate the suggested strong correlation of the satellite galaxies, and it would become more challenging to explain them as luminous, dark matter dominated sub-structures.

The other main step forward will be when new proper motion measurements become available. Some measurements have already been started to derive proper motions for dSphs satellites of the Milky Way with the Hubble Space Telescope, but the main improvement will take place with more accurate measurements from forthcoming space missions, such as NASA's SIM mission and the ESA mission Gaia, dedicated to measure accurate positions and proper motions of stars. These proper motions will allow to better constrain or exclude the proposed possible common motion of the dSphs within the disc-of-satellites of the Milky Way.

From the theoretical side it is very important to study the dSphs in more detail: models of dark matter free satellite galaxies, motivated by the tidal dwarf theory, are an important part of the puzzle concerning the origin of dSph satellite galaxies. Tidal dwarf galaxies are observed to form in galaxy encounters, and thus must be an inherent part of any cosmological model. But current large-scale hierarchical structure formation simulations do not account for tidal dwarf galaxies. Computer models that are used to study the formation of tidal dwarfs do not account for their long-term evolution and only cover the upper end of the possible mass-range of bound stellar systems. Detailed chemo-dynamical models are way to complex to be included in full scale simulations, thus being currently limited to single dwarf galaxy models. And detailed star-formation models are basically limited to single star-formation regions.

Computer models as described in this thesis can be run for a large range of parameters with our Superbox^{++} code, to fill the gap between the very large-scale structure formation and the very small-scale star-formation simulations. As in the last years deep photometric data and radial velocity measurements for hundreds of stars became available, it is now possible to compare the models with observations in more detail. This allows to better constrain the possible parameter space of dark matter free satellites. But it is also important to distinguish between "what is theoretically observable" in the models and "what is really observable" in nature. Here the automated analysis software – the virtual observer – has to be advanced, for example by including models of foreground contamination due to the Galaxy.

Chapter 7

Summary

This thesis presents a detailed study of the phase-space distribution of dwarf satellite galaxies in the Local Group, belonging to the two large spiral galaxies, the Milky Way and Andromeda, within the framework of hierarchical structure formation, and a critical test of the most recent CDM solutions. A theoretical model of dark matter free dSph satellites is presented, and a code, SUPERBOX++, is developed for future dynamical studies of the Local Group satellite galaxies.

In **Chapter 2**, a statistical method is presented that can be used to test the robustness of a plane-fit to the distribution of satellite galaxies. This method is based on the bootstrapping technique and statistical methods for the analysis of spherical data. We show that a central concentration of satellite galaxies that mimics a "thin" distribution can not explain the apparent presence of a **disc-of-satellites** (DoS) of the Milky Way. This DoS is highly inclined with respect to the stellar disc of the Milky Way. We find that it can be excluded with high significance that the three-dimensional distribution of the satellite galaxies is drawn randomly from a spherical or prolate parent distribution as found in CDM structure formation simulations. The Milky Way disc-of-satellites is not found to be related to the Andromeda system, or the intermediate scale structure, the supergalactic plane, contradicting the notion that the DoS was build up by the individual accretion of galaxies preferentially from the direction of the supergalactic plane.

The satellite galaxies of M31, the Andromeda galaxy, are also addressed. Therefore, first a coordinate system centred and co-aligned with the stellar disc of Andromeda is defined in the most general way. The Andromeda system is much more affected by the distance measurement uncertainties to the galaxies. To reduce possible biasses, two independent distance data-sets are analysed. It is found that the satellite galaxies are anisotropically distributed as well, also arranged in a disc-of-satellites. Two subsamples of satellite galaxies are analysed: one as previously proposed that was based on a morphological selection criterion, and one as proposed in this thesis, based on a kinematic selection criterion. Using a Monte Carlo method we show that the plane-like appearance of the morphologically motived subsample is most likely a chance alignment in one of the data-sets, and is systematically affected by the large distance uncertainties. In contrast, the kinematically motivated DoS is found to be unaffected by systematics, and is co-aligned with the DoS of the whole sample of M31 companions.

We also showed that those satellite galaxies that were discovered over the last few years for both large spirals, the Milky Way and Andromeda, are found close to the discs-of-satellites. This is remarkable as it is not expected if they were isotropically distributed, even if the sky coverage region of the SDSS is constrained towards the Galactic North Pole. Also Andromeda's recently announced companions fall on its DoS. It appears implausible that for both systems the disc-of-satellites is present due to observational biases only. That would be a very strange coincidence.

In **Chapter 3** the orbital properties of the satellite galaxies are analysed. New proper motion measurements of Milky Way satellite galaxies became available over the last years. The proper motions were used to calculate the orbital poles and their projected uncertainties for the satellites. A pole-distance distribution (PDD) is derived. As this distribution is biased for a small numbers of directions, we determined the measured random PDD using a Monte Carlo method, and derived an analytic fitting formula for the PDD that can be used to test a given distribution for randomness. For a set of six CDM realisations of a MW-like host galaxy we found that their satellite galaxies are consistent with being randomly drawn from an isotropic distribution. Their mean orbital poles point away from the minor axes of their spatial distribution. These pressure supported flattened tri-axial spheroids tend to disperse with time, and are found to be incompatible with the Milky Way satellites. In contrast, the Milky Way PDD shows an excess of small pole distances, which indicates that their orbits are correlated. The co-alignment of the mean orbital pole of six Milky Way satellite galaxies with the normal of the fitted disc-of-satellite implies the DoS to be a rotationally supported structure.

For the Andromeda galaxy it is not possible to directly constrain the orbital poles of its satellite galaxies. Only for two of the satellite galaxies in the M31 system proper motion measurements are available. But taking advantage of the different observational geometry, we presented a method that, to our knowledge for the first time, can be used to confine the possible orbits of M31 companions to so-called "restricted polar paths". The method is not limited to satellite galaxies, but may also be applied to globular clusters in the halo of Andromeda. This restriction criterion allowed us to constrain possible correlated orbital poles.

Finally, we addressed the question whether observed structural parameters of dSph galaxies can be accounted for by models of dark matter free, i.e. tidal dwarf satellite galaxies in **Chapter 4**. A set of such models was analysed that has been numerically evolved, orbiting in a MW-like dark matter host halo. It is found that after a Hubble time of evolution such stellar systems can seemingly have large dynamically derived mass-to-light ratios in agreement with the observed values for Milky Way and Andromeda satellite galaxies. Also other properties, such as the half-light radii and absolute magnitudes, fall in the range of values that are observed. It seems that the actually observed dSph galaxies can perfectly exist without containing dark matter.

To further study the properties of dark matter free satellite galaxies we implemented a high-performance code in C++ for galactic dynamics, SUPERBOX++, as described in **Chapter 5**. The software extensively uses multi-core capabilities of modern CPUs, and is very flexible and extensible, but at the same time very portable. This code was tested and compared to a widely used software, SUPERBOX, and is found to behave equivalently.

Appendix A

Uncertainties of the orbital poles

In Section 3.2, we calculate the orbital poles of the satellite galaxies from their three dimensional positions, proper motion, and radial velocities, as well as their projected uncertainties, which are plotted in Figure 3.2. These uncertainties were calculated incorporating the proper motion uncertainties only, as these contribute mostly to the total uncertainties. Here we give an estimation, why none of the other measurement uncertainties contribute significantly to the uncertainties of the specific angular momentum vectors. We repeat Eqn. (3.4) here for clarity:

$$\begin{pmatrix} \sigma_U^2 \\ \sigma_V^2 \\ \sigma_W^2 \end{pmatrix} = \mathsf{C} \begin{pmatrix} \sigma_{v_r}^2 \\ k^2 \left[(r\sigma_{\mu_{\alpha*}})^2 + (\mu_{\alpha*}\sigma_r)^2 \right] \\ k^2 \left[(r\sigma_{\mu_\delta})^2 + (\mu_\delta \sigma_r)^2 \right] \end{pmatrix} + 2\mu_{\alpha*}\mu_\delta k^2 \sigma_r^2 \begin{pmatrix} b_{12}\, b_{13} \\ b_{22}\, b_{23} \\ b_{32}\, b_{33} \end{pmatrix} \quad .$$

First, we consider the velocity vector in Galactic coordinates. From Equation (3.4) we find for the second and third component of the vector of the first term: $\left(k^2 \left[(r\sigma_\mu)^2 + (\mu\sigma_r)^2\right]\right)$. With $\sigma_\mu \sim 0.1\mu$ and $r \gg \sigma_r$, typical values are $\sigma_r \sim 0.01r$, we get

$$k^2\mu^2(0.01r^2 + 0.0001r^2) \approx k^2\sigma_\mu^2 r^2 \quad ,$$

which results in a velocity uncertainty of the order of $\sim 25\ \mathrm{km\,s^{-1}}$ for each component at a distance of 50 kpc. For the second term in Equation (3.4), the cross term, with $\mu_{\alpha*} \approx \mu_\delta$ it follows

$$2k^2\mu^2\sigma_r^2 \ll k^2\sigma_\mu^2 r^2 \quad .$$

Furthermore, for the rotation matrix B we find that $b_{ij}\, b_{ik} \leq 1$, so it is reasonable to neglect the distance uncertainties.

The radial velocity uncertainties are typically of the order of $5\ \mathrm{km\,s^{-1}}$, compared to $\sim 25\ \mathrm{km\,s^{-1}}$ for the two transverse velocity components as estimated above. The total absolute value of the velocity uncertainty is then estimated to be of the order

$$\begin{aligned} |\sigma_v| &= \sqrt{2 \cdot (25\ \mathrm{km\,s^{-1}})^2 + (5\ \mathrm{km\,s^{-1}})^2} \\ &\approx \sqrt{2 \cdot (25\ \mathrm{km\,s^{-1}})^2} \approx 35\ \mathrm{km\,s^{-1}} \quad , \end{aligned}$$

or $\approx 20\ \mathrm{km\,s^{-1}}$ for each component individually, assuming equipartition. Moreover, as we calculate the specific angular momentum vector given by $\boldsymbol{l} = \boldsymbol{r} \times \boldsymbol{v}$, the contribution to the

vector $\boldsymbol{v}$ from the radial velocity is almost parallel to the vector $\boldsymbol{r}$. The angle is at maximum of the order $\arctan(8.5\text{ kpc}/50\text{ kpc}) \approx 10^\circ$, so the radial velocity uncertainty contributes only little to the total uncertainty of the direction of the specific angular momentum vector.

Three measurement uncertainties contribute to the total variance of the position vector in Galactic Coordinates. The distance uncertainty to the satellite, the transverse position uncertainty in the direction of right ascension and declination, and the uncertainty of the distance to the Galactic centre. For the following estimation we consider a typical distance of a satellite galaxy of 50 kpc and assume equipartition of the individual components, i.e. $|r_i| \sim \sqrt{50^2/3}$ kpc ≈ 30 kpc, $i = 1,2,3$. Furthermore, we assume a typical distance uncertainty of the order 3 kpc at that distance (see Table 2.1), so that $|\sigma_i| \sim \sqrt{3^2/3}$ kpc ≈ 1.7 kpc. For the distance to the Galactic Centre we use the IAU recommended value 8.5 kpc, while some authors prefer a value of 8 kpc (e.g. Eisenhauer et al. 2003), so we assume the uncertainty to be 0.5 kpc. It follows that the maximum component of the distance uncertainty is of the order $\sqrt{1.3^2 + 0.5^2}$ kpc ≈ 1.8 kpc. The variance of a component of the specific angular momentum vector is given by $\sigma_{l_i} = \left(r_j^2\sigma_{v_k}^2 + v_k^2\sigma_{r_j}^2\right) + \left(r_k^2\sigma_{v_j}^2 + v_j^2\sigma_{r_k}^2\right)$, $i,j,k \in \{1,2,3\}$; $i \neq j \neq k$. The contribution due to the estimated velocity uncertainty to this sum is of the order $2 \cdot (30\text{ kpc})^2 \left(20\text{ km s}^{-1}\right)^2 = 720\,000 \left(\text{kpc km s}^{-1}\right)^2$,while the estimated position uncertainties contribute with less than a tens of this value, $2 \cdot \left(100\text{ km s}^{-1}\right)^2 (1.7\text{ kpc})^2 = 57\,800 \left(\text{kpc km s}^{-1}\right)^2$, i.e. the velocity uncertainty is the dominating contribution to the total sum. The transverse position uncertainties in the direction of right ascension and declination are much smaller than the distance uncertainties. At a typical distance of a satellite galaxy of the order of 50 kpc, a position uncertainty of $1'$ transforms into a spatial uncertainty of ≈ 15 pc, which is about two orders of magnitudes smaller than a typical distance uncertainty of 2 kpc.

For the motion of the LSR about the Galactic Centre we used the IAU recommended value of 220 km s^{-1} (Kerr & Lynden-Bell 1986; cf. also Xue et al. 2008). The uncertainty of this value is of the order 20 km s^{-1}. We checked that the results do not change significantly by once using 200 km s^{-1} and once 240 km s^{-1} for the circular motion. The uncertainties of the peculiar motion of the Sun with respect to the LSR as given by Dehnen & Binney (1998) are of the order of 0.5 km s^{-1}, much smaller than the other contributions and can be neglected.

The calculation done above assumed a typical distance of a satellite galaxy of 50 kpc or more. Sagittarius is much closer to the Sun, only about 24 kpc, but its geometric location is very special. It is located almost directly behind the Galactic Centre, i.e. $\boldsymbol{r} \| \boldsymbol{v}_r$. Moreover, Sagittarius is anyway not co-rotating with the DoS because of its spatial location with respect to the disc-of-satellites.

Appendix B

Superbox++ performance

It is interesting to know how Superbox++ "performs" compared to Superbox. Both programs were run on a workstation with 2 AMD Opteron^{TM} 265 (1.8 GHz) processors (4 CPU cores in total) and 4 GB RAM (cf. Fig. 5.2) to measure the runtime. Different (artificial) test scenarios were set-up to show the influence of some factors that determine the speed of the integration steps: the number of particles per sub-grid N_p, the number of co-moving sub-grids N_g, and the dimensions of the grids. For the test-runs models similar to the `twoiso` setup (§5.1.3) were used. Isothermal spheres were set-up with the following parameters: 150 km s^{-1} rotational velocity and 200 kpc cut-off radius. The radii of the grids were chosen to be $r_{system} = 400$ kpc, $r_{outer} = 64$ kpc, and $r_{core} = 16$ kpc, and the co-moving grids are tracking the centre-of-density. Each test was run with the same number of time-steps of 1 Myr each. The timing measurements[(a)] were done with an external script. From these timing measurements a "gain factor" was computed, $g = T_{sb}/T_{sb++}$, where T_{sb}, T_{sb++} are the measured execution times in seconds. Factors larger than 1 show that the performance in integration steps per seconds of Superbox++ is higher than for Superbox, factors smaller than 1 that it is lower – or in other words: Superbox++ performs the same simulation a factor of g times faster. Results are shown in Fig. B.1 for some runs. The vertical dashed line indicates the break-even gain factor of 1. For values below this line Superbox is faster than Superbox++, which is never the case. Indeed, Superbox++ is typically a factor of > 2.5 times faster than Superbox[(b)].

The larger the grid-size is chosen, the more important the efficiency of the code gets that calculates the values of the potential on the grid-cells, as the total number of grid-cells scales with N^3. We also performed some preliminary tests to do this particular calculation on a graphics card, including the relatively slow memory transfers to the graphics card. The calculations were run for a grid-size of 128^3 cells on an NVIDIA GeForce 8800GT with a G80 GPU and 1GB of total graphic memory, and compared to the results done on a dual-core host (AMD Athlon 64 X2 with 2GHz). It is found that the calculation on the

[(a)] A preliminary version of Superbox++ from November 2007 was used for the performance measurements.

[(b)] As a side note to understand how much the performance is really increased, it is important to know that Superbox has an intrinsic performance gain compared to Superbox++ just because mostly single precision operations are used: (i) single precision variables need less memory and (ii) single precision operations can efficiently be packed automatically by the compiler to be executed in parallel (SIMD). Using single precision operations can almost double the speed.

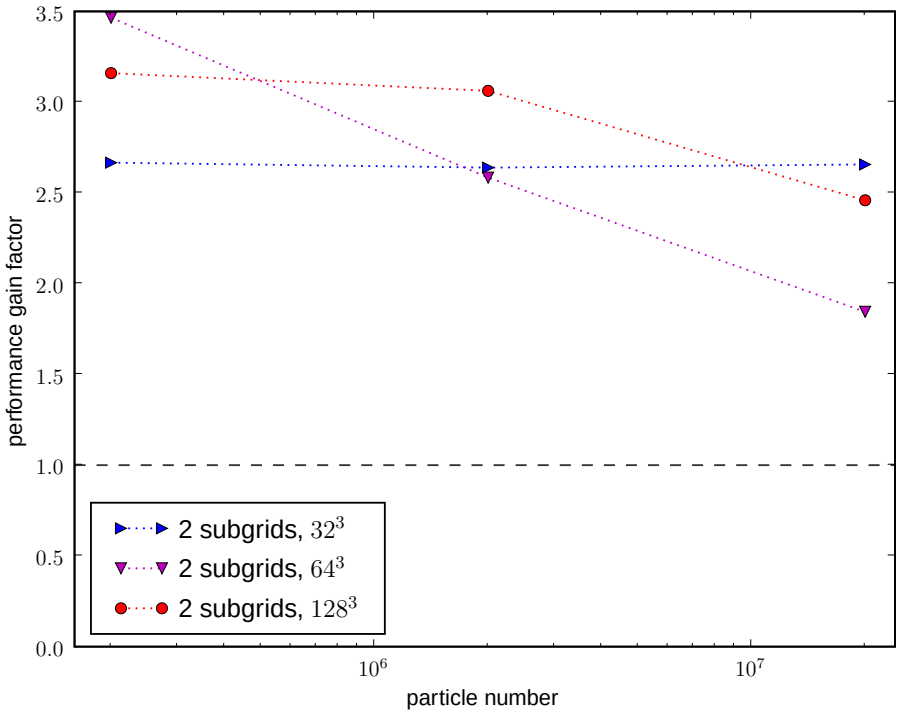

Figure B.1: Performance gain factor of Superbox++ compared to Superbox as a function of particle number. Runs with different grid-dimensions were performed as labelled in the figure. The horizontal dashed line shows the break even point, when both programs have equal execution time per integration step.

graphics card is a factor of 14 faster if only one of the hosts CPU-cores is used, and a factor of 9 faster if both CPU-cores are utilised for the FFT on the host.

Bibliography

Aaronson, M. 1983, ApJ, 266, L11

Aharonian, F., Akhperjanian, A. G., Bazer-Bachi, A. R., et al. 2008, Astroparticle Physics, 29, 55

Angus, G. W. & McGaugh, S. S. 2008, MNRAS, 383, 417

Baade, W. 1956, Mitteilungen der Astronomischen Gesellschaft Hamburg, 7, 51

Barnes, J. E. & Hernquist, L. 1992, Nature, 360, 715

Beers, T. C., Flynn, K., & Gebhardt, K. 1990, AJ, 100, 32

Bekenstein, J. & Milgrom, M. 1984, ApJ, 286, 7

Bekenstein, J. D. 2004, Phys. Rev. D, 70, 083509

Belokurov, V., Zucker, D. B., Evans, N. W., et al. 2007, ApJ, 654, 897

Belokurov, V., Zucker, D. B., Evans, N. W., et al. 2006, ApJ, 647, L111

Benson, A. J., Lacey, C. G., Baugh, C. M., Cole, S., & Frenk, C. S. 2002, MNRAS, 333, 156

Bertone, G., Hooper, D., & Silk, J. 2005, Phys. Rep., 405, 279

Bien, R., Fuchs, B., & Wielen, R. 1991, in The CP90 Europhysics Conference on Computational Physics, Amsterdam, The Netherlands, 10-13 September 1990; A. Tenner (ed.), World Scientific, Singapore, p. 3-13, 3–13

Biermann, P. L., Caramete, L., Munyaneza, F., & Stasielak, J. 2008, in American Institute of Physics Conference Series, Vol. 972, American Institute of Physics Conference Series, 365–373

Biermann, P. L. & Munyaneza, F. 2007, preprint astro-ph/0702173

Binney, J. 2008, MNRAS, L39+

Binney, J. & Tremaine, S. 1994, Galactic Dynamics (Princeton University Press)

Boily, C. M., Kroupa, P., & Peñarrubia-Garrido, J. 2001, New Astronomy, 6, 27

Bournaud, F. & Duc, P.-A. 2006, A&A, 456, 481

Bournaud, F., Duc, P.-A., Brinks, E., et al. 2007, Science, 316, 1166

Bristow, P., Piatek, S., & Pryor, C. 2005, Space Telescope European Coordinating Facility Newsletter, Volume 38, p.12, 38, 12

Brunthaler, A., Reid, M. J., Falcke, H., Greenhill, L. J., & Henkel, C. 2005, Science, 307, 1440

Brunthaler, A., Reid, M. J., Falcke, H., Henkel, C., & Menten, K. M. 2007, A&A, 462, 101

Bullock, J. S. 2002, in The shapes of galaxies and their dark halos, Proceedings of the Yale Cosmology Workshop "The Shapes of Galaxies and Their Dark Matter Halos", New Haven, Connecticut, USA, 28-30 May 2001. Edited by Priyamvada Natarajan. Singapore: World Scientific, 2002, ISBN 9810248482, p.109, ed. P. Natarajan, 109–+

Calura, F., Lanfranchi, G. L., & Matteucci, F. 2008, preprint arxiv:0801.2547

Chapman, S. C., Ibata, R., Lewis, G. F., et al. 2005, ApJ, 632, L87

Chien, L.-H., Barnes, J. E., Kewley, L. J., & Chambers, K. C. 2007, ApJ, 660, L105

Chojnacki, W., Brooks, M., van den Hengel, A., & Gawley, D. 2000, IEEE Transactions on pattern analysis and machine intelligence, 22, 1294

Cioni, M.-R. L. & Habing, H. J. 2005, A&A, 442, 165

Ciotti, L. & Binney, J. 2004, MNRAS, 351, 285

Clowe, D., Bradač, M., Gonzalez, A. H., et al. 2006, ApJ, 648, L109

Clowe, D., Randall, S. W., & Markevitch, M. 2007, Nuclear Physics B Proceedings Supplements, 173, 28

Cole, S., Lacey, C. G., Baugh, C. M., & Frenk, C. S. 2000, MNRAS, 319, 168

Coleman, M. G., de Jong, J. T. A., Martin, N. F., et al. 2007, ApJ, 668, L43

Colless, M., Dalton, G., Maddox, S., et al. 2001, MNRAS, 328, 1039

Corbelli, E. & Schneider, S. E. 1997, ApJ, 479, 244

Côté, P., Mateo, M., Olszewski, E. W., & Cook, K. H. 1999, ApJ, 526, 147

Dabringhausen, J., Hilker, M., & Kroupa, P. 2008, preprint arXiv:0802.0703

de Blok, W. J. G., McGaugh, S. S., & Rubin, V. C. 2001, AJ, 122, 2396

de Vaucouleurs, G. 1958, ApJ, 128, 465

de Vaucouleurs, G., de Vaucouleurs, A., Corwin, Jr., H. G., et al. 1991, Third Reference Catalogue of Bright Galaxies (Volume 1-3, XII, 2069 pp. 7 figs.. Springer-Verlag Berlin Heidelberg New York)

Dehnen, W. & Binney, J. J. 1998, MNRAS, 298, 387

Dekker, T. J. 1971, Numerische Mathematik, 18, 224

Delgado-Donate, E. J., Muñoz-Tuñón, C., Deeg, H. J., & Iglesias-Páramo, J. 2003, A&A, 402, 921

Diemand, J., Kuhlen, M., & Madau, P. 2007, ApJ, 667, 859

Diemand, J., Madau, P., & Moore, B. 2005a, MNRAS, 364, 367

Diemand, J., Zemp, M., Moore, B., Stadel, J., & Carollo, M. 2005b, MNRAS, 364, 665

Dinescu, D. I., Girard, T. M., van Altena, W. F., & López, C. E. 2005, ApJ, 618, L25

Dinescu, D. I., Keeney, B. A., Majewski, S. R., & Girard, T. M. 2004, AJ, 128, 687

Doroshkevich, A. G. 1973, Astrophys. Lett., 14, 11

Dubinski, J. & Carlberg, R. G. 1991, ApJ, 378, 496

Duc, P.-A., Bournaud, F., & Masset, F. 2004, A&A, 427, 803

Duc, P.-A. & Mirabel, I. F. 1998, A&A, 333, 813

Eggen, O. J., Lynden-Bell, D., & Sandage, A. R. 1962, ApJ, 136, 748

Einasto, J. & Lynden-Bell, D. 1982, MNRAS, 199, 67

Eisenhauer, F., Schödel, R., Genzel, R., et al. 2003, ApJ, 597, L121

Elmegreen, B. G., Kaufman, M., & Thomasson, M. 1993, ApJ, 412, 90

ESA. 1997, The Hipparcos and Tycho Catalogues

Evans, N. W., Wilkinson, M. I., Kleyna, J. T., Read, J. I., & Gilmore, G. 2005, in IAU Colloq. 198: Near-fields cosmology with dwarf elliptical galaxies, ed. H. Jerjen & B. Binggeli (Camebridge: Camebridge Univ. Press), 60–67

Feigelson, E. D. & Babu, G. J. 1992, ApJ, 397, 55

Fellhauer, M., Belokurov, V., Evans, N. W., et al. 2006, ApJ, 651, 167

Fellhauer, M., Evans, N. W., Belokurov, V., Wilkinson, M. I., & Gilmore, G. 2007a, MNRAS, 380, 749

Fellhauer, M., Evans, N. W., Belokurov, V., et al. 2007b, MNRAS, 375, 1171

Fellhauer, M. & Kroupa, P. 2002a, Ap&SS, 281, 355

Fellhauer, M. & Kroupa, P. 2002b, MNRAS, 330, 642

Fellhauer, M. & Kroupa, P. 2005, ApJ, 630, 879

Fellhauer, M., Kroupa, P., Baumgardt, H., et al. 2000, New Astronomy, 5, 305

Fellhauer, M., Wilkinson, M. I., Evans, N. W., et al. 2008, MNRAS, 385, 1095

Fisher, N., Lewis, T., & Embleton, B. 1987, Statistical analysis of spherical data (Cambridge University Press)

Fleck, J. & Kuhn, J. R. 2003, ApJ, 592, 147

Franx, M., Illingworth, G., & de Zeeuw, T. 1991, ApJ, 383, 112

Frebel, A., Aoki, W., Christlieb, N., et al. 2005, Nature, 434, 871

Frenk, C. S., Evrard, A. E., White, S. D. M., & Summers, F. J. 1996, ApJ, 472, 460

Frigo, M. & Johnson, S. G. 2005, Proceedings of the IEEE, 93, 216, special issue on "Program Generation, Optimization, and Platform Adaptation"

Gallagher, III, J. S. & Wyse, R. F. G. 1994, PASP, 106, 1225

Gentile, G., Famaey, B., Combes, F., et al. 2007, A&A, 472, L25

Gilmore, G., Wilkinson, M., Kleyna, J., et al. 2006, in UCLA Dark Matter 2006 conference, astro-ph/0608528

Gilmore, G., Wilkinson, M. I., Wyse, R. F. G., et al. 2007, ApJ, 663, 948

Gnedin, O. Y. & Zhao, H. 2002, MNRAS, 333, 299

Goerdt, T., Moore, B., Read, J. I., Stadel, J., & Zemp, M. 2006, MNRAS, 368, 1073

Grebel, E. K. 2000, in Bulletin of the American Astronomical Society, Vol. 32, 698–+

Grebel, E. K. 2001, Astrophysics and Space Science Supplement, 277, 231

Grebel, E. K. & Gallagher, J. S. 2004, ApJ, 610, L89

Grebel, E. K., Gallagher, J. S., & Harbeck, D. 2003, Astronomische Nachrichten Supplement, 324, 90

Grebel, E. K., Kolatt, T., & Brandner, W. 1999, in IAU Symposium, ed. P. Whitelock & R. Cannon, 447–+

Harris, W. E. 1996, AJ, 112, 1487

Hartwick, F. D. A. 2000, AJ, 119, 2248

Helmi, A. 2004a, MNRAS, 351, 643

Helmi, A. 2004b, ApJ, 610, L97

Helmi, A., Irwin, M. J., Tolstoy, E., et al. 2006, ApJ, 651, L121

Hensler, G., Theis, C., & Gallagher, J. 2004, A&A, 426, 25

Hodge, P. W. 1971, ARA&A, 9, 35

Holmberg, E. 1969, Arkiv för Astronomi, 5, 305

Hu, F. X., Yuan, Q. R., Su, H. J., Wu, G. X., & Liu, Y. Z. 1998, ApJ, 495, 179

Hubble, E. 1936, The Realm of the Nebulae (Yale University Press)

Hunsberger, S. D., Charlton, J. C., & Zaritsky, D. 1996, ApJ, 462, 50

Hunter, D. A., Hunsberger, S. D., & Roye, E. W. 2000, ApJ, 542, 137

Ibata, R., Irwin, M., Lewis, G. F., & Stolte, A. 2001a, ApJ, 547, L133

Ibata, R., Lewis, G. F., Irwin, M., Totten, E., & Quinn, T. 2001b, ApJ, 551, 294

Ibata, R., Martin, N. F., Irwin, M., et al. 2007, ApJ, 671, 1591

Ibata, R. A. & Lewis, G. F. 1998, ApJ, 500, 575

Ibata, R. A., Wyse, R. F. G., Gilmore, G., Irwin, M. J., & Suntzeff, N. B. 1997, AJ, 113, 634

Ikuta, C. & Arimoto, N. 2002, A&A, 391, 55

Irwin, M. & Hatzidimitriou, D. 1995, MNRAS, 277, 1354

Irwin, M. J., Ferguson, A. M. N., Huxor, A. P., et al. 2008, ApJ, 676, L17

Jarrett, T. H., Polletta, M., Fournon, I. P., et al. 2006, AJ, 131, 261

Jing, Y. P. & Suto, Y. 2002, ApJ, 574, 538

Johnson, D. R. H. & Soderblom, D. R. 1987, AJ, 93, 864

Johnston, K. V., Law, D. R., & Majewski, S. R. 2005, ApJ, 619, 800

Johnston, K. V., Majewski, S. R., Siegel, M. H., Reid, I. N., & Kunkel, W. E. 1999, AJ, 118, 1719

Johnston, K. V., Spergel, D. N., & Haydn, C. 2002, ApJ, 570, 656

Johnston, K. V., Spergel, D. N., & Hernquist, L. 1995, ApJ, 451, 598

Kahn, F. D. & Woltjer, L. 1959, ApJ, 130, 705

Kallivayalil, N., van der Marel, R. P., & Alcock, C. 2006a, ApJ, 652, 1213

Kallivayalil, N., van der Marel, R. P., Alcock, C., et al. 2006b, ApJ, 638, 772

Kang, X., Mao, S., Gao, L., & Jing, Y. 2005, A&A, 437, 383

Kauffmann, G., White, S. D. M., & Guiderdoni, B. 1993, MNRAS, 264, 201

Kazantzidis, S., Kravtsov, A. V., Zentner, A. R., et al. 2004a, ApJ, 611, L73

Kazantzidis, S., Mayer, L., Mastropietro, C., et al. 2004b, ApJ, 608, 663

Kerr, F. J. & Lynden-Bell, D. 1986, MNRAS, 221, 1023

King, I. R. 1962, AJ, 67, 471

Klessen, R. S. & Kroupa, P. 1998, ApJ, 498, 143

Kleyna, J. T., Wilkinson, M. I., Evans, N. W., & Gilmore, G. 2005, ApJ, 630, L141

Kleyna, J. T., Wilkinson, M. I., Gilmore, G., & Evans, N. W. 2003, ApJ, 588, L21

Klimentowski, J., Łokas, E. L., Kazantzidis, S., et al. 2007, MNRAS, 378, 353

Klypin, A., Kravtsov, A. V., Valenzuela, O., & Prada, F. 1999, ApJ, 522, 82

Knebe, A., Gill, S. P. D., Gibson, B. K., et al. 2004, ApJ, 603, 7

Koch, A. & Grebel, E. K. 2006, AJ, 131, 1405

Koch, A., Kleyna, J. T., Wilkinson, M. I., et al. 2007a, AJ, 134, 566

Koch, A., Wilkinson, M. I., Kleyna, J. T., et al. 2007b, ApJ, 657, 241

Kravtsov, A. V., Gnedin, O. Y., & Klypin, A. A. 2004, ApJ, 609, 482

Kronberger, T., Kapferer, W., Ferrari, C., Unterguggenberger, S., & Schindler, S. 2008, preprint arXiv:0801.3759

Kroupa, P. 1997, New Astronomy, 2, 139

Kroupa, P. 1998, MNRAS, 300, 200

Kroupa, P., Theis, C., & Boily, C. M. 2005, A&A, 431, 517

Kuhn, J. R. 1993, ApJ, 409, L13

Kuhn, J. R. & Miller, R. H. 1989, ApJ, 341, L41

Kunkel, W. E. & Demers, S. 1976, in The Galaxy and the Local Group, 241–+

Lacey, C. & Cole, S. 1993, MNRAS, 262, 627

Lake, G. & D'Onghia, E. 2008, preprint arXiv:0802.0001

Lee, J.-W., Carney, B. W., & Cheng, H. 2007, preprint arXiv:0710.0395

Lee, M. G. & Kim, S. C. 2000, AJ, 119, 777

Li, Y.-S. & Helmi, A. 2008, MNRAS, 307

Libeskind, N. I., Cole, S., Frenk, C. S., Okamoto, T., & Jenkins, A. 2007, MNRAS, 374, 16

Libeskind, N. I., Frenk, C. S., Cole, S., et al. 2005, MNRAS, 363, 146

Loeb, A. & Narayan, R. 2007, preprint arXiv:0711.3809

Loeb, A., Reid, M. J., Brunthaler, A., & Falcke, H. 2005, ApJ, 633, 894

Łokas, E. L. 2001, MNRAS, 327, L21

Lynden-Bell, D. 1976, MNRAS, 174, 695

Lynden-Bell, D. 1982, The Observatory, 102, 202

Lynden-Bell, D. 1983, in IAU Symposium, Vol. 100, Internal Kinematics and Dynamics of Galaxies, ed. E. Athanassoula, 89–91

Lynden-Bell, D. & Lynden-Bell, R. M. 1995, MNRAS, 275, 429

Mackey, A. D. & Gilmore, G. F. 2004, MNRAS, 355, 504

Mackey, A. D. & van den Bergh, S. 2005, MNRAS, 360, 631

Majewski, S. R. 1994, ApJ, 431, L17

Majewski, S. R., Bahcall, J. N., Geisler, D., et al. 2005, in Bulletin of the American Astronomical Society, Vol. 37, Bulletin of the American Astronomical Society, 454–+

Majewski, S. R., Beaton, R. L., Patterson, R. J., et al. 2007, ApJ, 670, L9

Majewski, S. R., Skrutskie, M. F., Weinberg, M. D., & Ostheimer, J. C. 2003, ApJ, 599, 1082

Mardia, K. V. & Jupp, P. E. 2000, Directional Statistics (John Wiley & Sons, Ltd)

Markevitch, M., Randall, S., Clowe, D., Gonzalez, A., & Bradac, M. 2006, in COSPAR, Plenary Meeting, Vol. 36, 36th COSPAR Scientific Assembly, 2655–+

Martin, N. F., Ibata, R. A., Irwin, M. J., et al. 2006, MNRAS, 371, 1983

Martínez-Delgado, D., Alonso-García, J., Aparicio, A., & Gómez-Flechoso, M. A. 2001, ApJ, 549, L63

Mashchenko, S., Wadsley, J., & Couchman, H. M. P. 2007, preprint arXiv:0711.4803

Mastropietro, C. & Burkert, A. 2007, preprint arXiv:0711.0967, 711

Mateo, M. L. 1998, ARA&A, 36, 435

Mayer, L., Governato, F., Colpi, M., et al. 2001, ApJ, 559, 754

Mayer, L., Governato, F., & Kaufmann, T. 2008, preprint arxiv:0801.3845

McConnachie, A. W., Arimoto, N., & Irwin, M. 2007a, MNRAS, 379, 379

McConnachie, A. W. & Irwin, M. J. 2006a, MNRAS, 365, 1263

McConnachie, A. W. & Irwin, M. J. 2006b, MNRAS, 365, 902

McConnachie, A. W., Irwin, M. J., Ferguson, A. M. N., et al. 2005, MNRAS, 356, 979

McConnachie, A. W., Peñarrubia, J., & Navarro, J. F. 2007b, MNRAS, 380, L75

Milgrom, M. 1983, ApJ, 270, 365

Milgrom, M. 2007, ApJ, 667, L45

Milosavljević, M., Koda, J., Nagai, D., Nakar, E., & Shapiro, P. R. 2007, ApJ, 661, L131

Mirabel, I. F., Dottori, H., & Lutz, D. 1992, A&A, 256, L19

Monreal-Ibero, A., Colina, L., Arribas, S., & García-Marín, M. 2007, A&A, 472, 421

Moore, B., Diemand, J., Madau, P., Zemp, M., & Stadel, J. 2006, MNRAS, 368, 563

Moore, B., Ghigna, S., Governato, F., et al. 1999, ApJ, 524, L19

Moore, G. 1965, Electronics Magazine, 38

Muñoz, R. R., Carlin, J. L., Frinchaboy, P. M., et al. 2006a, ApJ, 650, L51

Muñoz, R. R., Frinchaboy, P. M., Majewski, S. R., et al. 2005, ApJ, 631, L137

Muñoz, R. R., Majewski, S. R., & Johnston, K. V. 2007, preprint arxiv:0712.4312

Muñoz, R. R., Majewski, S. R., Zaggia, S., et al. 2006b, ApJ, 649, 201

Murray, C. A. 1983, Vectorial astrometry (Bristol: Adam Hilger, 1983)

Navarro, J. F., Abadi, M. G., & Steinmetz, M. 2004, ApJ, 613, L41

Newberg, H. J. & Yanny, B. 2004, in Bulletin of the American Astronomical Society, Vol. 36, Bulletin of the American Astronomical Society, 1582–+

Nipoti, C., Ciotti, L., Binney, J., & Londrillo, P. 2008, preprint arXiv:0802.1122

Nipoti, C., Londrillo, P., & Ciotti, L. 2007, ApJ, 660, 256

Nusser, A. 2008, MNRAS, 29

Oh, K. S., Lin, D. N. C., & Aarseth, S. J. 1995, ApJ, 442, 142

Okazaki, T. & Taniguchi, Y. 2000, ApJ, 543, 149

Ostriker, J. P. & Steinhardt, P. 2003, Science, 300, 1909

Palma, C., Majewski, S. R., & Johnston, K. V. 2002, ApJ, 564, 736

Palma, C., Majewski, S. R., Siegel, M. H., et al. 2003, AJ, 125, 1352

Pasetto, S., Chiosi, C., & Carraro, G. 2003, A&A, 405, 931

Peñarrubia, J., Kroupa, P., & Boily, C. M. 2002, MNRAS, 333, 779

Peñarrubia, J., McConnachie, A. W., & Navarro, J. F. 2007, ApJ, 672, 904

Peñarrubia, J., Navarro, J. F., & McConnachie, A. W. 2008, ApJ, 673, 226

Peebles, P. J. & Ratra, B. 2003, Reviews of Modern Physics, 75, 559

Peebles, P. J. E. 1989, JRASC, 83, 363

Piatek, S. & Pryor, C. 1995, AJ, 109, 1071

Piatek, S., Pryor, C., Bristow, P., et al. 2007, AJ, 133, 818

Piatek, S., Pryor, C., Bristow, P., et al. 2005, AJ, 130, 95

Piatek, S., Pryor, C., Bristow, P., et al. 2006, AJ, 131, 1445

Piatek, S., Pryor, C., Olszewski, E. W., et al. 2003, AJ, 126, 2346

Plummer, H. C. 1911, MNRAS, 71, 460

Power, C., Navarro, J. F., Jenkins, A., et al. 2003, MNRAS, 338, 14

Press, W. H., Teukolsky, S. A., Vetterling, W. T., & Flannery, B. P. 1992, Numerical recipes in FORTRAN. The art of scientific computing, 2nd edn. (Cambridge University Press)

Read, J. I., Pontzen, A. P., & Viel, M. 2006a, MNRAS, 371, 885

Read, J. I., Wilkinson, M. I., Evans, N. W., Gilmore, G., & Kleyna, J. T. 2006b, MNRAS, 367, 387

Recchi, S. & Hensler, G. 2006, A&A, 445, L39

Recchi, S., Hensler, G., Angeretti, L., & Matteucci, F. 2006, A&A, 445, 875

Recchi, S., Theis, C., Kroupa, P., & Hensler, G. 2007, A&A, 470, L5

Reif, K., Poschmann, H., Marien, K.-H., & Mueller, P. 2004, in Presented at the Society of Photo-Optical Instrumentation Engineers (SPIE) Conference, Vol. 5167, Focal Plane Arrays for Space Telescopes. Edited by Grycewicz, Thomas J.; McCreight, Craig R. Proceedings of the SPIE, Volume 5167, pp. 320-331 (2004)., ed. T. J. Grycewicz & C. R. McCreight, 320–331

Sakamoto, T. & Hasegawa, T. 2006, ApJ, 653, L29

Sales, L. V., Navarro, J. F., Abadi, M. G., & Steinmetz, M. 2007a, MNRAS, 379, 1475

Sales, L. V., Navarro, J. F., Abadi, M. G., & Steinmetz, M. 2007b, MNRAS, 379, 1464

Sánchez-Salcedo, F. J., Reyes-Iturbide, J., & Hernandez, X. 2006, MNRAS, 370, 1829

Sanders, R. H. & McGaugh, S. S. 2002, ARA&A, 40, 263

Sawa, T. & Fujimoto, M. 2005, PASJ, 57, 429

Schmidt, B. P., Keller, S. C., Francis, P. J., & Bessell, M. S. 2005, American Astronomical Society Meeting Abstracts, 206,

Scholz, R.-D. & Irwin, M. J. 1994, in IAU Symposium, Vol. 161, Astronomy from Wide-Field Imaging, ed. H. T. MacGillivray, 535–+

Schweitzer, A. E., Cudworth, K. M., & Majewski, S. R. 1997, in Astronomical Society of the Pacific Conference Series, Vol. 127, Proper Motions and Galactic Astronomy, ed. R. M. Humphreys, 103–+

Schweitzer, A. E., Cudworth, K. M., Majewski, S. R., & Suntzeff, N. B. 1995, AJ, 110, 2747

Schweizer, F. 1978, in IAU Symp. 77: Structure and Properties of Nearby Galaxies, ed. E. M. Berkhuijsen & R. Wielebinski, 279–284

Searle, L. 1977, in Evolution of Galaxies and Stellar Populations, ed. B. M. Tinsley & R. B. Larson, 219–+

Seigar, M. S., Barth, A. J., & Bullock, J. S. 2006, ArXiv Astrophysics e-prints

Sellwood, J. A. 1987, ARA&A, 25, 151

Shapley, H. 1938, Nature, 142, 715

Shetrone, M. D., Côté, P., & Sargent, W. L. W. 2001, ApJ, 548, 592

Siegel, M. H., Shetrone, M. D., & Irwin, M. 2008, preprint arXiv:0803.2489

Sohn, S. T., Majewski, S. R., Muñoz, R. R., et al. 2007, ApJ, 663, 960

Spergel, D. N., Bean, R., Doré, O., et al. 2007, ApJS, 170, 377

Springel, V. & Farrar, G. R. 2007, MNRAS, 380, 911

Springel, V., Frenk, C. S., & White, S. D. M. 2006, Nature, 440, 1137

Springel, V., White, S. D. M., Jenkins, A., et al. 2005, Nature, 435, 629

Stephens, M. A. 1974, Journal of the American Statistical Association, 347, 730

Stoehr, F., White, S. D. M., Tormen, G., & Springel, V. 2002, MNRAS, 335, L84

Straughn, A. N., Cohen, S. H., Ryan, R. E., et al. 2006, ApJ, 639, 724

Strigari, L. E., Bullock, J. S., Kaplinghat, M., et al. 2007, ApJ, 669, 676

Tegmark, M. 1996, ApJ, 470, L81+

Terlevich, R. & Melnick, J. 1981, MNRAS, 195, 839

Tiret, O. & Combes, F. 2007, A&A, 464, 517

Tolstoy, E., Irwin, M. J., Helmi, A., et al. 2004, ApJ, 617, L119

Toomre, A. & Toomre, J. 1972, ApJ, 178, 623

Unavane, M., Wyse, R. F. G., & Gilmore, G. 1996, MNRAS, 278, 727

van den Bergh, S. 1999, A&A Rev., 9, 273

van den Bergh, S. 2006, Nature, 444, 158

van den Bosch, F. C., Robertson, B. E., Dalcanton, J. J., & de Blok, W. J. G. 2000, AJ, 119, 1579

van der Marel, R. P., Alves, D. R., Hardy, E., & Suntzeff, N. B. 2002, AJ, 124, 2639

van der Marel, R. P. & Cioni, M.-R. L. 2001, AJ, 122, 1807

van der Marel, R. P. & Guhathakurta, P. 2007, preprint arXiv:0709.3747

Venn, K. A., Irwin, M., Shetrone, M. D., et al. 2004, AJ, 128, 1177

Vollmer, B., Cayatte, V., Balkowski, C., & Duschl, W. J. 2001, ApJ, 561, 708

Walcher, C. J., Fried, J. W., Burkert, A., & Klessen, R. S. 2003, A&A, 406, 847

Walker, M. G., Mateo, M., Olszewski, E. W., et al. 2006a, AJ, 131, 2114

Walker, M. G., Mateo, M., Olszewski, E. W., et al. 2006b, ApJ, 642, L41

Walsh, S. M., Jerjen, H., & Willman, B. 2007a, ApJ, 662, L83

Walsh, S. M., Willman, B., Sand, D., et al. 2007b, preprint arXiv:0712.3054, 712

Walter, F., Martin, C. L., & Ott, J. 2006, AJ, 132, 2289

Weilbacher, P. M., Duc, P.-A., & Fritze-v. Alvensleben, U. 2003, A&A, 397, 545

Weilbacher, P. M., Duc, P.-A., Fritze v. Alvensleben, U., Martin, P., & Fricke, K. J. 2000, A&A, 358, 819

Westfall, K. B., Majewski, S. R., Ostheimer, J. C., et al. 2006, AJ, 131, 375

Wetzstein, M., Naab, T., & Burkert, A. 2007, MNRAS, 375, 805

White, S. D. M. & Rees, M. J. 1978, MNRAS, 183, 341

Whitmore, B. C., Gilmore, D., Leitherer, C., et al. 2005, AJ, 130, 2104

Wilkinson, M. I., Kleyna, J., Evans, N. W., & Gilmore, G. 2002, MNRAS, 330, 778

Wilkinson, M. I., Kleyna, J. T., Evans, N. W., et al. 2005, in IAU Colloq. 198: Near-fields cosmology with dwarf elliptical galaxies, ed. H. Jerjen & B. Binggeli, 240–243

Wilkinson, M. I., Kleyna, J. T., Evans, N. W., et al. 2004, ApJ, 611, L21

Wilkinson, M. I., Kleyna, J. T., Evans, N. W., et al. 2006, in EAS Publications Series, ed. G. A. Mamon, F. Combes, C. Deffayet, & B. Fort, 105–112

Willman, B., Blanton, M. R., West, A. A., et al. 2005a, AJ, 129, 2692

Willman, B., Dalcanton, J. J., Martinez-Delgado, D., et al. 2005b, ApJ, 626, L85

Wilson, A. G. 1955, PASP, 67, 27

Xue, X. X., Rix, H. W., Zhao, G., et al. 2008, preprint arXiv:0801.1232

York, D. G., Adelman, J., Anderson, Jr., J. E., et al. 2000, AJ, 120, 1579

Zentner, A. R., Kravtsov, A. V., Gnedin, O. Y., & Klypin, A. A. 2005, ApJ, 629, 219

Zhao, H. 1998, ApJ, 500, L149+

Zhao, H. 2007, preprint arXiv:0704.0094

Zucker, D. B., Belokurov, V., Evans, N. W., et al. 2006a, ApJ, 650, L41

Zucker, D. B., Belokurov, V., Evans, N. W., et al. 2006b, ApJ, 643, L103

Zucker, D. B., Kniazev, A. Y., Bell, E. F., et al. 2004, ApJ, 612, L121

Zucker, D. B., Kniazev, A. Y., Martínez-Delgado, D., et al. 2007, ApJ, 659, L21

Zwicky, F. 1933, Helvetica Physica Acta, 6, 110

Zwicky, F. 1956, Ergebnisse der exakten Naturwissenschaften, 29, 34

List of Figures

List of Tables

List of Publications

Refereed publications

- "The spatial distribution of the Milky Way and Andromeda satellite galaxies", 2007, MNRAS, 374, 1125–1145, **Manuel Metz**, P. Kroupa, & H. Jerjen
  (Chapter 2, and Sections 3.3 & 3.4)
- "Dwarf spheroidal satellites: are they of tidal origin?", 2007, MNRAS, 376, 387–392, **Manuel Metz** & P. Kroupa
  (Chapter 4)
- "The orbital poles of Milky Way satellite galaxies: a rotationally supported disc-of-satellites", 2008, accepted for publication ApJ , **Manuel Metz**, P. Kroupa, & N. Libeskind
  (Chapter 3, Sections 3.1, 3.2, & 3.4)
- "3D distribution of Local Group satellite galaxies: the new dwarf spheroidals", 2008, submitted to MNRAS, **Manuel Metz**, P. Kroupa, & H. Jerjen
  (in Chapter 2)

Conference proceedings

- "Anisotropies of the satellite systems around the Milky Way and Andromeda", 2005, IAU Colloq. 198: Near-fields cosmology with dwarf elliptical galaxies, ed. H. Jerjen & B. Binggeli, 259–260, **Manuel Metz**, P. Kroupa, & H. Jerjen
- "Where are tidal dwarf galaxies?", 2005, Astronomische Nachrichten, 326, 599–600, **Manuel Metz** & P. Kroupa
- "New results on the spatial distribution of Local Group galaxies", 2006, The Magellanic Clouds and dSph satellites: a nearby laboratory for galaxy evolution, `http://www.univie.ac.at/viennasat`, **Manuel Metz**
- "The satellite galaxies of the Milky Way and Andromeda. Are they of tidal origin?", 2007, A New Zeal for Old Galaxies, `http://astronomy.swin.edu.au/research/conferences/nz2007`, **Manuel Metz** & P. Kroupa
- "The spatial distribution and kinematical properties of the MW and M31 satellite galaxies", 2007, The Milky Way Halo – Stars and Gas, `http://www.astro.uni-bonn.de/~mwhalo`, **Manuel Metz** & P. Kroupa

Acknowledgement

I would like to express my deep and sincere gratitude to all those who gave me the possibility to complete this thesis.

My supervisor, Prof. Dr. Pavel Kroupa, inspired and encouraged me to work on this interesting and very important topic. I am deeply grateful for his support and advices.

Prof. Dr. Klaas S. de Boer has been always there to give advice. It was a great pleasure to me to learn from him and benefit from his broad knowledge.

I would like to thank Dr. Helmut Jerjen for very helpful discussions, Prof. Dr. Duncan Forbes for a great and inspiring time visiting Swinburne, and Dr. Noam I. Libeskind for kindly providing me the data of his work.

I wish to thank all members of the Argelander-Institut für Astronomie, especially of the Sternwarte who created a warm and friendly atmosphere, for an interesting and inspiring time at the Institute and many useful discussions. In particular I am grateful to Dr. Ole Marggraf, Dr. Oliver-Mark Corder, Jan Pflamm-Altenburg, Dr. Holger Baumgardt, and Dr. Michael Geffert.

Finally I wish to thank my parents and my family. I would like to give my special thanks to my wife Ann-Kristin. Her patient love enabled me to complete this work.